Technische Universität München

Fakultät für Mathematik
Lehrstuhl M2 – Fachgebiet Numerische Mathematik (Prof. Wohlmuth)

Multi-scale modeling of flow and transport processes in arterial networks and tissue

Tobias Thomas Köppl

Vollständiger Abdruck der von der Fakultät für Mathematik der Technischen Universität München zur Erlangung des akademischen Grades eines

Doktors der Naturwissenschaften (Dr. rer. nat.)

genehmigten Dissertation.

Vorsitzender: Univ.-Prof. Dr. Michael Ulbrich

Prüfer der Dissertation:

1. Univ.-Prof. Dr. Barbara Wohlmuth
2. Univ.-Prof. Dr. Boris Vexler
3. Univ.-Prof. Dr. Rainer Helmig, Universität Stuttgart

Die Dissertation wurde am 14.01.2015 bei der Technischen Universität München eingereicht und durch die Fakultät für Mathematik am 28.04.2015 angenommen.

Danksagung

Mein größter Dank gilt der Betreuerin meiner Arbeit: Prof. Dr. Barbara Wohlmuth. Ihr fachlicher Rat war mir bei vielen Problemen von großem Nutzen. Darüber hinaus konnte sie mir gute Kontakte zu anderen Arbeitsgruppen verschaffen. An dieser Stelle möchte ich mich ganz besonders bei Prof. Dr. Rainer Helmig (Institut für Hydromechanik, Stuttgart) für die Zeit, die er in viele Beratungsgespräche investiert hat, bedanken. Prof. Dr. Ulrich Pohl (Walter-Brendel-Zentrum, München) gebührt mein Dank für seine Hilfestellung bei medizinischen Fragen. Des Weiteren danke ich allen Mitgliedern des Lehrstuhls *Numerische Mathematik* (M2). Ihre Hilfe in Lehre und Forschung während der vergangenen Jahre, hat mir die tägliche Arbeit stark erleichtert. Schließlich möchte ich mich bei meiner Familie und meinen Freunden bedanken. Insbesondere danke ich meinen Eltern, die mich in schwierigen Situationen immer wieder aufgebaut haben und mir Zuversicht vermitteln konnten.

Abstract

This thesis is concerned with the simulation of blood flow and mass transport in vascularized human tissue. Our mathematical model is based on a domain decomposition approach, i.e., we separate the blood vessel network from the tissue and assign different flow and transport models to them. To simulate the transfer between the blood vessels and the tissue, appropriate coupling conditions are designed. The performance of our model is illustrated by some applications from bio-mechanics.

Zusammenfassung

In dieser Arbeit beschäftigen wir uns mit der Simulation von Blutfluss und Transportprozessen in vaskularisiertem menschlichen Gewebe. Unser Modell basiert auf einem Gebietszerlegungsansatz, d.h. wir trennen das Gefäßnetzwerk von dem Gewebe und beschreiben die Strömungs- und Transportprozesse mit verschiedenen Modellen. Um den Austausch zwischen den Gefäßen und dem Gewebe simulieren zu können, werden Kopplungsbedingungen aufgestellt. Das Modell wird auf Probleme aus der Biomechanik angewandt.

Contents

1 Introduction

Mathematical models have become more and more important in many applications from medicine and biology [9, 21, 24, 31, 34, 38, 109]. From metabolism and other processes taking place on the micro-level up to the modeling of the regulatory mechanisms of organs; bio-mathematical models provide the opportunity of gaining non-invasive insight into important physiological processes. This methodology can, thus make a huge contribution to understanding diseases.

In this thesis, we are concerned with the simulation of blood flow and mass transport, e.g., oxygen transport, from the heart through the arterial vessel system to the peripheral vessels and tissue. In particular, the impact of arterial stenoses on blood flow and oxygen supply is investigated. A stenosis is an abnormal narrowing in a blood vessel. Such a narrowing may arise from atherosclerosis, a specific form of arteriosclerosis, which is caused by the accumulation of fatty plaques and cholesterol. Typically, it appears in large- or middle-sized arteries. In carotid arteries, for example, stenoses are main causes of brain ischemia, when they become occluded either by a growing stenosis or, more acutely, by the development of a thrombus in the stenotic area [67, 75, 91]. In order to prevent diseases related to the formation of a stenosis such as myocardial infarction and stroke, one has to determine critical narrowing degrees and locations of stenoses. In this context, mathematical models enable us to determine the parameters of interest with less effort and fewer inaccuracies than invasive measurements.

When developing a mathematical model for blood flow and mass transport, we have to consider the basic structure of the human blood vessel system. The human blood vessels are divided into arteries and veins. These categories are further subdivided into various classes. In the case of the arteries, we have large- and middle-sized arteries, arterioles and capillaries. The vessels belonging to these classes exhibit very different features (see Table 1.1) and have specific roles within the circulatory system.

Table 1.1: Average sizes of the different vessel types [13].

Vessel type	**average diameter** $[cm]$	**number of vessels**	**average velocity** $[cm/s]$	**average pressure** $[mmHg]$
Large- and middle sized arteries	$\approx$ 0.3 – 3.0	≈ 55	$\approx 15-20$	**systolic:** 100 – 130 **diastolic:** 60 – 80
Arterioles	$\approx$ 0.002 – 0.3	$\approx 0.16 \cdot 10^9$	$\approx 1-15$	40 – 60
Capillaries	$\approx$ $9.0e-4$	$\approx 5.0 \cdot 10^9$	$\approx 0-1$	5 – 40
Venules	$\approx$ 0.0025 – 0.7	$\approx 0.5 \cdot 10^9$	$\approx 5-10$	0 – 5

While the large- and middle-sized arteries are responsible for transporting, for example, oxygen and nutrients to the organs, the arterioles have to decrease the blood velocity and pressure to make biochemical processes on the capillary level possible [13]. The veins are divided into capillaries, venules and large- and middle-sized veins. These vessels belong to the low-pressure region and are responsible for transporting the blood that is low in oxygen from the organs to the heart and the lungs. In this thesis, we restrict ourselves to arterial blood flow and its coupling with human tissue, whereas the venous vessel system will be accounted for by simplified or lumped parameter models.

Modeling blood flow and transport processes from large vessels down to the capillaries is a very complex matter, since one has to simulate flow on different scales through a huge number of vessels. To resolve every vessel within the arterial tree is unaffordable in terms of numerical simulation. Therefore, we take only the most important arteries of the vessel system into account, i.e., we truncate the network after some bifurcations. For our simulations, we use two different blood vessel networks, depicted in Figure 1.1. Both networks only contain some larger arteries of the whole arterial tree. When we consider the flow velocities in Table 1.1, it becomes obvious that flow in the larger vessels is fast compared with the flow in the arterioles and the rather diffusion-dominated flow in the capillaries and tissue. Because of this heterogeneous flow behavior, we require for the numerical modeling a scheme that uses small time steps for the fast flow region and large time steps for the slow flow region.

In order to keep the computational cost low, it is necessary to establish for the network flow a model which causes low computational effort in each time step. In this context, 1D reduced models proved very effective [16, 24, 37, 38, 113]. These models have the form of hyperbolic transport equation systems and can be derived from the Navier-Stokes equations and a convection-diffusion equation. In order to model flow and transport through a whole network, a *domain decomposition approach* has been applied, i.e., the network is split into its single vessels and the reduced 1D models are assigned to each vessel. At each bifurcation, the adjacent 1D models are coupled by characteristic information from the involved hyperbolic systems, pressure continuity and mass conservation. The resistance and compliance of the omitted vessels are accounted for by lumped parameter models [2, 4, 3] which are given by a system of ordinary differential equations (ODEs, 0D models). At the outlets of the terminal vessels of the network, these 0D models are coupled with the 1D models governing flow and transport within the corresponding vessels.

The flow and transport processes from the blood vessels into the surrounding tissue are modeled with the help of the coupling strategies presented in [24, 25, 26]. In these publications, human tissue and the feeding capillaries are regarded as a three-dimensional (3D) porous medium. Within the porous medium, flow and transport are governed by a diffusion-reaction equation, Darcy's law and a convection-diffusion equation. The challenge now consists in coupling these partial differential equations (PDEs) with the 1D problems modeling the flow and transport within the blood vessels. The 1D problems are defined on curves within the 3D tissue volume, where the curves are given by the main axes of the corresponding blood vessels.

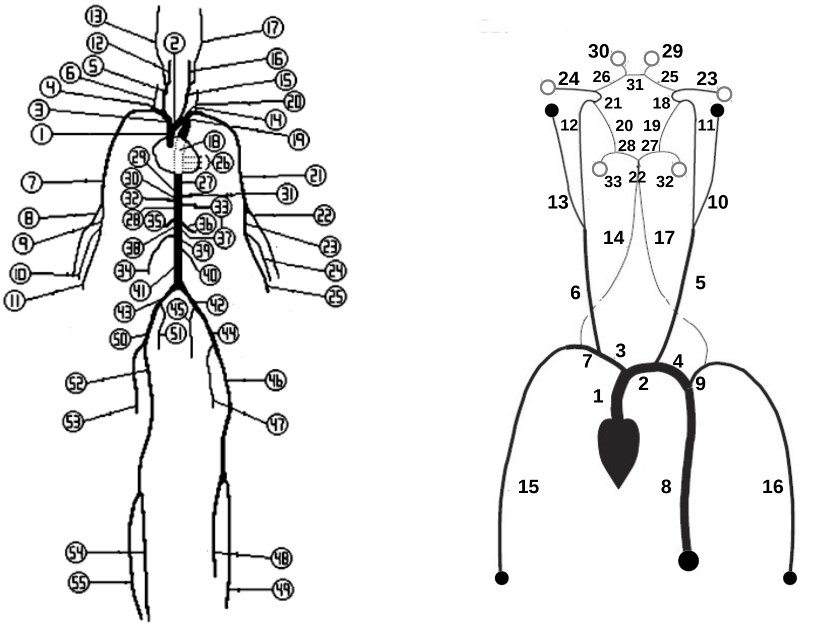

Figure 1.1: Arterial networks which are used for our simulations. The network on the left consists of 55 vessels including the aorta, carotids, and the most important arteries in legs and arms, while the network on the right exhibits only 33 vessels. Besides the aorta, it is composed of the carotids and the cerebral vessels supplying the brain tissue [3, 118].

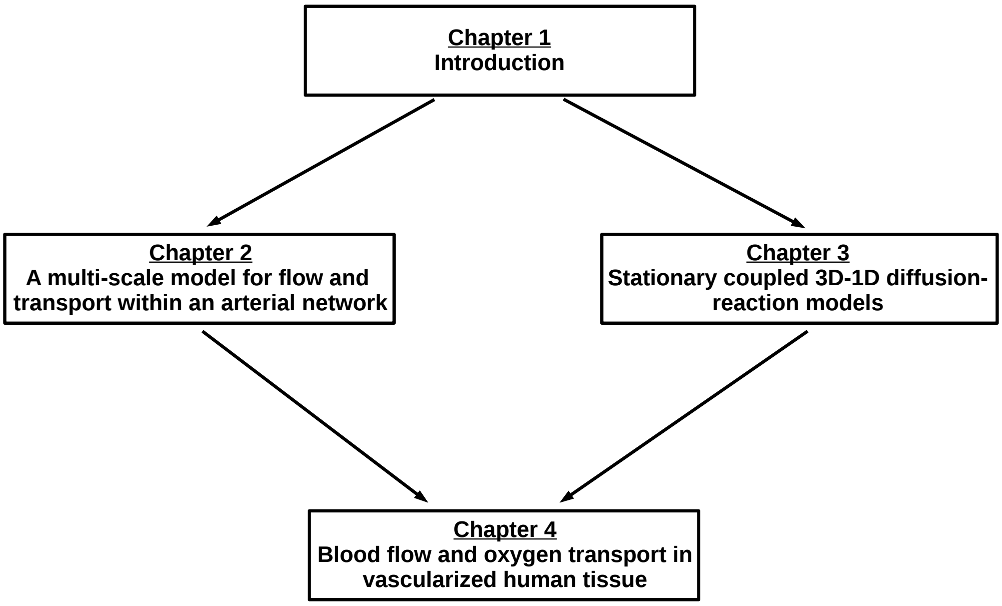

Figure 1.2: Structure of the thesis.

Since this kind of coupling is not standard, the basic principles were first introduced by means of elliptic model problems in 1D and 3D [26]. It is revealed that the PDEs in 1D and 3D can be coupled by their source terms, where the source term of the 3D problem is given by a weighted Dirac source term concentrated on the 1D curve. Due to the Dirac source term, the solution in 3D becomes singular at the 1D curve. The associated regularity reduction makes the analysis of such PDE systems more complicated and impairs the convergence of numerical schemes like Finite Elements or Finite Differences [98]. In order to facilitate the numerical analysis, weighted Sobolev spaces were introduced to study elliptic PDEs with Dirac source terms. Furthermore, locally refined meshes (graded meshes [6]) around the singular points or lines were considered to improve the convergence behavior of numerical schemes. In this context, optimal Finite element convergence rates have been shown by using weighted Sobolev norms and graded meshes. The theoretical insights gained by works like [6, 26] or [24, Chapters 3,4,5], have created the foundation for developing a model for flow and transport through blood vessels in tissue [24, Chapter 6].

The thesis is structured as follows (see Figure 1.2): in *Chapter 2*, we outline how a domain decomposition approach and spatially reduced models can be used to compute flow and transport through a network composed of large- and middle-sized vessels. In particular, it is shown how existing models can be extended to compute not only the flow but also the transport of given species like oxygen. The influence of stenoses is simulated by lumped parameter models presented in [108, 100, 120]. For the numerical treatment of the 1D transport equation systems, stabilized discontinuous Galerkin methods (DG methods) are used, where the schemes proposed in [58, 61, 62] had to be generalized to treat not only scalar transport equations, but also the transport equation systems under consideration. Furthermore, we perform some numerical tests to demonstrate the accuracy of these discretization methods. In the final section of this chapter, the numerical model is used to study the impact of a unilateral carotid stenosis on brain oxygenation.

The next chapter (*Chapter 3*) is concerned with the numerical analysis and solution of elliptic PDEs with Dirac source terms. Before we investigate the numerical approximation of coupled problems, a standard Poisson problem with Dirac point sources is considered which can be derived under some simplifying assumptions from a 3D-1D diffusion-reaction problem (see Section 3.1). It is shown that standard Finite Elements applied to such a type of problem exhibit no pollution effect, i.e., the method converges optimally with respect to a L^2-semi-norm excluding the locations of the Delta source terms. For the proof of this result, no graded meshes are required; it is sufficient to use a family of uniform meshes. Numerical tests in two and three space dimensions confirm our theoretical results. In the remainder of this chapter, iterative solution schemes for coupled problems are discussed. The idea of these solution schemes relies on the principle of decoupling the subproblems such that only standard elliptic problems have to be solved in each iteration.

Finally, in *Chapter 4*, we put all the models and techniques developed in *Chapter 2* and *Chapter 3* together to simulate the influence of a peripheral arterial stenosis on local tissue perfusion and flow within the network. For our simulations we used the arterial tree, depicted on the left-hand side of Figure 1.1. The stenosis and the outflow boundaries are modeled by 0D models, the network flow and transport are governed by 1D transport equation systems and the transfer from the blood vessels to the tissue is modeled by a

3D-1D coupling according to *Chapter 3*. All in all, this results in a *3D-1D-0D multi-scale model* to investigate the issue of interest. At the end of this chapter, some simulation results are presented.

2 A multi-scale model for flow and transport within an arterial network

As a first step towards a complete model for flow and mass transport in tissue surrounding an arterial network, we derive in this chapter a model for network flow and transport. Flow and transport within the tissue and the coupling between the network and the tissue are described in the following chapters. The model for the network is based on a domain decomposition technique, i.e., we split the network into its single vessels and assign in a first step to each vessel a decoupled model. In the second step, the independent subsystems are interconnected by suitable coupling conditions (see Figure 2.1).

Flow and transport within a single vessel are computed by the help of existing models for blood flow and mass transport. These models are given by one-dimensional non-linear transport equation systems for larger vessels and linear transport equation systems for middle sized vessels, which exhibit only small deformations of their section areas. For small vessels we use a model, consisting of a system of ordinary differential equations (ODEs). In the references [16, 24], the transport equation systems are often called *1D reduced models*, whereas the ODE systems are known as *0D lumped parameter models* [83]. Due to the fact that models of different space dimensions are used, we have a multi-scale model for the network (see Subsection 2.1).

To solve the transport equation systems numerically, we use limited DG methods developed in [58, 60, 61, 62]. The accuracy of these methods is illustrated by convergence and mass conservation tests (see Subsection 2.2 and 2.4).

If the considered network is composed of vessels having different length scales and other different physical properties, it is beneficial to use these different numerical model types to take the special features of the vessels into account. In Subsection 2.3, we outline how the different model types can be interconnected at a bifurcation. Moreover, it is explained how inflow and outflow boundary conditions can be incorporated into the numerical scheme.

Finally, in Subsection 2.4, an application from medical engineering is considered, i.e., the simulation of brain oxygenation. In particular, we focus on the influence of a unilateral carotid artery stenosis on the oxygen supply of brain tissue. The impact of a stenosis is modeled by a system of ODEs, which is similar to the lumped parameter model for the small vessels [100, 108, 120]. A further system of ODEs is used, to simulate the resistance at the outlets of the arterial vessel system and the oxygen consumption within the brain tissue [4],[24, Section 2.5].

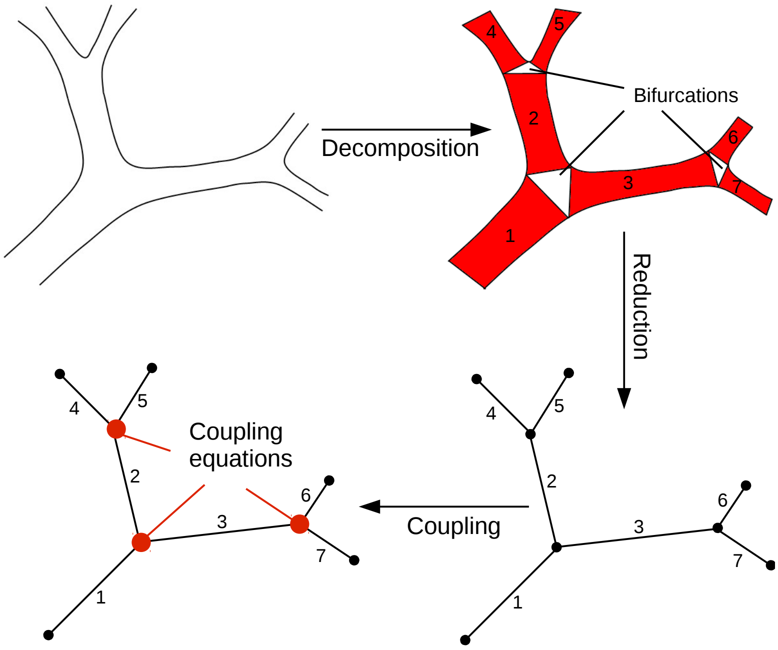

Figure 2.1: This figure illustrates the basic steps of our domain decomposition approach. In the upper left corner of this figure, we can see a small network, which exhibits three bifurcations. We split the network into its single vessels and assign a number to each vessel. Next spatially reduced models are attached to every vessel, to compute flow and transport processes in a single vessel. Finally the models adjacent to a bifurcation are coupled by suitable coupling conditions.

2.1 Modeling a single vessel

In order to avoid expensive 3D computations in terms of flow and mass transport within in a single vessel, 3D models like the Navier-Stokes equations are replaced by 1D reduced models or 0D lumped parameter models. There are in principle two ways for the derivation of a 1D model. The first one is based on mass conservation and the balance of momentum [4, 103], while the second approach uses averaging techniques to deduce the 1D model from an existing 3D model. In the following, we briefly describe the first approach. For a discussion of the second approach, we refer to [16, 24].

2.1.1 One dimensional modeling based on balance equations

For simplicity, we assume that the considered vessel can be represented by an axisymmetric domain $\Omega \subset \mathbb{R}^3$, whose main axis is aligned with a coordinate axis, e.g., the z-axis (see Figure 2.2). The domain Ω is parameterized at each time t by cylindrical coordinates:

$$\Omega(t) = \left\{ (r, \varphi, z) \in \mathbb{R}^3 \,|\, 0 \leq z \leq l,\ 0 \leq \varphi < 2\pi,\ 0 \leq r \leq R(z,t) \right\} \tag{2.1}$$

By $R(z,t)$, we denote the radius of the section $S(z,t)$ located at z and for the time point t. l is the length of the vessel. The area of $S(z,t)$ is given by: $A(z,t) = R^2(z,t)\pi \ \left[cm^2\right]$.

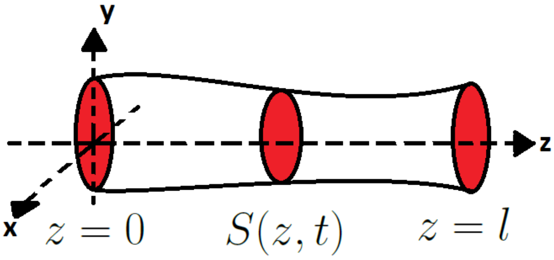

Figure 2.2: Simplified geometry. The vessel is assumed to be a straight cylinder with circular section.

As a first step towards our 1D model, we consider a small portion of the vessel Ω, having the length Δz. Computing the mass balance for this small segment, we have:

$$\frac{\partial}{\partial t}\rho A(z)\Delta z = \rho Q(z) - \rho Q\left(z+\Delta z\right) + \phi'_M$$

or in differential form for the limit $\Delta z \to 0$:

$$\frac{\partial A}{\partial t} + \frac{\partial Q}{\partial z} = \phi_M, \tag{2.2}$$

where we assume that the fluid is incompressible. By $\rho \ \left[kg/cm^3\right]$, we denote the density of the fluid. It is taken to be constant. $\phi'_M \ [kg/s]$ and $\phi_M \ \left[cm^2/s\right]$ are source terms. The variable $Q \ \left[cm^3/s\right]$ is the mass flux through the section $S(z,t)$.

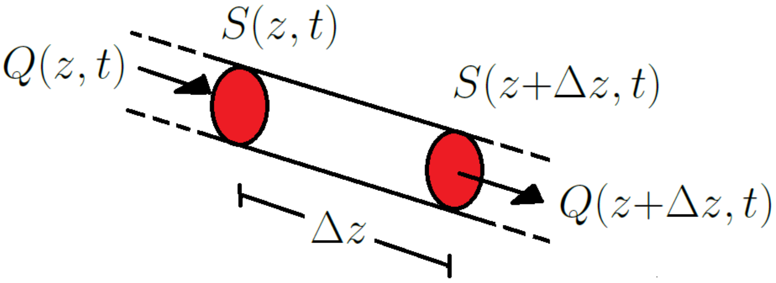

Figure 2.3: Mass conservation at a small segment.

The momentum balance equation for the control volume depicted in Figure 2.3, reads as follows:

$$\frac{\partial}{\partial t}\rho Q\Delta z = \rho\left(Av^2\right)(z) - \rho\left(Av^2\right)(z+\Delta z) + \phi'_l$$

or in differential form for $\Delta z \to 0$:

$$\frac{\partial Q}{\partial t} + \frac{\partial}{\partial z}\left(\frac{Q^2}{A}\right) = \phi_l, \tag{2.3}$$

where we assume again that the fluid is incompressible. The 1D velocity field v is given by:

$$v = \frac{Q}{A}. \tag{2.4}$$

$\phi_l' \left[\frac{kg\cdot m}{s^2}\right]$ and $\phi_l \left[\frac{m^3}{s}\right]$ are momentum source terms. In our model the source term ϕ_l depends on a friction term f and the pressure p:

$$\phi_l = \underbrace{f}_{\text{friction term}} \underbrace{-\frac{A}{\rho}\frac{\partial p}{\partial z}}_{\text{pressure term}} .$$

The friction force term per unit length is given by [4, 16, 107]:

$$f(z,t) = 2\mu\pi R(z,t)\left[\frac{\partial u}{\partial r}\right]_{r=R},$$

where μ is the viscosity of the fluid and $u\,(r,\varphi,z,t)$ is the 3D velocity field in cylindrical coordinates. A possible function of the 3D velocity field satisfying the no-slip condition is given by:

$$u\,(r,\varphi,z,t) = \frac{Q}{A}(z,t)\frac{\gamma+2}{\gamma}\left[1-\left(\frac{r}{R(z,t)}\right)^{\gamma}\right], \tag{2.5}$$

which yields the following friction term:

$$f(z,t) = -2\mu\pi\,(\gamma+2)\,\frac{Q}{A}(z,t).$$

The parameter γ determines the shape of the velocity profile. The choice $\gamma = 2$, e.g., corresponds to a parabolic velocity profile (Figure 2.4), which yields a Poiseuille's resistance term: $f = -8\mu\pi Q/A$. In order to compute the propagation of a substance's concentration within the fluid, we use a scalar transport equation whose 1D velocity field is given by (2.4):

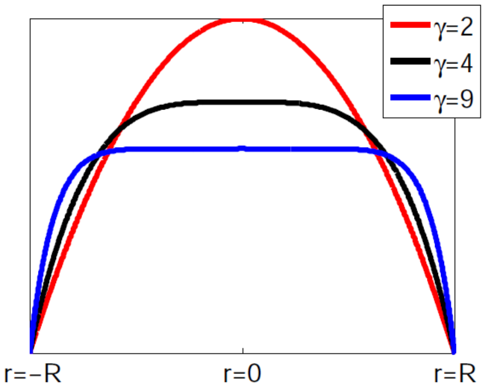

Figure 2.4: The picture shows some velocity profiles for the z-component u_z in dependence of the radial coordinate r.

$$\frac{\partial\Gamma}{\partial t} + \frac{\partial}{\partial z}\left(\frac{Q\Gamma}{A}\right) = -\phi_p\frac{\Gamma}{A}, \tag{2.6}$$

the variable $\Gamma \left[\frac{mmol}{cm}\right]$ is the averaged concentration of a certain substance. The factor $\phi_p \left[\frac{cm^2}{s}\right]$ is linked to the permeability of the vessel wall. Summarizing (2.2),(2.3) and (2.6), we have the following transport equation system in one space dimension:

$$\frac{\partial A}{\partial t} + \frac{\partial Q}{\partial z} = \phi_M, \quad z \in (0,l),\ t > 0, \tag{2.7a}$$

$$\frac{\partial Q}{\partial t} + \frac{\partial}{\partial z}\left(\frac{Q^2}{A}\right) + \frac{A}{\rho}\frac{\partial p}{\partial z} = -2\mu\pi\,(\gamma+2)\,\frac{Q}{A}, \quad z \in (0,l),\ t > 0, \tag{2.7b}$$

$$\frac{\partial \Gamma}{\partial t} + \frac{\partial}{\partial z}\left(\frac{Q\Gamma}{A}\right) = -\phi_p \frac{\Gamma}{A}, \quad z \in (0,l),\ t > 0. \tag{2.7c}$$

The initial state with respect to the unknowns (A,p,Q,Γ) is given by: $(A,p,Q,\Gamma) = (A_0,0,0,0)$. Within this PDE system, the number of unknowns exceeds the number of equations. Therefore we have to provide an additional equation for the pressure, linking the variable A to the pressure. In the context of blood flow simulations (see Subsection 2.4), the system is closed by the following relationship between pressure and cross-section area [35, 36, 37, 40, 78]:

$$p(z,t) = G_0\left(\sqrt{\frac{A(z,t)}{A_0(z)}} - 1\right),\ G_0 = \frac{\sqrt{\pi}h_0 E}{\left(1-\nu^2\right)\sqrt{A_0}}, \tag{2.8}$$

where E is the Young's modulus, h_0 is the vessel thickness, A_0 is the vessel area for $t = 0$ and ν denotes the Poisson ration of the vessel wall.

Remark 2.1. *The relation given by* (2.8) *is based on a model, describing the dynamics of the vessel wall [37]. Neglecting the inertia effect and using the relation of static equilibrium in radial direction for a cylindrical tube,* (2.8) *can be derived. For the sake of simplicity, we consider the parameters A_0 and G_0 as constant with respect to space and time. The steps required to incorporate the effect of a tapered vessel are reported in [37].*

For the derivative of the pressure it follows from Remark 2.1:

$$\frac{\partial p}{\partial z} = \frac{\partial p}{\partial A}\frac{\partial A}{\partial z} + \frac{\partial p}{\partial A_0}\frac{\partial A_0}{\partial z} + \frac{\partial p}{\partial G_0}\frac{\partial G_0}{\partial z} = \frac{G_0}{2}\sqrt{\frac{1}{AA_0}}\frac{\partial A}{\partial z}.$$

Inserting this expression into (2.7b), we have due to $\frac{A}{\rho}\frac{\partial p}{\partial z} = \frac{G_0}{3\rho\sqrt{A_0}}\frac{\partial}{\partial z}A^{\frac{3}{2}}$:

$$\frac{\partial A}{\partial t} + \frac{\partial Q}{\partial z} = \phi_M, \quad z \in (0,l),\ t > 0, \tag{2.9a}$$

$$\frac{\partial Q}{\partial t} + \frac{\partial}{\partial z}\left(\frac{Q^2}{A}\right) + \frac{G_0}{3\rho\sqrt{A_0}}\frac{\partial}{\partial z}A^{\frac{3}{2}} = -2\mu\pi\,(\gamma+2)\,\frac{Q}{A}, \quad z \in (0,l),\ t > 0, \tag{2.9b}$$

$$\frac{\partial \Gamma}{\partial t} + \frac{\partial}{\partial z}\left(\frac{Q\Gamma}{A}\right) = -\phi_p \frac{\Gamma}{A}, \quad z \in (0,l),\ t > 0. \tag{2.9c}$$

Having the values A and Γ, the volumetric concentration $c\ \left[mmol/cm^3\right]$ can be computed by:

$$c = \frac{\Gamma}{A}.$$

Thus the PDE system (2.9a)-(2.9c) can be written in conservation form:

$$\frac{\partial \mathbf{U}}{\partial t} + \frac{\partial \mathbf{F}(\mathbf{U})}{\partial z} = \mathbf{S}(\mathbf{U}) \tag{2.10}$$

The flux function $\mathbf{F}$ and the source term $\mathbf{S}$ of the transport equation (2.11) are given by:

$$\mathbf{F}(\mathbf{U}) = \begin{pmatrix} Q \\ \frac{Q^2}{A} + \frac{G_0}{3\rho\sqrt{A_0}} A^{\frac{3}{2}} \\ \frac{\Gamma Q}{A} \end{pmatrix}, \qquad \mathbf{S}(\mathbf{U}) = \begin{pmatrix} \phi_M \\ -2\mu\pi\left(\gamma+2\right)\frac{Q}{A} \\ -\phi_p \frac{\Gamma}{A} \end{pmatrix}. \tag{2.11}$$

$\mathbf{U} = (A, Q, \Gamma)$ denotes the vector of unknowns. It is obvious that the transport equations for A, Q are independent of the third variable Γ. Thus they can be regarded as a subsystem, having its own flux function $\mathbf{F}_{AQ}$ and source term $\mathbf{S}_{AQ}$:

$$\mathbf{F_{AQ}}(\mathbf{U_{AQ}}) = \begin{pmatrix} Q \\ \frac{Q^2}{A} + \frac{G_0}{3\rho\sqrt{A_0}} A^{\frac{3}{2}} \end{pmatrix}, \qquad \mathbf{S_{AQ}}(\mathbf{U_{AQ}}) = \begin{pmatrix} \phi_M \\ -2\mu\pi\left(\gamma+2\right)\frac{Q}{A} \end{pmatrix}. \tag{2.12}$$

where $\mathbf{U}_{AQ} = (A, Q)$. The flux function $\mathbf{F}_\Gamma$ and source term $\mathbf{S}_\Gamma$ for the third transport equation are given by:

$$\mathbf{F_\Gamma}(\mathbf{U}) = \frac{Q\Gamma}{A}, \qquad \mathbf{S_\Gamma}(\mathbf{U}) = -\phi_p \frac{\Gamma}{A}. \tag{2.13}$$

All in all we have:

$$\frac{\partial \mathbf{U_{AQ}}}{\partial t} + \frac{\partial}{\partial z}\mathbf{F_{AQ}}(\mathbf{U_{AQ}}) = \mathbf{S_{AQ}}(\mathbf{U_{AQ}}), \tag{2.14a}$$

$$\frac{\partial \Gamma}{\partial t} + \frac{\partial}{\partial z}\left(\frac{Q\Gamma}{A}\right) = -\phi_p \frac{\Gamma}{A}. \tag{2.14b}$$

Obviously, this PDE-system consists of a non-linear part (2.14a) and a linear part (2.14b). Between these two parts, we have an unilateral interconnection. The non-linear PDE system provides the velocity field for the scalar transport equation. On the other hand, the averaged concentration Γ does not occur in (2.14a).

In order to obtain more insight into the behavior of the solution $\mathbf{U}$, we compute the characteristics of (2.14a). As a first step, (2.14a) is written in quasi-linear form:

$$\frac{\partial \mathbf{U_{AQ}}}{\partial t} + \mathbf{H}\left(\mathbf{U_{AQ}}\right)\frac{\partial \mathbf{U_{AQ}}}{\partial z} = \mathbf{S_{AQ}}(\mathbf{U_{AQ}}). \tag{2.15}$$

The flux matrix $\mathbf{H}\left(\mathbf{U_{AQ}}\right)$ is given by:

$$\mathbf{H}\left(\mathbf{U_{AQ}}\right) = \frac{\partial \mathbf{F_{AQ}}}{\partial \mathbf{U_{AQ}}}\left(\mathbf{U_{AQ}}\right) = \begin{pmatrix} 0 & 1 \\ c_{AQ}^2 - v^2 & 2v \end{pmatrix}, \tag{2.16}$$

where

$$c_{AQ}^2 = \frac{G_0}{2\rho}\sqrt{\frac{A}{A_0}} \text{ and } v = \frac{Q}{A}. \tag{2.17}$$

The value c_{AQ} is often referred to as the *sound speed* of the physical system. The next step consists of a decoupling of the two equations in (2.14a). For this purpose, we decompose the flux matrix $\mathbf{H}\left(\mathbf{U_{AQ}}\right)$ as follows:

$$\mathbf{H}\left(\mathbf{U_{AQ}}\right) = L^{-1}\left(\mathbf{U_{AQ}}\right)\Lambda\left(\mathbf{U_{AQ}}\right)L\left(\mathbf{U_{AQ}}\right),$$

where $\Lambda\left(\mathbf{U_{AQ}}\right)$ is a diagonal matrix consisting of the two eigenvalues of $\mathbf{H}\left(\mathbf{U_{AQ}}\right)$. $L\left(\mathbf{U_{AQ}}\right)$ denotes the matrix of left eigenvectors. By the help of this decomposition and (2.15) it follows:

$$L\left(\mathbf{U_{AQ}}\right)\frac{\partial \mathbf{U_{AQ}}}{\partial t} + \Lambda\left(\mathbf{U_{AQ}}\right)L\left(\mathbf{U_{AQ}}\right)\frac{\partial \mathbf{U_{AQ}}}{\partial z} = L\left(\mathbf{U_{AQ}}\right)\mathbf{S}\left(\mathbf{U_{AQ}}\right).$$

Defining the characteristic variables $\mathbf{W_{AQ}} = \left(W_1^{AQ}, W_2^{AQ}\right)^T$ by:

$$\frac{\partial \mathbf{W_{AQ}}}{\partial \mathbf{U_{AQ}}} = L\left(\mathbf{U_{AQ}}\right), \quad \mathbf{W}^0 = \mathbf{W_{AQ}}\left(\mathbf{U^0_{AQ}}\right), \quad \mathbf{U^0_{AQ}} = \left(A_0, 0\right)^T, \tag{2.18}$$

we have the following decoupled system:

$$\frac{\partial \mathbf{W_{AQ}}}{\partial t} + \Lambda\left(\mathbf{W_{AQ}}\right)\frac{\partial \mathbf{W_{AQ}}}{\partial z} = L\left(\mathbf{W_{AQ}}\right)\mathbf{S}\left(\mathbf{W_{AQ}}\right).$$

In order to compute explicit formulas for W_1^{AQ} and W_2^{AQ}, one needs to integrate the characteristic differential equation (2.18). To do so, the eigenvalues in $\Lambda\left(\mathbf{U_{AQ}}\right)$ and the left eigenvectors in $L\left(\mathbf{U_{AQ}}\right)$ have to be computed.

Property 2.1. *The matrix* $\mathbf{H}\left(\mathbf{U_{AQ}}\right)$ *admits two real eigenvalues:*

$$\lambda_1 = v - c_{AQ} \textit{ and } \lambda_2 = v + c_{AQ},$$

associated with the corresponding left eigenvectors:

$$l_1 = -\frac{1}{A}\begin{pmatrix} -c_{AQ} - v \\ 1 \end{pmatrix} \textit{ and } l_2 = \frac{1}{A}\begin{pmatrix} c_{AQ} - v \\ 1 \end{pmatrix}.$$

Property 2.1 can be verified by some simple computations. The matrix $L\left(\mathbf{U_{AQ}}\right)$ is given then by: $L\left(\mathbf{U_{AQ}}\right) = \begin{pmatrix} l_1^T \\ l_2^T \end{pmatrix}$.

Remark 2.2. *For our application areas, we can assume that $c_{AQ} > v$ holds. Consequently, it holds $\lambda_1 < 0$ and $\lambda_2 > 0$. This means that the characteristic variable W_1^{AQ} can be regarded as a backward travelling wave, whereas the characteristic variable W_2^{AQ} can be regarded as a forward travelling wave (see Figure 2.5). In order to guarantee a well-posed system, for the fluid equations, we have to impose at each end of the vessel one boundary condition, while for the mass transport, the prescription of a boundary condition depends on the sign of the velocity field v.*

Theorem 2.1. *The characteristics* $\mathbf{W_{AQ}} = \left(W_1^{AQ}, W_2^{AQ}\right)^T$ *of the system* (2.14a) *are given by:*

$$W_1^{AQ} = -v + 4c_{AQ} = -\frac{Q}{A} + 4\sqrt{\frac{G_0}{2\rho}}\left(\frac{A}{A_0}\right)^{\frac{1}{4}},$$
$$W_2^{AQ} = v + 4c_{AQ} = \frac{Q}{A} + 4\sqrt{\frac{G_0}{2\rho}}\left(\frac{A}{A_0}\right)^{\frac{1}{4}}.$$

Proof. The formulas can be computed by integrating the equation: $\dfrac{\partial \mathbf{W_{AQ}}}{\partial \mathbf{U_{AQ}}} = L\left(\mathbf{U_{AQ}}\right)$, which reads as:

$$\frac{\partial \mathbf{W_{AQ}}}{\partial \mathbf{U_{AQ}}} = \frac{1}{A}\begin{pmatrix} c_{AQ}+v & -1 \\ c_{AQ}-v & 1 \end{pmatrix}$$

□

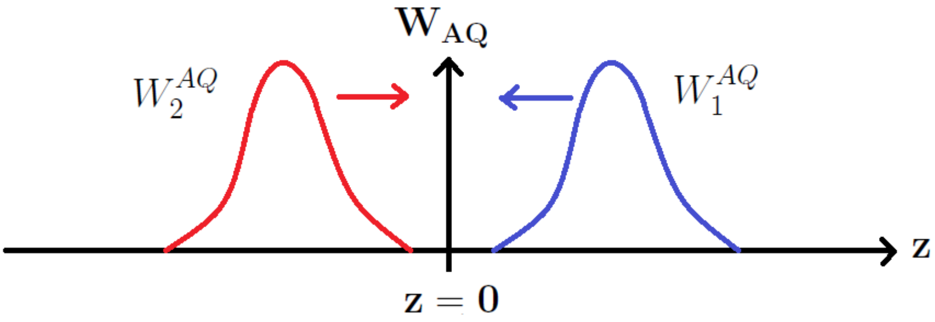

Figure 2.5: Directions of motion of the characteristics W_1^{AQ} and W_2^{AQ}.

Based on Theorem 2.1, we can determine the primary variables by:

$$A = \left(\frac{W_2^{AQ} + W_1^{AQ}}{8}\right)^4 \frac{A_0}{c_{AQ,0}^4}, \quad Q = \left(\frac{W_2^{AQ} - W_1^{AQ}}{2}\right) A, \quad c_{AQ,0} = \sqrt{\frac{G_0}{2\rho}}. \tag{2.19}$$

Due to the fact that equation (2.14b), which models the mass transport:

$$\frac{\partial \Gamma}{\partial t} + \frac{\partial}{\partial z}\left(\frac{Q\Gamma}{A}\right) = -\phi_p \frac{\Gamma}{A},$$

is scalar and linear in Γ, the direction of motion of Γ depends on the sign of the velocity field v, provided by System (2.14a).

2.1.2 Linearized model

The non-linear transport equation (2.14a) can be further simplified by linearizing the flux function $\mathbf{F_{AQ}}\left(\mathbf{U_{AQ}}\right)$ and the source term $\mathbf{S_{AQ}}\left(\mathbf{U_{AQ}}\right)$ about the initial state

$$\mathbf{U^0_{AQ}} = (A_0, 0)\,.$$

The new variables a, p and q can be considered as pertubation variables for the section area, pressure and volume flux:

$$(A, p, Q) = (A_0 + a, p, q)\,.$$

If the deformation of the vessels are small or can be neglected, the linearized model yields sufficiently precise results.

Theorem 2.2. *The linearized flux* $\mathbf{F_{pq}}\left(\mathbf{U_{pq}}\right)$ *and source term* $\mathbf{S_{pq}}\left(\mathbf{U_{pq}}\right)$ *of* (2.14a) *are given by:*

$$\mathbf{F_{pq}}\left(\mathbf{U_{pq}}\right) = \begin{pmatrix} \frac{q}{C_{1D}} \\ \frac{p}{L_{1D}} \end{pmatrix}, \quad \mathbf{S_{pq}}\left(\mathbf{U_{pq}}\right) = \begin{pmatrix} \phi_M / C_{1D} \\ -R_{1D} q \end{pmatrix}, \tag{2.20}$$

where

$$L_{1D} = \frac{\rho}{A_0}, \quad C_{1D} = \frac{A_0}{\rho c^2_{AQ,0}}, \quad R_{1D} = \frac{2(\gamma+2)\pi\mu}{A_0^2} \text{ and } \mathbf{U_{pq}} = \begin{pmatrix} p \\ q \end{pmatrix}. \tag{2.21}$$

Proof. Defining $\mathbf{U_l} = \begin{pmatrix} a \\ q \end{pmatrix}$, we have for the Taylor expansion of first order applied to $\mathbf{F_{AQ}}\left(\mathbf{U_{AQ}}\right)$ and $\mathbf{S_{AQ}}\left(\mathbf{U_{AQ}}\right)$ (2.12):

$$\mathbf{F_{AQ}}\left(\mathbf{U_{AQ}}\right) = \mathbf{F_{AQ}}\left(\mathbf{U^0_{AQ}} + \mathbf{U_l}\right) \approx \mathbf{F}\left(\mathbf{U^0_{AQ}}\right) + \mathbf{H}(\mathbf{U^0_{AQ}}) \underbrace{\left(\mathbf{U_{AQ}} - \mathbf{U^0_{AQ}}\right)}_{\mathbf{U}_l} =$$

$$= \begin{pmatrix} 0 \\ \frac{2}{3} c^2_{AQ,0} A_0 \end{pmatrix} + \begin{pmatrix} 0 & 1 \\ c^2_{AQ,0} & 0 \end{pmatrix} \begin{pmatrix} a \\ q \end{pmatrix},$$

$$\mathbf{S_{AQ}}\left(\mathbf{U_{AQ}}\right) = \mathbf{S_{AQ}}\left(\mathbf{U^0_{AQ}} + \mathbf{U_l}\right) \approx \mathbf{S}\left(\mathbf{U^0_{AQ}}\right) + \frac{\partial \mathbf{S}\left(\mathbf{U^0_{AQ}}\right)}{\partial \mathbf{U_{AQ}}} \underbrace{\left(\mathbf{U_{AQ}} - \mathbf{U^0_{AQ}}\right)}_{\mathbf{U}_l} = \begin{pmatrix} \phi_M \\ -R_{1D} q \end{pmatrix}.$$

Linearizing the pressure in (2.8) about A_0 yields:

$$p(A) \approx p\left(A_0\right) + \frac{\partial}{\partial A} p\left(A_0\right)\left(A - A_0\right) = \frac{a}{C_{1D}}.$$

Due to $\frac{\partial}{\partial z}\mathbf{F}\left(\mathbf{U^0_{AQ}}\right) = 0$, we can neglect the constant term $\mathbf{F}\left(\mathbf{U^0_{AQ}}\right)$ and the linearized system of (2.14a) in p and q reads as follows:

$$\frac{\partial}{\partial t}\begin{pmatrix} p \\ q \end{pmatrix} + \frac{\partial}{\partial z}\begin{pmatrix} \frac{q}{C_{1D}} \\ \frac{p}{L_{1D}} \end{pmatrix} = \begin{pmatrix} \phi_M / C_{1D} \\ -R_{1D} q \end{pmatrix}. \tag{2.22}$$

Using (2.22) the formulas for the linearized flux and source term can be deduced. □

The scalar transport equation does not have to be linearized, because it is already linear in Γ. Under the assumption $A \approx A_0$, it follows based on (2.9c):

$$\frac{\partial c}{\partial t} + \frac{\partial}{\partial z}\left(\frac{cq}{A_0}\right) = -\frac{\phi_p}{A_0}c, \tag{2.23}$$

where $c = \frac{\Gamma}{A_0}\ \left[\frac{mmol}{cm^3}\right]$. Introducing the matrix:

$$H_l = \begin{pmatrix} 0 & \frac{1}{C_{1D}} \\ \frac{1}{L_{1D}} & 0 \end{pmatrix}$$

and summarizing (2.20)-(2.23), we have the following linearized system for flow and mass transport:

$$\frac{\partial}{\partial t}\begin{pmatrix} p \\ q \end{pmatrix} + H_l \frac{\partial}{\partial z}\begin{pmatrix} p \\ q \end{pmatrix} = \begin{pmatrix} \phi_M / C_{1D} \\ -R_{1D}q \end{pmatrix}, \tag{2.24a}$$

$$\frac{\partial c}{\partial t} + \frac{\partial}{\partial z}\left(\frac{cq}{A_0}\right) = -\frac{\phi_p}{A_0}c. \tag{2.24b}$$

A comparison of (2.24a),(2.24b) and (2.14a),(2.14b) yields that we have again a one-directional coupling between the subsystem modeling the flow and the subsystem modeling the mass transport. Here (2.24a) provides the velocity field $v = \frac{Q}{A_0}$ for (2.24b).

To get a better understanding of the hydraulic parameters L_{1D}, C_{1D}, R_{1D}, and the variables p and q, it is helpful to establish an analogy to electricity. In this context, the pressure p can be compared to the voltage within an electric circuit, whereas the flow rate q can be regarded as the counterpart to the electric current. The parameter L_{1D} accounting for the inertia of the fluid is the equivalent to the inductance of a choke. C_{1D} depends on the elasticity of the vessel wall and the initial section area A_0, thus it determines, how much fluid volume can be absorbed within a certain vessel. In electricity the capacity of a condensator reveals how much charge can be stored by a certain condensator. R_{1D} is linked to the viscosity μ of the fluid. Therefore, it measures the resistance for the flow and can be considered as the counterpart of the electric resistance. In Table 2.1, the different parameters and variables are summarized.

Table 2.1: Analogy between hydraulic and electric networks [38].

Hydraulic	**Electric**
pressure p	voltage
flow rate q	current
compliance C_{1D}	capacity
inertia L_{1D}	inductance
viscosity R_{1D}	resistance

As in the previous section, we are interested in the characteristic variables of the system in order to impose the boundary conditions in a correct way and to get more insight into the structure of the solution (see also Remark 2.2). To this end, one has to transform the matrix H_l into a diagonal matrix, containing the eigenvalues of H_l.

Property 2.2. *The matrix H_l admits two real eigenvalues:*

$$\lambda_1 = -\frac{1}{\sqrt{C_{1D} \cdot L_{1D}}} = -c_{AQ,0} \text{ and } \lambda_2 = \frac{1}{\sqrt{C_{1D} \cdot L_{1D}}} = c_{AQ,0}, \quad c_{AQ,0} = \sqrt{\frac{G_0}{2\rho}},$$

associated with the corresponding left eigenvectors:

$$l_1 = \frac{1}{2}\begin{pmatrix} -\sqrt{\frac{C_{1D}}{L_{1D}}} \\ 1 \end{pmatrix} \text{ and } l_2 = \frac{1}{2}\begin{pmatrix} \sqrt{\frac{C_{1D}}{L_{1D}}} \\ 1 \end{pmatrix}.$$

Defining L and Λ_l by: $L = \begin{pmatrix} l_1^T \\ l_2^T \end{pmatrix}$ and $\Lambda_l = \begin{pmatrix} \lambda_1 & 0 \\ 0 & \lambda_2 \end{pmatrix}$, we have the following decomposition:

$$H_l = L \cdot \Lambda_l \cdot L^{-1}.$$

Similar computations, as for the derivation of (2.18) yield that the characteristic variables $\mathbf{W_{pq}} = (W_1^{pq}, W_2^{pq})^T$ of (2.24a) have to satisfy the following differential equation:

$$\frac{\partial \mathbf{W_{pq}}}{\partial \mathbf{U_{pq}}} = L, \quad \mathbf{W}^0 = (0,0)^T. \tag{2.25}$$

After solving (2.25), we have explicit formulas for the characteristic variables W_1^{pq} and W_2^{pq}.

Theorem 2.3. *The characteristic variables $\mathbf{W_{pq}} = (W_1^{pq}, W_2^{pq})^T$ of* (2.24a) *are given by:*

$$W_1^{pq} = \frac{1}{2}\left(-\sqrt{\frac{C_{1D}}{L_{1D}}}p + q\right) \text{ and } W_2^{pq} = \frac{1}{2}\left(\sqrt{\frac{C_{1D}}{L_{1D}}}p + q\right).$$

Based on Theorem 2.3 we can easily compute the primary variables p and q by:

$$p = -\sqrt{\frac{L_{1D}}{C_{1D}}}\left(W_1^{pq} - W_2^{pq}\right) \text{ and } q = W_1^{pq} + W_2^{pq}. \tag{2.26}$$

Remark 2.3. *As the flux matrix in the non-linear case* (2.15)*, H_l has also two eigenvalues with different sign: $\lambda_1 < 0$ and $\lambda_2 > 0$. Consequently we have to impose at each end of the vessel one boundary condition for the linear fluid equations* (2.24a)*. For the mass transport, the situation is also the same as in the non-linear case. Depending on the sign of the velocity field in* (2.24b)*, we have to prescribe a boundary value or not.*

2.1.3 Lumped parameter model

Let us suppose that our network consists of vessels whose lengths differ significantly. In this setting, it is reasonable to model the flow and mass transport through the smaller vessels by different models than those which were introduced in the previous subsections. This is motivated as follows: If we have a sufficiently high velocity of the fluid, pressure and velocity waves propagate almost instantaneously from one point of a small vessel to another point of a small vessel.

As an example, one can consider the human arterial tree. Within this network, there are vessels having a length of several centimeters, e.g., the aorta (length 4.0 cm) and some vessels whose lengths are below 1.0 cm, e.g., the anterior communicating artery (abbreviation: ACoA, length 0.3 cm) [3, 33, 85]. The typical arterial blood flow velocity ranges from 10 $\frac{cm}{s}$ to 20 $\frac{cm}{s}$ [97]. Modeling the ACoA by a 1D model very small step sizes are required to resolve the propagation of a certain variable like pressure. Thus, it is not meaningful to consider the changes in space, it is sufficient to compute only changes in time. In order to deduce an ordinary differential equation system (0D lumped parameter model) [34, 83] from the linearized 1D model, we integrate (2.24a) and (2.24b) along z over $[0, l]$.

This yields the following lumped ODE–system, where we assume that the parameters C_{1D}, L_{1D}, R_{1D}, ϕ_M, A_0 and q_c are constant along z:

$$\frac{\partial \hat{p}}{\partial t} + \frac{1}{C_{0D}} \left(q_{out} - q_{in} \right) = \frac{\phi_M}{C_{0D}}, \quad t > 0, \tag{2.27a}$$

$$\frac{\partial \hat{q}}{\partial t} + \frac{1}{L_{0D}} \left(p_{out} - p_{in} \right) = -R_{1D} \hat{q}, \quad t > 0, \tag{2.27b}$$

$$\frac{\partial \hat{c}}{\partial t} + \frac{1}{A_{0D}} \left(q_{out} \cdot c_{out} - q_{in} \cdot c_{in} \right) = -\frac{\phi_p}{A_{0D}} \hat{c}, \quad t > 0, \tag{2.27c}$$

where $q_{in}(t) = q(0,t)$, $q_{out}(t) = q(l,t)$, $p_{in}(t) = p(0,t)$, $p_{out}(t) = p(l,t)$, $c_{in}(t) = c(0,t)$, $c_{out}(t) = c(l,t)$ are the flow rates, pressures and concentrations at the inlet and the outlet of the domain (see Figure 2.6). The other symbols are defined as follows: $C_{0D} = C_{1D} \cdot l$, $L_{0D} = L_{1D} \cdot l$ and $A_{0D} = A_0 \cdot l$.

$$\hat{p}(t) = \frac{1}{l} \int_0^l p \, dz, \quad \hat{q}(t) = \frac{1}{l} \int_0^l q \, dz \quad \text{and} \quad \hat{c}(t) = \frac{1}{l} \int_0^l c \, dz \tag{2.28}$$

are the mean pressure, flow rate and concentration, respectively. Approximating the first two integrals in (2.28) by

$$\hat{p}(t) \approx p_{out}(t), \; \hat{q}(t) \approx q_{in}(t) \text{ or } \hat{p}(t) \approx p_{in}(t), \; \hat{q}(t) \approx q_{out}(t), \tag{2.29}$$

it can be shown that a finite number N of ODE–systems (2.27a)-(2.27b), each with a length of l/N discretize the 1-D linear transport equations system (2.24a)-(2.24b) at first order accuracy in space [34, 83]. For the approximation of $\hat{c}$, we check the sign of $\hat{q}$:

Case (i): $\hat{q}(t) < 0$. In this case, fluid enters the considered vessel from the left ($z = 0$), and $c_{in}(t)$ is given by a boundary condition or possibly obtained from some other reduced model, whereas the average value $\hat{c}(t)$ is approximated by $c_{out}(t)$.

Case (ii): $\hat{q}(t) \geq 0$. In this case, $c_{out}(t)$ is prescribed externally, and $\hat{c}(t)$ is approximated by $c_{in}(t)$.

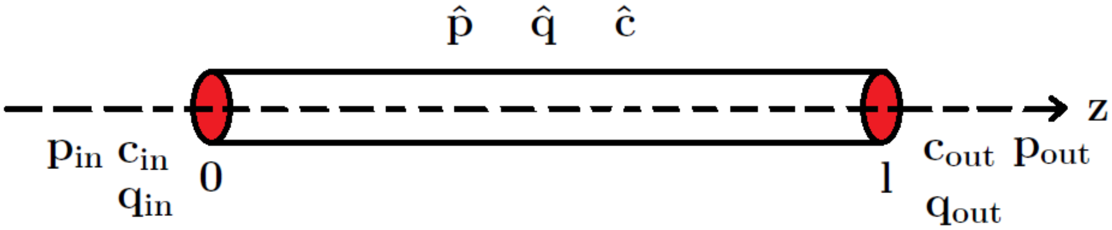

Figure 2.6: Variables of the 0-D lumped parameter model.

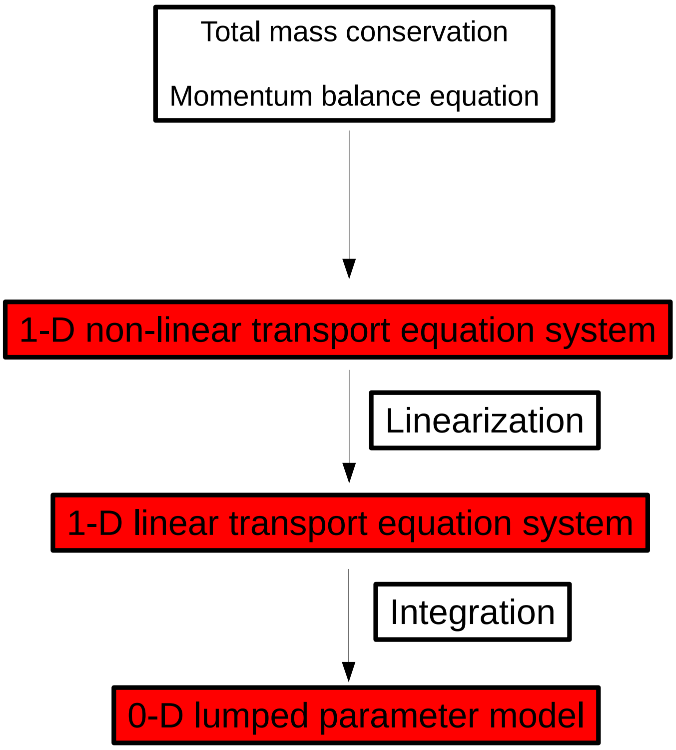

Figure 2.7: Overview on the model reduction approach.

2.2 Numerical methods for transport equations

This section is concerned with the numerical solution of PDEs, having the following form:

$$\frac{\partial \mathbf{U}}{\partial t} + \frac{\partial \mathbf{F}}{\partial z}\left(\mathbf{U}\right) = \mathbf{S}\left(\mathbf{U}\right). \tag{2.30}$$

Supplied with suitable initial and boundary conditions, this type of PDE is also called transport equation. The simplest problem is the *Cauchy Problem*, in which (2.30) holds for $z \in \mathbb{R}$ and $t \geq 0$. In this case one has to provide only an initial condition [70]:

$$\mathbf{U}\left(z,0\right) = \mathbf{U_0}(z),\ z \in \mathbb{R}.$$

By $\mathbf{U}$, we denote a vector of state variables, which depends only on a single space variable and the time variable:

$$\mathbf{U} : \mathbb{R} \times [0,\infty) \to \mathbb{R}^n, \quad (z,t) \mapsto \begin{pmatrix} U_1(z,t) \\ \vdots \\ U_n(z,t) \end{pmatrix}, \quad n \geq 1.$$

The functions

$$\mathbf{F} : \mathbb{R}^n \to \mathbb{R}^n, \quad \mathbf{U} \mapsto \mathbf{F}(\mathbf{U}) \quad \text{and} \quad \mathbf{S} : \mathbb{R}^n \to \mathbb{R}^n, \quad \mathbf{U} \mapsto \mathbf{S}(\mathbf{U})$$

are called flux function and source term, respectively. Considering our 1-D models (2.14a), (2.14b) and (2.24a), (2.24b) from the last subsection, it becomes obvious that these PDEs are transport equations. In (2.14a), the flux function and the source term are non-linear, whereas in the remaining transport equations the flux function and the source term depend linearly on the state variables.

If $\mathbf{F} \in C^1\left(\mathbb{R}^n, \mathbb{R}^n\right)$ holds, (2.30) can be written in quasi-linear form:

$$\frac{\partial \mathbf{U}}{\partial t} + \mathbf{H}(\mathbf{U})\frac{\partial \mathbf{U}}{\partial z}\left(\mathbf{U}\right) = \mathbf{S}\left(\mathbf{U}\right), \tag{2.31}$$

where $\mathbf{H}(\mathbf{U}) = \frac{\partial \mathbf{F}}{\partial \mathbf{U}}\left(\mathbf{U}\right)$.

Definition 2.1. *The PDE* (2.31) *is called* hyperbolic, *if for each value* $\mathbf{U}$ *the matrix* $\mathbf{H}(\mathbf{U})$ *has only real eigenvalues and if* $\mathbf{H}(\mathbf{U})$ *is diagonalizable, i.e., there is a complete set of* n *linearly independent eigenvectors [70].*

2.2.1 Mathematical difficulties

For simplicity, we assume that the source term $\mathbf{S}$ is equal to zero $\mathbf{S} \equiv 0$. In this case, the equation can be considered as a conservation law. Due to

$$\frac{d}{dt}\int_{z_0}^{z_1} \mathbf{U}(z,t)\, dz = -\int_{z_0}^{z_1} \frac{\partial \mathbf{F}}{\partial z}\left(\mathbf{U}(z,t)\right)\, dz = \mathbf{F}\left(\mathbf{U}\left(z_0,t\right)\right) - \mathbf{F}\left(\mathbf{U}\left(z_1,t\right)\right), \tag{2.32}$$

changes in time are only determined by the flux function at z_0 and z_1. For a Cauchy problem this means that the total quantity

$$\int_{-\infty}^{\infty} U_i(z,t)\; dz,\; i \in \{1,\dots,n\}$$

should be constant with respect to time t. To outline the most important mathematical issues in terms of hyperbolic transport equations, it is sufficient to study the scalar case, i.e., $n = 1$. For this purpose, we study the following Cauchy problem:

$$\frac{\partial u}{\partial t} + \frac{\partial f}{\partial z}(u) = 0, \quad u(z,0) = u_0(z), \tag{2.33}$$

with the scalar flux function f. Choosing $f(u) = au,\ a \in \mathbb{R} \setminus \{0\}$, we have the following model problem (*linear advection equation*):

$$\frac{\partial u}{\partial t} + a\frac{\partial u}{\partial z} = 0, \quad u(z,0) = u_0(z). \tag{2.34}$$

If $u_0 \in C^1(\mathbb{R},\mathbb{R})$ one can show that the solution of (2.34) is given by [89]:

$$u(z,t) = u_0(z - at),$$

which means that the solution u is constant on the *characteristic curves* in $\mathbb{R} \times [0,\infty)$:

$$z(t) = at + z_0,$$

on the curve $z(t)$ the solution u is equal to $u_0(z_0)$. However, the regularity requirement $u_0 \in C^1(\mathbb{R},\mathbb{R})$ is often too strict. This problem becomes evident, if the initial condition exhibits discontinuities. In this situation, the initial condition is not differentiable and thus the solution can not be computed in a classical sense. This yields to difficulties in many application areas, in particular if we want to simulate the propagation of a non-smooth concentration profile u under a constant velocity a. Therefore, we have to define a solution

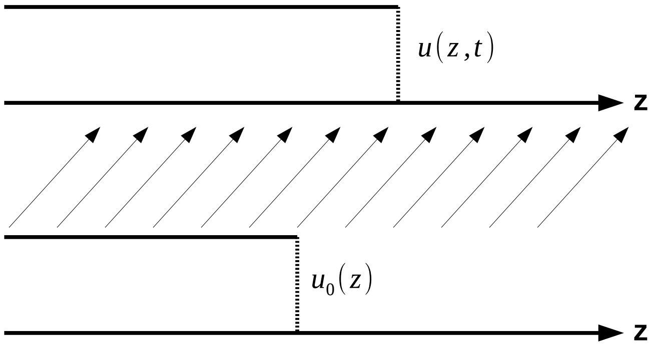

Figure 2.8: Characteristics and solution for the advection equation, with a discontinuous initial condition u_0.

term (*weak solution*), which allows discontinuous solutions. Multiplying (2.33) by a test function $\Phi \in C_c^{\infty}\left(\mathbb{R} \times [0,\infty)\right)$ and integrating over $\mathbb{R} \times [0,\infty)$, it follows:

$$\int_0^{\infty} \int_{\mathbb{R}} \Phi(z,t)\partial_t u(z,t) + \Phi(z,t)\partial_z f\left(u(z,t)\right)\, dzdt = 0.$$

Partial integration yields:

$$\int_0^{\infty} \int_{\mathbb{R}} \partial_t \Phi(z,t) u(z,t) + \partial_z \Phi(z,t) f\left(u(z,t)\right)\, dzdt = -\int_{\mathbb{R}} \Phi(z,0) f\left(u_0(z)\right)\, dz. \tag{2.35}$$

Having (2.35) at hand, we can define the term *weak solution* [32].

Definition 2.2. *A function $u \in L^{\infty}\left(\mathbb{R} \times [0,\infty)\right)$ is called weak solution of* (2.33)*, if the integral equation* (2.35) *holds for all test functions $\Phi \in C_c^{\infty}\left(\mathbb{R} \times [0,\infty)\right)$.*

Due to the fact that in (2.35) the derivatives were shifted from the solution u to the test functions Φ, a weak solution u does not have to be differentiable. However it has to guarantee that the integral expressions in (2.35) exist. Thus functions $u \in L^{\infty}\left(\mathbb{R} \times [0,\infty)\right)$ with discontinuities may fulfill the integral equation.

The definition of the term "weak solution" poses a further difficulty. Often there is more than one weak solution to problem (2.34), even if the initial condition is not changed. Usually the transport equations are modeling a certain phaenomen from physics or engineering, consequently we are interested to choose the solution that is physically meaningful. The existence of other spurious solutions arises from the fact that it is only a model of the reality and some effects have been ignored. Considering the 1D models in Subsection 2.1, it becomes obvious that they result from simplifying 3D models like the Navier-Stokes equation. To pick the correct weak solution we have to formulate additional constraints for the solution of the integral equation (2.35). These are generally called *entropy condition* by in analogy with thermodynamics [32, 70].

Definition 2.3. *A function $u \in L^{\infty}\left(\mathbb{R} \times (0,\infty)\right)$ is an entropy solution of the Cauchy-problem* (2.33)*, provided that*

(i) u is a weak solution in the sense of Definition 2.2 and

(ii) $u(z+x,t) - u(z,t) \leq C\left(1 + \frac{1}{t}\right) z$, for some constant $C \geq 0$ and almost every $x, z \in \mathbb{R}$, $t > 0$ with $z > 0$.

Theorem 2.4. *If f in* (2.33) *is convex and if $f \in C^1\left(\mathbb{R},\mathbb{R}\right)$. Then there exists, up to a set of measure zero, at most one entropy solution of* (2.35)*.*

Our task is now to provide numerical schemes converging towards an entropy solution of a transport equation.

2.2.2 Numerical difficulties

Numerical methods for 1D hyperbolic transport equations are based on a combination of an ODE solver and a space discretization scheme [48]. Discretizing a transport equation in space yields a system of ODEs, which is treated by the ODE solver. The convergence analysis of numerical schemes relies on the concepts of consistency and stability. According to Lax [70] there is the following equivalence.

Theorem 2.5. *Let us assume that problem* (2.33) *is discretized in space by a mesh size h and in time by a step size Δt. A linear numerical scheme yielding the approximation $u_{h,\Delta t}$ converges towards the entropy solution u of* (2.33) *iff it is consistent and stable. We say that the numerical scheme converges towards u with respect to a norm $\|\cdot\|$, if:*

$$\lim_{\Delta t, h \to 0} \|u_{h,\Delta t} - u\| = 0.$$

As a consequence of this equivalence, we have to check for convergence, if the numerical scheme is consistent and stable.

Definition 2.4. *A numerical scheme is consistent if the local discretization error $\tau_{h,\Delta t}$ tends to zero*

$$\tau_{h,\Delta t} = \|\mathcal{L}_{h,\Delta t}(u) - \mathcal{L}(u)\| \to 0,$$

for $h, \Delta t \to 0$ in a suitable norm $\|\cdot\|$. By $\mathcal{L}_{h,\Delta t}$ we denote the discretization of the continuous differential operator $\mathcal{L}$.

In the case of the Cauchy-problem (2.34), we have: $\mathcal{L} = \frac{\partial}{\partial t} + a\frac{\partial}{\partial z}$.

Definition 2.5. *Let us denote the numerical approximation for $t = n \cdot \Delta t$ by u_h^n. A numerical scheme is stable, if for all time steps n there is constant C with*

$$\|u_h^n\| \leq C \|u_0\|$$

with respect to a suitable norm $\|\cdot\|$.

Even if the numerical scheme is stable and consistent, the numerical solution provided by such a scheme can be of poor quality. To illustrate this, we consider two well known finite difference methods and apply them to the linear transport equation (2.34):

(i) **Lax-Friedrichs:**

$$u_i^{n+1} = \frac{1}{2}\left(u_{i-1}^n + u_{i+1}^n\right) - \frac{\Delta t}{2h}a\left(u_{i+1}^n - u_{i-1}^n\right),$$

(ii) **Lax-Wendroff:**

$$u_i^{n+1} = u_i^n - \frac{\Delta t}{2h}a\left(u_{i+1}^n - u_{i-1}^n\right) + \frac{\Delta t^2}{2h^2}a^2\left(u_{i+1}^n - 2u_i^n + u_{i-1}^n\right),$$

where u_i^n denotes an approximation at (z_i, t_n), $t_n = n \cdot \Delta t$, $n \in \mathbb{N}_0$ and $z_i = i \cdot h, i \in \mathbb{Z}$. For suitable norms one can show that if the *CFL-Condition*:

$$|a| \frac{\Delta t}{h} < 1$$

is fulfilled both methods are stable and consistent [89] and thus they are convergent. Moreover we have the following consistency errors:

(i) **Lax-Friedrichs:**

$$\tau_{h,\Delta t} = \mathcal{O}\left(\frac{h^2}{\Delta t} + h + \Delta t\right),$$

(ii) **Lax-Wendroff:**

$$\tau_{h,\Delta t} = \mathcal{O}\left(h^2 + \Delta t^2\right).$$

We study the results for $t = 1$ and $z \in [0, 1]$ of both methods for $a = 0.5$ and

$$u_0(z) = \begin{cases} 1, & \text{if } z \leq 0, \\ 0, & \text{if } z > 0. \end{cases}$$

As a second experiment, we change the initial condition to

$$u_0(z) = \begin{cases} 0.5 \cdot \cos\left(4\pi\left(z + 0.2\right)\right) + 0.5, & \text{if } 0.05 < z < 0.55, \\ 0, & \text{else} \end{cases}$$

and report the numerical results for $t = 0.5$ and $z \in [0, 1]$ of both methods for $a = 0.5$. For the discretization, we use $h = 1/200$ and $\Delta t = 1/1000$.

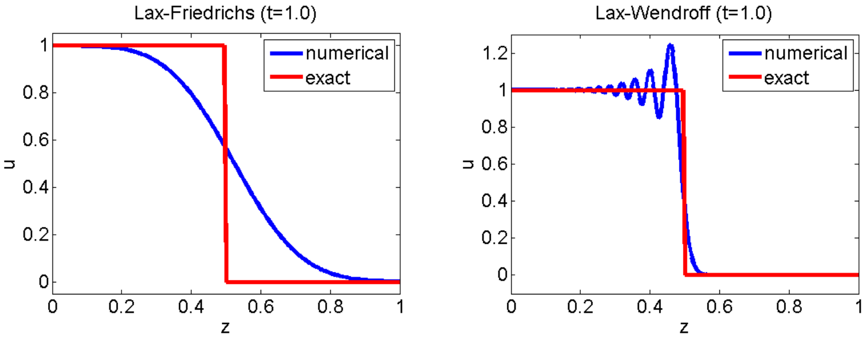

Figure 2.9: Numerical approximations of the Lax-Friedrichs and the Lax Wendroff methods applied to the scalar advection equation for $a = 0.5$ and a discontinuous initial condition.

In Figure 2.9, we observe that the low order method (Lax-Friedrichs) shows no unphysical oscillations but a very diffusive solution around the jump of the exact solution. The Lax-Wendroff method, which is of higher order exhibits spurious oscillations in the vicinity of the discontinuity, but is not significantly smeared at the jump.

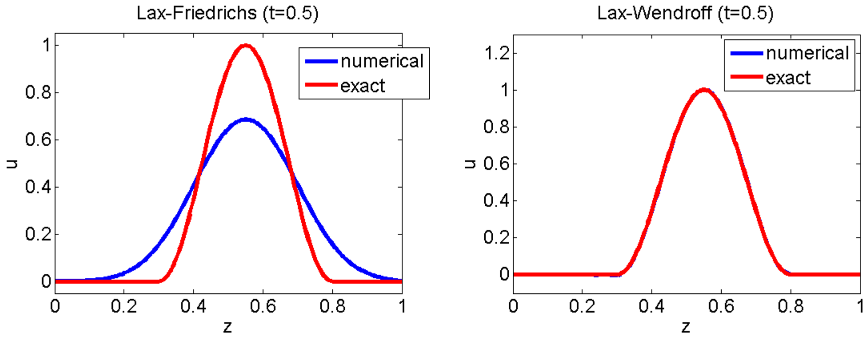

Figure 2.10: Numerical approximations of the Lax-Friedrichs and the Lax-Wendroff methods applied to the scalar advection equation for $a = 0.5$ and a smooth initial condition.

In Figure 2.10, it can be seen that the low order method (Lax-Friedrichs) does not preserve the initial condition. It tends to smear the initial profile. As the Lax-Wendroff method is of second order in both space and time the solution for the smooth initial condition is approximated very well.

It is demonstrated by these examples that consistency and stability do not imply that a numerical approximation has a good quality. On the one hand, high-order methods yield a good approximation if the solution is smooth. Yet, they tend to create oscillations in the vicinity of discontinuities. Thus we need further mathematical criteria to keep the numerical solution free of non-physical effects and close to the exact solution. Based on these criteria further numerical methods have to be developed, which exhibit non-oscillatory behavior around discontinuities and simultaneously approximate the solution well in its smooth parts.

(i) **Monotonicity:** Let us suppose that a Cauchy-problem like (2.33) has initial conditions u_0 and v_0, where $u_0(z) \geq v_0(z)$. Then, we have for the corresponding solutions: $u(z,t) \geq v(z,t)$ for all $z \in \mathbb{R},\ t \in [0, \infty)$. A numerical scheme that preserves this inequality for each time step n:

$$u_i^n \geq v_i^n \Rightarrow u_i^{n+1} \geq v_i^{n+1},$$

is called monotone. If a numerical method satisfies this condition, minima and maxima cannot increase. This implies that the formation of oscillations is prevented [110].

(ii) **Total Variation Diminishing Schemes:** The total variation of a function u is defined as follows:

$$TV(u) = \int_{-\infty}^{\infty} |\partial_z u| \ dz.$$

It can be shown that for a solution of (2.33) it holds [68]:

$$TV\left(u\left(\cdot, t_2\right)\right) \leq TV\left(u\left(\cdot, t_1\right)\right), \forall t_2 \geq t_1.$$

i.e., the total variation of a function solving a conservation law does not increase. We call such a function *total variation diminishing* (TVD). For a numerical solution at the time step n the term TV is defined as follows:

$$TV\left(u_h^n\right) = \sum_i \left|u_{i+1}^n - u_i^n\right|.$$

A numerical discretization is called TVD, if the corresponding the numerical solution satisfies:

$$TV\left(u_h^{n+1}\right) \leq TV\left(u_h^n\right) \tag{2.36}$$

for all time levels n. For TVD schemes, a uniform upper bound for the TV is given by the TV of the initial condition u_0, where we assume that the quantity $TV\left(u_0\right)$ exists. In [71], it is proved that every TVD scheme is monotonicity preserving and consequently non-oscillatory. However, the TVD-property can be checked easier using Harten's theorem [52]. In Harten's theorem it is stated that an explicit discretization is TVD, if the coefficients concerning the spatial discretization are positive and its sum is less or equal than one. Taking further requirements into account, one can show that a consistent numerical scheme, whose TV is uniformly bounded is convergent.

(iii) **Positivity:** In many application areas one is interested to simulate the transport of physical units which are not negative, e.g., the transport of a certain substance's concentration. This is a further feature that is not guaranteed by the convergence Theorem 2.5. However, it is very important in order to provide meaningful simulation results.

(iv) **Conservation:** Considering (2.32), it becomes obvious that the total mass $\int_{z_0}^{z_1} u(z,t)\, dz$ is changed only by the fluxes at z_0 and z_1. Due to the absence of a source term there is no loss or gain of mass. This physical feature should also be incorporated into a numerical method for transport problems.

2.2.3 Stabilized Discontinuous Galerkin methods

Considering the numerical difficulties, which occur in the context of transport equations (see previous subsection) we have to choose for the numerical treatment of transport equations like (2.14a),(2.14b) and (2.24a), (2.24b) a numerical method

(i) of higher order in space and time to avoid numerical diffusion,

(ii) which allows for a stabilization to prevent spurious oscillations.

A numerical method providing a higher order approximation in space, while keeping the discretization stencils local, is the *discontinuous Galerkin method* (DG-method) [90]. Contrary to the standard Galerkin method, this discretization scheme can exhibit discontinuities at the boundaries of an element. Combined with suitable limiter techniques [70, 62, 58, 57] this property allows us to incorporate jumps in a solution and simultaneously prevent spurious oscillations.

To derive this numerical scheme, we compute the weak formulation of the system (2.30) on a finite interval $[0,l] \subset \mathbb{R}$. Multiplying every component i of (2.30) by a test function $\Phi_i \in C_c^{\infty}([0,l])$ and integrating over $[0,l]$ yields:

$$\int_0^l \left(\frac{\partial U_i}{\partial t} + \frac{\partial F_i}{\partial z}(\mathbf{U}) - S_i(\mathbf{U}) \right) \cdot \Phi_i \, dz = 0, \ i = 1, \dots, n.$$

In the following, we write $\mathbf{U} = (U_1, \dots, U_n)^T$, $\mathbf{\Phi} = (\Phi_1, \dots, \Phi_n)^T$ and define the componentwise product of two vectors $\mathbf{A} = (A_1, \dots, A_n)^T$, $\mathbf{B} = (B_1, \dots, B_n)^T$ as follows:

$$\mathbf{A} \cdot \mathbf{B} = (A_1 \cdot B_1, \dots, A_n \cdot B_n)^T.$$

The interval $[0,l]$ may be subdivided in m disjoint subintervals $\Omega_e = \left(z_e^l, z_e^r\right)$ such that:

$$[0,l] = \bigcup_{e=1}^{m} \overline{\Omega_e}$$

holds. Using these definitions, we have:

$$\sum_{e=1}^{m} \int_{\Omega_e} \left(\frac{\partial \mathbf{U}}{\partial t} + \frac{\partial \mathbf{F}}{\partial z}(\mathbf{U}) - \mathbf{S}(\mathbf{U}) \right) \cdot \mathbf{\Phi} \, dz = 0.$$

Partial integration yields for every summand:

$$\int_{\Omega_e} \frac{\partial \mathbf{U}}{\partial t} \cdot \mathbf{\Phi} - \mathbf{F}(\mathbf{U}) \frac{\partial \mathbf{\Phi}}{\partial z} \, dz + [\mathbf{F}(\mathbf{U}) \cdot \mathbf{\Phi}]_{z_e^l}^{z_e^r} - \int_{\Omega_e} \mathbf{S}(\mathbf{U}) \cdot \mathbf{\Phi} \, dz = 0, \quad \forall e \in \{1, \dots, m\}.$$

This equation is attached to every element Ω_e to keep the discretization stencils local. A global solution is obtained by coupling the elements at the interfaces by the flux term $[\mathbf{F}(\mathbf{U}) \cdot \mathbf{\Phi}]_{z_e^l}^{z_e^r}$. Due to the fact that the solution at the element boundaries may have discontinuities, the computation of the coupling term is not well defined. At $z = z_e^l$, e.g., we have two values $\mathbf{U}\left(z_{e-1}^r\right)$ and $\mathbf{U}\left(z_e^l\right)$ (Figure 2.11). The value to be chosen, depends on the flux function $\mathbf{F}$. An analysis of the characteristics of (2.30) (see Subsection 2.1) reveals how information is propagated. Based on this analysis one knows which value has to be incorporated into the coupling term or how the characteristic variables have to be integrated.

On an element Ω_e the numerical solution $\mathbf{U_h}$ is represented by a polynom of degree p. Inserting $\mathbf{U_h}$ into the previous equation, it follows by the help of the standard $L^2(\Omega_e)$ scalar product $(u,v)_{\Omega_e} = \int_{\Omega_e} u \cdot v \, dz$:

$$\left(\frac{\partial \mathbf{U_h}}{\partial t}, \mathbf{\Phi} \right)_{\Omega_e} - \left(\mathbf{F}(\mathbf{U_h}), \frac{\partial \mathbf{\Phi}}{\partial z} \right)_{\Omega_e} + [\mathbf{F}(\mathbf{U_h}) \cdot \mathbf{\Phi}]_{z_e^l}^{z_e^r} - (\mathbf{S}(\mathbf{U_h}), \mathbf{\Phi})_{\Omega_e} = 0, \quad \forall e \in \{1, \dots, m\}.$$

The numerical solution $\mathbf{U_h}$ can be represented by a linear combination of the basis functions $(\varphi_j)_{j=0}^p$ of the polynomial space $\mathbb{P}^p(\Omega_e)$:

$$\mathbf{U_h}(z,t) = \sum_{j=0}^{p} \mathbf{u}_j^{(e)}(t) \cdot \varphi_j(z),\ \forall z \in \Omega_e. \tag{2.37}$$

The global numerical solution can be discontinuous at the element boundaries but is continuous on a single element (see Figure 2.11).

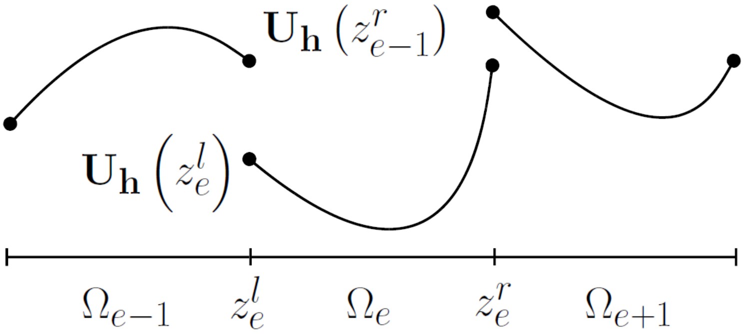

Figure 2.11: Discontinuous numerical solution, given by a polynom on each element.

Based on this expansion, we can define for $i \in \{1,\dots,n\}$ the value $\mathbf{u}_{j,i}^{(e)}$ by the i-th component of the vector $\mathbf{u}_j^{(e)}$. Choosing the test functions as $\mathbf{\Phi}_i = \varphi_k$, we have for the component i the *semi-discrete* formulation:

$$\sum_{j=0}^{p} \frac{\partial \mathbf{u}_{j,i}^{(e)}}{\partial t}(t)\left(\varphi_j,\varphi_k\right)_{\Omega_e} - \left(\mathbf{F}_i\left(\mathbf{U_h}\right), \frac{\partial \varphi_k}{\partial z}\right)_{\Omega_e} + \left[\mathbf{F}_i^{up}\left(\mathbf{U_h}\right)\cdot\varphi_k\right]_{z_e^l}^{z_e^r} - \left(\mathbf{S}_i\left(\mathbf{U_h}\right),\varphi_k\right)_{\Omega_e} = 0 \tag{2.38}$$

$\forall e \in \{1,\dots,m\}$ and $\forall k \in \{0,\dots,p\}$. By the help of (2.38) we can derive an ODE for the coordinate vector:

$$\alpha_i^{(e)} = \left(\mathbf{u}_{0,i}^{(e)},\dots,\mathbf{u}_{p,i}^{(e)}\right)^T. \tag{2.39}$$

Defining the element mass matrix $M^{(e)}$ by:

$$M^{(e)} = \left(m_{jk}^{(e)}\right)_{0\le j,k\le p} = \left(\int_{\Omega_e} \varphi_j \cdot \varphi_k \, dz\right)_{0\le j,k\le p} \in \mathbb{R}^{(p+1)\times(p+1)}, \tag{2.40}$$

it follows from (2.38) that:

$$M^{(e)} \frac{d\alpha_i^{(e)}}{dt} = r\left(\mathbf{U_h},t\right),\ \forall e \in \{1,\dots,m\},\ \forall i \in \{1,\dots,n\}, \tag{2.41}$$

where the k-th component of the right hand side is given by:

$$(r(\mathbf{U_h}, t))_k = \left(\mathbf{F}_i(\mathbf{U_h}), \frac{\partial \varphi_k}{\partial z}\right)_{\Omega_e} - \left[\mathbf{F}_i^{up}(\mathbf{U_h}) \cdot \varphi_k\right]_{z_e^l}^{z_e^r} + \left(\mathbf{S}_i(\mathbf{U_h}), \varphi_k\right)_{\Omega_e} \tag{2.42}$$

The integrals occurring in (2.42) and in $M^{(e)}$ are approximated by a quadrature rule, e.g., the Gauß-Legendre quadrature rule [27]. Its approximation order should be chosen such that at least the entries of the mass matrix $M^{(e)}$ are computed without an error. As the discretization stencils are defined locally for each element, it is possible to choose a different polynomial degree and a different basis for every element. In the next subsection, we present two appropriate choices for the basis $(\varphi_j)_{j=0}^p$.

2.2.4 Polynomial bases

In the literature one can find several bases for polynomial spaces. In the context of DG-methods the following two bases for the polynomial spaces are widely used [57, 58, 60, 61, 62], because they allow the development of effective limiter techniques, as we will see in Subsection 2.2.6.

(i) Legendre basis: To avoid the inversion of the mass matrix $M^{(e)}$ in (2.41), one has to use a polynomial basis, which is orthogonal with respect to the standard L^2-scalar product. A basis, which has this special property consists of the Legendre-polynomials. These polynomials are defined by the following three-term recursion on the reference interval $[-1, 1]$ [56]:

$$(n+1)\, L_{n+1}(x) = (2n+1)\, x L_n(x) - n L_{n-1}(x),\ n \geq 1,$$

where

$$L_0(x) = 1 \text{ and } L_1(x) = x.$$

The first four Legendre-polynomials (see Figure 2.12) are given by:

$$L_0(x) = 1,\ L_1(x) = x,\ L_2(x) = \frac{1}{2}\left(3x^2 - 1\right) \text{ and } L_3(x) = \frac{1}{2}\left(5x^3 - 3x\right).$$

We note that $L_n(-1) = (-1)^n$ and $L_n(1) = 1$ holds $\forall n \in \mathbb{N}$. In order to represent the Legendre polynomials on an arbitrary element $\Omega_e = \left(z_e^l, z_e^r\right)$, we use the affine mapping:

$$z_e : [-1, 1] \to \Omega_e, \quad x \mapsto z_e(x) = \frac{z_e^r}{2}(1+x) + \frac{z_e^l}{2}(1-x).$$

By the help of this mapping, we can compute for $\varphi_j(z) = L_j(z_e(x)) =: L_j^{(e)}(z)$ the element mass matrix $M^{(e)}$ [39]:

$$\begin{aligned} m_{jk}^{(e)} &= \int_{\Omega_e} L_j^{(e)}(z) \cdot L_k^{(e)}(z)\, dz = \int_{-1}^{1} L_j(z_e(x)) \cdot L_k(z_e(x)) \cdot \frac{dz_e}{dx}\, dx \\ &= \int_{-1}^{1} L_j(z_e(x)) \cdot L_k(z_e(x)) \cdot \frac{z_e^r - z_e^l}{2}\, dx = \frac{h_e}{2} \cdot \frac{2}{2j+1}\delta_{jk} = \frac{h_e}{2j+1}\delta_{jk}, \end{aligned}$$

where $h_e := z_e^r - z_e^l$.

(ii) Taylor basis: A second basis is obtained by expanding the exact solution around the center $z_e^c = 0.5 \cdot \left(z_e^r + z_e^l\right)$ of an element Ω_e into a Taylor series [76, 81, 119]:

$$\mathbf{U}(z,t) = \mathbf{U}\left(z_e^c, t\right) + \frac{\partial \mathbf{U}}{\partial z}\left(z_e^c, t\right)\left(z - z_e^c\right) + \ldots + \frac{1}{p!}\frac{\partial^p \mathbf{U}}{\partial z^p}\left(z_e^c, t\right)\left(z - z_e^c\right)^p + \mathcal{O}\left(|z - z_e^c|^{p+1}\right).$$

If one neglects the error term $\mathcal{O}\left(|z - z_e^c|^{p+1}\right)$ the remaining Taylor polynomial provides a numerical approximation:

$$\mathbf{U_h}(z,t) = \mathbf{U}\left(z_e^c, t\right) + \frac{\partial \mathbf{U}}{\partial z}\left(z_e^c, t\right)\left(z - z_e^c\right) + \ldots + \frac{1}{p!}\frac{\partial^p \mathbf{U}}{\partial z^p}\left(z_e^c, t\right)\left(z - z_e^c\right)^p$$

Denoting the average value $\overline{\mathbf{U_h}} = \frac{1}{|\Omega_e|}\int_{\Omega_e} \mathbf{U_h}(z)\ dz$ of $\mathbf{U_h}$ on Ω_e the previous equation can be rewritten as follows:

$$\mathbf{U_h}(z,t) = \overline{\mathbf{U_h}}\left(z_e^c, t\right) + \frac{\partial \mathbf{U}}{\partial z}\left(z_e^c, t\right)\left(z - z_e^c\right) + \ldots + \frac{\partial^p \mathbf{U}}{\partial z^p}\left(z_e^c, t\right)\left(\frac{\left(z - z_e^c\right)^p}{p!} - \frac{\overline{\left(z - z_e^c\right)^p}}{p!}\right).$$

Defining the basis functions by:

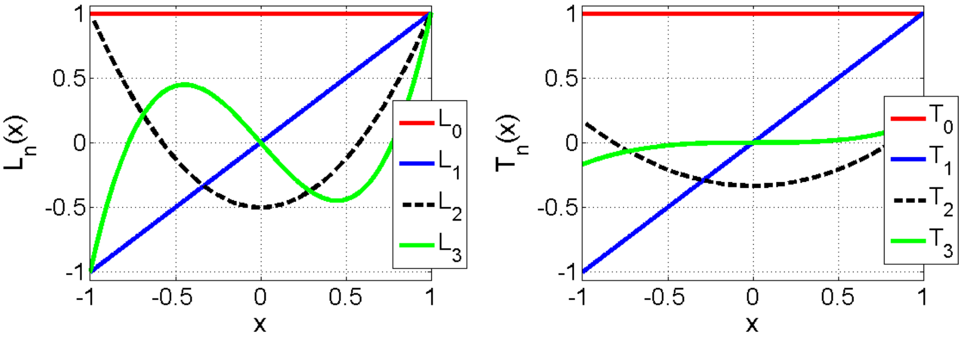

Figure 2.12: The first four Legendre polynomials L_0, L_1, L_2 and L_3 (left). The first four Taylor basis functions T_0, T_1, T_2 and T_3 on $[-1,1]$ (right).

$$T_0^e(z) = 1, \qquad T_p^e(z) = \frac{\left(z - z_e^c\right)^p}{p!} - \frac{\overline{\left(z - z_e^c\right)^p}}{p!},\ p \geq 1,$$

the numerical solution $\mathbf{U_h}$ on an element Ω_e can be written as:

$$\mathbf{U_h}(z,t) = \sum_{k=0}^{p} a_k(t) T_k^e(z), \quad \text{where } a_k(t) = \begin{cases} \overline{\mathbf{U_h}}\left(z_e^c, t\right) & \text{for } k = 0, \\ \frac{\partial^k \mathbf{U}}{\partial z^k}\left(z_e^c, t\right) & \text{for } k \neq 0. \end{cases} \tag{2.43}$$

This representation of $\mathbf{U_h}$ is motivated as follows: The coefficients $a_k(t)$ allow the development of an effective limiter technique. For $k \geq 1$ the coefficients contain the derivatives of the solution at the center z_e^c, hence the absolute values of these coefficients are large, if the solution exhibits oscillations. A possible way to make the numerical solution smooth, is to multiply the coefficients $a_k(t)$ by suitable correction factors $\gamma_k \in [0,1]$ to rule out higher derivatives, if it is necessary (see Subsection 2.2.6).

However, a disadvantage of the Taylor basis is the fact that the mass matrix $M^{(e)}$ is not diagonal for $p > 2$. Thus the inverse of the matrix $M^{(e)}$ in (2.41) has to be computed. To avoid the inversion of a dense mass matrix one can apply mass lumping techniques, by setting all off-diagonal entries to zero. In this context, one should note that the accuracy of the numerical approximation is deteriorated by mass lumping [60, 61, 76].

2.2.5 Time-stepping scheme

The local ODEs in (2.41) can be used by means of (2.37) and (2.39) to establish a global ODE-system, depending on the global vector $\mathbf{u}$:

$$\mathbf{u} = \left(\alpha_1^{(1)}, \dots, \alpha_n^{(1)}, \dots, \alpha_1^{(m)}, \dots, \alpha_n^{(m)}\right)^T \in \mathbb{R}^{(p+1)\cdot m\cdot n}.$$

Introducing the global block diagonal mass matrix M, which consists of the local mass matrices $M^{(e)}$ the global ODE-system can be written as:

$$\frac{d}{dt}\mathbf{u}(t) = M^{-1}R\left(\mathbf{u}(t), t\right) =: R_M\left(\mathbf{u}(t), t\right),\ \mathbf{u}(0) = \mathbf{u}_0, \tag{2.44}$$

where the global right hand side R incorporates the discretized convective term and the fluxes across the element interfaces, which are listed in (2.42). To complete the discretization of the semi-discrete form (2.38), in [83, 102] standard Runge-Kutta methods or Adams-Bashford methods [50] were used. However, it turns out that an arbitrary Runge-Kutta or multi-step scheme does not preserve the TVD-properties of the solution $\mathbf{u}$. The total variation of $\mathbf{u}(t)$ is given by:

$$TV\left(\mathbf{u}(t)\right) = \sum_{j=0}^{p}\sum_{e=1}^{m-1} \left\|\mathbf{u}_j^{e+1}(t) - \mathbf{u}_j^{e}(t)\right\|_2.$$

According to (2.36) $\mathbf{u}$ is TVD, if

$$TV\left(\mathbf{u}(t_{n+1})\right) \leq TV\left(\mathbf{u}(t_n)\right)$$

holds for two subsequent time points t_n and t_{n+1}. Therefore, the authors of [45, 46] introduced a family of explicit time stepping schemes, which ensure that the TVD-property of the time stepping scheme is preserved within one time step. In general, an explicit $s-$step method is given by:

$$\mathbf{u}^{(0)} = \mathbf{u}\left(t_n\right), \tag{2.45a}$$

$$\mathbf{u}^{(l)} = \sum_{k=0}^{l-1}\left(\alpha_{lk}\cdot\mathbf{u}^{(k)} + \Delta t\cdot\beta_{lk}\cdot R_M\left(\mathbf{u}^{(k)}\right)\right), \quad l \in \{1, \dots, s\}, \tag{2.45b}$$

$$\mathbf{u}\left(t_{n+1}\right) = \mathbf{u}^{(s)}, \tag{2.45c}$$

where $\Delta t = t_{n+1} - t_n$. If all coefficients are nonnegative, i.e., $\alpha_{kl} \geq 0$, $\beta_{kl} \geq 0$ and taking to account the consistency condition $\sum_{k=0}^{l} \alpha_{kl} = 1$, formula (2.45b) consists of a convex combination of forward Euler steps, with Δt replaced by $\frac{\beta_{kl}}{\alpha_{kl}}\Delta t$. Thus, a stability condition can only be formulated in terms of a time step restriction for the forward Euler method.

Theorem 2.6. *Let us suppose that the forward Euler method applied to* (2.44) *is TVD on the condition of a time step restriction:*

$$\Delta t \leq \Delta t_{FE}.$$

Then, a Runge-Kutta method given by (2.45a)-(2.45c) *is TVD, if the following time step restriction*

$$\Delta t \leq c \cdot \Delta t_{FE}, \quad c = \min_{k,l} \frac{\alpha_{lk}}{\beta_{lk}} \leq 1,$$

and

$$\alpha_{lk} \geq 0, \quad \beta_{lk} \geq 0$$

holds.

Proof. The proof of this theorem can be found in [104]. □

Remark 2.4. *If the forward Euler method is stable with respect to an arbitrary norm $\|\cdot\|$ under a certain time step restriction, a Runge-Kutta method fulfilling the conditions of Theorem 2.6 is called **strong stability preserving** with respect to the norm $\|\cdot\|$ (**SSP-method**).*

In the following, we use an explicit 3−step method of third order, which is TVD if $\Delta t \leq \frac{1}{2}\Delta t_{FE}$. For an autonomous right hand side R_M, it is given by [45]:

$$\mathbf{u}^{(1)} = \mathbf{u}(t_n) + \Delta t R_M (\mathbf{u}(t_n)) \tag{2.46a}$$

$$\mathbf{u}^{(2)} = \frac{3}{4}\mathbf{u}(t_n) + \frac{1}{4}\left(\mathbf{u}^{(1)} + \Delta t R_M \left(\mathbf{u}^{(1)}\right)\right) \tag{2.46b}$$

$$\mathbf{u}(t_{n+1}) = \frac{1}{3}\mathbf{u}(t_n) + \frac{2}{3}\left(\mathbf{u}^{(2)} + \Delta t R_M \left(\mathbf{u}^{(2)}\right)\right). \tag{2.46c}$$

In order to derive a Butcher-Table for this time stepping scheme, we first consider the usual notation for an explicit Runge-Kutta method:

$$\mathbf{u}(t_{n+1}) = \mathbf{u}(t_n) + \Delta t \left(\sum_{i=1}^{s} b_i k_i\right), \quad k_i = R_M\left(\mathbf{u}(t_n) + \Delta t \sum_{j=1}^{i-1} a_{ij} k_j, t_n + c_i \Delta t\right). \tag{2.47}$$

A comparison of the coefficients in (2.47) and (2.46a)-(2.46c) yields together with the consistency condition

$$c_i = \sum_{j=1}^{s} a_{ij} \quad i = 1, \dots, s,$$

for $s = 3$:

$$\begin{array}{c|ccc} c_1 & a_{11} & a_{12} & a_{13} \\ c_2 & a_{21} & a_{22} & a_{23} \\ c_3 & a_{31} & a_{32} & a_{33} \\ \hline & b_1 & b_2 & b_3 \end{array} = \begin{array}{c|ccc} 0 & & & \\ 1 & 1 & & \\ \frac{1}{2} & \frac{1}{4} & \frac{1}{4} & \\ \hline & \frac{1}{6} & \frac{1}{6} & \frac{4}{6} \end{array}.$$

All in all, we have a stable time stepping scheme of higher order. The drawback of this method is clearly the time step restriction, which forces us for very stiff problems to exert many time steps. However one time step of our 1D and 0D lumped parameter models is computationally inexpensive compared to a 3D model. Our numerical simulations show that for the problems which are considered in this thesis, step sizes of a reasonable size can be used.

2.2.6 Stabilization techniques

Combining the numerical tools of the previous subsections we have a numerical method to treat transport equations given by (2.30). The higher order approximations in space by the DG-Galerkin method and in time by the explicit third order SSP method enable us to approximate smooth solutions with a high accuracy. For solutions, which exhibit discontinuities this approximation scheme tends to create spurious oscillations in the vicinity of discontinuities. Let us consider, e.g., the linear advection equation (2.34) for $a = \frac{1}{2}$ and

$$u_0(z) = \begin{cases} 1, & \text{if } z \leq 0, \\ 0, & \text{if } z > 0. \end{cases} \tag{2.48}$$

The solution is computed for $z \in [0, 1]$ and $t = 1$. The discretization parameters are chosen as follows: For the mesh size h and the time step Δt, we use $h = \frac{1}{200}$ and $\Delta t = 10^{-3}$. The solution on each element is approximated by polynomials of degree $p = 2$. The choice of the basis is not of relevance in this context. Both the Taylor basis and the Legendre basis yield approximately the same results. The upwinded flux $\mathbf{F}^{up}$ in (2.38) at an element

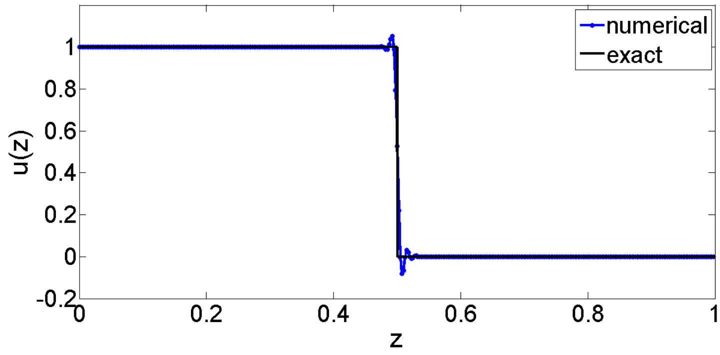

Figure 2.13: Exact solution and a quadratic DG-approximation ($p = 2$) of the linear advection equation for $a = 0.5$, $z \in [0, 1]$, $t = 1$ and a discontinuous initial condition.

interface $z = z_e^r = z_{e+1}^l$ for the scalar linear advection equation, having the flux function $\mathbf{F}(\mathbf{u_h}) = a \cdot \mathbf{u_h}$, is computed by:

$$\mathbf{F}^{up}(\mathbf{u_h}) = \begin{cases} a \cdot \mathbf{u_h}\left(z_e^r\right) & \text{if } a \geq 0 \\ a \cdot \mathbf{u_h}\left(z_{e+1}^l\right) & \text{if } a < 0. \end{cases}$$

Compared to the solution, provided by the Lax-Wendroff method (see Figure 2.9), the DG-method combined with the time integrator (2.46a)-(2.46c) produces less oscillations around the jump at $z = 0.5$. However, the oscillations are not completely removed, despite the fact that the time integrator is TVD. Therefore, we need further numerical techniques for the DG-method and the third order SSP-method to guarantee not only convergence but also a numerical solution, which is physical meaningful. In the remainder of this section we briefly describe two limiter techniques, which were designed for the two polynomial bases in Subsection 2.2.4.

Limiter technique for the Legendre basis

This limiter technique is described in [57, 58] and is often referred to as *moment limiter*. The basic idea is to estimate the slope of the numerical solution between two neighboring elements. For simplicity, we first restrict ourselves to the scalar case, which is extended to a system of transport equations in a second step.

(i) Scalar equation

For $n = 1$ in (2.37) the vectors $\mathbf{u}_j^{(e)}$ become scalars $u_j^{(e)}$. We show that the coefficients $u_j^{(e)}$ of the discrete solution $\mathbf{U_h}$ approximate the derivatives of $\frac{\partial^j}{\partial z^j}\mathbf{U_h}$ on Ω_e [58].

Lemma 2.1. *For the coefficients of the discrete solution* $\mathbf{U_h}$ *it holds on* Ω_e*:*

$$u_j^{(e)} = C h_e^j \cdot \frac{\partial^j}{\partial z^j}\mathbf{U_h} + \mathcal{O}\left(h_e^{j+1}\right), \tag{2.49}$$

where $C = \frac{j!}{(2j)!}$*. For the corresponding derivatives it holds:*

$$\frac{\partial^j}{\partial z^j}\mathbf{U_h} = \left(\frac{2}{h_e}\right)^j \frac{(2j)!}{2^j j!} \cdot u_j^{(e)} + \left(\frac{2}{h_e}\right)^j \frac{\partial^j}{\partial x^j} \sum_{l>j}^{p} u_l^{(e)} L_l(x), \tag{2.50}$$

where the Legendre polynomials L_l *are defined on the reference interval* $[-1, 1]$.

Proof. The proof of this lemma can be found in [58, Section 2]. For convenience we repeat it here. Choosing $\varphi_l = L_l$ in (2.37), we have for the derivatives of $\mathbf{U_h}$:

$$\frac{\partial^j}{\partial z^j}\mathbf{U_h}(z) = u_j^{(e)} \frac{\partial^j}{\partial z^j} L_j^{(e)}(z) + \frac{\partial^j}{\partial z^j} \sum_{l>j}^{p} u_l^{(e)} L_l^{(e)}(z),$$

where $L_l^{(e)}(z) = L_l\left(x(z)\right)$. $x(z)$ is the affine mapping from Ω_e to the reference element $[-1, 1]$. Due to

$$\frac{\partial^j}{\partial z^j} L_j^{(e)}(z) = \frac{\partial^j}{\partial x^j} L_j(x) \left(\frac{\partial x}{\partial z}\right)^j = \frac{\partial^j}{\partial x^j} L_j(x) \left(\frac{2}{h_e}\right)^j = \frac{(2j)!}{2^j j!} \cdot \left(\frac{2}{h_e}\right)^j$$

it follows the second equation (2.50). The first equation (2.49) is proved by induction. For $j = p$, we have by (2.50):

$$\frac{\partial^p}{\partial z^p} \mathbf{U_h}(z) = \left(\frac{2}{h_e}\right)^p \frac{(2p)!}{2^p p!} \cdot u_p^{(e)} \text{ and } u_p^{(e)} = \frac{p!}{(2p)!} \cdot h_e^p \cdot \frac{\partial^p}{\partial z^p} \mathbf{U_h}(z) = C h_e^p \frac{\partial^p}{\partial z^p} \mathbf{U_h}(z).$$

Let us now assume that (2.49) holds for $l > j$. Based on this assumption, we can conclude by (2.50):

$$\frac{\partial^j}{\partial z^j} \mathbf{U_h} = \left(\frac{2}{h_e}\right)^j \cdot \frac{(2j)!}{2^j j!} \cdot u_j^{(e)} + \mathcal{O}\left(h_e\right) \qquad \text{or} \qquad u_j^{(e)} = C h_e^j \cdot \frac{\partial^j}{\partial z^j} \mathbf{U_h} + \mathcal{O}\left(h_e^{j+1}\right).$$

□

Theorem 2.7. *If the solution $\mathbf{U_h}$ is smooth on $\overline{\Omega}_e \cup \overline{\Omega}_{e+1}$, then it holds for the j-th coefficient u_j^e:*

$$u_j^{(e)} = \frac{u_{j-1}^{(e+1)} - u_{j-1}^{(e)}}{2 \cdot (2j-1)} + \mathcal{O}\left(h^{j+1}\right), \tag{2.51}$$

where $h_e = h_{e+1} = h$ is taken into account.

Proof. This theorem has already been proved in [58, Section 2]: A derivative $\frac{\partial^j}{\partial z^j} \mathbf{U_h}$ can be represented by the first order forward difference quotient:

$$\frac{\partial^j}{\partial z^j} \mathbf{U_h} = \frac{1}{h} \left(\frac{\partial^{j-1}}{\partial z^{j-1}} \mathbf{U_h} \bigg|_{\Omega_{e+1}} - \frac{\partial^{j-1}}{\partial z^{j-1}} \mathbf{U_h} \bigg|_{\Omega_e} \right) + \mathcal{O}\left(h\right).$$

Using (2.50) it follows:

$$\left(\frac{2}{h}\right)^j \frac{(2j)!}{2^j j!} u_j^{(e)} + \left(\frac{2}{h}\right)^j \frac{\partial^j}{\partial x^j} \sum_{l>j}^{p} u_l^{(e)} L_l(x) = \left(\frac{2}{h}\right)^j \frac{1}{2} \frac{(2j-2)!}{2^{j-1}(j-1)!} \left(u_{j-1}^{(e+1)} - u_{j-1}^{(e)}\right)$$
$$+ \left(\frac{2}{h}\right)^j \frac{\partial^{j-1}}{\partial x^{j-1}} \sum_{l>j-1}^{p} \frac{1}{2} \left(u_l^{(e+1)} - u_l^{(e)}\right) L_l(x) + O(h).$$

Division by $\left(\frac{2}{h}\right)^j$ and comparing the coefficients on both sides of the equation, yields (2.51). □

A similar approximation as in Theorem 2.7 can be derived by representing the derivatives using the first order backward difference quotient:

$$u_j^{(e)} = \frac{u_{j-1}^{(e)} - u_{j-1}^{(e-1)}}{2 \cdot (2j-1)} + \mathcal{O}\left(h^{j+1}\right). \tag{2.52}$$

For a smooth solution and a sufficiently small h it follows from (2.51) and (2.52):

$$u_j^{(e)} \approx \underbrace{\frac{u_{j-1}^{(e+1)} - u_{j-1}^{(e)}}{2 \cdot (2j-1)}}_{=:D_f} \approx \underbrace{\frac{u_{j-1}^{(e)} - u_{j-1}^{(e-1)}}{2 \cdot (2j-1)}}_{=:D_b}, \quad j \in \{1, \ldots, p\}, \quad e \in \{2, \ldots, m-1\}.$$

In the vicinity of a discontinuity, these approximations are not valid and numerical oscillations are produced (see Figure 2.9). To prevent the formation of numerical oscillations, one possibility is to damp the coefficients, if the sign of the coefficient and the corresponding forward and the backward differences are different. To enforce a smoothing of the solution, we additionaly choose the smallest absolute value of the three approximations ($j = 1, \ldots, p$):

$$\tilde{u}_j^{(e)} = \operatorname{minmod}\left(u_j^{(e)}, \gamma_j \left(u_{j-1}^{(e+1)} - u_{j-1}^{(e)}\right), \gamma_j \left(u_{j-1}^{(e)} - u_{j-1}^{(e-1)}\right)\right), \quad \frac{1}{2\,(2j-1)} \leq \gamma_j \leq 1, \tag{2.53}$$

where the minmod function is defined by:

$$\operatorname{minmod}(a, b, c) = \begin{cases} \operatorname{sign}(a) \cdot \min(|a|, |b|, |c|), & \text{if } \operatorname{sign}(a) = \operatorname{sign}(b) = \operatorname{sign}(c), \\ 0, & \text{else.} \end{cases} \tag{2.54}$$

Depending on the choice of the parameter γ_j the solution is more or less smoothed. The damping or *limiting* strategy for the coefficients is carried out as described in Algorithm 1.

Algorithm 1 Hierarchical limiting

```
for $j = p$ to 1 do
    Compute $\tilde{u}_j^{(e)}$ by (2.53);
    if $\tilde{u}_j^{(e)} == u_j^{(e)}$ then
        Stop the limiting process;
    else
        $u_j^{(e)} = \tilde{u}_j^{(e)}$;
    end if
end for
```

This algorithm is known as *hierarchical limiting* [58]. The counterpart of this limiting strategy is called *uniform limiting*, when all the coefficients are limited (see Algorithm 2).

Algorithm 2 Uniform limiting

```
for $j = p$ to 1 do
    Compute $\tilde{u}_j^{(e)}$ by (2.53);
    $u_j^{(e)} = \tilde{u}_j^{(e)}$;
end for
```

The hierarchical limiting damps first the higher coefficients corresponding to the higher derivatives and leaves the lower coefficients unchanged. As a consequence of this method the flattening of smooth extrema is avoided. By a slight modification of the SSP method from Subsection 2.2 the limiting process can be integrated into the solution process:

$$\mathbf{u}^{(\mathbf{1})} = \Phi\left\{\mathbf{u}\left(t_n\right) + \Delta t R_M\left(\mathbf{u}\left(t_n\right)\right)\right\} \tag{2.55}$$

$$\mathbf{u}^{(\mathbf{2})} = \Phi\left\{\frac{3}{4}\mathbf{u}\left(t_n\right) + \frac{1}{4}\left(\mathbf{u}^{(\mathbf{1})} + \Delta t R_M\left(\mathbf{u}^{(\mathbf{1})}\right)\right)\right\} \tag{2.56}$$

$$\mathbf{u}\left(t_{n+1}\right) = \Phi\left\{\frac{1}{3}\mathbf{u}\left(t_n\right) + \frac{2}{3}\left(\mathbf{u}^{(\mathbf{2})} + \Delta t R_M\left(\mathbf{u}^{(\mathbf{2})}\right)\right)\right\}, \tag{2.57}$$

where Φ denotes the *limiting operator*. The discrete right hand side R_M is determined by the semi discrete formulation (2.38). The application of the limiting operator to every sub step in (2.55) -(2.55) is necessary to avoid that oscillations are created within the sub steps of the Runge-Kutta method. In order to test the performance of the limited DG-method, we solve again the linear advection equation for $a = \frac{1}{2}$ and the discontinuous initial condition (2.48). We choose again: $p = 2$, $h = \frac{1}{200}$ and $\Delta t = 10^{-3}$. As a limiting parameter, we keep the parameter γ_j equal to 1 in order to enforce at least a moderate smoothing. In Figure 2.14 it can be clearly seen that even a weak damping factor removes the oscillations around the jump, which could not be prevented by the unlimited DG-method (see Figure 2.13). The importance of the hierarchical limiting (Algorithm 1) is illustrated by the following linear advection problem:

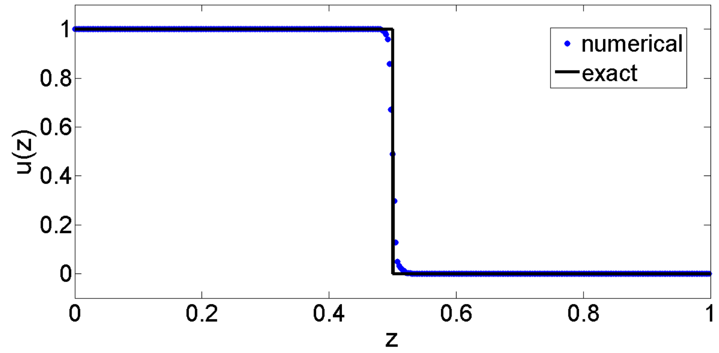

Figure 2.14: Exact solution and DG-approximation of the linear advection equation for $a = 0.5$, $z \in [0, 1]$, $t = 1$ and a discontinuous initial condition. The DG-approximation was stabilized by a moment limiter to remove the oscillations around the jump.

$$\begin{gathered}\partial_t u(z,t) + \frac{1}{2}\partial_z u(z,t) = 0, \quad t > 0,\\ u_0(z) = \sin(10\pi z).\end{gathered} \tag{2.58}$$

The exact solution of this problem is given by:

$$u(z,t) = \sin\left(-5\pi t + 10\pi z\right).$$

For the numerical treatment the following parameters are used: $p = 3$, $h = 10^{-2}$ and $\Delta t = 10^{-3}$. The results depicted in Figure 2.15 for $z \in [0, 1]$ and $t = 0.2$ reveal that the hierarchical limiting preserves the smooth extrema of the sine wave, whereas the uniform limiting causes a flattening of the smooth extrema. Obviously, the solution of (2.58) is smooth and exhibits no discontinuities. Thus, the application of a limiting method would not be necessary to compute a good numerical solution. Nevertheless a meaningful limiting strategy applied to a smooth solution should produce a numerical approximation, which leaves a smooth solution unchanged. This can be achieved by the hierarchical limiting method (Algorithm 1), which starts the limiting process at the rough components or the higher derivatives of the solution.

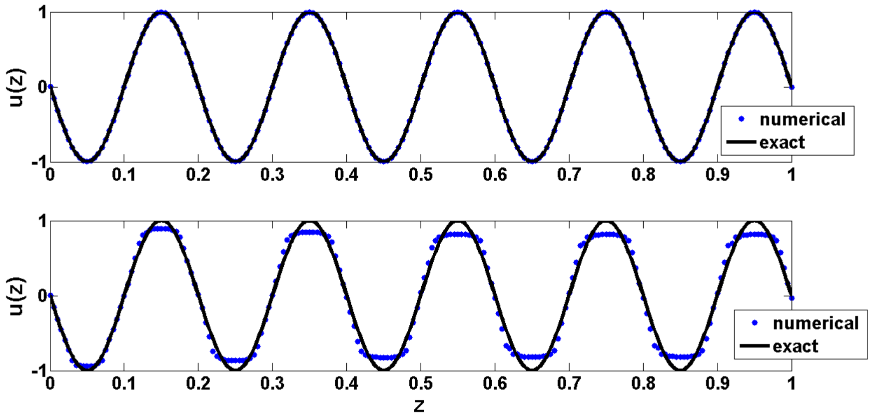

Figure 2.15: Exact solution and DG-approximation of the linear advection equation (2.58) for $z \in [0, 1]$ and $t = 0.2$. The DG-approximation is based on cubic Legendre polynomials ($p = 3$). To stabilize the numerical solution a hierarchical moment limiter (top) and a uniform moment limiter (bottom) is used.

In order to obtain more insight into the behavior of the hierarchical limiting method, we consider again the scalar advection problem (2.59). The initial condition u_0 for $z \in [0, 1]$ contains several jumps and sharp corners (see Figure 2.16).

$$
\begin{aligned}
\partial_t u(z,t) + \frac{1}{5}\partial_z u(z,t) &= 0, \quad t > 0, z \in (0,1) \\
u(z,0) = u_0(z) &= \begin{cases} 10z, & \text{if} \quad 0.0 \leq z \leq 0.1 \\ -10(z-0.2), & \text{if} \quad 0.1 < z \leq 0.2 \\ -1, & \text{if} \quad 0.3 \leq z \leq 0.5 \\ 1, & \text{if} \quad 0.6 \leq z \leq 0.8 \\ 0, & \text{else} \end{cases} \\
u(0,t) &= \sin(-\pi t), \quad t > 0.
\end{aligned} \tag{2.59}
$$

As a boundary condition for $z = 0$, we choose the smooth function $\sin(-\pi t)$. At the other boundary $z = 1$, we use an upwinding method to compute an appropriate boundary condition. For a time point $t_n = n \cdot \Delta t$ the boundary condition is interpolated from the data of the last time step:

$$\mathbf{U_h}\left(1,t_n\right)=\mathbf{U_h}\left(1-\frac{1}{5}\Delta t,t_{n-1}\right).$$

For $t=1$, we expect that the solution is given by the initial condition shifted by 0.2 to the right and a negative half sine wave at the left hand side of the computational domain.

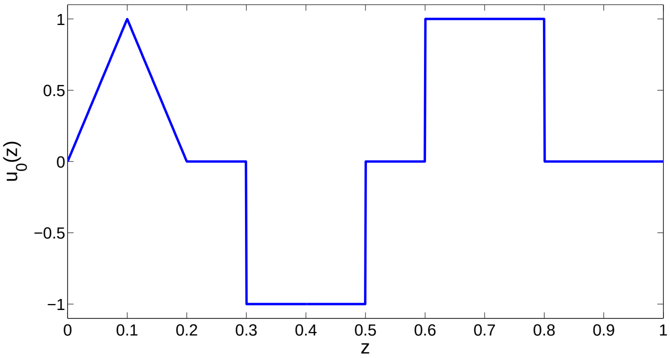

Figure 2.16: Graph of the initial condition u_0 in (2.59).

In the following three figures (Figure 2.17-2.19), the behavior of the moment limiter for different polynomial degrees. We observe that the extrema are better resolved for $p\in\{2,3\}$. The jumps are also approximated very well.

The behavior of the moment limiter for each polynomial degree p is depicted in the graph beneath the numerical solution. In these figures, a dot (one dot for each element) denotes the number of coefficients, which are limited. For example a dot at the value 2 and the polynomial degree $p=2$ means that coefficient 2 and 1 are limited, while coefficient 0 remains unchanged. In the vicinity of the discontinuities, it can be seen that for every polynomial degree almost every coefficient is damped. In the smooth parts of the solution none of the coefficients are limited. All in all we note that the smoother the solution is, less coefficients are damped and the nearer the element is located to a discontinuity, the more coefficients have to be damped to rule out numerical oscillations.

Finally, we want to test, if the hierarchical limiting reduces the convergence order of the numerical scheme. For this purpose we consider the transport problem:

$$\begin{aligned}\partial_t u(z,t)+\frac{1}{2}\partial_z u(z,t)&=0, \quad t>0, z\in(0,1)\\ u(z,0)&=10\sin(2\pi z), \quad z\in(0,1)\\ u(0,t)&=10\sin(-\pi t), \quad t>0.\end{aligned} \tag{2.60}$$

At the right boundary $z=1$ we use again a standard upwinding method to prescribe suitable boundary data. The solution u of this problem is given by:

$$u(z,t)=10\sin(-\pi t+2\pi z). \tag{2.61}$$

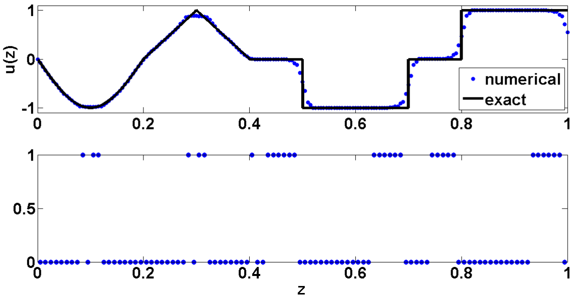

Figure 2.17: Behavior of the moment limiter applied to (2.59), for $p = 1$, $\Delta z = 10^{-1}$ and $\Delta t = 10^{-3}$. A dot in the figure at the bottom denotes for every element the number of coefficients, which are limited, starting from the highest coefficient.

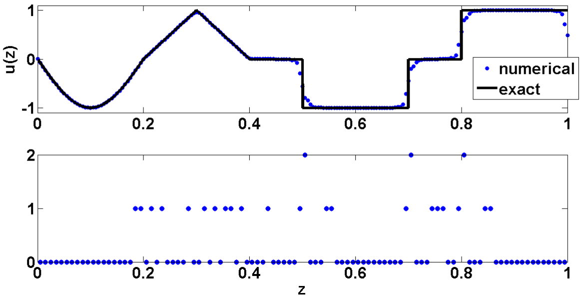

Figure 2.18: Behavior of the moment limiter applied to (2.59), for $p = 2$, $\Delta z = 10^{-1}$ and $\Delta t = 10^{-3}$. A dot in the figure at the bottom denotes for every element the number of coefficients, which are limited, starting from the highest coefficient.

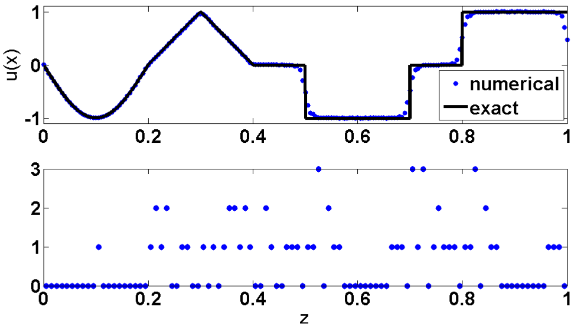

Figure 2.19: Behavior of the moment limiter applied to (2.59), for $p = 3$, $\Delta z = 10^{-1}$ and $\Delta t = 10^{-3}$. A dot in the figure at the bottom denotes for every element the number of coefficients, which are limited, starting from the highest coefficient.

Due to the fact that $u \in C^{\infty}\left(\Omega \times (0,\infty), \mathbb{R}\right)$, an optimal DG-method using a polynomial degree p should converge in space with respect to a suitable norm by order $p+1$. Table 2.2

	$p = 1:$		$p = 2:$		$p = 3:$	
Δz	L^1-error	eco	L^1-error	eco	L^1-error	eco
1/8	$9.66e-1$	—	$5.22e-2$	—	$4.43e-3$	—
1/16	$2.80e-1$	1.79	$5.13e-3$	3.35	$2.23e-4$	**4.31**
1/32	$6.52e-2$	**2.10**	$5.01e-4$	**3.36**	$1.03e-5$	**4.44**
1/64	$1.41e-2$	**2.21**	$5.15e-5$	**3.28**	$3.69e-7$	**4.81**
1/128	$2.94e-3$	**2.26**	$5.28e-6$	**3.29**	$9.62e-9$	**5.26**

Table 2.2: Spatial convergence of the DG-method for problem (2.59). The DG-method is based on Legendre polynomials and stabilized by the hierarchical moment limiter. For the time integration the SSP method (2.46a)-(2.46c) is used. eco abbreviates the term estimated convergence order. The time step size Δt is set to 10^{-4}.

contains the numerical errors produced by the limited DG-method based on Legendre polynomials, while Table 2.3 shows the approximation errors resulting from the corresponding unlimited DG-method. The errors in each case are computed with respect to the L^1-norm. The tables reveal that the approximation errors related to the limited DG-method are larger than those of the unlimited DG-method. An exception is the error for $p = 3$ and $h = 1/128$. In both cases this error is equal. This is due to the fact that the limiter is active for all the other degrees and mesh sizes. In this single case we observe that the solution on no element is limited, otherwise the limiter is always active and enlarges the error. The convergence rates of the unlimited DG-method behave as it has been expected. The limited DG-method exhibits convergence rates that are even better as predicted. Especially for $p = 3$ and $h = 1/128$ the convergence rate is remarkably high. While for $h = 1/64$ the solution is still limited, the solution for $h = 1/128$ is not limited anymore. Thus the method converges in this case better than it can be expected.

	$p = 1:$		$p = 2:$		$p = 3:$	
Δz	L^1-error	eco	L^1-error	eco	L^1-error	eco
1/8	$2.25e-1$	—	$1.20e-2$	—	$5.98e-4$	—
1/16	$5.28e-2$	**2.10**	$1.52e-3$	**3.04**	$3.67e-5$	**4.03**
1/32	$1.27e-2$	**2.06**	$1.90e-4$	**3.01**	$2.28e-6$	**4.01**
1/64	$3.10e-3$	**2.03**	$2.35e-5$	**3.01**	$1.41e-7$	**4.01**
1/128	$7.66e-4$	**2.02**	$2.84e-6$	**3.05**	$9.62e-9$	**3.88**

Table 2.3: Spatial convergence of the DG-method for problem (2.59). The DG-method is based on Legendre polynomials. For the time integration the SSP method (2.46a)-(2.46c) is used. eco abbreviates the term estimated convergence order. The time step size Δt is set to 10^{-4}.

(ii) Transport equation system

By now the limiter technique can only be applied to scalar equations. Considering our models for flow (see (2.14a) and (2.24a)), the limiter technique must be enhanced so that it is useable for systems of transport equations. According to [22, 58] a limiter technique for systems has to be applied to the characteristic variables, to prevent the formation of spurious oscillations in the vicinity of discontinuities. Therefore, one has to transform the primary variables $\mathbf{U}$ to its characteristic variables $\mathbf{W}$. This is done by the following formula (see e.g. (2.18)): $\mathbf{W} = L(\mathbf{U})\,\mathbf{U}$, where $L(\mathbf{U})$ denotes the matrix of left eigenvectors of the flux matrix $H(\mathbf{U}) = \frac{\partial \mathbf{F}}{\partial \mathbf{U}}$.

The limiting is performed in the following way:

$$\left(\widehat{L\mathbf{u}_i^{(e)}}\right)_j = \operatorname{minmod}\left(\left(L\mathbf{u}_i^{(e)}\right)_j, \left(L\left(\mathbf{u}_{i-1}^{(e)} - \mathbf{u}_{i-1}^{(e-1)}\right)\right)_j, \left(L\left(\mathbf{u}_{i-1}^{(e+1)} - \mathbf{u}_{i-1}^{(e)}\right)\right)_j\right), \quad (2.62)$$

$j = 1, \dots, n$. n is the dimension of the transport system, $\mathbf{u}_i^{(e)}$ denotes the i-th coefficient of the expansion (2.37) of the numerical solution $\mathbf{U}_h$ on an element Ω_e. Due to the fact that L can depend on the solution $\mathbf{U}$, one has to choose a suitable vector of primary variables $\overline{\mathbf{U}}^{(e)}$, to assign to each element Ω_e a suitable flux matrix $H\left(\overline{\mathbf{U}}^{(e)}\right)$. The authors of [92, 114] suggest to use the so called *Roe-Average*. In order to define the *Roe-Average*, we first have to introduce the *Roe-Matrix.*

Definition 2.6. *Let F be the flux function of a system of transport equations and let H be the corresponding flux matrix. A matrix $\widehat{H}_e$ for $\Omega_e = \left(z_e^l, z_e^r\right)$ is called* Roe-Matrix, *if it holds:*

- *(i)* $\widehat{H}_e\left(\mathbf{U}_r^{(e)}, \mathbf{U}_l^{(e)}\right)\left(\mathbf{U}_r^{(e)} - \mathbf{U}_l^{(e)}\right) = \mathbf{F}\left(\mathbf{U}_r^{(e)}\right) - \mathbf{F}\left(\mathbf{U}_l^{(e)}\right)$
- *(ii)* $\widehat{H}_e\left(\mathbf{U}_r^{(e)}, \mathbf{U}_l^{(e)}\right)$ *is diagonalizable with real eigenvalues*
- *(iii)* $\widehat{H}_e\left(\mathbf{U}_r^{(e)}, \mathbf{U}_l^{(e)}\right) \to \frac{\partial \mathbf{F}}{\partial \mathbf{U}}\left(\widehat{\mathbf{U}}\right), \quad \mathbf{U}_r^{(e)}, \mathbf{U}_l^{(e)} \to \widehat{\mathbf{U}},$

where $\mathbf{U}_r^{(e)} = \mathbf{U}\left(z_e^r\right)$ *and* $\mathbf{U}_l^{(e)} = \mathbf{U}\left(z_l^{(e)}\right)$.

Definition 2.7. *Let $\widehat{H}_e$ be a Roe-Matrix, then $\overline{\mathbf{U}^{(e)}}\left(\mathbf{U}_r^{(e)}, \mathbf{U}_l^{(e)}\right)$ is defined as Roe-Average for Ω_e, if it holds:*

$$\widehat{H}_e\left(\mathbf{U}_r^{(e)}, \mathbf{U}_l^{(e)}\right) = H\left(\overline{\mathbf{U}^{(e)}}\right).$$

By L_e we denote the left eigenvector matrix of $H\left(\overline{\mathbf{U}^{(e)}}\right)$.

Having these definitions at hand, we can replace a non-linear flux $\mathbf{F}(\mathbf{U})$ on Ω_e locally by $H\left(\overline{\mathbf{U}^{(e)}}\right) \cdot \mathbf{U}$. This yields a linearized transport system, which is much easier to analyse than a non-linear system. The items (i)-(iii) in Definition 2.6 are motivated as follows:

- Property (i) incorporates mass conservation into the local system on Ω_e

- Property (ii) preserves the signs of the eigenvalues
- Property (iii) guarantees that the local system is consistent with the linearized problem

For a linear flux function $\mathbf{F}(\mathbf{U}) = H \cdot \mathbf{U}$ the Roe-Matrix $\widehat{H}_e$ is equal to H. As the flux matrix H is independent of $\mathbf{U}$, we can choose the Roe-Average, e.g., as: $\overline{\mathbf{U}^{(e)}} = 0.5 \cdot \left(\mathbf{U}_r^{(e)} + \mathbf{U}_l^{(e)}\right)$. If the flux function $\mathbf{F}(\mathbf{U})$ is non-linear, the computation of the Roe-Matrix and the Roe-Average is more complex, as it can be seen based on (2.14a).

Theorem 2.8. *The Roe-Matrix* $\widehat{H_e}$ *and the Roe-Average* $\overline{\mathbf{U}^{(e)}}$ *for the transport system* (2.14a) *are given by:*

$$\widehat{H}_e\left(\mathbf{U}_r^{(e)}, \mathbf{U}_l^{(e)}\right) = \frac{\partial \mathbf{F_{AQ}}}{\partial \mathbf{U_{AQ}}}\left(\overline{\mathbf{U}^{(e)}}\right), \quad \overline{\mathbf{U}^{(e)}} = \begin{pmatrix} \overline{A^{(e)}} \\ \overline{Q^{(e)}} \end{pmatrix},$$

where

$$\overline{A^{(e)}} = \left(\frac{2}{3} \cdot \left(\frac{A_r^{(e)} + \sqrt{A_r^{(e)} \cdot A_l^{(e)}} + A_l^{(e)}}{\sqrt{A_r^{(e)}} + \sqrt{A_l^{(e)}}}\right)\right)^2, \quad \overline{Q^{(e)}} = \overline{A^{(e)}} \cdot \frac{\sqrt{A_r^{(e)}}\frac{Q_r^{(e)}}{A_r^{(e)}} + \sqrt{A_l^{(e)}}\frac{Q_l^{(e)}}{A_l^{(e)}}}{\sqrt{A_r^{(e)}} + \sqrt{A_l^{(e)}}}$$

and

$$\mathbf{U}_r^{(e)} = \begin{pmatrix} A_r^{(e)} \\ Q_r^{(e)} \end{pmatrix}, \qquad \mathbf{U}_l^{(e)} = \begin{pmatrix} A_l^{(e)} \\ Q_l^{(e)} \end{pmatrix}.$$

Proof. Property (i) in Definition 2.6 can be verified by some straightforward computations that are omitted here. In order to proof property (ii) we compute the eigenvalues of the flux matrix:

$$H(\mathbf{U_{AQ}}) = \frac{\partial \mathbf{F_{AQ}}}{\partial \mathbf{U_{AQ}}} = \begin{pmatrix} 0 & 1 \\ c_{AQ}^2 - v^2 & 2v \end{pmatrix}, \text{ where } c_{AQ}^2 = \frac{G_0}{2\rho}\sqrt{\frac{A}{A_0}}, \ v = \frac{Q}{A}$$

and $\mathbf{U_{AQ}} = (A, Q)^T$. For H, we obtain the following eigenvalues: $\lambda_1 = v - c_{AQ}$ and $\lambda_2 = v + c_{AQ}$. The matrix of left eigenvectors $\mathbf{L}(\mathbf{U_{AQ}})$ and its inverse $\mathbf{L}(\mathbf{U_{AQ}})^{-1}$ is given by:

$$\mathbf{L}(\mathbf{U_{AQ}}) = \frac{1}{A}\begin{pmatrix} c_{AQ} + v & -1 \\ c_{AQ} - v & 1 \end{pmatrix} \text{ and } \mathbf{L}(\mathbf{U_{AQ}})^{-1} = \frac{A}{2c_{AQ}}\begin{pmatrix} 1 & 1 \\ v - c_{AQ} & v + c_{AQ} \end{pmatrix}$$

Defining $\Lambda(\mathbf{U_{AQ}})$ by $\Lambda(\mathbf{U_{AQ}}) = \operatorname{diag}(\lambda_1, \lambda_2)$ the following identity holds:

$$H(\mathbf{U_{AQ}}) = \mathbf{L}(\mathbf{U_{AQ}})^{-1}\Lambda(\mathbf{U_{AQ}})\,\mathbf{L}(\mathbf{U_{AQ}}).$$

Thus, $\widehat{H}_e$ has real eigenvalues and fulfills property (ii) in Definition 2.6. For the proof of property (iii), we assume:

$$A_r^{(e)}, A_l^{(e)} \to \hat{A} \ \text{ and } \ Q_r^{(e)}, Q_l^{(e)} \to \hat{Q}.$$

Considering these limits, we have:

$$\overline{A^{(e)}} \to \hat{A} \qquad \text{and} \qquad \overline{Q^{(e)}} \to \hat{Q},$$

from this it follows that $\widehat{H}_e\left(\mathbf{U}_r^{(e)}, \mathbf{U}_l^{(e)}\right) \to \frac{\partial \mathbf{F_{AQ}}}{\partial \mathbf{U_{AQ}}}\left(\widehat{\mathbf{U}}\right)$, where $\widehat{\mathbf{U}} = \left(\hat{A}, \hat{Q}\right)^T$. This means that property (iii) is also fulfilled. $\square$

Algorithm 3 Hierarchical limiting for systems of transport equations

```
for $e = 1$ to $m$ do
  for $j = 0$ to $p$ do
    Compute $\mathbf{u}_j^{(e)}$ (see (2.37));
  end for
  Determine the Roe-Average $\overline{\mathbf{U}^{(e)}}$ and the matrix $L_e$ (see Definition 2.6 and 2.7);
  for $j = 0$ to $p$ do
    Compute $L_e \cdot \mathbf{u}_j^{(e)}$;
  end for
  for $j = 1$ to $n$ do
    Compute $\left(\widehat{L_e \mathbf{u}_i^{(e)}}\right)_j$ (see (2.62));
    for $i = p$ to $1$ do
      if $\left(\left(\widehat{L_e \cdot u_i^{(e)}}\right)\right)_j == \left(\left(L_e \cdot u_i^{(e)}\right)\right)_j$ then
        Stop the limiting process;
      else
        Compute the limited coefficients by: $\left(\widehat{u_i^{(e)}}\right)_j = \left(L_e^{-1} \cdot \left(\widehat{L_e \cdot u_i^{(e)}}\right)\right)_j$;
      end if
    end for
  end for
end for
```

By the help of the left eigenvectors L_e and its inverse L_e^{-1} the limited coefficients $\widehat{u_i^{(e)}}$ can be computed by transforming the limited characteristic variables back to the primary variables:

$$\widehat{u_i^{(e)}} = L_e^{-1} \cdot \left(\widehat{L_e \cdot u_i^{(e)}}\right).$$

In Algorithm 3, we present a short description of the hierarchical limiting technique for systems.

Limiter technique for the Taylor basis

In the following we present a limiter technique for the Taylor basis developed in [60, 61]. In these publications a limiting strategy of Barth and Jepsen [11] for a piecewise linear approximation (see Subsection (ii) Taylor basis):

$$\mathbf{U_h}\big|_{\Omega_e} \approx \mathbf{U}\left(z_e^c\right) + \left.\frac{\partial \mathbf{U}}{\partial z}\right|_{z=z_e^c}\left(z - z_e^c\right) = \overline{\mathbf{U_h}} + \left.\frac{\partial \mathbf{U}}{\partial z}\right|_{z=z_e^c}\left(z - z_e^c\right) \tag{2.63}$$

has been used. As it was already pointed out, the approximation in (2.63) is a Taylor expansion around the element center $z_e^c = \frac{z_e^r + z_e^l}{2}$. The idea of Barth and Jepsen [11] is to replace the slope $\frac{\partial \mathbf{U}}{\partial z}$ in $z = z_e^c$ by a damped slope $\alpha_e \cdot \frac{\partial \mathbf{U}}{\partial z}$, such that the limited solution is given by:

$$\mathbf{U_h}\big|_{\Omega_e} \approx \mathbf{U}\left(z_e^c\right) + \alpha_e \cdot \left.\frac{\partial \mathbf{U}}{\partial z}\right|_{z=z_e^c}\left(z - z_e^c\right). \tag{2.64}$$

The damping parameter α_e should fulfill the following inequalities:

$$\mathbf{U}_l^{e,min} \leq \mathbf{U_h}\left(z_e^l\right) \leq \mathbf{U}_l^{e,max} \quad \text{and} \quad \mathbf{U}_r^{e,min} \leq \mathbf{U_h}\left(z_e^r\right) \leq \mathbf{U}_r^{e,max}, \tag{2.65}$$

where $\Omega_e = \left(z_e^l, z_e^r\right)$ and

$$\begin{aligned}
\mathbf{U}_l^{e,min} &= \min\left(\mathbf{U}\left(z_{e-1}^c\right), \mathbf{U}\left(z_e^c\right)\right), \quad & \mathbf{U}_l^{e,max} &= \max\left(\mathbf{U}\left(z_{e-1}^c\right), \mathbf{U}\left(z_e^c\right)\right), \\
\mathbf{U}_r^{e,min} &= \min\left(\mathbf{U}\left(z_{e+1}^c\right), \mathbf{U}\left(z_e^c\right)\right), \quad & \mathbf{U}_r^{e,max} &= \max\left(\mathbf{U}\left(z_{e+1}^c\right), \mathbf{U}\left(z_e^c\right)\right).
\end{aligned}$$

Please note that the min and max functions are applied component wise in the previous formula.

Theorem 2.9. *A possible choice for α_e, which fulfills* (2.65) *is given by [60, 61]:*

$$\alpha_e = \min(\alpha_e^l, \alpha_e^r), \quad \alpha_e^{l,r} = \begin{cases} \min\left(1, \frac{\mathbf{U}_{l,r}^{e,max} - \mathbf{U}_c}{\mathbf{U}_h^{l,r} - \mathbf{U}_c}\right), & \text{if} \quad \mathbf{U}_h^{l,r} - \mathbf{U}_c > 0, \\ 1, & \text{if} \quad \mathbf{U}_h^{l,r} - \mathbf{U}_c = 0, \\ \min\left(1, \frac{\mathbf{U}_{l,r}^{e,min} - \mathbf{U}_c}{\mathbf{U}_h^{l,r} - \mathbf{U}_c}\right), & \text{if} \quad \mathbf{U}_h^{l,r} - \mathbf{U}_c < 0, \end{cases}$$

where $\mathbf{U}_h^{l,r} = \mathbf{U}_h\left(z_e^{l,r}\right)$, $\mathbf{U_c} = \mathbf{U}\left(z_e^c\right)$.

Proof. Considering the definitions of $\mathbf{U}_{l,r}^{e,min}$ and $\mathbf{U}_{l,r}^{e,min}$, it follows that:

$$\mathbf{U}_{l,r}^{e,min} - \mathbf{U_c} \leq 0 \leq \mathbf{U}_{l,r}^{e,max} - \mathbf{U_c}.$$

By (2.64) and (2.65), we have for $\mathbf{U}_h^l$:

$$\mathbf{U}_{l,r}^{e,min} - \mathbf{U_c} \leq \underbrace{\alpha_e^l \cdot \left.\frac{\partial \mathbf{U}}{\partial z}\right|_{z=z_e^c}\left(z_e^l - z_e^c\right)}_{=\alpha_e^l\left(\mathbf{U}_h^l - \mathbf{U}_c\right)} \leq \mathbf{U}_{l,r}^{e,max} - \mathbf{U_c}.$$

Using the cases in Theorem 2.9 it follows the first inequality in (2.65). Analogously one can show that α_e^r fulfills the second inequality in (2.65). It remains to show that α_e fulfills both inequalities in (2.65). First we show that α_e matches the first inequality:

$$\begin{aligned}
&\frac{\mathbf{U}_l^{e,min} - \mathbf{U}_c}{\mathbf{U}_h^l - \mathbf{U}_c} \leq 0 \leq \alpha_e \leq \alpha_e^l \leq \frac{\mathbf{U}_l^{e,max} - \mathbf{U}_c}{\mathbf{U}_h^l - \mathbf{U}_c}, && \text{if} \quad \mathbf{U}_h^l - \mathbf{U}_c > 0\\
&\frac{\mathbf{U}_l^{e,min} - \mathbf{U}_c}{\mathbf{U}_h^l - \mathbf{U}_c} \geq \alpha_e^l \geq \alpha_e \geq 0 \geq \frac{\mathbf{U}_l^{e,max} - \mathbf{U}_c}{\mathbf{U}_h^l - \mathbf{U}_c}, && \text{if} \quad \mathbf{U}_h^l - \mathbf{U}_c < 0\\
&\mathbf{U}_l^{e,min} - \mathbf{U}_c \leq 0 \leq \mathbf{U}_l^{e,max} - \mathbf{U}_c, && \text{if} \quad \mathbf{U}_h^l - \mathbf{U}_c = 0
\end{aligned}$$

The second inequality is proved in an analogous way. □

Having a closer look at the correction factors provided in Theorem 2.9, we note that $0 \leq \alpha_e \leq 1$ holds. Thus, these factors can be interpreted as damping factors, which can rule out unphysical numerical oscillations. The computation of these factors can be implemented in an efficient way, as $\mathbf{U_c}$ is equal to the coefficient associated with the constant polynomial T_0. Thus this value is already computed and can be directly used for the limiting process. The values for $\mathbf{U}_{l,r}^{e,min}$ and $\mathbf{U}_{l,r}^{e,max}$ can be interpolated.

In order to determine the correction factors for the higher derivatives, we derive a linear approximation for the higher derivatives. Due to

$$\frac{\partial^k T_k}{\partial z^k}(z) = T_0(z) = 1, \qquad \frac{\partial^{k-1} T_k}{\partial z^{k-1}}(z) = T_1(z) = z - z_e^c \tag{2.66}$$

we have:

$$\left.\frac{\partial^k \mathbf{U}_h}{\partial z^k}\right|_{\Omega_e} = \underbrace{\left.\frac{\partial^k \mathbf{U}}{\partial z^k}\right|_{z=z_e^c} + \left.\frac{\partial^{k+1} \mathbf{U}}{\partial z^{k+1}}\right|_{z=z_e^c} (z - z_e^c)}_{=\text{linear part}} + r(z). \tag{2.67}$$

$r(z)$ denotes a polynomial of degree higher than 1, except for $k = p$. The linear part is treated as the linear approximation in (2.63), replacing $\mathbf{U}$ by $\frac{\partial^k \mathbf{U}_h}{\partial z^k}$ and $\mathbf{U}_h^{l,r}$ by $\frac{\partial^k \mathbf{U}_h^{l,r}}{\partial z^k}$. All in all, we have for the k-th derivative of $\mathbf{U}_h$ a correction factor $\alpha_e^{(k)}$, $k \in \{1, \ldots, p\}$.

Analogously to the limiter technique for the Legendre basis, it is crucial to apply a hierarchical limiting. The coefficient associated to the k-th Taylor basis polynomial is equal to the k-th derivative of the solution at the element center. Therefore we start the limiting by computing the damping factor $\alpha_e^{(p)}$ (see Theorem 2.9). In order to limit the k-th derivative we compute $\alpha_e^{(k)}$ by Theorem 2.9. The correction factor $\alpha_e^{(k)}$ should be equal or larger than the correction factors $\alpha_e^{(l)}$, $l > k$, to prevent the flattening of smooth extrema:

$$\alpha_e^{(k)} = \max_{k \leq l \leq p} \left\{ \alpha_e^{(l)} \right\}.$$

If $\alpha_e^{(k)} = 1$ for a certain damping factor, we have $\alpha_e^{(i)} = 1 \; \forall i < k$. Thus, the limiting process can be stopped, if one damping factor is equal to 1 (see Algorithm 4). To illustrate the robustness and stability of this limiter technique, we consider again the linear advection

Algorithm 4 Hierarchical limiting for the Taylor basis

```
for $e = 1$ to $m$ do
  Compute $a_k$ according to (2.43) and determine the numerical solution $\mathbf{U}_h$ on $\Omega_e$;
end for
for $e = 1$ to $m$ do
  for $i = p$ to 1 do
    Compute $\alpha_e^{(i)}$ according to Theorem 2.9 and (2.66),(2.67);
    Compute $\alpha_e^{(i)} = \max_{i \leq l \leq p} \left\{ \alpha_e^{(l)} \right\}$;
    if $\alpha_e^{(i)} == 1$ then
      BREAK;
    end if
  end for
end for
```

equation for $a = 1$ on $\Omega = (0, 1)$ and $t = 0.5$. At the left boundary ($z = 0$), we prescribe two different inflow profiles:

$$u_{\text{smooth}}(t) = \begin{cases} \sin\left(\frac{\pi}{0.2} t\right) & \text{if} \quad 0 \leq t \leq 0.2, \\ 0.0 & \text{if} \quad 0.2 < t \leq 1, \end{cases} \quad \text{and } u_{\text{jump}}(t) = 1, \text{ for } 0 \leq t \leq 1.$$

At the outflow boundary ($z = 1$), we impose again a free outflow condition, i.e., the boundary data in each time step are computed by standard upwinding. For the DG-method, we use the following parameters: $p = 2$, $\Delta z = 1/200$ and $\Delta t = 10^{-4}$. The results for the different inflow profiles can be seen in Figure 2.20. Besides, the numerical solution the correction factors $\alpha_e^{(1)}$ and $\alpha_e^{(2)}$ are reported for each element.

Algorithm 5 Uniform limiting for the Taylor basis

```
for $e = 1$ to $m$ do
  Compute $a_k$ according to (2.43) and determine the numerical solution $\mathbf{U}_h$ on $\Omega_e$;
end for
for $e = 1$ to $m$ do
  for $i = p$ to 1 do
    Compute $\alpha_e^{(i)}$ according to Theorem 2.9 and (2.66),(2.67);
  end for
end for
```

Our results show that in both cases the hierarchical limiter combined with the SSP as a time integrator yield satisfying results. By limiting, the correction factors $\alpha_e^{(2)}$ around the sharp corners at the zeros of the half sine wave (see Figure 2.20 (top left)) and in the vicinity of the jump (see Figure 2.20 (top right)) the formation of spurious oscillations can be prevented. The necessity to use a hierarchical limiter instead of an uniform limiter technique (see Algorithm 5) can be seen in Figure 2.21.

While the hierarchical limiter preserves the smooth extremum of the half sine wave, the uniform limiter causes a flattening of the smooth extremum. The correction factors $\alpha_e^{(2)}$ in

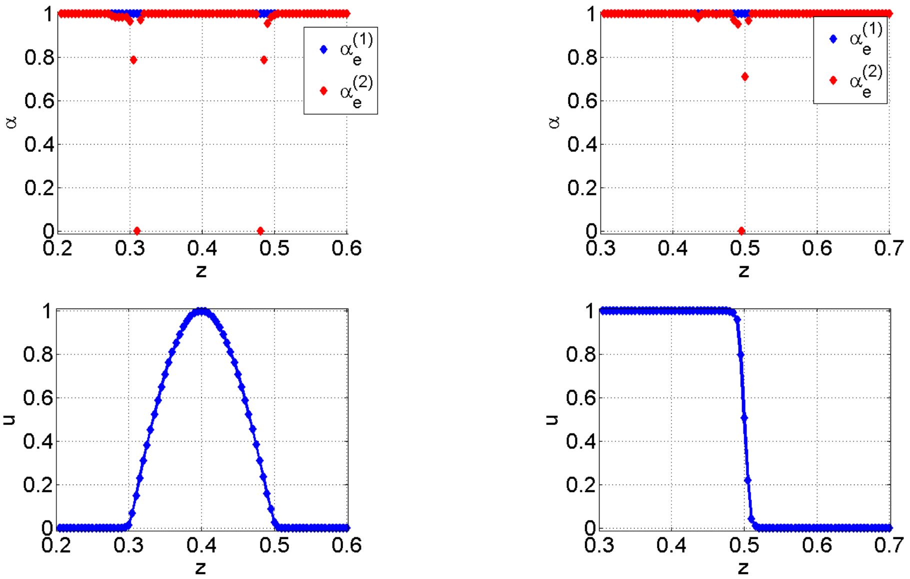

Figure 2.20: Correction factors $\alpha_e^{(i)}$ of the hierarchical slope limiting method, u_{smooth} (top left), u_{jump} (top right), Numerical approximations computed by quadratic Taylor polynomials ($p = 2$) and stabilized by the hierarchical slope limiting method for u_{smooth} (bottom left) and u_{jump} (bottom right)

the uniform case are within the interval $[0.9, 1.0]$ and in the vicinity of the extremum $\alpha_e^{(1)}$ is equal to zero. This behavior can be prevented using the formula $\alpha_e^{(k)} = \max_{k \leq l \leq p} \left\{ \alpha_e^{(l)} \right\}$.

By now, we used only orthogonal polynomial bases, since the Legendre basis is orthogonal for all degrees with respect to the standard L^2-product. Some straightforward computations reveal that the Taylor basis is only orthogonal with respect to the L^2-scalar product for $p \leq 2$. Thus, for $p \geq 3$, we have a non-diagonal mass matrix. According to [60, 61, 82] the off-diagonal entries of the mass matrix introduce an implicit coupling between the unlimited derivatives of all orders. As a consequence, the application of the limiter technique (Algorithm 4) yields an approximation, which is on the one hand side non-oscillatory but on the other hand very inaccurate (see Figure 2.22 (top)).

A possible way to circumvent this problem is to use a lumped mass matrix M_L, consisting only of the diagonal entries of the full mass matrix M_C. Although, this approach is conservative, it results in a loss of accuracy [60]. Therefore the potential of higher order approximation is lost. As a consequence in [61] the full mass matrix was used and additional limiting for the involved time derivatives was introduced. The mass lumping error is compensated, by adding the off-diagonal part to the right-hand side of the lumped mass matrix discretization.

This results in a modified time integrator compared to the standard SSP method, presented in Subsection 2.2.5. For convenience of the reader we rewrite the standard SSP method

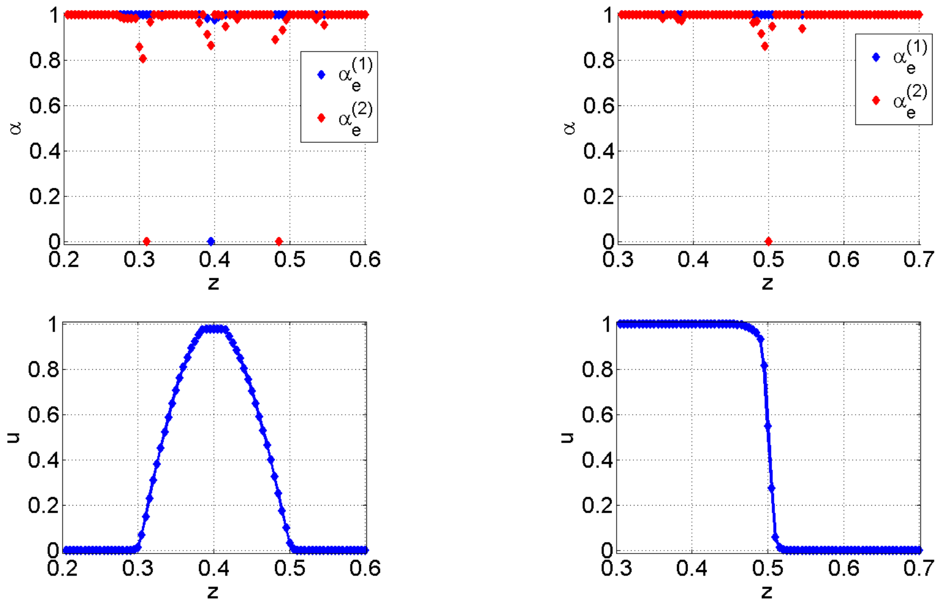

Figure 2.21: Correction factors $\alpha_e^{(i)}$ of the uniform slope limiting method, u_{smooth} (top left), u_{jump} (top right), Numerical approximations computed by quadratic Taylor polynomials ($p = 2$). The approximations are limited by the uniform slope limiting method, u_{smooth} (bottom left), u_{jump} (bottom right).

here:

$$\mathbf{u^{(1)}} = \mathbf{u}(t_n) + \Delta t \cdot M_C^{-1} R(\mathbf{u}(t_n)) \tag{2.68a}$$

$$\mathbf{u^{(2)}} = \frac{3}{4}\mathbf{u}(t_n) + \frac{1}{4}\left(\mathbf{u^{(1)}} + \Delta t \cdot M_C^{-1} R\left(\mathbf{u^{(1)}}\right)\right) \tag{2.68b}$$

$$\mathbf{u}(t_{n+1}) = \frac{1}{3}\mathbf{u}(t_n) + \frac{2}{3}\left(\mathbf{u^{(2)}} + \Delta t \cdot M_C^{-1} R\left(\mathbf{u^{(2)}}\right)\right). \tag{2.68c}$$

In the slope-limited version of the SSP Runge–Kutta scheme, we update the solution in the k-th sub step as follows ($\mathbf{u^{(0)}} = \mathbf{u}(t_n)\,, \mathbf{u}(t_{n+1}) = \mathbf{u^{(3)}}$):

1. Given $\mathbf{u^{(k-1)}}$, calculate the vector of discretized time derivatives given by:

$$\dot{\mathbf{u}}^{\mathbf{(k)}} = M_C^{-1} R\left(\mathbf{u^{(k-1)}}\right). \tag{2.69}$$

2. Apply the hierarchical limiter Φ to the predictor $\dot{\mathbf{u}}^{\mathbf{(k)}}$ and calculate:

$$\tilde{\mathbf{u}}^{\mathbf{(k)}} = \mathbf{u^{(k-1)}} + \Delta t \cdot M_L^{-1}\left[(M_L - M_C)\,\Phi\left(\dot{\mathbf{u}}^{\mathbf{(k)}}\right) + R\left(\mathbf{u^{(k-1)}}\right)\right], \tag{2.70}$$

where $M_L := \operatorname{diag}\{m_{ii}\}$ denotes the diagonal part of the mass matrix M_C.

3. Apply the hierarchical limiter Φ to the convex average of $\mathbf{u}(t_n)$ and $\tilde{\mathbf{u}}^{(\mathbf{k})}$:

$$\mathbf{u}^{(\mathbf{k})} = \Phi\left(\omega_k \mathbf{u}(t_n) + (1-\omega_k)\,\tilde{\mathbf{u}}^{(\mathbf{k})}\right), \tag{2.71}$$

where $\omega_k \in [0,1]$ is the weight for step k of the SSP Runge–Kutta scheme.

Note that if we set $M_L = M_C$, omit the calculations in (2.69) and do not perform any limiting in (2.70) and in (2.71), we obtain the original third order SSP Runge–Kutta scheme. The results of the additional limiting are shown in Figure 2.22 (bottom). It can be seen that despite the usage of an non-orthogonal Taylor basis ($p = 3$) very accurate results are computed.

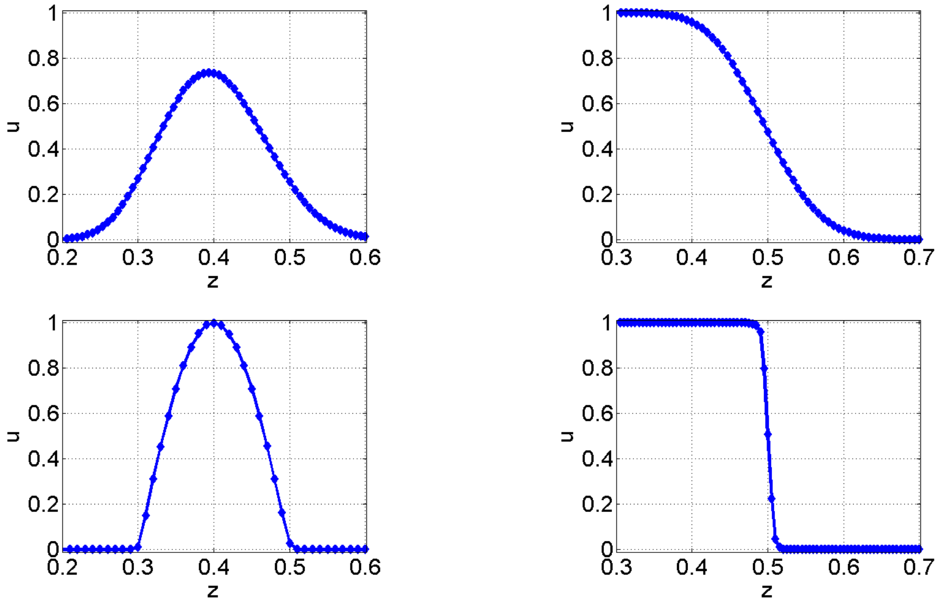

Figure 2.22: The numerical approximations shown in the figures are based on cubic Taylor polynomials ($p = 3$). For the solutions in the figures at the top we use a standard SSP (2.68a)-(2.68c) to complete the discretization. The solutions shown at the bottom use the slope limited SSP (2.69)-(2.71). All four solutions are reported at the time point $t = 0.5$. At the left u_{smooth} is prescribed at the inflow boundary, at the right u_{jump} is used at the inflow boundary.

To test the convergence behavior of the hierarchical vertex limiter for $p \in \{1,2,3\}$, we consider again the following transport problem:

$$\begin{aligned} \partial_t u(z,t) + \frac{1}{2}\partial_z u(z,t) &= 0, \quad t > 0, z \in (0,1) \\ u(z,0) &= 10\sin(2\pi z), \quad z \in (0,1) \\ u(0,t) &= 10\sin(-\pi t), \quad t > 0. \end{aligned} \tag{2.72}$$

At the right boundary $z = 1$, we use a standard upwinding method to prescribe suitable boundary data. Due to the fact that $u \in C^{\infty}(\Omega \times (0,\infty), \mathbb{R})$, an optimal DG-method using

	$p = 1:$		$p = 2:$		$p = 3:$	
Δz	L^1-error	eco	L^1-error	eco	L^1-error	eco
1/8	$9.66e-1$	—	$6.67e-2$	—	$2.24e-2$	—
1/16	$2.80e-1$	1.79	$1.09e-2$	2.62	$1.45e-3$	**3.95**
1/32	$6.52e-2$	**2.10**	$1.26e-3$	**3.11**	$8.52e-5$	**4.09**
1/64	$1.41e-2$	**2.21**	$1.41e-4$	**3.16**	$4.64e-6$	**4.20**
1/128	$2.94e-3$	**2.26**	$1.49e-5$	**3.24**	$2.56e-7$	**4.18**

Table 2.4: Spatial convergence of the DG-method for problem (2.59). The DG-method is based on Taylor polynomials and stabilized by the hierarchical vertex limiter. For the time integration we use the slope-limited SSP-method (2.69)-(2.71). eco abbreviates the term estimated convergence order. The time step size Δt is set to 10^{-4}.

a polynomial degree p should converge in space with respect to a suitable norm by order $p+1$. The results in Table 2.4 reveal that the L^1-error decays for the above problem by order $p+1$. Thus we can conclude that also the hierarchical vertex limiter does not reduce the convergence order of an optimal DG-method. However, all the errors are larger than those produced by the unlimited DG-method (see Table 2.3). Apparently, the solution computed by the DG-method combined with the hierarchical vertex limiter, is limited for each polynomial degree p and mesh size h. All in all, we can observe that this limiter technique is stricter than the moment limiter developed for the Legendre basis.

Limiter technique for boundary elements

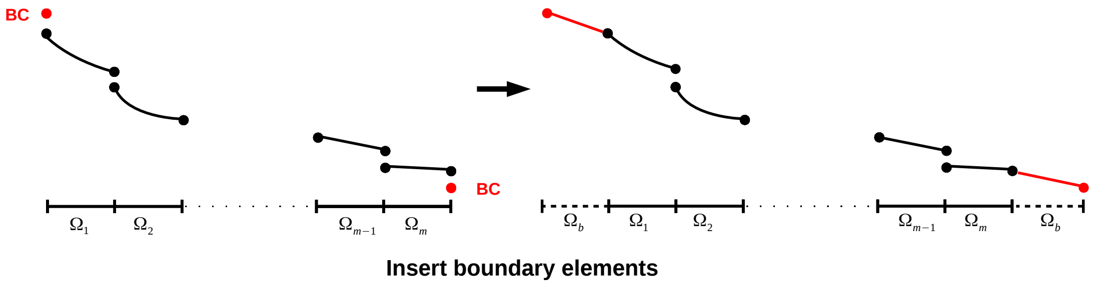

Figure 2.23: DG-approximation on the elements Ω_e, $e \in \{1, \dots, m\}$, the boundary conditions (BC) at the boundaries are marked by red dots (left). Insertion of additional elements Ω_b at the boundaries of the computational domain. The red lines indicate the linear auxiliary solutions based on the boundary conditions and the solution value at the corresponding boundary (right).

According to Equation (2.53) and Theorem 2.9 the moment and vertex limiter technique require for the limiting process on the element Ω_e information from the neighboring elements Ω_{e+1} and Ω_{e-1}. As it can be easily seen, there is one neighboring element missing at each boundary. As a consequence the limiter techniques cannot be applied to the boundary elements in the same way as for the inner elements.

In order to replace the information from the missing neighboring elements, we attach to each boundary element an additional element Ω_b (see Figure 2.23). On these additional elements, we compute by the help of the boundary conditions and the solution values at the boundaries a linear auxiliary solution (red lines on Ω_b, Figure 2.23), by interpolating the two values. This means that the solutions on Ω_b are combined by a constant and a linear basis function, if the solution on the other elements $\Omega_1, \dots, \Omega_m$ is given by polynomials of higher order, the corresponding coefficients of the auxiliary solutions on Ω_b are set to zero. These auxiliary solutions provide the missing information for the limiting process on the boundary elements and guarantee the fulfillment of the maximum principle and the TVD-property.

Comparison of both limiter techniques

In the previous subsections, we discussed the numerical difficulties associated with transport equations or systems of transport equations. It was stated that the conservation of mass, positivity, monotonicity and the TVD property are the major problems in this context. Our numerical investigations and references from literature reveal that higher order DG-methods, stabilized by a moment or a vertex limiter technique can tackle these problems. In this subsection, we summarize some features of both stabilization techniques:

Moment limiter:	**Vertex limiter:**
• Positivity, monotonicity and the TVD property of the solution are maintained	• Positivity, monotonicity and the TVD property of the solution are maintained
• higher order convergence in smooth regions is maintained by hierarchical limiting	• higher order convergence in smooth regions is maintained by hierarchical limiting
• higher order approximations yield no significant loss or gain of mass	• higher order approximations yield no significant loss or gain of mass
• mass matrix is diagonal for all polynomial degrees, thus an additional limiting of the time derivatives is *not* required	• mass matrix is not diagonal for $p > 2$, thus an additional limiting of the time derivatives is required

Taking the different features of the limiter techniques into account, it becomes obvious that only the Taylor basis exhibits a certain drawback. For Taylor polynomials having a higher degree than 2, a non diagonal mass matrix enforces additional limiting steps for the time derivatives.

Based on this comparison, we determine which limiter technique is the most appropriate for the models from Section 2.1. First we note that for the numerical treatment of the 1D systems (2.14a), (2.14b) and (2.24a), (2.24b), it is sufficient to use a limiter technique only for (2.14b) and (2.24b), respectively. Each system consists of three coupled transport equations, where the first two equations do not depend on the solution of the last equation. The first two equations model the propagation of pressure and velocity, which exhibit in our applications no discontinuities. The third equation models the transport of a certain substance, whose concentration can jump instantaneously from one value to another value. Thus, only the solution of the last equation has to be limited. The moment limiter does not require a limiting of time variables. Furthermore, no transformation to characteristic variables is needed for a scalar equation. Therefore, it is more efficient to use the moment limiter technique in this context.

2.3 Computing boundary data

In the previous sections of this thesis, we presented three models for the simulation of flow and mass transport within a single vessel. These models take the form of non-linear or linear 1D transport equation systems or ODE systems (0D lumped parameter models) (see Section 2.1). In order to solve these systems numerically, stabilized discontinuous Galerkin methods for the space discretization and SSP Runge Kutta methods for the time discretization were considered (see Section 2.2). Up to this point, we applied the numerical methods to scalar linear transport equations (2.34) for test purposes. In this context the incorporation of inflow and outflow boundary conditions as well as the interconnection of two neighboring elements is carried out by standard upwinding methods. However, for transport equation systems the computation of the coupling values at the element interfaces is not trivial. Furthermore, we have to establish coupling conditions for the subsystems adjacent to a bifurcation, in order to simulate flow and mass transport through a whole network.

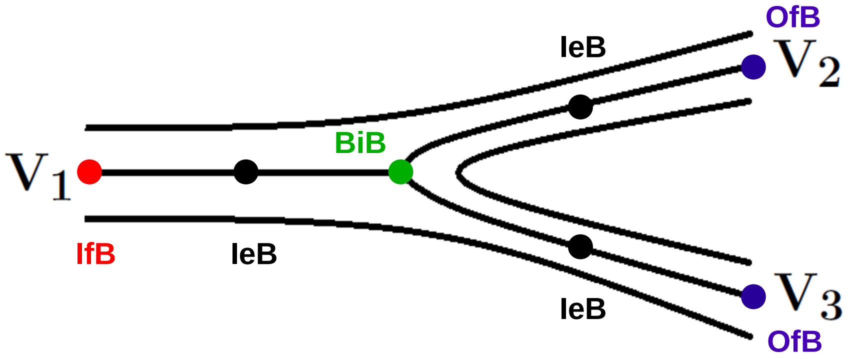

Figure 2.24: Types of boundaries occurring in a network

The different cases, occurring at a boundary of an element are summarized in Figure 2.24. We denote an inflow boundary by **IfB**, an outflow boundary by **OfB** and an interface between two inner elements by **IeB**. If one element boundary is adjacent to a bifurcation we assign to these boundaries the abbreviation **BiB**. The main axis of a vessel V_i is parameterized by an interval $[0, l_i]$, where l_i is the length of the vessel V_i. Before we discuss the different cases, it is pointed out that in this thesis we consider only networks whose terminal vessels are modeled by 1D transport equations. The 0D models are used to simulate flow and mass transport through small vessels in the inner part of the network. Furthermore they model the impact of small vessels beyond an outflow boundary.

2.3.1 Computing data at an inflow boundary (IfB)

Within the discontinuous Galerkin framework, an inflow boundary condition is incorporated into the numerical scheme by computing an appropriate upwinded flux $\mathbf{F}^{up}(z)$ at the inflow boundary $z = 0$ (see (2.38) and (2.42)). The upwinded flux is given by inserting a vector of upwinded values $\mathbf{U}_\mathbf{h}^\mathbf{up}(z)$ at $z = 0$ into the flux function $\mathbf{F}$ of the considered transport equation system. The crucial issue is how to determine these upwinded values $\mathbf{U}_\mathbf{h}^\mathbf{up}(0)$ with respect to inflow boundary conditions. In the non-linear case (2.14a),(2.14b) we have to calculate the values $(A^{up}, Q^{up}, \Gamma^{up})^T$ and in the linear case (2.24a), (2.24b) the values $(p^{up}, q^{up}, c^{up})^T$. This means that in both cases, three equations are required to determine the upwinded values. These equations are established by the help of the characteristic analysis from Section 2.1. Following Remark 2.2 and 2.3, we have at each boundary an outgoing and an ingoing characteristic for the AQ or pq subsystem. At the inflow boundary the outgoing characteristic is given by:

$$W_{1,in}^{AQ} := -\frac{Q_{in}}{A_{in}} + 4\sqrt{\frac{G_0}{2\rho}} \left(\frac{A_{in}}{A_0}\right)^{\frac{1}{4}}$$

in the non-linear case and by

$$W_{1,in}^{pq} := \frac{1}{2}\left(-\sqrt{\frac{C_{1D}}{L_{1D}}} p_{in} + q_{in}\right)$$

in the linear case, where we denote by f_{in} a function, which is evaluated at $z = 0$ on the first element Ω_1: $f_{in} = f\,|_{\Omega_1}(0)$. For the ingoing characteristics W_1^{AQ} and W_1^{pq} we have to provide a suitable boundary condition g_{AQ} or g_{pq}. However, in practice there is usually no boundary condition for the characteristics, but only for the pressure or the flow rate. Therefore, we have to transform the given pressure or flow rate profile in a condition for the ingoing characteristic. For convenience of the reader, we restrict ourselves to the transformation of the flow rate. The considerations for the pressure p can be found e.g., in [36]. Based on Theorem 2.1 and 2.3 we have:

$$Q = \frac{A}{2}\left(W_2^{AQ} - W_1^{AQ}\right) \qquad \text{and} \qquad q = W_1^{pq} + W_2^{pq}.$$

If W_1^{AQ} and W_1^{pq} are equal to its initial values $W_{1,0}^{AQ}$ and $W_{1,0}^{pq}$, we have by $Q(t) = g_{AQ}(t)$, $q(t) = g_{pq}(t)$ and $A = A_0$ for the ingoing characteristics $W_{2,in}^{AQ}$ and $W_{2,in}^{pq}$ at $z = 0$:

$$W_{2,in}^{AQ} = 2\frac{g_{AQ}(t)}{A_0} + W_{1,0}^{AQ} \qquad \text{and} \qquad W_{2,in}^{pq} = g_{pq}(t) - W_{1,0}^{pq}.$$

Despite the fact that these relations impose the flow rate profiles only implicitly and not directly, it has been proven that they are very effective and exhibit non-reflecting properties [36]. Now we have for each case two equations to compute the upwinded values for the flow:

$$W_{1,in}^{AQ} = -\frac{Q_{up}}{A_{up}} + 4\sqrt{\frac{G_0}{2\rho}}\left(\frac{A_{up}}{A_0}\right)^{\frac{1}{4}} \qquad \text{and} \qquad W_{2,in}^{AQ} = \frac{Q_{up}}{A_{up}} + 4\sqrt{\frac{G_0}{2\rho}}\left(\frac{A_{up}}{A_0}\right)^{\frac{1}{4}}, \tag{2.73}$$

$$W_{1,in}^{pq} = \frac{1}{2}\left(-\sqrt{\frac{C_{1D}}{L_{1D}}}p_{up} + q_{up}\right) \qquad \text{and} \qquad W_{2,in}^{pq} = \frac{1}{2}\left(\sqrt{\frac{C_{1D}}{L_{1D}}}p_{up} + q_{up}\right). \tag{2.74}$$

It remains to compute the values Γ_{up} and c_{up}. Since the behavior of Γ and c is determined by scalar transport equations (2.9c) (2.24b), whose velocity fields are given by $v_{AQ} = \frac{Q}{A}$ or $v_{pq} = \frac{q}{A_0}$, the upwinded values Γ_{up} and c_{up} can be computed by standard upwinding, depending on the sign of the velocity fields v_{AQ} or v_{pq}:

$$\Gamma_{up}(t) = \begin{cases} \Gamma\,|_{\Omega_1}(0,t)\,, & \text{if } v_{AQ} < 0, \\ c_{inflow}(t) \cdot A_{up}(t), & \text{if } v_{AQ} \geq 0, \end{cases} \tag{2.75}$$

and

$$c_{up}(t) = \begin{cases} c\,|_{\Omega_1}(0,t)\,, & \text{if } v_{pq} < 0, \\ c_{inflow}(t), & \text{if } v_{pq} \geq 0, \end{cases} \tag{2.76}$$

where the function c_{inflow} denotes a concentration profile, which is prescribed externally at the inflow boundaries. In most applications, it is set to a fixed concentration value c_0 of a certain substance: $c_{inflow} \equiv c_0$. Finally (2.73),(2.75) and (2.74),(2.76) form two systems of equations which can be used to compute the upwinded values at an inflow boundary.

2.3.2 Computing data at an outflow boundary (OfB)

As for the inflow boundary, we have to compute at the outflow boundary three upwinded values $(A_{up}, Q_{up}, \Gamma_{up})$ or (p_{up}, q_{up}, c_{up}) to integrate boundary conditions at outflow boundaries into the numerical scheme. This requires again the establishment of two systems of equations. At an outflow boundary $(z = l_i)$, there are analogously to an inflow boundary one outgoing and one ingoing characteristic for the $AQ-$ and $pq-$subsystem (2.14a) (2.24a). Contrary to the inflow boundary the characteristics W_1^{AQ} and W_1^{pq} are entering the computational domain, while W_2^{AQ} and W_2^{pq} are leaving the computational domain. Thus, W_2^{AQ} and W_2^{pq} can be computed by the values A_{out}, Q_{out} and p_{out}, q_{out}. A function f_{out}, $f \in \{A, Q, p, q\}$ is defined as:

$$f_{out}(t) := f\,|_{\Omega_m}(l,t)\,,$$

where Ω_m is the last element discretizing the computational domain $[0, l]$. For the outgoing characteristics $W_{2,out}^{AQ}$ and $W_{2,out}^{pq}$, it holds according to Theorem 2.1 and 2.3:

$$W_{2,out}^{AQ} = \frac{Q_{out}}{A_{out}} + 4\sqrt{\frac{G_0}{2\rho}}\left(\frac{A_{out}}{A_0}\right)^{\frac{1}{4}} \text{ and } W_{2,out}^{pq} = \frac{1}{2}\left(\sqrt{\frac{C_{1D}}{L_{1D}}}p_{out} + q_{out}\right).$$

Having the values $W_{2,out}^{AQ}$ and $W_{2,out}^{pq}$ at hand, one can establish a first equation for each model:

$$W_{2,out}^{AQ} = \frac{Q_{up}}{A_{up}} + 4\sqrt{\frac{G_0}{2\rho}} \left(\frac{A_{up}}{A_0} \right)^{\frac{1}{4}}, \tag{2.77}$$

$$W_{2,out}^{pq} = \frac{1}{2} \left(\sqrt{\frac{C_{1D}}{L_{1D}}} p_{up} + q_{up} \right). \tag{2.78}$$

It remains to derive a formula for the ingoing characteristic variables $W_{1,out}^{AQ}$ and $W_{1,out}^{pq}$ with respect to a prescribed outflow boundary condition. In this thesis, we consider two different types of outflow boundary conditions:

Free outflow boundary

In order to simulate a free outflow boundary, the authors of [36, 103] suggest to fix the incoming characteristic variables to their initial value, i.e.:

$$W_{1,out}^{AQ}(t) \equiv W_1^{AQ}(l,0) = 4\sqrt{\frac{G_0}{2\rho}} \quad \text{and} \quad W_{1,out}^{pq}(t) \equiv W_1^{pq}(l,0) = 0.$$

These conditions yield besides (2.77) and (2.78) the second equation for the computation of (A_{up}, Q_{up}) and (p_{up}, q_{up}):

$$W_{1,out}^{AQ} = -\frac{Q_{up}}{A_{up}} + 4\sqrt{\frac{G_0}{2\rho}} \left(\frac{A_{up}}{A_0} \right)^{\frac{1}{4}} \tag{2.79}$$

and

$$W_{1,out}^{pq} = \frac{1}{2} \left(-\sqrt{\frac{C_{1D}}{L_{1D}}} p_{up} + q_{up} \right). \tag{2.80}$$

Peripheral vessels

Since we are often interested in a small part of the human arterial tree, we have to truncate the blood vessel network after some bifurcations. To account for both resistive and compliant effects of the omitted vessels, the 1D models associated with a terminal vessel of the considered subnetwork are coupled to a 0D lumped parameter model (see Figure 2.25). In [2, 3, 4, 86] four-element parameter models, consisting of two resistances R_1 and R_2, a compliance C and an inductance L, are used to simulate the effect of the omitted vessel system on the flow in the subsystem. These 0D models yield for each time step and each outflow boundary two intermediate values (A^*, Q^*) or (p^*, q^*) at $t = t_{n+1}$ which originate from the states (A_{out}, Q_{out}), (p_{out}, q_{out}) and the coupling values (A_{coup}, Q_{coup}), (p_{coup}, q_{coup}) at $t = t_n$. The coupling values (A_{coup}, Q_{coup}), (p_{coup}, q_{coup}) determine the ingoing characteristics:

$$W_{1,out}^{AQ} = -\frac{Q_{coup}}{A_{coup}} + 4\sqrt{\frac{G_0}{2\rho}} \left(\frac{A_{coup}}{A_0} \right)^{\frac{1}{4}} \quad \text{and} \quad W_{1,out}^{pq} = \frac{1}{2} \left(-\sqrt{\frac{C_{1D}}{L_{1D}}} p_{coup} + q_{coup} \right),$$

while (A_{out}, Q_{out}) and (p_{out}, q_{out}) govern the outgoing characteristics $W_{2,out}^{AQ}$ and $W_{2,out}^{pq}$.

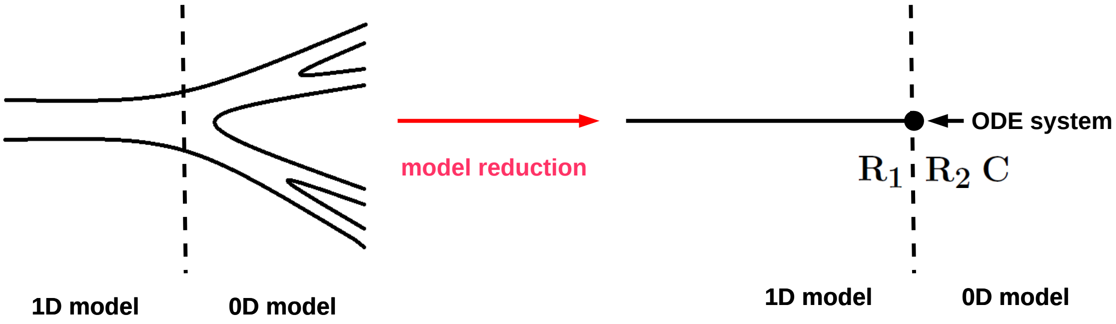

Figure 2.25: Modeling the effect of peripheral vessels by a three-element parameter model

Finally, we have for each model the missing second equation for the compution of the upwinded values:

$$W_{1,out}^{AQ} = -\frac{Q_{up}}{A_{up}} + 4\sqrt{\frac{G_0}{2\rho}}\left(\frac{A_{up}}{A_0}\right)^{\frac{1}{4}} \tag{2.81}$$

and

$$W_{1,out}^{pq} = \frac{1}{2}\left(-\sqrt{\frac{C_{1D}}{L_{1D}}}p_{up} + q_{up}\right). \tag{2.82}$$

The crucial issue is now to determine the coupling values (A_{coup}, Q_{coup}) or (p_{coup}, q_{coup}). According to [2, 3, 4] the boundary condition is imposed by assuming that

$$W_1^{AQ}(A^*, Q^*) = W_1^{AQ}(A_{coup}, Q_{coup}), \quad W_2^{AQ}(A^*, Q^*) = W_2^{AQ}(A_{out}, Q_{out})$$

and

$$W_1^{pq}(p^*, q^*) = W_1^{pq}(p_{coup}, q_{coup}), \quad W_2^{pq}(p^*, q^*) = W_2^{pq}(p_{out}, q_{out})$$

holds. By the help of Theorem 2.1 and 2.3 and the assumption $A_{coup} = A_{out}$ or $p_{coup} = p_{out}$, it follows:

$$Q_{coup} = A_{out}\left(2\frac{Q^*}{A^*} - \frac{Q_{out}}{A_{out}}\right) \quad \text{and} \quad q_{coup} = 2q^* - q_{out}. \tag{2.83}$$

For the incorporation of the resistive and compliant effects of the omitted vessels, we consider the (R_1CLR_2) parameter model. Doing so, we recall the analogy between hydraulic and electric networks, presented in Table 2.1. The resistance of the terminal vessel is measured by R_1, while the resistance of the vessels lying beyond the outflow boundary is measured by R_2. The compliance C of the omitted vessels can be regarded as the capacity of a capacitor, while the parameter L is the inductance of the omitted vessels. Within the four parameter model, R_1 and R_2, L are linked by the capacitor C (see Figure 2.26). Rewriting Ohm's law using hydraulic variables instead of electric variables, it follows for the first resistance R_1:

$$Q^* = \frac{p(A^*) - p_c}{R_1} \quad \text{or} \quad q^* = \frac{p^* - p_c}{R_1}, \tag{2.84}$$

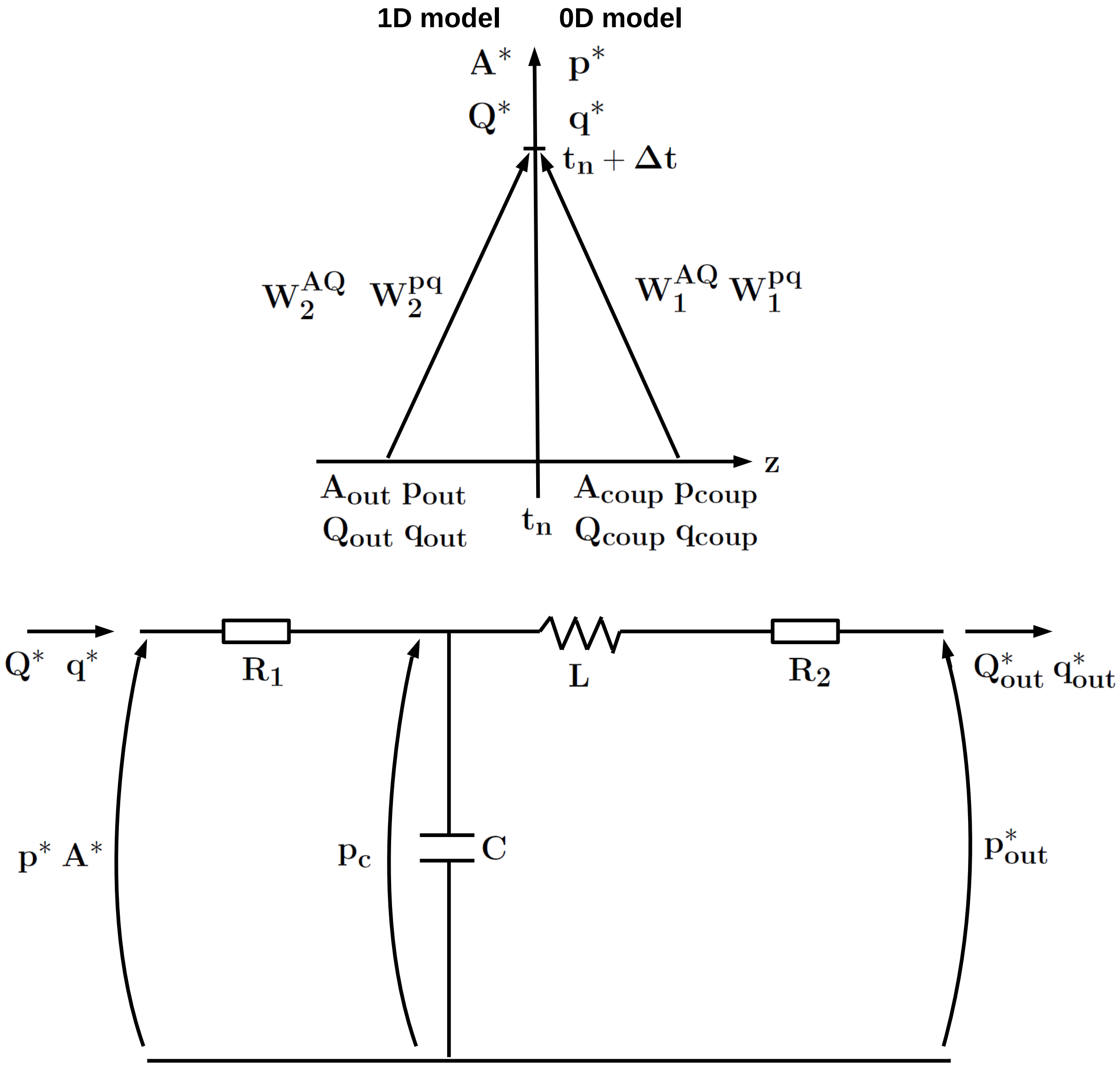

Figure 2.26: Notation for the variables at the interface between a 1D model and a 0D outflow model (top), outline of a four element outflow model (bottom).

$p(A^*)$ is given by (2.8). q^*_{out} and p^*_{out} denote the average pressure and average flow rate at the outflow boundaries of the omitted vessels. The pressure p_c within the CLR_2 system is governed by (2.27a). Replacing $\hat{p}$ by p_c, q_{out} by Q^*_{out} or q^*_{out}, C_{0D} by C and q_{in} by Q^* or

q^*, we have for $\phi_M \equiv 0$:

$$C \cdot \frac{dp_c}{dt} = Q^* - Q^*_{out} \quad \text{or} \quad C \cdot \frac{dp_c}{dt} = q^* - q^*_{out}. \tag{2.85}$$

For the flow rate within the CLR_2 system it holds using (2.27b), $L = L_{0D}$ and $R_2 = L_{0D} \cdot R_{1D}$:

$$L \cdot \frac{dQ^*_{out}}{dt} = p_c - p^*_{out} - R_2 \cdot Q^*_{out} \quad \text{or} \quad L \cdot \frac{dq^*_{out}}{dt} = p_c - p^*_{out} - R_2 \cdot q^*_{out}. \tag{2.86}$$

A first order discretization of (2.85) and (2.86) for the time interval $[t_n, t_{n+1}]$, $\Delta t = t_{n+1} - t_n$ is written as:

$$C \cdot \frac{(p_c)^{n+1} - (p_c)^n}{\Delta t} = Q^* - \left(Q^*_{out}\right)^{n+1}, \tag{2.87}$$

$$C \cdot \frac{(p_c)^{n+1} - (p_c)^n}{\Delta t} = q^* - \left(q^*_{out}\right)^{n+1} \tag{2.88}$$

and

$$L \cdot \frac{\left(Q^*_{out}\right)^{n+1} - \left(Q^*_{out}\right)^n}{\Delta t} = (p_c)^{n+1} - \left(p^*_{out}\right)^{n+1} - R_2 \cdot \left(Q^*_{out}\right)^{n+1}, \tag{2.89}$$

$$L \cdot \frac{\left(q^*_{out}\right)^{n+1} - \left(q^*_{out}\right)^n}{\Delta t} = (p_c)^{n+1} - \left(p^*_{out}\right)^{n+1} - R_2 \cdot \left(q^*_{out}\right)^{n+1}, \tag{2.90}$$

where $(p_c)^n = 0$, $\left(Q^*_{out}\right)^n = \left(q^*_{out}\right)^n = 0$ for the initial time step $n = 0$. The value $\left(p^*_{out}\right)^n$ is kept constant to an average value p^*_{out} for all time steps n: $\left(p^*_{out}\right)^n \equiv p^*_{out}$. Combining (2.87) and (2.89) as well as (2.88) and (2.90) yields:

$$\phi \cdot (p_c)^{n+1} = \frac{R_2 C}{\Delta t}(p_c)^n + R_2 Q^* + \frac{R_2}{L + \Delta t R_2}\left[\Delta t p^*_{out} - L\left(Q^*_{out}\right)^n\right],$$

$$\phi \cdot (p_c)^{n+1} = \frac{R_2 C}{\Delta t}(p_c)^n + R_2 q^* + \frac{R_2}{L + \Delta t R_2}\left[\Delta t p^*_{out} - L\left(q^*_{out}\right)^n\right],$$

where $\phi = \frac{R_2 C}{\Delta t} + \frac{R_2 \Delta t}{L + \Delta t R_2}$. By these equations and (2.84) it follows:

$$Q^* = \frac{\phi \cdot p(A^*)}{R_2 + \phi R_1} - \frac{R_2 \cdot C (p_c)^n}{R_2 + \phi R_1} - \frac{R_2\left(\Delta t p^*_{out} - L\left(Q^*_{out}\right)^n\right)}{(R_2 + \phi R_1)(L + \Delta t R_2)} \tag{2.91}$$

and

$$q^* = \frac{\phi \cdot p^*}{R_2 + \phi R_1} - \frac{R_2 \cdot C (p_c)^n}{R_2 + \phi R_1} - \frac{R_2\left(\Delta t p^*_{out} - L\left(q^*_{out}\right)^n\right)}{(R_2 + \phi R_1)(L + \Delta t R_2)}. \tag{2.92}$$

Using (2.91),

$$W_2^{AQ}(A^*, Q^*) = W_2^{AQ}(A_{out}, Q_{out}),$$

the area-pressure law (2.8) and Theorem 2.1, we can derive a non-linear equation for the determination of A^*. This equation can be solved by means of Newton's method with the initial guess $A^* = A_{out}$. Once A^* has been obtained, Q^* is computed by (2.91). Then, the values A^* and Q^* can be used to determine the upwinded flux.

For the linear model, we have by (2.92) and

$$W_2^{pq}\left(p^*, q^*\right) = W_2^{pq}\left(p_{out}, q_{out}\right)$$

an equation for the determination of p^*. p^* occurs only linearly in this equation. The value for p^* can be determined by some straightforward computations. Having p^* at hand, q^* is obtained by (2.92). The coupling values p_{coup}, q_{coup} for the missing ingoing characteristic $W_{1,out}^{pq}$ are determined by (2.83). Finally, we have the ingoing and outgoing characteristics for each model which enables us to compute the upwinded values at the corresponding outflow boundaries.

The upwinded values for the mass transport Γ_{up} and c_{up} are again determined by standard upwinding methods analogously to (2.75) and (2.76), depending on the sign of the velocity fields v_{AQ} or v_{pq} at the outlets of the considered vessels:

$$\Gamma_{up}(t) = \begin{cases} \Gamma\left|_{\Omega_m}\left(l,t\right)\right., & \text{if } v_{AQ} > 0, \\ c_{outflow}(t) \cdot A_{up}(t), & \text{if } v_{AQ} \leq 0, \end{cases} \tag{2.93}$$

and

$$c_{up}(t) = \begin{cases} c\left|_{\Omega_m}\left(l,t\right)\right., & \text{if } v_{pq} > 0, \\ c_{outflow}(t), & \text{if } v_{pq} \geq 0, \end{cases} \tag{2.94}$$

where the function $c_{outflow}$ denotes a concentration profile which is prescribed externally at the outflow boundaries.

2.3.3 Computing data at an inner boundary (IeB)

Let us consider an inner element $\Omega_e = \left(z_e^l, z_e^r\right)$, having the neighbors $\Omega_{e-1} = \left(z_{e-1}^l, z_{e-1}^u\right)$ and $\Omega_{e+1} = \left(z_{e+1}^l, z_{e+1}^u\right)$. To improve readability, we restrict ourselves to the interface $z = z_e^r = z_{e+1}^l$ between element Ω_e and Ω_{e+1}, the other interface $z = z_e^l = z_{e-1}^u$ can be treated in the same manner. Given a piecewise continuous function f, we denote by f_l and f_r its left and right limiting values at $z = z_e^r = z_{e+1}^l$:

$$f_l = f\left|_{\Omega_e}\left(z_e^r\right)\right., \quad f_r = f\left|_{\Omega_{e+1}}\left(z_{e+1}^l\right)\right.$$

As already discussed in Theorem 2.1 and 2.3, we have at $z = z_e^r = z_{e+1}^l$ the following characteristic information:

$$W_{1,in}^{AQ} = -\frac{Q_r}{A_r} + 4\sqrt{\frac{G_0}{2\rho}}\left(\frac{A_r}{A_0}\right)^{\frac{1}{4}}, \quad W_{2,out}^{AQ} = \frac{Q_l}{A_l} + 4\sqrt{\frac{G_0}{2\rho}}\left(\frac{A_l}{A_0}\right)^{\frac{1}{4}}, \tag{2.95}$$

for the non-linear model and

$$W_{1,in}^{pq} = \frac{1}{2}\left(-\sqrt{\frac{C_{1D}}{L_{1D}}}p_r + q_r\right), \quad W_{2,out}^{pq} = \frac{1}{2}\left(\sqrt{\frac{C_{1D}}{L_{1D}}}p_l + q_l\right). \tag{2.96}$$

for the linear model. By (2.95) and (2.96), we have for the computation of the upwinded values (A_{up}, Q_{up}) or (p_{up}, q_{up}) two systems of equations:

$$W_{1,in}^{AQ} = -\frac{Q_{up}}{A_{up}} + 4\sqrt{\frac{G_0}{2\rho}}\left(\frac{A_{up}}{A_0}\right)^{\frac{1}{4}}, \quad W_{2,out}^{AQ} = \frac{Q_{up}}{A_{up}} + 4\sqrt{\frac{G_0}{2\rho}}\left(\frac{A_{up}}{A_0}\right)^{\frac{1}{4}}, \tag{2.97}$$

$$W_{1,in}^{pq} = \frac{1}{2}\left(-\sqrt{\frac{C_{1D}}{L_{1D}}}p_{up} + q_{up}\right), \quad W_{2,out}^{pq} = \frac{1}{2}\left(\sqrt{\frac{C_{1D}}{L_{1D}}}p_{up} + q_{up}\right). \tag{2.98}$$

The choice of Γ_{up} or c_{up} depends again on the sign of the flow rate Q_{up} or q_{up}, respectively:

$$\Gamma_{up} = \begin{cases} \Gamma_r, & \text{if } Q_{up} < 0, \\ \Gamma_l, & \text{if } Q_{up} \geq 0, \end{cases} \quad \text{or} \quad c_{up} = \begin{cases} c_r, & \text{if } Q_{up} < 0, \\ c_l, & \text{if } Q_{up} \geq 0. \end{cases}$$

2.3.4 Computing data at a bifurcation boundary (BiB)

The domain decomposition approach which has been described at the beginning of this chapter (see Figure 2.1) allows us to cast the global problem into a set of three decoupled subsystems at a branching point. To interconnect the different subsystems, we require suitable interface conditions guaranteeing a physically meaningful solution. Here, the interface conditions are given by a system of algebraic equations yielding boundary conditions for a 0D lumped parameter model or upwinded values for the reduced 1D models. Due to the fact that different types of models (non-linear 1D model (NL), linear 1D model (L), 0D lumped parameter model (0D)) can be adjacent to a bifurcation several kinds of equation systems have to be established. To be able to distinguish between the different cases, every type of equation system receives a triple containing the types of the models.

Let us assume that we have at each bifurcation two vessel inlets and one vessel outlet.The vessel corresponding to the outlet is denoted as the main vessel (Ω_{mv}), while the remaining vessels are denoted as branch right (Ω_{br}) and branch left (Ω_{bl}) (see Figure 2.27, left). The three subsystems are coupled at the bifurcation point $z^* = z_{mv}(l_{mv}) = z_{br}(0) = z_{bl}(0)$. Based on these definitions, we assign to each bifurcation the following triple:

$$(\text{ type of } \Omega_{mv}, \text{ type of } \Omega_{br}, \text{ type of } \Omega_{bl}), e.g., (\text{NL}, \text{NL}, \text{L}).$$

In the following, we discuss the different types of bifurcations, where we assume that at least one vessel adjacent to a bifurcation is governed by a 1D model, i.e., NL or L. The coupling equations for the flow variables of the uniform 1D cases, i.e., $(\text{NL}, \text{NL}, \text{NL})$ and $(\text{L}, \text{L}, \text{L})$ have already been discussed in [103, 24]. In this thesis we extended them by some coupling equations for the concentration variables. Furthermore we show how different different types of models can be coupled at a bifurcation. For further reading we refer to [65, 63].

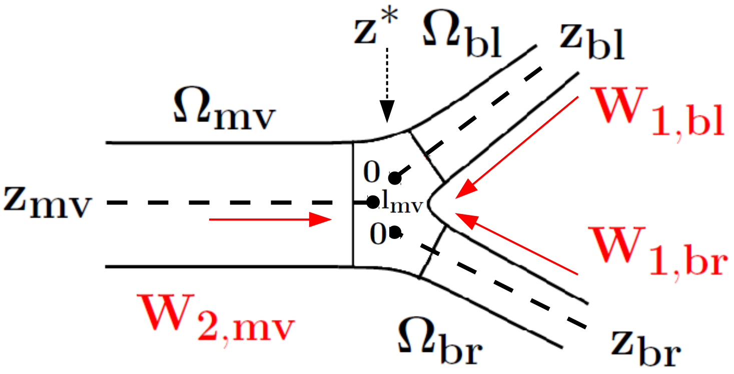

Figure 2.27: Bifurcation with outgoing characteristic variables.

Coupling of 1D models (NL/L) at a bifurcation

(i) Non-linear case: (NL,NL,NL)

At first the coupling of three non-linear systems is considered (see also [65, Section 5.2]). To realize the coupling, we have to determine nine unknowns for the upwinded fluxes:

$$U_{up}^{mv} = \left(A_{up}^{mv}, Q_{up}^{mv}, \Gamma_{up}^{mv}\right)^T, \; U_{up}^{br} = \left(A_{up}^{br}, Q_{up}^{br}, \Gamma_{up}^{br}\right)^T, \; U_{up}^{bl} = \left(A_{up}^{bl}, Q_{up}^{bl}, \Gamma_{up}^{bl}\right)^T$$

at the outlet or inlet of Ω_i, $i \in \{mv, br, bl\}$. This requires to establish an equation system consisting of nine equations. The first three equations can be obtained by computing the corresponding outgoing characteristic variables. Depending on the given parameterization, we have three outgoing characteristics W_{out}^{mv}, W_{out}^{br} and W_{out}^{bl} at each bifurcation which can be computed by the corresponding numerical approximations and Theorem 2.1. According to Figure 2.27, we have:

$$W_{out}^{mv} = \frac{Q_{up}^{mv}}{A_{up}^{mv}} + 4\sqrt{\frac{G_0^{mv}}{2\rho}} \left(\frac{A_{up}^{mv}}{A_0^{mv}}\right)^{\frac{1}{4}}, \tag{2.99a}$$

$$W_{out}^{br} = -\frac{Q_{up}^{br}}{A_{up}^{br}} + 4\sqrt{\frac{G_0^{br}}{2\rho}} \left(\frac{A_{up}^{br}}{A_0^{br}}\right)^{\frac{1}{4}}, \tag{2.99b}$$

$$W_{out}^{bl} = -\frac{Q_{up}^{bl}}{A_{up}^{bl}} + 4\sqrt{\frac{G_0^{bl}}{2\rho}} \left(\frac{A_{up}^{bl}}{A_0^{bl}}\right)^{\frac{1}{4}}. \tag{2.99c}$$

A_0^i is the section area for the respective vessel. G_0^i is the elasticity coefficient for vessel Ω_i, $i \in \{mv, br, bl\}$.

Remark 2.5. *Within a larger network, the orientation of the coordinate axes may differ from those depicted in Figure 2.27, i.e., the bifurcation point* z^* *might also be given by* $z^* = z_{mv}(0) = z_{br}(l_{br}) = z_{bl}(l_{bl})$. *In this case the equations for the outgoing characteristics* W_{out}^{mv},

W^{br}_{out} and W^{bl}_{out} differ from those in (2.99a)-(2.99c) *and must be reestablished, depending on the direction of motion of the corresponding characteristics.*

To close the system for the A and Q variables, we need three additional equations. One of them is obtained from the continuity of the mass flux:

$$Q^{mv}_{up} = Q^{br}_{up} + Q^{bl}_{up}. \tag{2.100}$$

The two missing equations can be derived from the continuity of the total pressure, where the total pressure is defined as follows:

$$p_{t,i} = \frac{\rho}{2}\left(\frac{Q^i_{up}}{A^i_{up}}\right)^2 + G^i_0\left(\sqrt{\frac{A^i_{up}}{A^i_0}} - 1\right),\ i \in \{mv, br, bl\},$$

$$\begin{aligned} p_{t,mv} &= p_{t,br}, && (2.101)\\ p_{t,mv} &= p_{t,bl}. && (2.102)\end{aligned}$$

The equations given by (2.99a) - (2.102) define a non-linear system of algebraic equations which allows us to determine the values A^i_{up} and Q^i_{up}, $i \in \{mv, br, bl\}$. It remains, to establish the equations for the averaged concentration Γ. Here we have to face the problem that the evolution of Γ depends on the velocity field $v^i_{up} = \frac{Q^i_{up}}{A^i_{up}}$. Based on the sign of v^i_{up}, we have to decide whether we are able to compute the corresponding concentration value by evaluating the solution at the boundary or not. Γ^{mv}_{up} can only be computed by upwinding, if $Q^{mv}_{up} \geq 0$ holds. Γ^{br}_{up} and Γ^{bl}_{up} can only be computed by upwinding, if $Q^{br}_{up} \leq 0$ and $Q^{bl}_{up} \leq 0$ hold, respectively.

Taking these relations into account and observing (2.117), we note that only in the trivial case $Q^{mv}_{up} = Q^{br}_{up} = Q^{bl}_{up} = 0$, all three values Γ^{mv}_{up}, Γ^{br}_{up} and Γ^{bl}_{up} can be directly computed. In all other cases, at most two values but at least one value of Γ^{mv}_{up}, Γ^{br}_{up} and Γ^{bl}_{up} can be obtained, and at least one additional condition is required to close the system. In the following, we consider the two cases separately.

One value of Γ^{mv}_{up}, Γ^{br}_{up} and Γ^{bl}_{up} can be computed by upwinding

Let Γ^{mt}_{up} be the value that can be computed by upwinding, in order to determine the remaining values Γ^{b1}_{up} and Γ^{b2}_{up}, $b1, b2 \in \{mv, br, bl\} \setminus \{mt\}$, we have to establish two further equations. Let us denote by N_{mt} the number of particles that are transported through the main vessel into the bifurcation. By N_{b1} and N_{b2}, we denote the number of particles entering the branches. In order to close the system, we consider the conservation of the number of particles:

$$N_{mt} = N_{b1} + N_{b2}. \tag{2.103}$$

We assume that during a small time period δt a fluid volume $Vol_{mt} = \delta t\left|Q^{mt}_{up}\right|$ enters the bifurcation and that $Vol_{b1} = \delta t\left|Q^{b1}_{up}\right|$ and $Vol_{b2} = \delta t\left|Q^{b2}_{up}\right|$ are leaving the bifurcation. The number of particles N_i, $i \in \{mt, b1, b2\}$ can be expressed by the product of the concentration $C_i = \frac{\Gamma^i_{up}}{A^i_{up}}$ and the volume Vol_i:

$$N_i = C_i \cdot V_i = C_i \cdot \left|Q^i_{up}\right| \delta t.$$

By (2.103) we have:

$$C_{mt} \left|Q^{mt}_{up}\right| = C_{b1} \left|Q^{b1}_{up}\right| + C_{b2} \left|Q^{b2}_{up}\right|.$$

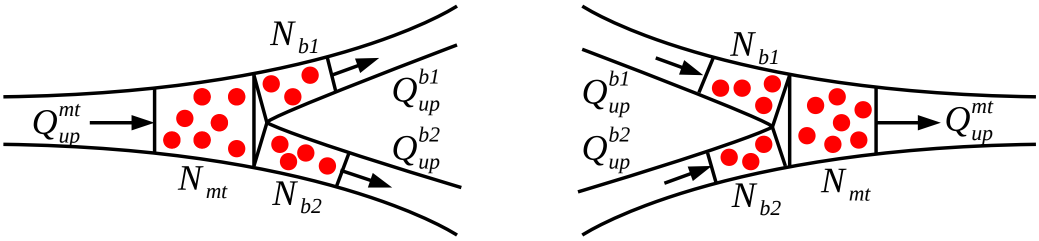

Figure 2.28: Mass transport through the main vessel into two branches (left), mass transport through the branches into the main vessel.

Enforcing the continuity of the concentration, i.e.,

$$\begin{aligned} C_{mt} &= C_{b1}, && (2.104) \\ C_{mt} &= C_{b2}, && (2.105) \end{aligned}$$

we recover the mass conservation $\left|Q^{mt}_{up}\right| = \left|Q^{b1}_{up}\right| + \left|Q^{b2}_{up}\right|$. By Γ^{mt}_{up}, (2.104) and (2.105), we have a closed system in order to compute all the unknowns at a bifurcation. Figure 2.28 shows the mass transport at the interface for the different situations.

Two values of Γ^{mv}_{up}, Γ^{br}_{up} and Γ^{bl}_{up} can be computed by upwinding

Let Γ^{b1}_{up} and Γ^{b2}_{up} be the values that can be computed by upwinding, ($b1, b2 \in \{mv, br, bl\}$), consequently we need only one additional equation in order to determine the missing value Γ^{mt}_{up}, $mt \in \{mv, br, bl\} \setminus \{b1, b2\}$. Let us consider again the conservation of particles:

$$N_{mt} = N_{b1} + N_{b2}.$$

As in the previous case, we can replace N_i, $i \in \{mt, b1, b2\}$ by $C_i \left|Q^i_{up}\right| \delta t$:

$$C_{mt} \left|Q^{mt}_{up}\right| = C_{b1} \left|Q^{b1}_{up}\right| + C_{b2} \left|Q^{b2}_{up}\right|.$$

Using $C_i = \frac{\Gamma^i_{up}}{A^i_{up}}$ we have:

$$\frac{\Gamma^{mt}_{up}\left|Q^{mt}_{up}\right|}{A^{mt}_{up}} = \frac{\Gamma^{b1}_{up}\left|Q^{b1}_{up}\right|}{A^{b1}_{up}} + \frac{\Gamma^{b2}_{up}\left|Q^{b2}_{up}\right|}{A^{b2}_{up}}. \tag{2.106}$$

Thus, Γ^{b1}_{up}, Γ^{b2}_{up} and (2.106) close the system and we are able to compute all unknowns at a bifurcation.

(ii) Linear case: (L,L,L)

The pure linear case exhibits a similar structure as the pure non-linear case. The first three equations for the computation of the upwinded values

$$U_{up}^{mv} = \left(p_{up}^{mv}, q_{up}^{mv}, c_{up}^{mv}\right)^T, \ U_{up}^{br} = \left(p_{up}^{br}, q_{up}^{br}, c_{up}^{br}\right)^T, \ U_{up}^{bl} = \left(p_{up}^{bl}, q_{up}^{bl}, c_{up}^{bl}\right)^T$$

are provided by the outgoing characteristics W_{out}^{mv}, W_{out}^{br} and W_{out}^{bl} (see Figure 2.27):

$$W_{out}^{mv} = \frac{1}{2}\left(\sqrt{\frac{C_{1D}^{mv}}{L_{1D}^{mv}}}p_{mv} + q_{mv}\right), \tag{2.107a}$$

$$W_{out}^{br} = \frac{1}{2}\left(-\sqrt{\frac{C_{1D}^{br}}{L_{1D}^{br}}}p_{br} + q_{br}\right), \tag{2.107b}$$

$$W_{out}^{bl} = \frac{1}{2}\left(-\sqrt{\frac{C_{1D}^{bl}}{L_{1D}^{bl}}}p_{bl} + q_{bl}\right). \tag{2.107c}$$

C_{1D}^i and L_{1D}^i, $i \in \{mv, br, bl\}$ denote the compliance and the inductance of the corresponding vessel. The values for W_{out}^{mv}, W_{out}^{br} and W_{out}^{bl} can be determined by Theorem 2.3 and the numerical data at the inlets or the outlets of the vessels. Two further equations can be derived from the continuity of the pressure:

$$p_{mv} = p_{br}, \tag{2.108}$$

$$p_{mv} = p_{bl}. \tag{2.109}$$

The missing equation for the p and q values is given by the mass conservation:

$$q_{up}^{mv} = q_{up}^{br} + q_{up}^{bl}. \tag{2.110}$$

For the determination of the concentration values, we consider a similar case study as in the non-linear case. Due to (2.110) at most two values but at least one value of c_{up}^{mv}, c_{up}^{br} and c_{up}^{bl} can be obtained by evaluating the numerical solution at the boundaries adjacent to the bifurcation. Again at least one additional condition is required to close the system.

One value of c_{up}^{mv}, c_{up}^{br} and c_{up}^{bl} can be computed by upwinding

Let c_{up}^{mt} be the value that is computed by upwinding. In order to guarantee the conservation of the number of particles (see Equation (2.103)) transported through the bifurcation, we postulate the continuity of the concentration:

$$c_{up}^{mt} = c_{up}^{b1}, \tag{2.111}$$

$$c_{up}^{mt} = c_{up}^{b2}, \tag{2.112}$$

where $b1, b2 \in \{mv, br, bl\} \setminus \{mt\}$. All in all the upwinded value c_{up}^{mt}, (2.111) and (2.112) close the system in this case.

Two values of c_{up}^{mv}, c_{up}^{br} and c_{up}^{bl} can be computed by upwinding

Let us assume that c_{up}^{b1} and c_{up}^{b2} are the values which are provided by the numerical scheme at the boundaries of two vessels. Here, the conservation of particles (see Equation (2.103)) is enforced by the following balance equation:

$$c_{up}^{mt}\left|q_{up}^{mt}\right| = c_{up}^{b1}\left|q_{up}^{b1}\right| + c_{up}^{b2}\left|q_{up}^{b2}\right|, \tag{2.113}$$

which closes the system in this case.

(iii) Mixed cases, e.g., (NL,NL,L)

First of all, we note that the numbering of Ω_{bl} and Ω_{br} is arbitrary. Thus, triples like, (NL,NL,L) and (NL,L,NL) stand for the same physical situation. To enable a better readability, we discuss here only the case (NL,NL,L). The remaining cases can be derived by some small modifications. Here, we have to determine at the artery interfaces the following nine upwinded coupling values:

$$U_{up}^{mv} = \left(A_{up}^{mv}, Q_{up}^{mv}, \Gamma_{up}^{mv}\right)^T,\; U_{up}^{br} = \left(A_{up}^{br}, Q_{up}^{br}, \Gamma_{up}^{br}\right)^T,\; U_{up}^{bl} = \left(p_{up}^{bl}, q_{up}^{bl}, c_{up}^{bl}\right)^T.$$

The first three equations are given by the following outgoing characteristic variables arising from non-linear and linear models:

$$W_{out}^{mv} = \frac{Q_{up}^{mv}}{A_{up}^{mv}} + 4\sqrt{\frac{G_0^{mv}}{2\rho}}\left(\frac{A_{up}^{mv}}{A_0^{mv}}\right)^{\frac{1}{4}}, \tag{2.114a}$$

$$W_{out}^{br} = -\frac{Q_{up}^{br}}{A_{up}^{br}} + 4\sqrt{\frac{G_0^{br}}{2\rho}}\left(\frac{A_{up}^{br}}{A_0^{br}}\right)^{\frac{1}{4}}, \tag{2.114b}$$

$$W_{out}^{bl} = \frac{1}{2}\left(-\sqrt{\frac{C_{1D}^{bl}}{L_{1D}^{bl}}}p_{bl} + q_{bl}\right). \tag{2.114c}$$

The values for W_{out}^{mv}, W_{out}^{br} and W_{out}^{bl} can again be determined by Theorem 2.1, Theorem 2.3 and the numerical data at the inlets or the outlets of the vessels. The continuity of the pressure yields in this case:

$$G_0^{mv}\left(\sqrt{\frac{A_{up}^{mv}}{A_0^{mv}}} - 1\right) = G_0^{br}\left(\sqrt{\frac{A_{up}^{br}}{A_0^{br}}} - 1\right), \tag{2.115}$$

$$G_0^{mv}\left(\sqrt{\frac{A_{up}^{mv}}{A_0^{mv}}} - 1\right) = p_{up}^{bl}. \tag{2.116}$$

The mass conservation is given by:

$$Q_{up}^{mv} = Q_{up}^{br} + q_{up}^{bl}. \tag{2.117}$$

For the computation of the concentration values, we have to consider two cases as in the previous subsections.

One concentration value can be computed by upwinding

If fluid volume enters the bifurcation through one vessel and leaves the bifurcation through two vessels, we require the continuity of the volumetric concentration:

$$c_{up}^{mv} = c_{up}^{br} = c_{up}^{bl}, \text{where} \quad c_{up}^{l} = \frac{\Gamma_{up}^{l}}{A_{up}^{l}},\ l \in \{mv, br\}\,. \tag{2.118}$$

The missing unknowns Γ_{up}^{mv}, Γ_{up}^{br} or c_{up}^{bl} at the inlet or the outlet of the vessel through which fluid volume enters the bifurcation is computed by evaluating the numerical approximations.

Two concentration values can be computed by upwinding

If fluid volume enters the bifurcation through two vessels and leaves the bifurcation through one vessel, two of the unknowns Γ_{up}^{mv}, Γ_{up}^{br}, c_{up}^{bl} are determined by the numerical approximations at the inlets or the outlets of the vessels, through which fluid volume enters the bifurcation. In this case the system is closed by the following balance equation:

$$c_{up}^{b1}\left|f_{up}^{b1}\right| + c_{up}^{b2}\left|f_{up}^{b2}\right| = c_{up}^{mt}\left|f_{up}^{mt}\right|,\ f \in \{q, Q\}\,, \tag{2.119}$$

where $b1,\ b2 \in \{mv, br, bl\}$ indicate the inflow branches and $mt \in \{mv, br, bl\} \setminus \{b1, b2\}$ indicates the outflow vessel.

The systems for the other cases, e.g., (NL,L,L) exhibit the same structure and can be easily adapted, by modifying the formulas for the outgoing characteristics and exchanging some variables.

Coupling of linear 1D models (L) and 0D models (0D) at a bifurcation

As it was already discussed in Subsection 2.1.3, it can be meaningful to model flow and mass transport through small vessels by lumped 0D models. However by now, we have only considered bifurcations linking non-linear or linear 1D models, therefore we still require coupling equations for 1D models and 0D models at bifurcations. In this context, it is assumed that at least one model at a bifurcation is given by a 1D model and that a 0D model is only connected to a linear 1D model. For a better readability, we examine here only the case (L,0D,0D). Establishing the equation system for this case, one notices that the structure of this equation system is slightly different from those arising from the pure 1D cases. Since no characteristic variables can be determined for the 0D models, we can not provide outgoing characteristic variables at the inlets or the outlets of the corresponding vessels. According to (2.29) there are two possibilities to approximate the average values $\hat{p}$ and $\hat{q}$ in (2.27a) and (2.27b):

$$(i)\ \hat{p}(t) \approx p_{out}(t) \text{ and } \hat{q}(t) \approx q_{in}(t),$$

$$(ii)\ \hat{p}(t) \approx p_{in}(t) \text{ and } \hat{q}(t) \approx q_{out}(t).$$

In the following, we use the first possibility (i). As a consequence of this choice and (2.27a),(2.27b), it remains to determine the values p_{in} or q_{out} to couple the models which are linked at the bifurcation. Let us assume that the outlet of the main vessel and the inlets of the branches (see Figure 2.27) are adjacent to the bifurcation. Based on this assumption, we have to compute the following pressure and flow values as boundary values for the 0D models or upwinded values for the 1D model:

$$p_{up}^{mv},\ p_{in}^{br},\ p_{in}^{bl} \text{ and } q_{up}^{mv}.$$

One equation for these unknowns is given by the outgoing characteristic W_{out}^{mv}:

$$W_{out}^{mv} = \frac{1}{2}\left(\sqrt{\frac{C_{1D}^{mv}}{L_{1D}^{mv}}}p_{up}^{mv} + q_{up}^{mv}\right), \tag{2.120}$$

whose value can be again be determined by the numerical data at hand. Two further equations are obtained by the pressure continuity:

$$p_{up}^{mv} = p_{in}^{br}, \tag{2.121}$$
$$p_{up}^{mv} = p_{in}^{bl}. \tag{2.122}$$

The system for pressure and flow rate is closed by mass conservation:

$$q_{up}^{mv} = q_{in}^{br} + q_{in}^{bl}, \tag{2.123}$$

where the values q_{in}^{br} and q_{in}^{bl} are provided by the 0D models associated to the branches Ω_{br} and Ω_{bl}.

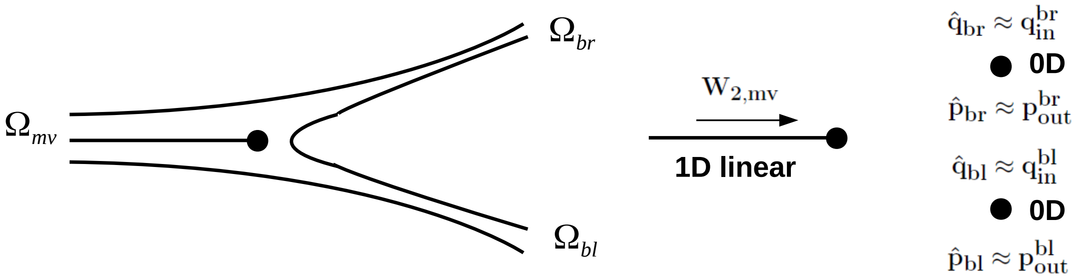

Figure 2.29: Left: Bifurcation consisting of two small branches Ω_{br} and Ω_{bl}. Right: Modeling the bifurcation by a linear 1D model and two 0D models. The average values $\hat{q}_i$ and $\hat{p}_i$ are approximated by q_{in}^i and p_{out}^i, $i \in \{br, bl\}$. At the inlets of the branches, the outgoing characteristics are replaced by q_{in}^i, $i \in \{br, bl\}$, while at the outlet of the main vessel the outgoing characteristic is still given by $W_{2,mv}$.

The computation of the concentration values is carried out as in the previous subsection. If only one concentration value can be determined either by evaluation of the 1D solution or directly by the lumped parameter model, we close the system by the continuity of the concentration (see (2.118)). If two concentration values can be determined either by interpolation or directly, the system is closed by a balance equation such as (2.119).

The remaining cases, which might be of interest for a network, i.e., (L,L,0D), (0D,L,L) and (L,0D,L) can be treated similarly, by adapting the formulas for the outgoing characteristic variables and the coupling values.

2.4 Simulation of arterial networks

In the final section of this chapter, we want to test the performance of the numerical model for network flow and mass transport developed in the previous sections. For this purpose blood flow and oxygen transport through two different arterial vessel trees are considered. The first network consists of 13 large and middle sized arteries including the aorta and the vessels branching out of it. The second network is an extension of the first network (see Figure 2.30). Besides the aorta and its branches, it incorporates also the cerebral arteries **(Circle of Willis, CoW)**. In the following, these networks are used to investigate two different issues. The smaller network serves as a test network for the conservation properties of the numerical model, by the help of the second one we simulate the influence of a unilateral stenosis. Considering the structure of both vessel systems, we observe that there is only one inflow boundary which is adjacent to the heart. Therefore at this boundary, we require conditions simulating the influence of the heart beats as accurate as possible.

Modeling the heart beats

According to medical literature, e.g., [97] the heart pumps 5 l to 6 l per minute into the arterial vessel system. In order to simulate pulsatile blood flow within an arterial vessel system, we prescribe the following flow rate profile at the inlet of the aorta (inflow boundary):

$$Q(t) = \begin{cases} 485 \cdot \sin\left(\frac{\pi}{T}t\right)\ \frac{cm^3}{s} & \text{for } 0.0s \leq t \leq T, \\ 0\ \frac{cm^3}{s} & \text{for } T < t \leq 1.0s. \end{cases} \tag{2.124}$$

For $t > 1$ it holds: $Q(t) = Q(t+1)$. In medical research, the time period $[0.0, T]$ is referred to as **systole**, while the time period $(T, 1.0]$ is known as **diastole**. For our simulations, we choose $T = 0.3s$. Integrating the function in (2.124) over one minute yields:

$$\int_{0s}^{60s} Q(t)\ dt = 5.5577 \cdot 10^3\ cm^3 = 5.5577\ l,$$

which means that the profile in (2.124) fulfills the requirements in literature. As a boundary condition for the volumetric concentration, we prescribe the mean value of the volumetric oxygen concentration in blood [24][Chapter 2]:

$$C_{O_2} = 8.75\ \frac{\mu mol}{cm^3}.$$

Parameter values

Table 2.5 summarizes the values for blood density ρ, blood viscosity η and some parameters, we use within the following two simulations. Since biological tissue is nearly incompressible, we choose the Poisson's ratio: $\nu = 0.5$ for the elasticity parameters G_0 (2.8) and C_{1D} (2.21). The parameters ϕ_M and ϕ_p (see e.g. in (2.9a) and (2.9c)) are taken to be zero, i.e., we assume that the vessel walls are impermeable. Finally, we initially assume that $A_i(z,0) = A_{0,i},\ Q_i(z,0) = 0,\ \Gamma_i(z,0) = 0$ and $p_i(z,0) = 0,\ q_i(z,0) = 0,\ c_i(z,0) = 0$ holds in the corresponding vessels.

Table 2.5: List of the fluid parameters and Poisson ratio.

Physical Parameter	symbol	value	unit
blood density	ρ	1.028	g/cm^3
blood viscosity	η	4.500	$mPa\ s$
Poisson ratio	ν	0.500	$---$
permeability (blood)	ϕ_M	0.0	$\frac{cm^2}{s}$
permeability (oxygen)	ϕ_p	0.0	$\frac{cm^2}{s}$

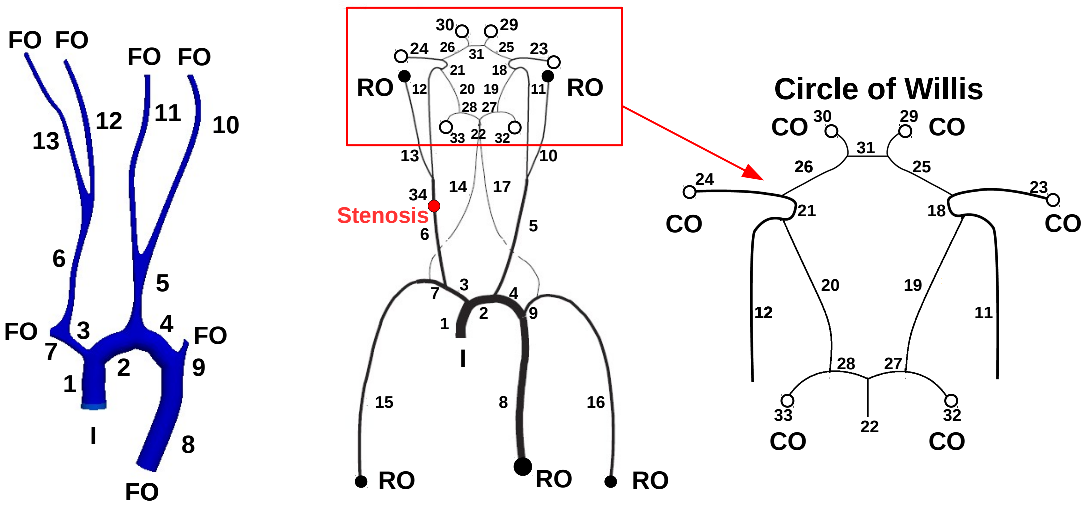

Figure 2.30: Outlines of the networks used within this section. The test network (left) consists of the 13 main arteries. The second network (right) incorporates besides these vessels also the cerebral arteries. By (I) we denote an inflow boundary, (FO) abbreviates the term free outflow boundary, (RO) denotes an outflow boundary linked to a RCR model with fixed resistances (see Subsection 2.3.2) and (CO) marks cerebral outflow boundaries.

2.4.1 Conservation properties of the numerical model

For this first scenario, we assign to each vessel of the first network (Figure 2.30, left) the non-linear transport model given by (2.9a)-(2.9c). At the bifurcations the adjacent models are coupled by the algebraic equation system established in Subsection 2.3.4 (non-linear case). Considering again Figure 2.30, one notes that the network exhibits 7 outflow boundaries, which are treated as free outflow boundaries (see Subsection 2.3.2). The values of the different vessel lengths, radii, wall thicknesses and elasticity parameters are provided in Table 2.8.

In order to be able to examine the conservation properties of the numerical model, we report at the inflow boundary **(I)** and at the outflow boundaries **(FO)** the flow rate $Q\ \left[cm^3/s\right]$, the section area $A\ \left[cm^2\right]$ and the averaged concentration $\Gamma\ \left[mmol/cm\right]$. In this context, the index set of the vessels adjacent to an outflow boundary *indOut* is given by:

$$indOut = \{7,\ 8,\ 9,\ 10,\ 11,\ 12,\ 13\}\,.$$

Having the data of A, Q and Γ at hand, we compute at the outflow boundaries and the inflow boundary the amount of fluid mass within the time interval $[0s, 20s]$

$$V_{out} = \sum_{i \in indOut} \int_{0s}^{20s} Q_i\left(l_i, t\right)\, dt, \qquad V_{in} = \int_{0s}^{20s} Q_1\left(0, t\right)\, dt.$$

and the number of oxygen molecules which are leaving and entering the network within the time interval $[t^*, 20s]$:

$$N_{out} = \sum_i \int_{t^*}^{20s} \frac{\Gamma_i\left(l_i, t\right) Q_i\left(l_i, t\right)}{A_i\left(l_i, t\right)}\, dt, \qquad N_{in} = \int_{t^*}^{20s} \frac{\Gamma_1\left(0, t\right) Q_1\left(0, t\right)}{A_1\left(0, t\right)}\, dt,$$

where we denote by t^* a time point at which the whole network is uniformly covered by the volumetric concentration of oxygen in blood. According to Figure 2.32 the whole network is covered by the same concentration value from no earlier than $t^* = 10s$. The corresponding conservation errors are given by:

$$e_V = \frac{|V_{out} - V_{in}|}{|V_{in}|} \quad \text{and} \quad e_N = \frac{|N_{out} - N_{in}|}{|N_{in}|}.$$

Starting from a mesh size and time step $(\Delta z_0, \Delta t_0) = \left(1.0\, cm, 10^{-4}\, s\right)$, we report the relative errors e_V and e_N for each refinement step $\left(2^{-i}\Delta z_0, 2^{-i}\Delta t_0\right)$, $i \in \{0, 1, 2, 3\}$. For the space discretization Legendre elements of polynomial order $p = 3$ were used. The concentration component Γ was stabilized by means of a hierarchical limiter technique (see Algorithm 1). The errors e_V and e_N for $p = 3$ are provided in Table 2.6:

Table 2.6: Relative conservation errors for different mesh sizes and $p = 3$.

i :	0	1	2	3
e_V	$5.45 \cdot 10^{-4}$	$1.43 \cdot 10^{-4}$	$6.05 \cdot 10^{-5}$	$9.06 \cdot 10^{-6}$
e_N	$5.37 \cdot 10^{-4}$	$1.28 \cdot 10^{-4}$	$4.63 \cdot 10^{-5}$	$5.19 \cdot 10^{-6}$

Based on these results, we can assume that our numerical model is consistent and prevents an excessive loss of fluid mass and oxygen. However, one should note that this first setting produces no realistic data and can only be used for test purposes, e.g., conservation tests. Due to the fact that we treat each outflow boundary as a free outflow boundary, we neglect the influence of the omitted vessel system. Comparing the pressure curve in the middle of the aorta with measured data, huge differences with respect to the shape of the curve and the numerical values can be observed.

According to the literature [97, 105], the systolic pressure ranges from 100 $mmHg$ to 130 $mmHg$, while the diastolic pressure ranges from 60 $mmHg$ to 85 $mmHg$. The pressure curve produced by this setting falls back to 0 $mmHg$ during the diastole and has its peak at 46 $mmHg$. The slow decay of the pressure curve during the diastole (see, e.g. [105][Kap. 8]) is caused by the resistive and conductive properties of the smaller vessels beyond the outflow boundaries. The issue of incorporating these effects into the numerical model is discussed in the next subsection.

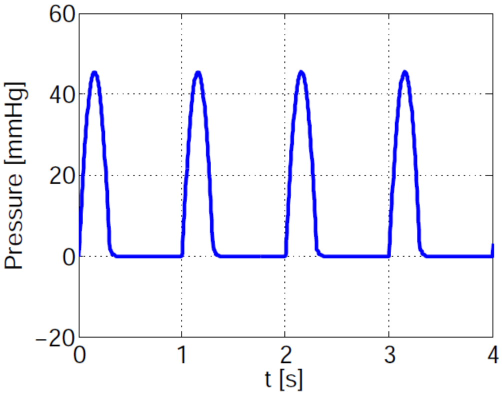

Figure 2.31: Pressure reported at the middle of the aorta (Vessel 1) for $t \in [0s, 4s]$.

Table 2.7: Physiological data used within the first scenario [3, 33, 84, 85].

Arterial segment	Length l $[cm]$	Radius r $[cm]$	Thick. h $[cm]$	E. mod. E $[10^6\ Pa]$
1. Ascending aorta	4.0	1.200	0.163	0.4
2. Aortic arch I	2.0	1.120	0.126	0.4
3. Brachiocephalic	3.4	0.620	0.080	0.4
4. Aortic arch II	3.9	1.070	0.115	0.4
5. L. com. carotid	20.8	0.250	0.063	0.4
6. R. com. carotid	17.7	0.250	0.063	0.4
7. R. subclavian	3.4	0.423	0.067	0.4
8. Thoracic aorta	15.6	0.999	0.110	0.4
9. L. subclavian	3.4	0.423	0.067	0.4
10. L. ext. carotid	17.7	0.150	0.038	0.8
11. L. int. carotid I	17.7	0.200	0.050	0.8
12. R. int. carotid I	17.7	0.200	0.050	0.8
13. R. ext. carotid	17.7	0.150	0.038	0.8

2.4.2 Influence of a unilateral stenosis on brain oxygenation

In this subsection we present some results which were already published in the following paper by the author [63]:

T. Köppl and M. Schneider and U. Pohl and B. Wohlmuth:
The influence of an unilateral carotid artery stenosis on brain oxygenation
Medical Engineering and Physics, 36(7), 905-914, 2014

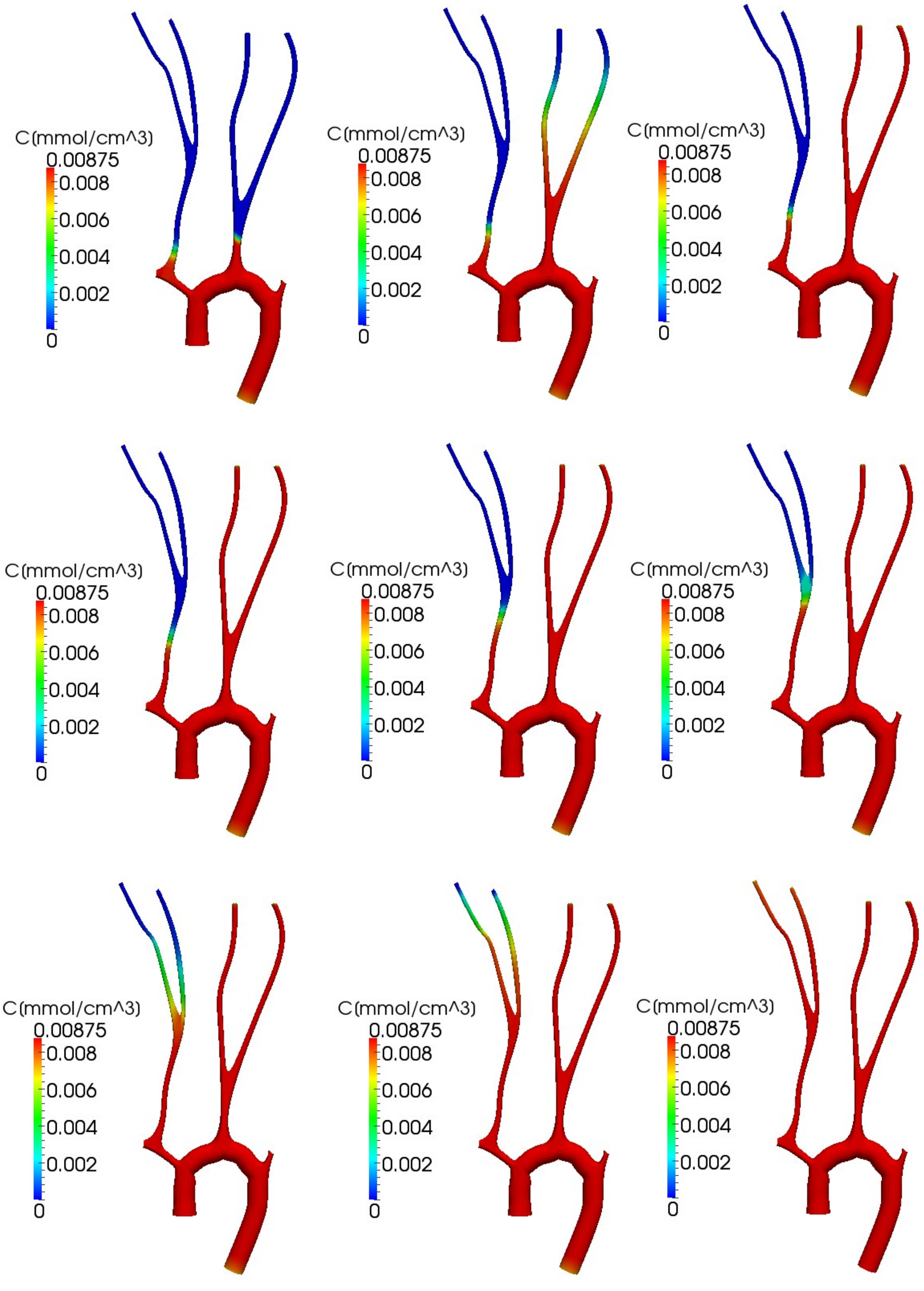

Figure 2.32: Volumetric oxygen concentration $C = \Gamma/A$ in an arterial network after $2s$, $3s$, $4s$, $5s$, $6s$, $7s$, $8s$, $9s$ and $10s$.

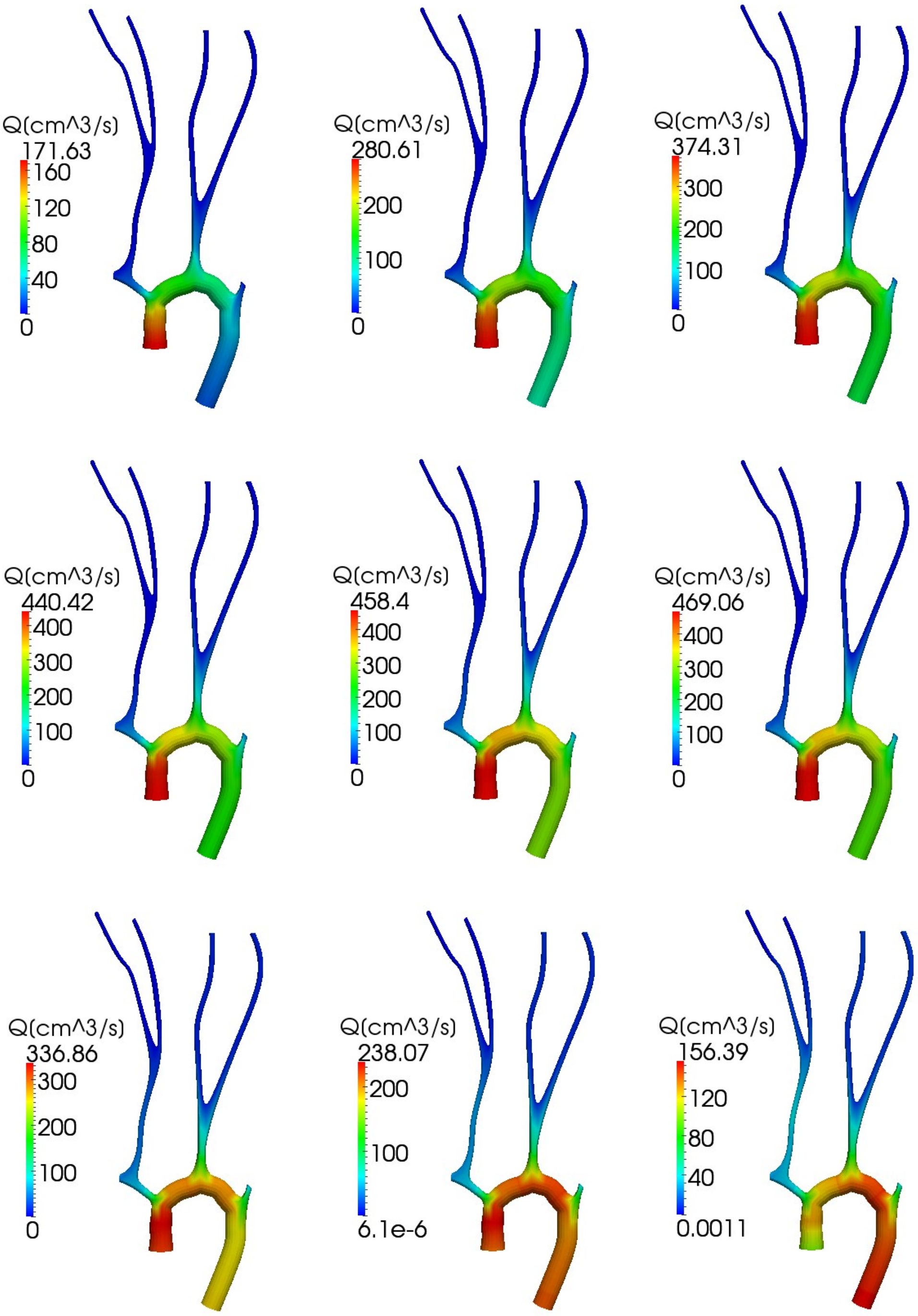

Figure 2.33: Flow rate Q in an arterial network after $0.026s$, $0.052s$, 0.078, $0.104s$, $0.130s$, $0.156s$, $0.182s$, $0.208s$ and $0.260s$.

Despite improvements in primary prevention, the incidence of atherosclerotic vascular lesions and their consequences for organ function and integrity will remain a major medical problem in an aging society [67]. Stenoses in the carotid arteries are relevant causes of brain ischemia [91] when they become occluded either by an increasing stenosis or, more acutely, by the development of a thrombus in the stenotic area. The reduction of blood flow due to a stenosis in one carotid artery can potentially be compensated by blood flow through collateral vessels known as the circle of Willis (CoW) [77] being fed by the contralateral carotid artery (see Figure 2.30, right).

This compensatory collateral blood flow is also important when during a surgical intervention a stenotic segment has to be removed, the vessels have to be transiently occluded [75, 88]. Therefore, it is of considerable medical interest to predict which degree of stenosis can be tolerated before the patient's brain suffers from reduced blood flow and ischemia. Such a prediction may preferably be based on a model using the patient's individual data [51, 115] on the degree of stenosis and assuming an intact CoW. The latter, however, can be incomplete in a significant number of patients due to anatomic variations [77, 115].

Not surprisingly, there exist many approaches to model this situation mathematically in order to predict the amount of blood flow, that, under a given degree of stenosis, can be supplied by the contralateral carotid artery via the CoW. In order to avoid time consuming 3D computations, we use the reduced 1D and 0D lumped parameter models, described in Section 2.1. Based on these reduced and lumped parameter models, different multi-scale models for pulsatile blood flow within arterial networks were developed. To incorporate the impact of a stenosis, in some publications [73, 100, 108, 120] a 0D lumped parameter model replaces the stenosis and couples the reduced models adjacent to a stenosis. Such types of models are also used to account for the resistive and compliant effects of the vessels beyond the outflow boundaries [2, 29, 102, 103, 121]. These models use, except for the outflow boundaries and the stenoses, a monolithic approach, i.e., only one type of model (either 1D non-linear or 1D linear or 0D lumped parameter model) for all vessels belonging to each considered network.

For our multi-scale model [63], we interconnect different types of reduced 1D or 0D lumped parameter models at the bifurcations of the arterial network (see Section 2.3). By this, the different features of large and middle sized vessels and also small vessels can be better accounted for (Table 2.9). In addition to that, the numerical effort can be reduced compared to the model using only non-linear models, because the coupling of the linearized 1D models and the 0D lumped parameter models can be described by linear systems of equations instead of non-linear ones (see Subsection 2.3.4). A similar approach was investigated in [23], where a 3D model is used for the abdominal aorta and a 1D model is used for the remaining vessel system. Furthermore, none of the mentioned models considers the consequences of collateral blood flow for the oxygen supply of brain tissue. Since the brain is an organ with high oxygen consumption and without relevant oxygen storage, a blood supply which maintains a certain tissue oxygen level is essential for a healthy brain function. Therefore, we modify and generalize existing models including metabolic cerebral auto regulation [2], to understand the consequences for mean oxygen tension in brain areas at risk under conditions of varying unilateral stenoses and collateral blood flows.

Network data

For the simulation of blood flow and oxygen transport from the heart to the brain, we consider the arterial vessel system, presented in [2, 3].

It consists of 34 arteries, containing the circle of Willis and the most important arteries, branching out of the heart (see Figure 2.30). Considering the given vessel system, it becomes obvious that this network is composed of arteries having different length scales (see Table 2.8). Therefore, it is beneficial to use different models taking the special features of the vessels into account. The arteries within or near the CoW exhibit elastic properties which differ considerably from those of the aorta (Vessel 1 in Figure 2.30). We apply non-linear transport equation systems [2, 16] [24, Chapter 2] to the larger vessels Ω_i, numbered by $i \in \{1, \ldots, 9, 15, 16, 34\}$ and linear transport equation systems, incorporating the small displacement property, to the vessels Ω_i, numbered by $i \in \{10, \ldots, 14, 17, \ldots, 26, 29, 30, 32, 33\}$ (see Figure 2.30). Due to their small length (below 1 cm) and section area, the blood flow and oxygen transport through the remaining vessels Ω_i numbered by $i \in \{27, 28, 31\}$ are computed by 0D lumped parameter models [3, 4].

Modeling the outflow boundaries and the metabolic cerebral auto regulation

Since we consider only a small part of the full arterial tree, we truncate our 1D network after some bifurcations. To account for the haemodynamic effects of the omitted vessels, we couple the terminal vessels of our 1D network with 0D models, given by a three element $(R_{1,T}, C_T, R_{2,T})$ windkessel model for a terminal vessel Ω_T. Setting the inductance L to zero, the equations governing the three element $(R_{1,T}, C_T, R_{2,T})$ windkessel model are given in Subsection 2.3.2 (Peripheral vessels). Here, we do not use the four element $(R_{1,T}, C_T, L_T, R_{2,T})$ windkessel model, because the data for the inductances L_T have not been available. Furthermore a comparison in [4, Section 3.1] reveals that the three element and the four element windkessel model yield approximatly the same results.

$R_{2,T}$ and C_T denote the resistance and the compliance of the peripheral vessels, following a terminal vessel Ω_T, respectively [2, 3, 4]. The values for the total resistance $R_T = R_{1,T} + R_{2,T}$ and C_T are listed in Table 2.8. For $R_{1,T}$ the authors of [2, 3, 4] suggest to choose the characteristic impedance

$$Z_T = \rho \cdot c_0 \left(A_{0,T}\right) / A_{0,T} \tag{2.125}$$

of the terminal vessel Ω_T in order to avoid non physical reflections. The characteristic wave speed $c_0 \left(A_{0,T}\right)$ is given by (2.17).

At the cerebral outlets (marked by **CO** in Figure 2.30) we apply an auto regulation mechanism which can adjust each resistance at the outlet of a terminal vessel Ω_n to provide enough blood flow for the supply of the brain $n \in \{23, 24, 29, 30, 32, 33\}$. For the remaining outlets (marked by **RO** in Figure 2.30), we keep the resistances $R_{2,T}$ fixed. A suitable modification of the cerebral resistances caused by the distal vessels can be achieved by changing the corresponding resistances $R_{2,n}$ of the $(R_{1,n}, C_n, R_{2,n})$ −model.

The authors of [2] suggest a cerebral auto regulation model based on the concentration of CO_2 in the brain tissue C_tCO_2. The cerebral resistance $R_{2,n}$ is increased, if C_tCO_2 is

Table 2.8: Physiological data used within the second scenario [3, 33, 84, 85]. The units of the elasticity parameters, peripheral resistances and the peripheral compliances are given by $\left[10^6\ Pa\right]$, $\left[10^9\ Pa\ s\ m^{-3}\right]$ and $\left[10^{-10} m^3 Pa^{-1}\right]$ respectively.

Arterial segment	Length $l\ [cm]$	Radius $r\ [cm]$	Thickness $h\ [cm]$	Elastic modulus E	Periph. res. R	Periph. comp. C
1. Ascending aorta	4.0	1.200	0.163	0.4	—	—
2. Aortic arch I	2.0	1.120	0.126	0.4	—	—
3. Brachiocephalic	3.4	0.620	0.080	0.4	—	—
4. Aortic arch II	3.9	1.070	0.115	0.4	—	—
5. L. com. carotid	20.8	0.250	0.063	0.4	—	—
6. R. carotid (prox.)	13.7	0.250	0.063	0.4	—	—
7. R. subclavian	3.4	0.423	0.067	0.4	—	—
8. Thoracic aorta	15.6	0.999	0.110	0.4	0.18	38.70
9. L. subclavian	3.4	0.423	0.067	0.4	—	—
10. L. ext. carotid	17.7	0.150	0.038	0.8	5.43	1.27
11. L. int. carotid I	17.7	0.200	0.050	0.8	—	—
12. R. int. carotid I	17.7	0.200	0.050	0.8	—	—
13. R. ext. carotid	17.7	0.150	0.038	0.8	5.43	1.27
14. R. vertebral	14.8	0.136	0.034	0.8	—	—
15. R. brachial	42.2	0.403	0.067	0.4	2.68	2.58
16. L. brachial	42.2	0.403	0.067	0.4	2.68	2.58
17. L. vertebral	14.8	0.136	0.034	0.8	—	—
18. L. int. carotid II	0.50	0.200	0.050	1.6	—	—
19. L. PCoA	1.5	0.073	0.018	1.6	—	—
20. R. PCoA	1.5	0.073	0.018	1.6	—	—
21. R. int. carotid II	0.50	0.200	0.050	1.6	—	—
22. Basilar	2.9	0.162	0.040	1.6	—	—
23. L. MCA	11.9	0.143	0.036	1.6	5.97	1.16
24. R. MCA	11.9	0.143	0.036	1.6	5.97	1.16
25. L. ACA, A1	1.2	0.117	0.029	1.6	—	—
26. R. ACA, A1	1.2	0.117	0.029	1.6	—	—
27. L. PCA, P1	0.5	0.107	0.027	1.6	—	—
28. R. PCA, P1	0.5	0.107	0.027	1.6	—	—
29. L. ACA, A2	10.3	0.120	0.030	1.6	8.48	0.82
30. R. ACA, A2	10.3	0.120	0.030	1.6	8.48	0.82
31. ACoA	0.3	0.074	0.019	1.6	—	—
32. L. PCA, P2	8.6	0.105	0.026	1.6	11.08	0.62
32. R. PCA, P2	8.6	0.105	0.026	1.6	11.08	0.62
34. R. carotid (dist.)	3.0	0.250	0.063	0.4	—	—

beyond a critical value of C_tCO_2, otherwise it is decreased.

Table 2.9: Overview of the reduced models used for the different vessels. By NL we indicate a vessel modeled by a non-linear transport equation system, by L we indicate a vessel modeled by a linear transport equation system. The term OD denotes a vessel associated with a lumped parameter model.

1	2	3	4	5	6	7	8	9	10	11	12	13
NL	NL	NL	NL	NL	NL	NL	NL	NL	L	L	L	L
14	15	16	17	18	19	20	21	22	23	24	25	26
L	NL	NL	L	L	L	L	L	L	L	L	L	L
27	28	29	30	31	32	33	34	—	—	—	—	—
OD	OD	L	L	OD	L	L	NL	—	—	—	—	—

Here, the driving force for changes in $R_{2,n}$ is the concentration of O_2 in the brain tissue $\left(C_tO_2\right)_n$ which is computed from the blood oxygen concentration $(c_n(t))$ in $\frac{ml\ O_2}{ml\ blood}$ at the cerebral outflow boundaries. The governing equation for the tissue concentration $\left(C_tO_2\right)_n$ in $\frac{ml\ O_2}{ml\ brain}$ is given by:

$$V_n \frac{d}{dt}\left(C_tO_2\right)_c(t) = q_n(t)\left(c_n(t) - \sigma \cdot \left(C_tO_2\right)_n(t)\right) - v\left(\left(C_tO_2\right)_n, t\right). \tag{2.126}$$

V_n is the tissue volume which is perfused by the artery Ω_n. σ denotes the partition coefficient, and v is the metabolic rate of consumption of oxygen. This ODE can be found e.g. in [24, Chapter 2, Section 2.5], its right hand side consists of three terms. The first term quantifies the amount of oxygen supplying the corresponding brain tissue, the second term accounts for the amount of oxygen extraction from the blood under normal conditions. Finally the third term simulates the metabolic demand of the corresponding brain tissue.

A possible choice for the consumption rate is the Michaelis–Menten law that reads [49, Chapter 10]:

$$v\left(\left(C_tO_2\right)_n, t\right) = 2 \cdot K_0 \cdot V_n \cdot \frac{\left(C_tO_2\right)_n(t)}{\overline{C_tO_2} + \left(C_tO_2\right)_n(t)}, \tag{2.127}$$

where $\overline{C_tO_2}$ is the average oxygen concentration in brain tissue, and K_0 is the average consumption rate. The partition coefficient σ is determined such that the following balance holds:

$$q_{0,n} \cdot \left(C_{O_2} - \sigma \cdot \overline{C_tO_2}\right) - K_0 \cdot V_n = 0, \tag{2.128}$$

where $q_{0,n}$ is the mean flow rate within Ω_n and C_{O_2} is the mean oxygen concentration in blood. In [2], the dynamic for $R_{2,n}$ was based on C_tCO_2, here we determine $R_{2,n}$ depending on the partial pressure of oxygen P_nO_2 and the mean partial pressure of oxygen $\overline{P_nO_2}$:

$$\frac{dA_R}{dt} = G_R \cdot \left(P_nO_2 - \overline{P_nO_2}\right). \tag{2.129}$$

A_R represents an activation of metabolic auto regulation for $R_{2,n}$ to change, G_R is a suitable proportional gain. The ODEs (2.126) and (2.129) are linked by Henry's law:

$$\left(C_tO_2\right)_n = \alpha_G \cdot P_nO_2. \tag{2.130}$$

Having A_R at hand, the resistance $R_{2,n}$ is determined as follows:

$$R_{2,n} = \frac{R_L + R_U e^{A_R - \hat{C}}}{1 + e^{A_R - \hat{C}}},\ \hat{C} = -\ln\left[\frac{R_{n,sp} - R_L}{R_U - R_{n,sp}}\right]. \tag{2.131}$$

$R_{n,sp}$ denotes the setpoint of the cerebral resistance $R_{2,n}$. It is computed from $R_{1,n}$ given by the characteristic impedance of Ω_n [2, 3] and the total resistance

$$R_n = R_{1,n} + R_{n,sp} \tag{2.132}$$

listed in [3, Table 2.1]. R_U and R_L are the upper and lower bounds of $R_{2,n}$ which are chosen as: $R_U = 1.30 \cdot R_{n,sp}$ and $R_L = 0.74 \cdot R_{n,sp}$. We remark that $\hat{C}$ is determined in such a way that $A_R = 0$ holds for $R_{2,n} = R_{n,sp}$.

In each time step, we solve the ODEs (2.126) and (2.129), where q_n and c_n are computed from the outlet of the terminal vessel Ω_n. Note that the single volumes V_n have to sum up to the total volume of the brain $V_{br} = 1.071\ dm^3$ and are distributed among the cerebral arteries Ω_n in the same relation as the flow distribution for $R_{2,n} = R_{n,sp}$.

Modeling the stenosis

Our model of a carotid artery stenosis is based on a domain decomposition, i.e., we split the right carotid artery into three parts: vessel 6, the stenosis and vessel 34. The minimal section area of the stenosis is denoted by A_{st} and its length by l_{st}. According to Figure 2.30 and Table 2.9, blood flow and oxygen transport is governed by the non-linear 1D model. Therefore we have to determine at the inlet of vessel 34 and at the outlet of vessel 6 the unknowns $\left(A_{up}^{34}, Q_{up}^{34}, \Gamma_{up}^{34}\right)$ and $\left(A_{up}^{6}, Q_{up}^{6}, \Gamma_{up}^{6}\right)$ for the flux unwinding (see Figure 2.34).

Due to its small length, we model the stenosis just as the small vessels $27, 28$ and 31 by a 0D lumped parameter model. The lumped parameter model for the stenosis is slightly different as the one, given by (2.27a),(2.27b). While the equation for the average pressure $\hat{p}_{st}$ is identical to (2.27a), the equation for the averaged flow rate $\hat{q}_{st}$ is modified to account for a pressure drop $\Delta p_{st} = p_{34} - p_6$ and a reduced flow rate in vessel 34:

$$C_{st}\frac{\partial \hat{p}_{st}}{\partial t} = Q_6 - Q_{34}, \tag{2.133}$$

$$-\frac{K_u \rho l_{st}}{A_0}\frac{\partial \hat{q}_{st}}{\partial t} = \Delta p_{st} + \frac{K_v \eta}{A_0 D_0}\hat{q}_{st} + \frac{K_t \rho}{2{A_0}^2}\left(\frac{A_0}{A_{st}} - 1\right)^2 \hat{q}_{st}\left|\hat{q}_{st}\right|. \tag{2.134}$$

The second equation is developed in [100, 108, 120]. For simplicity, we assume that the vessels 6 and 34 have the same section area at rest: $A_0 = A_{0,34} = A_{0,6}$. Table 2.10 and Table 2.11 give a summary of all parameters of the ODE-system. The averaged values $\hat{p}_{st}$ and $\hat{q}_{st}$ are approximated by the trapezoidal rule, which is at least of order 1. This approximation yields:

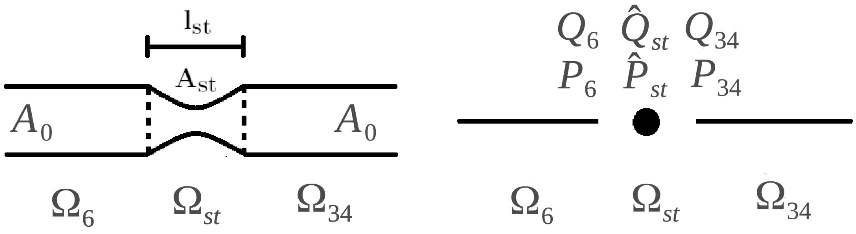

Figure 2.34: Domain decomposition of the right carotid artery (left), model reduction applied to the stenosis (right)

$$\hat{p}_{st} \approx \frac{p_6 + p_{34}}{2}, \qquad \hat{q}_{st} \approx \frac{Q_6 + Q_{34}}{2}. \tag{2.135}$$

Table 2.10: Stenosis parameters, presented in [100, 108, 120]

Parameter	description
η	blood viscosity
ρ	blood density
A_0	section area of Ω_{st}
D_0	diameter of Ω_{st}
A_{st}	smallest cross-section area of the stenosis
D_{st}	smallest diameter of the stenosis
l_{st}	length of the stenosis
C_{st}	compliance of the stenosis: $(A_{st} \cdot l_{st}) / \left(\rho \cdot c_0 (A_{st})^2\right)$

Table 2.11: Empirical parameters [73].

Parameter	value
K_u	1.20
K_v	$32.0 \cdot (0.83 \cdot l_{st} + 1.64 \cdot D_{st}) \cdot (A_0/A_{st})^2 / D_0$
K_t	1.52

By means of (2.135), the pressure-area law (2.8) and the outgoing characteristics (see Theorem 2.1), we are able to compute the four upwinded values: $\left(A_{up}^6, Q_{up}^6\right)$ and $\left(A_{up}^{34}, Q_{up}^{34}\right)$. Now we require two additional equations in order to determine the two missing values Γ_{up}^6 and Γ_{up}^{34}. One equation is based on the observation that the volumetric concentration of oxygen in arterial blood is almost constant, i.e.,

$$\frac{\Gamma_{up}^6}{A_{up}^6} = \frac{\Gamma_{up}^{34}}{A_{up}^{34}}. \tag{2.136}$$

For the derivation of the second equation, we distinguish between the following two cases:

Case (i): $\hat{q}_{st} \geq 0$. In this case, oxygen is transported from Ω_6 to Ω_{34}. Thus we can determine the volumetric concentration $\hat{c}_{st}$ by the values Γ_6 and A_6, evaluated from the finite element approximation on the last element of Ω_6:

$$\hat{c}_{st} = \frac{\Gamma_6}{A_6} = \frac{\Gamma_6^{up}}{A_6^{up}}. \tag{2.137}$$

Case (ii): $\hat{q}_{st} < 0$. In this case, we close the system replacing 6 by 34 in (2.137).

Numerical results and discussion

We run each simulation for several periods until the numerical solution becomes periodic. For our network this takes about 8-10 periods. After the numerical solution becomes periodic, we compute the average flow rates $q_{0,c}$ in the cerebral vessels, which are needed to determine the partition coefficients at the cerebral outlets (2.128) and run the simulation again. Then after 10 heart cycles, the cerebral auto regulation given by (2.126) and (2.129) is started. To model the influence of the stenosis, we shrink within the time interval $[14s, 15s]$ the section area A_{st} of the stenosis linearly from $A_{0,6}$ to $\beta \cdot A_{0,6}$. After $45s$ the simulation is stopped.

The simulation described in the previous subsection is run for each $\beta \in \{0.05, 0.10, 0.15\}$ and an intact and anatomically complete CoW. The acute narrowing in the right carotid artery causes a pressure drop and a remarkable reduction of the flow rate within vessel 34 (distal part of the right common carotid).

Pressure and flow rate in the middle of vessel 34 for the time interval $[14s, 16s]$ are shown in Figure 2.35. For $[14s, 15s]$ we recognize the typical behavior of an arterial pressure curve. The values for the systolic pressure (about 130 mmHg) and the diastolic pressure (about 60 mmHg) are within a reasonable range (see, e.g., [97]).

The influence of the stenosis can be seen within the next heart cycle $[15s, 16s]$. We observe that for a narrowing of 95 percent ($\beta = 0.05$) the maximum of the pressure curve drops about 36.41 mmHg and that of the flow rate about 7.17 cm^3/s. For a narrowing of 90 percent ($\beta = 0.10$) and 85 percent ($\beta = 0.15$) there is a pressure drop of 25.56 mmHg and 17.68 mmHg, respectively. The flow rate peak decreases about 5.08 cm^3/s and 3.54 cm^3/s, respectively.

Figure 2.38 shows the influence on the flow rate within the CoW, while the modifications of the cerebral resistances are reported in Figure 2.39. Please note that the resistance values were normalized by their corresponding setpoint values listed in [3, Table 2.1]. We see that the communicating vessels 20 and 31 play an important role in compensating the reduced flow rate through vessel 12 (R. int. carotid I). This observation is in agreement with the results of [121, Section 3]. The cerebral resistances corresponding to R_{24} and R_{30} are decreased up to 22%, whereas the resistances at the opposite side of the CoW (R_{23} and R_{29}) are reduced about 10-12% and there is no significant change in R_{32} and R_{33}.

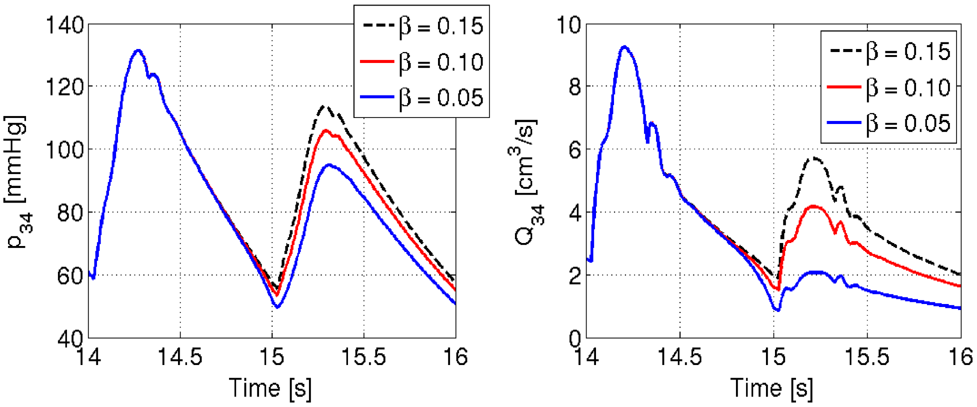

Figure 2.35: Pressure (left) and flow rate (right) charted at the middle of vessel 34 for the time interval $[14s, 16s]$

A comparison between our auto-regulation model and the model described in [2], which is based on the concentration of CO_2 within the brain tissue, reveals that the cerebral resistance R_{24} exhibits a similar behavior as the cerebral resistance R_{24} in [2]. The difference between the results is that the values of R_{24} at the end of the simulation are about 5-8 percent smaller than our resistance values.

Analyzing the P_nO_2 concentration over time at the cerebral outflow boundaries, it can be observed that the P_nO_2 reaches its minimum in the time interval $[17s, 18s]$. In order to estimate the drop of the P_nO_2 caused by the stenosis, we compute for each cerebral outflow boundary the averaged P_nO_2 within the time interval $[17s, 18s]$ and compare it to the setpoint of P_nO_2, which can be assumed to be an average value of 25 mmHg. In Figure 2.36 for each β and each cerebral outflow boundary, the ratio of the averaged P_nO_2 and the setpoint $\overline{P_nO_2}$ is computed. It can be seen, that for P_nO_2, $n \in \{24, 25\}$ the averaged P_nO_2 drops significantly, due to their neighborhood to the stenosis located in the right carotid. The variations at the other cerebral boundaries are within 0.84% and 8.50%.

To evaluate whether a sufficient oxygen delivery can be restored at the cerebral outflow boundaries, we compute within the time interval $[44s, 45s]$ the average value of P_nO_2 and compare it to the set point $\overline{P_nO_2} = 25$ mmHg.

In Figure 2.36, it can be seen that the averaged P_nO_2 are reduced about less than 1%, except for $n = 24$ and $\beta = 0.05$, here we have a reduction rate of: 1.29%. Thus it can be concluded that the complete CoW combined with the metabolic cerebral auto regulation can restore the P_nO_2 within the brain tissue.

The significance of a complete CoW and the metabolic cerebral auto-regulation concerning the restorement of the P_nO_2, is studied by two further simulations, where we redo the previous simulation with two changes: Firstly, we remove vessel 31 (anterior communicating

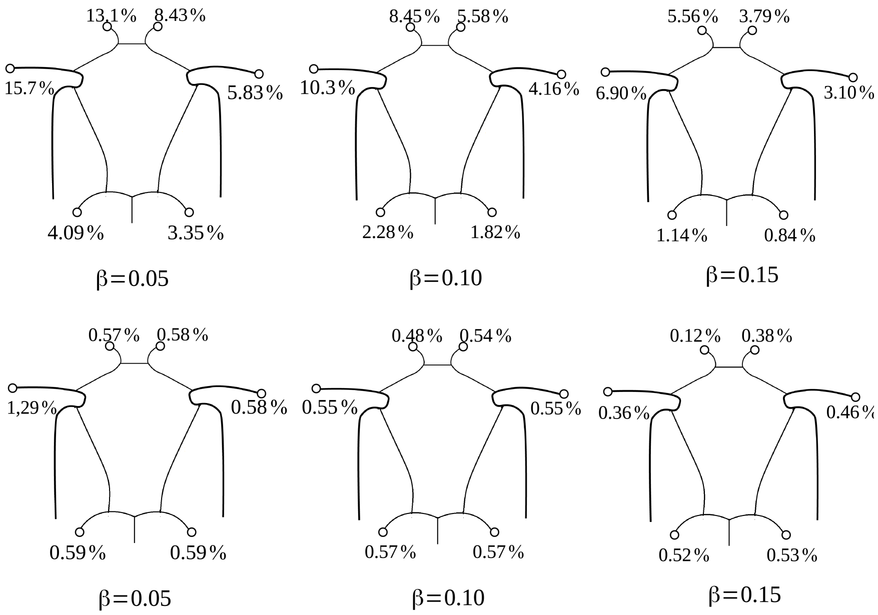

Figure 2.36: Reduction of the average P_nO_2 within the time interval $[17s, 18s]$ (top) and the time interval $[44s, 45s]$ (bottom), for the narrowing factors $\beta \in \{0.05, 0.1, 0.15\}$. The numbers at the cerebral outflow boundaries express the percentage of reduction of the averaged P_nO_2.

artery). In Figure 2.38, it can be seen that this vessel plays a crucial role in balancing the reduced flow rate. The peak of the flow rate in 31 is about 3.17 cm^3/s for $\beta = 0.05$. The narrowing factors $\beta = 0.1$ and $\beta = 0.15$ cause flow rate peaks of: 2.10 cm^3/s and 1.35 cm^3/s, respectively. Secondly, we consider again the complete CoW, but switch off the metabolic cerebral auto regulation.

For each scenario, we report the average value of P_nO_2 within the time interval $[44s, 45s]$ and compute again the reduction rate in percent with respect to the setpoint $\overline{P_nO_2} = 25$ mmHg. In Figure 2.37 the variation rates for both scenarios are reported. Both diagrams, reveal that P_nO_2 for $n \in \{24, 30\}$ can not be restored for a stenosis degree of 95% ($\beta = 0.05$). In the other cases, the reduction rates are smaller than 3%. Please note that the mean partial pressure of oxygen reflects a wide range of local partial pressure of oxygen values in the brain tissue, ranging from values as low as 5 mmHg up to values near the arterial partial pressure of oxygen [47]. Thus, it must be emphasized that the re-establishment of a mean partial pressure of oxygen in the brain tissue of 25 mmHg as observed in this model may not exclude any local ischemia in the area at risk.

Conclusion

Our numerical results reveal that the drops of the partial pressure of oxygen caused by an acute unilateral stenosis can only be compensated, if the CoW is complete and if

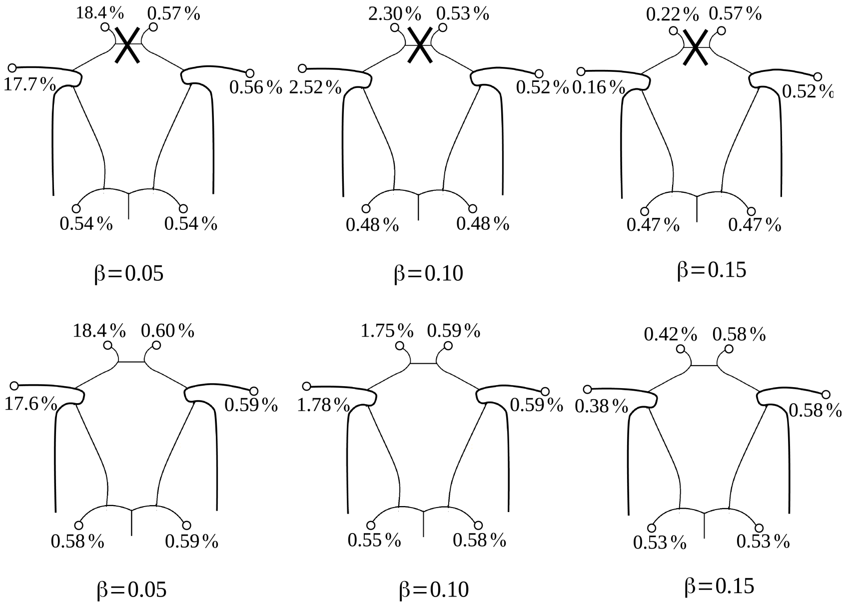

Figure 2.37: Reduction of the average P_nO_2 within the final time interval $[44s, 45s]$, for the narrowing factors $\beta \in \{0.05, 0.1, 0.15\}$, without vessel 31 (top) and without cerebral auto regulation (bottom). The numbers at the cerebral outflow boundaries express the percentage of reduction of the averaged P_nO_2.

the cerebral resistances can be reduced sufficiently. The model can provide information to predict the impact of severe unilateral carotid artery stenoses on cerebral oxygen supply. Provided that malformations of the CoW and diameters of all collateral vessels forming it can be obtained with sufficient accuracy and the actual blood carrying capacity of the blood is known, the model principally allows to predict the mean oxygenation of the brain area supplied by the collateral flow. Having these data at hand, the model allows a much better evaluation of the risk of hypoxia than determinations of vessel diameters and collateral blood flow alone. However, our cerebral auto regulation mechanism is only based on the metabolic regulation. This is only one component of the total cerebral auto regulation, there are also the myogenic and the neurogenic auto regulation, which could be incorporated into the numerical model.

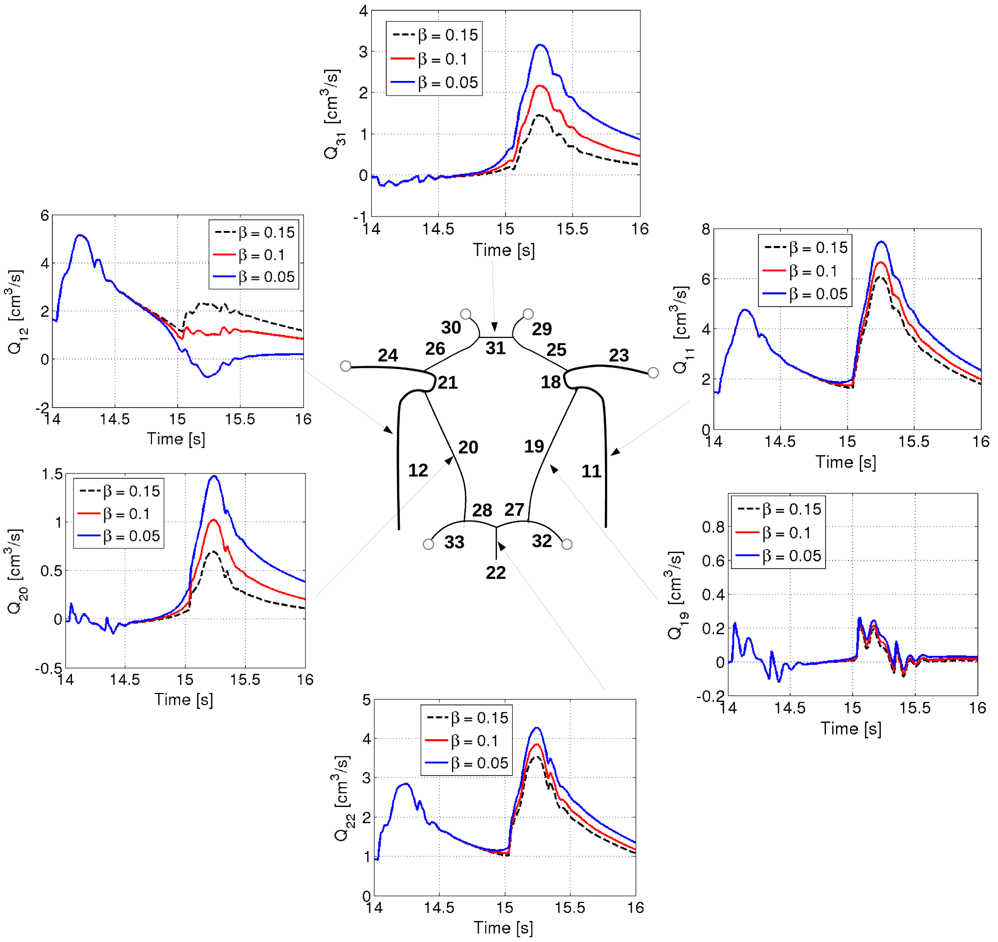

Figure 2.38: Flow rates within the complete CoW for the time interval $[14s, 16s]$, charted at the middle of some vessels. The flow rates under normal conditions can be seen for the time interval $[14s, 15s]$, while the impact of the stenosis can be observed for the time interval $[15s, 16s]$.

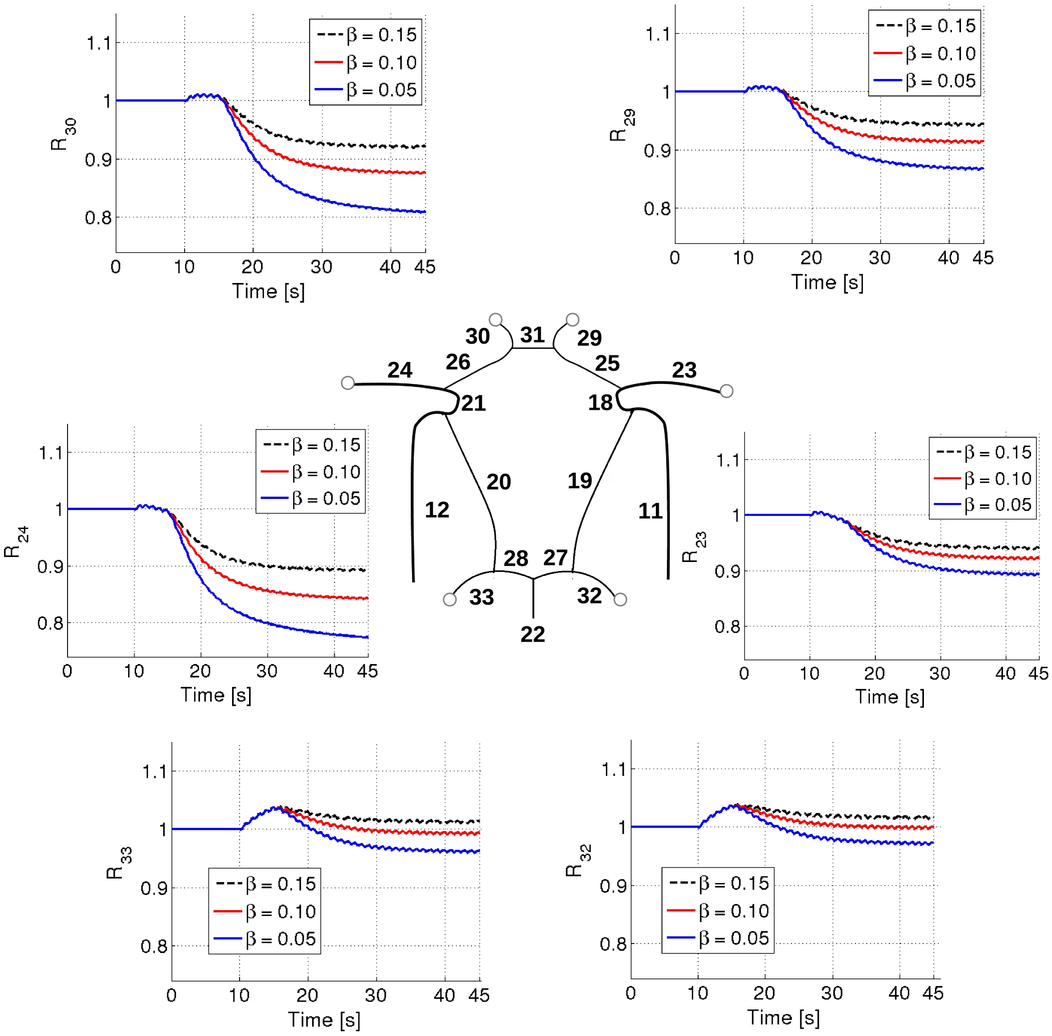

Figure 2.39: Normalized cerebral resistances for the time interval $[0s, 45s]$.

3 Stationary coupled 3D-1D diffusion-reaction models

In the last chapter, we presented a multi-scale model for flow and mass transport in an arterial network. Instead of expensive 3D models, reduced 1D models have been used to compute pressures, flow rates and concentration values within the network. To establish a 3D model describing flow and mass transport within a vascularized 3D tissue volume, it is necessary to derive a coupling between the 1D model for the network and the 3D models governing the flow and mass transport within the 3D tissue. In this thesis, we consider the tissue as a porous medium. The standard equations for flow and mass transport within a porous medium are usually provided by homogenized 3D models representing the considered phenomena related to the micro scale structures without resolving the fine component parts of the porous matrix. Here, we use a parabolic PDE and Darcy's equation to compute pressure and velocity and a convection-diffusion equation to simulate the mass transport in the porous matrix [53][Chapter 3]. Besides the fact that the computational costs are remarkably reduced by the usage of 1D models for the network, this approach has a further advantage, i.e, it makes the need of refined computational meshes near the network obsolete. This allows for a large saving in memory and CPU [24].

However, the coupling conditions between the 3D porous medium and the reduced 1D models are not standard. Therefore the basic coupling concepts between 1D and 3D models are introduced by taking the example of stationary diffusion-reaction models, before we derive in the next chapter a model for the dynamics of network flow and transport processes within a porous medium. The diffusion-reaction models are given by elliptic second order PDE systems, where the single equations depend on each other by some exchange terms. Such types of systems are much simpler to analyze than the time dependent systems coupling 1D transport equations and dynamic 3D models. By this mean, one can obtain a better insight into the mathematical and numerical difficulties associated with coupled 3D-1D systems.

The current chapter is organized as follows: At first we introduce some notation and definitions following the lines of [24][Chapter 3.2]. Based on these definitions, a coupled 3D-1D system consisting of two elliptic equations is derived. Both equations are coupled by its source terms, where the source term of the 3D equation contains a *Dirac measure* concentrated on curves which determine the location of the network. The presence of a Dirac measure in the source term of the 3D problem results in low regularity of a weak solution. It can be shown that the analytic solution exhibits singularities at the position of the Dirac measures [32]. Therefore the derivation of finite element approximations for such PDE systems and the numerical analysis are not straightforward. In this context, the impact of Dirac measures on the local convergence behavior of standard finite element methods is investigated by means of an elliptic model problem with a Dirac right hand side. Finally, we present an iterative solution scheme for the numerical solution of coupled problems.

3.1 Model equations

Let us denote the porous matrix containing a 1D network by $\Omega_{3d} \subset \mathbb{R}^3$. As a first step towards the coupled 3D-1D problem, we introduce the space occupied by the vessel and the interface between the vessel and the porous medium. According to Figure 3.1 these objects can be defined as follows:

(i) The 1D curve representing the vessel is denoted by $\Lambda \subset \Omega_{3d}$. For the sake of simplicity, we assume that Λ is a single straight line:

$$\Lambda := \{\mathbf{x} \in \Omega_{3d} \,|\mathbf{x} = \mathbf{x_c}(s), \quad s \in [0, L]\}, \tag{3.1}$$

where s is the curve parameter, L is the length of the line and $\mathbf{x_c} : [0, L] \to \mathbb{R}^3$ is the parameterization of the curve Λ. Furthermore it should hold for the parameterization $\mathbf{x_c}$:

$$\left\|\mathbf{x_c}'(s)\right\| = 1, \; \forall s \in (0, L).$$

This construction can be extended to consider also networks (see Chapter 4).

(ii) The radius of the considered vessel is given by a positive constant $R > 0$. By this, the actual volume covered by the vessel is defined as the set of points closer than $R > 0$ to Λ:

$$V_R := \{\mathbf{x} \in \Omega_{3d} \,|\mathrm{dist}\,(\mathbf{x}, \Lambda) < R\}. \tag{3.2}$$

We will use this domain to study the coupling between the porous matrix and the one-dimensional vessel, where we assume that $\overline{V_R} \subset \overline{\Omega_{3d}}$. The domain V_R is composed of the following three sets:

$$V_R^T = \left\{\mathbf{x} \in \mathbb{R}^3 \,|\mathbf{x} = x_T\,(r, \theta)\,, (r, \theta) \in [0, R) \times [0, 2\pi)\right\}, \tag{3.3a}$$

$$V_R^I = \left\{\mathbf{x} \in \mathbb{R}^3 \,|\mathbf{x} = x_I\,(s, r, \theta)\,, (s, r, \theta) \in (0, L) \times [0, R) \times [0, 2\pi)\right\}, \tag{3.3b}$$

$$V_R^B = \left\{\mathbf{x} \in \mathbb{R}^3 \,|\mathbf{x} = x_B\,(r, \theta)\,, (r, \theta) \in [0, R) \times [0, 2\pi)\right\}, \tag{3.3c}$$

where

$$x_T\,(r, \theta) = \mathbf{x_c}(L) + \mathbf{n}(L) r \cos\theta + \mathbf{b}(L) r \sin\theta, \tag{3.4a}$$

$$x_I\,(s, r, \theta) = \mathbf{x_c}(s) + \mathbf{n}(s) r \cos\theta + \mathbf{b}(s) r \sin\theta, \tag{3.4b}$$

$$x_B\,(r, \theta) = \mathbf{x_c}(0) + \mathbf{n}(0) r \cos\theta + \mathbf{b}(0) r \sin\theta. \tag{3.4c}$$

$\mathbf{n}(s)$ and $\mathbf{b}(s)$ are the normal and Bi normal vectors on the curve Λ. The Bi normal vector $\mathbf{b}(s)$ is given by the cross product of the corresponding tangent vector $\mathbf{t}(s)$ and the normal vector $\mathbf{n}(s)$:

$$\mathbf{b}(s) = \frac{\mathbf{t}(s) \times \mathbf{n}(s)}{\|\mathbf{t}(s) \times \mathbf{n}(s)\|}.$$

(iii) We will denote by

$$\Omega_{3d}^R = \Omega_{3d} \setminus \overline{V_R} \tag{3.5}$$

the domain of the porous medium which is not covered by the vessel. The interface Γ^R between the vessel and the porous medium is given by:

$$\Gamma^R = \partial V_R. \tag{3.6}$$

The lateral surface of the set Γ^R that belongs to the boundary of V_R^I will be denoted by

$$\Gamma_0^R = \left\{ \mathbf{x} \in \mathbb{R}^3 \, | \mathbf{x} = x_I\left(s, R, \theta\right), \; (s, \theta) \in (0, L) \times [0, 2\pi) \right\}. \tag{3.7}$$

(iv) Γ_{3d} is the boundary of the porous matrix: $\Gamma_{3d} = \partial\Omega_{3d}$. This implies: $\partial\Omega_{3d}^R = \Gamma^R \cup \Gamma_{3d}$.

(v) Finally, the basic assumption on the vessel geometry is that the projection from V_R to Λ is unique:

$$\forall \mathbf{x} \in V_R : \exists! \mathbf{x_0} \in \Lambda : \operatorname{dist}\left(\mathbf{x}, \Lambda\right) = \left\| \mathbf{x} - \mathbf{x_0} \right\|. \tag{3.8}$$

The projection $\mathbf{x_0}$ exists because Λ is a compact set. It can be shown that (3.8) is fulfilled if the curve Λ is smooth enough and the radius R small. As a consequence, we have:

$$\operatorname{dist}\left(x_I\left(s, r, \theta\right), \Lambda\right) = r, \; \forall \left(s, r, \theta\right) \in (0, L) \times [0, R) \times [0, 2\pi). \tag{3.9}$$

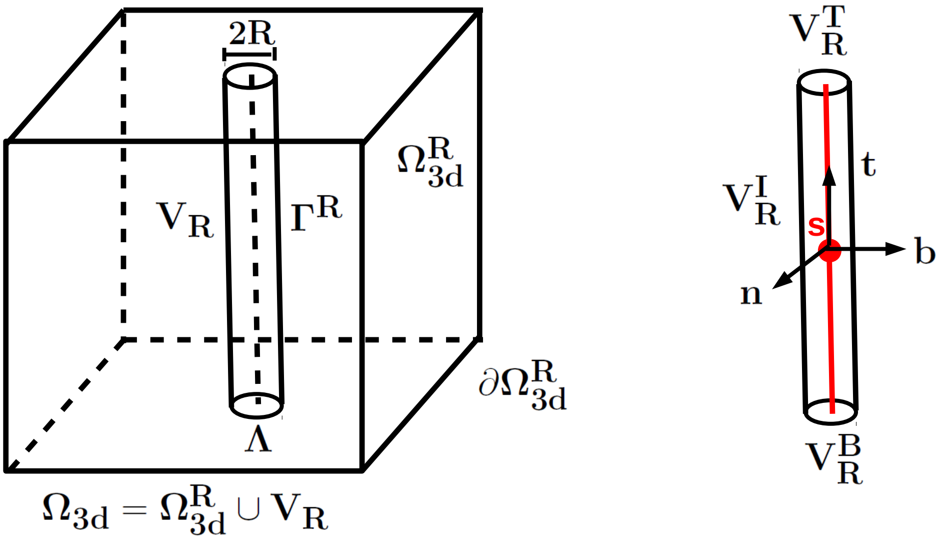

Figure 3.1: Sub domains in Ω_{3d}: The 1D curve Λ, the actual 3D vessel domain V_R and the porous matrix Ω_{3d}^R. At the right hand side one can see the subsets of the vessel V_R: V_R^T, V_R^I and V_R^B and the vectors $\mathbf{t}$, $\mathbf{n}$ and $\mathbf{b}$ for the curve parameter $s \in [0, L]$.

Now let $\{\psi_i\}$ be a partition of unity such that $\psi_i : V_R \to \mathbb{R}$ is a non-negative smooth function with $\operatorname{supp}(\psi_i) \subset \overline{V_R^i}$ and $\sum_{i\in\{T,B,I\}} \psi_i = 1$ on V_R. For a suitable function $g : V_R \to \mathbb{R}$, it follows:

$$\int_{V_R} g \, d\mathbf{x} = \int_0^{2\pi} \int_0^R \int_0^L g_I(s,r,\theta) r \, dsdrd\theta,$$

where

$$g_i := (g\psi_i) \circ x_i^{-1}, \quad i \in \{T,B,I\}.$$

For the surface integral, we have:

$$\int_{\Gamma^R} g \, d\mathbf{S} = \int_0^{2\pi} \int_0^L g_I(s,R,\theta) R \, dsd\theta + \sum_{i\in\{T,B\}} \int_0^{2\pi} \int_0^R g_i(r,\theta) \cdot r \, drd\theta.$$

If g is continuous on V_R, it follows:

$$\lim_{\epsilon\to 0} \frac{1}{\epsilon} \int_{\Gamma_0^{\epsilon R}} g \, d\mathbf{S} = \lim_{\epsilon\to 0} \int_0^{2\pi} \int_0^L g_I(s,\epsilon R,\theta) R \, dsd\theta = \int_0^L 2\pi \, g(s) R \, ds = 2\pi R \int_\Lambda g(s) \, ds, \tag{3.10}$$

where $g(s) = g\left(x_I(s,0,0)\right)$. The averaging operator with respect to the surface Γ_0^R is defined as follows:

$$\overline{g}(s) = \int_0^1 g\left(x_I(s,R,2\pi\theta)\right) \, d\theta.$$

Because Γ_0^R scales as R, we have by $g_\epsilon(s,r,\theta) = g(s,r/\epsilon,\theta)$:

$$\lim_{\epsilon\to 0} \frac{1}{\epsilon} \int_{\Gamma_0^{\epsilon R}} g_\epsilon \, d\mathbf{S} = 2\pi \, R \int_0^L \overline{g}(s) \, ds. \tag{3.11}$$

Now we study the behavior of the solution when a suitable rescaling is applied and R tends to zero so that Ω_{3d}^R expands to the whole matrix Ω_{3d}. Assuming that the model for the vessel flow is already one-dimensional, we have for the unknown u_{3d} in the 3D porous medium and the unknown u_{1d} in the vessel the following model:

$$-\nabla \cdot (K_{3d} \nabla u_{3d}) + m_{3d} u_{3d} + r_{3d} = 0 \quad \text{in} \quad \Omega_{3d}^R, \tag{3.12}$$

$$u_{3d} = 0 \quad \text{on} \quad \Gamma_{3d}, \tag{3.13}$$

$$K_{3d} \partial_{\mathbf{n}} u_{3d} = q \quad \text{on} \quad \Gamma^R, \tag{3.14}$$

$$-\frac{d}{ds}\left(K_{1d} \frac{du_{1d}}{ds}\right) + f = 0 \quad \text{in} \quad \Lambda, \tag{3.15}$$

$$u_{1d}(0) = u_{1d,0}, \quad K_{1d} \frac{d}{ds} u_{1d}(L) = 0, \tag{3.16}$$

where K_{3d}, m_{3d} and r_{3d} are a diffusion, reaction and source term for the 3D porous medium respectively, while K_{1d} is the diffusion coefficient for the 1D vessel domain. The q term which is defined on Γ^R between the vessel and the porous medium denotes the mass transfer term (per unit surface) from the porous matrix to the vessel. To enforce a conservation of the global flux Φ across the interface Γ^R the source term f of the one-dimensional vessel has to fulfill the following balance equation:

$$\Phi = \int_0^L f(s)\ ds = \int_{\Gamma^R} q\ dS.$$

The boundary conditions for the 3D problem are of mixed Dirichlet and Neumann type. For the 1D model we have a Dirichlet condition at $s = 0$ and a homogeneous Neumann condition at $s = L$. We point out that other combinations could be considered as well. Now we study the limit $R \to 0$, by means of the following 3D problem for the scaled vessel radius ϵR, $\epsilon \in (0, 1]$:

$$-\nabla \cdot (K_{3d} \nabla u_{3d}^{\epsilon}) + m_{3d} u_{3d}^{\epsilon} + r_{3d} = 0 \quad \text{in} \quad \Omega_{3d}^{\epsilon R}, \tag{3.17}$$

$$u_{3d}^{\epsilon} = 0 \quad \text{on} \quad \Gamma_{3d}, \tag{3.18}$$

$$K_{3d} \partial_{\mathbf{n}} u_{3d}^{\epsilon} = q_{\epsilon} \quad \text{on} \quad \Gamma^{\epsilon R}. \tag{3.19}$$

To keep the total flux across $\Gamma^{\epsilon R}$ unchanged, the flux q_ϵ on $\Gamma_0^{\epsilon R}$ for the scaled problem must be equal to

$$q_\epsilon\left(s, \epsilon R, \theta\right) = \frac{1}{\epsilon} q\left(s, R, \theta\right).$$

By changing the integration variables we have:

$$\Phi = \int_{\Gamma_0^{\epsilon R}} q_\epsilon\ dS = \int_{\Gamma_0^R} q\ dS = \int_0^L f(s)\ ds \qquad \forall \epsilon \in (0, 1].$$

Multiplying the equations of the scaled problem by an arbitrary test function in $C_0^\infty(\Omega)$ and integrating over $\Omega_{3d}^{\epsilon R}$, we obtain:

$$\int_{\Omega_{3d}^{\epsilon R}} K_{3d} \nabla u_{3d}^{\epsilon} \cdot \nabla \phi\ d\Omega + \int_{\Omega_{3d}^{\epsilon R}} m_{3d} u_{3d}^{\epsilon} \phi\ d\Omega + \int_{\Omega_{3d}^{\epsilon R}} r_{3d} \phi\ d\Omega = \int_{\Gamma_0^{\epsilon R}} q_\epsilon \phi\ dS, \quad \forall \phi \in C_0^\infty(\Omega). \tag{3.20}$$

Since

$$\int_{\Gamma_0^{\epsilon R}} q_\epsilon \phi\ dS = \int_0^{2\pi} \int_0^L q\left(x_I(s, R, \theta)\right) \phi\left(s, \epsilon R, \theta\right) R\ ds d\theta$$

we have similar to (3.10) and (3.11):

$$\lim_{\epsilon \to 0} \int_{\Gamma_0^{\epsilon R}} q_\epsilon \phi\ dS = 2\pi R \int_\Lambda \bar{q} \phi\ ds, \text{ where } \bar{q}(s) = \int_0^1 q\left(s, R, 2\pi\theta\right)\ d\theta.$$

Thus the 1D source term can be given by the following expression:

$$f(s) = 2\pi R \bar{q}(s).$$

Let us suppose that $u_{3d}^{\epsilon} \to u_{3d}$ with respect to a suitable norm so that for $\epsilon \to 0$ we have:

$$\int_{\Omega_{3d}} K_{3d} \nabla u_{3d} \cdot \nabla \phi\ d\Omega + \int_{\Omega_{3d}} m_{3d} u_{3d} \phi\ d\Omega + \int_{\Omega_{3d}} r_{3d} \phi\ d\Omega = \int_\Lambda f(s) \phi\ ds, \quad \forall \phi \in C_0^\infty(\Omega). \tag{3.21}$$

Thus the following problem is a candidate for our 3D asymptotic problem:

$$\begin{aligned} -\nabla \cdot (K_{3d} \nabla u_{3d}) + m_{3d} u_{3d} + r_{3d} = f(s)\delta_\Lambda \quad \text{in} \quad \Omega_{3d}, \\ u_{3d} = 0 \quad \text{on} \quad \partial\Omega_{3d}, \end{aligned} \tag{3.22}$$

where δ_Λ is a Dirac measure concentrated on Λ. For the 1D problem the function $f(s)$ acts as a sink term in the 1D problem:

$$\begin{aligned} -\frac{d}{ds}\left(K_{1d}\frac{du_{1d}}{ds}\right) + f(s) = 0 \quad \text{in} \quad \Lambda, \\ u_{1d}(0) = u_{1d,0}, \quad K_{1d}\frac{d}{ds}u_{1d}(L) = 0. \end{aligned} \tag{3.23}$$

We observe that the mass exchange term f appears as a function in the 1D equation and as a weighting factor for the measure in the 3D equation. It is well known that $\delta_\Lambda \notin H^{-1}(\Omega)$. Thus if a solution u_{3d} exists, it will not be in $H^1(\Omega)$ due to the fact that an elliptic problem with line source has a singularity near the line, whose derivates are not in $L^2(\Omega)$. Up to now the 3D problem and the 1D problem are decoupled, to model diffusion-reaction problems for a network in a porous medium, we have to establish a coupling between the two sub problems. Here, this is done by using the following linear constitutive law for the flux q [24, Chapter 3]:

$$q(s,\theta) = D\left(u_{1d}(s) - u_{3d}\left(x_I(s,R,\theta)\right)\right).$$

By this, both systems are no longer decoupled. Finally the reduced problem has the following form:

Model problem 1:

$$-\nabla \cdot (K_{3d} \nabla u_{3d}) + m_{3d} u_{3d} + r_{3d} = f\left(u_{3d}, u_{1d}, s\right)\delta_\Lambda \quad \text{in} \quad \Omega_{3d}, \tag{3.24}$$

$$\begin{aligned} u_{3d} = 0 \quad \text{on} \quad \partial\Omega_{3d}, \\ -\frac{d}{ds}\left(K_{1d}\frac{du_{1d}}{ds}\right) + f\left(u_{3d}, u_{1d}, s\right) = 0 \quad \text{in} \quad \Lambda, \\ u_{1d}(0) = u_{1d,0}, \quad K_{1d}\frac{d}{ds}u_{1d}(1) = 0, \end{aligned} \tag{3.25}$$

where f is a suitable functional, modeling the linear flux. We compute:

$$\begin{aligned} f\left(u_{3d}, u_{1d}, s\right) &= 2\pi R D\left(u_{1d}(s) - \int_0^1 u_{3d}\left(x_I\left(s,R,2\pi\theta\right)\right)\, d\theta\right) \\ &= 2\pi R D\left(u_{1d}(s) - \overline{u_{3d}(s)}\right). \end{aligned} \tag{3.26}$$

From this first model problem, we derive some further model problems, which are investigated in the following sections. If the solution for the one-dimensional problem is constant and equal to u_0, i.e., $u_{1d} \equiv u_0 > 0$, we have by $K_{3d} = I$ and $m_{3d} = r_{3d} = 0$ on the unit cube $\Omega_{3d} = (0,1)^3$:

Model problem 2:

$$\begin{aligned} -\Delta u = 2\pi RD\left(u_0-\bar{u}\right)\delta_\Lambda \quad &\text{in} \quad \Omega_{3d}, \\ u = 0 \quad &\text{on} \quad \partial\Omega_{3d}. \end{aligned} \tag{3.27}$$

where $\bar{u}$ is given by: $\int_0^1 u\left(\mathbf{x_I}\left(s,R,2\pi\theta\right)\right)\,d\theta$. If we assume that Λ is a straight line, i.e.,

$$\Lambda = \mathbf{x_0}\times(0,1),\ \mathbf{x_0}\in\Omega_{2d}=(0,1)^2,\ \mathbf{x_0}=\left(x_{0,1},x_{0,2}\right)^T,$$

the exact solution of the differential equation in (3.27) is given by:

$$u_e\left(\mathbf{x}\right) = -u_0\frac{RD}{1-RD\ln R}\ln r,\ \mathbf{x}=\left(x_1,x_2,x_3\right)^T,\ r=\sqrt{\left(x_1-x_{0,1}\right)^2+\left(x_2-x_{0,2}\right)^2}.$$

Obviously, the solution u_e does not depend on the third coordinate x_3, consequently the 3D problem (**Model problem 2**) can be reduced to a 2D problem:

Model problem 3:

$$\begin{aligned} -\Delta u = 2\pi RD\left(u_0-\bar{u}\right)\delta_{\mathbf{x_0}} \quad &\text{in} \quad \Omega_{2d}, \\ u = u_e \quad &\text{on} \quad \partial\Omega_{2d}, \end{aligned} \tag{3.28}$$

$$u_e\left(\mathbf{x}\right) = -u_0\frac{RD}{1-RD\ln R}\ln r, \tag{3.29}$$

where $\mathbf{x}=\left(x_1,x_2\right)^T,\ r=\sqrt{\left(x_1-x_{0,1}\right)^2+\left(x_2-x_{0,2}\right)^2}$, $\delta_{\mathbf{x_0}}$ denotes a Dirac measure concentrated on $\mathbf{x_0}\in\Omega_{2d}\subset\mathbb{R}^2$. Related to Model problem 3, we define a further model problem having the shape of a simple Poisson problem. If $RD\left(u_0-\bar{u}\right)\equiv 1$ holds, we obtain:

Model problem 4:

$$\begin{aligned} -\Delta u = 2\pi\delta_{\mathbf{x_0}} \quad &\text{in} \quad B_1(0), \\ u = 0 \quad &\text{on} \quad \partial B_1(0). \end{aligned} \tag{3.30}$$

The fundamental solution of this problem is given by: $u=-\ln r$. Elliptic PDE systems like **Model problem 1-4** can be found in many applications besides porous media flow, e.g., in the mathematical modeling of electromagnetic fields [55] and in the adjoint equation of optimal control problems [17, 18]. Furthermore the use of measures plays an important role in controllability for elliptic and parabolic equations, see the recent contributions [19, 20, 69] and the references therein. Thus it is not surprising that there is a variety of literature on the mathematical and numerical difficulties associated with such a type of problem.

Existence and uniqueness of the solution corresponding to **Model problem 1-4**, has been shown in [25][24][Chapter 4] by the help of weighted Sobolev spaces [59] and the inf-sup condition of Necaš-Theorem. The convergence behavior of standard Finite elements in the context with elliptic problems having a Dirac source term has been investigated in a series of papers. In an early publication of Scott [98], it has been proved that the global L^2-error for

Model problem 4 exhibits the suboptimal asymptotic $\mathcal{O}\left(h^{2-\frac{d}{2}}\right)$, if $\Omega \subset \mathbb{R}^d$, $d \in \{2,3\}$, where h denotes the mesh size of the grid. Even more general right hand sides are considered in [17]. Similar results for parabolic problems with a homogeneous boundary condition on a smooth domain $\Omega \subset \mathbb{R}^d$, $d \in \{2,3\}$, where the source term is given by a measure $\mu \in [C(\Omega)]^*$ are provided in [101]. Interior point wise error estimates for a standard Finite element approximation of the Green's function are derived in [96, Theorem 6.1]. One of these estimates reveals that the L^∞-error exhibits an optimal convergence behavior on sub domains, having a fixed distance to the singularity and to the boundary of the computational domain.

The authors of [6] have shown that on a graded mesh linear Finite elements converge by $\mathcal{O}\left(h^2 \left|\ln h\right|^{\frac{3}{2}}\right)$. Graded meshes consist of triangles T whose diameter h_T are scaled by their distance r_T to the location of the Dirac measure $\mathbf{x_0}$ (see Figure 3.2):

$$h_T \approx \begin{cases} h^2 & \text{if } r_T = 0, \\ h\sqrt{r_T} & \text{if } r_T > 0. \end{cases}$$

Note that the number of elements of such a triangulation is in $\mathcal{O}\left(h^{-2}\right)$, see, e.g., [7]. Such meshes can be constructed via a coordinate transformation, [6] or by dyadic refinement [41] or a combination of both [72].

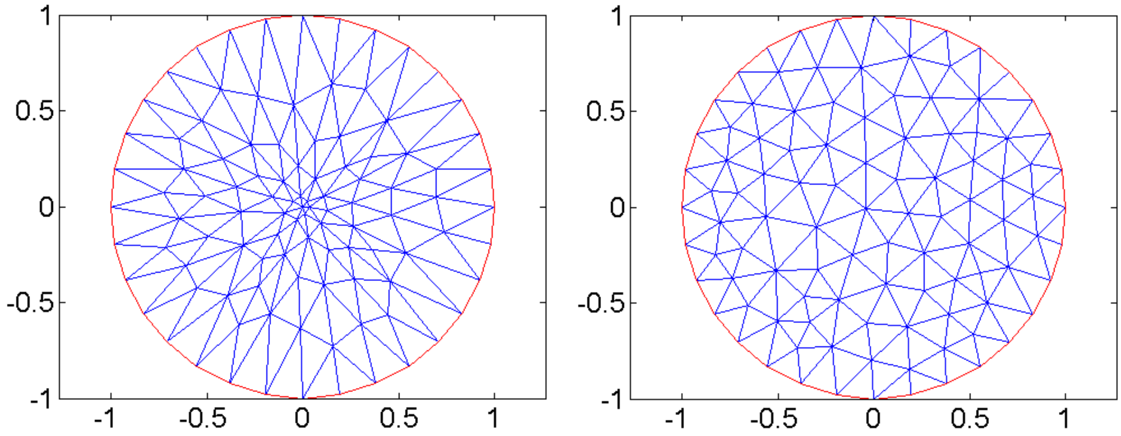

Figure 3.2: Quasi-Uniform mesh on an unit disk centered at $\mathbf{x_0} = (0,0)$ (right), graded mesh with respect to the point $\mathbf{x_0} = (0,0)$ on an unit disk (left)

Optimal a priori estimates for **Model problem 2-3** have been derived in [25]. Using graded meshes it is possible to prove that standard Finite element methods converge optimal with respect to weighted Sobolev norms.

On closer examination, one observes that the above publications are focused on global error estimates and adapted meshes. However in terms of **Model problem 1-2** the solution of the 3D problem within the network is of low interest since there the physical behavior is governed by the flow within the single fractures. In fact we are interested to provide an accurate solution in $\Omega \setminus V_R$ and on Γ_0^R (see (3.7)) to keep the errors for the average values $\bar{u}$ low. In order to meet these requirements, we have to ensure that the singularities associated to the Dirac measures do not pollute the numerical solution in $\Omega \setminus V_R$.

As a first test case, we consider **Model problem 4** on $\Omega = B_1(\mathbf{x_0})\,,\ \mathbf{x_0} = (0,0)^T$ (unit disk around $\mathbf{x_0}$) and report the L^2-error on $\Omega \setminus B_R(\mathbf{x_0})\,,\ R \in [0,1)$. For the numerical solution of the problem, we use linear finite elements. First of all one notes that the numerical error is concentrated in the vicinity of the singularity (see Figure 3.3). Thus it can be expected that the *local* L^2-error in $\Omega \setminus B_R(\mathbf{x_0})$ exhibits a better convergence rate than the *global* L^2-error in Ω. In Tables 3.1 and 3.2 we report the errors on uniform and graded meshes, where *non* abbreviates the term number of nodes and *eco* abbreviates the term numerical convergence order. It can be seen that the local L^2-errors for $R \in \{0.05, 0.1, 0.2, 0.3\}$ exhibit on both uniform and graded meshes optimal convergence orders. For $R = 0$ we have on uniform meshes an suboptimal convergence order, which is in agreement with the results proved by Scott [98]. On graded meshes we obtain for $R = 0$ an convergence order close to the optimal convergence order for linear finite elements. This observation confirms the results of [6].

Table 3.1: Local errors for uniform meshes.

non	$R = 0$	$R = 0.05$	$R = 0.1$	$R = 0.2$	$R = 0.3$
102	$1.04e-1$	$1.04e-1$	$4.79e-2$	$3.03e-2$	$2.04e-2$
380	$3.28e-2$	$2.69e-2$	$1.21e-2$	$5.36e-3$	$3.60e-3$
1425	$1.90e-2$	$6.41e-3$	$2.72e-3$	$1.43e-3$	$9.25e-4$
5505	$1.41e-2$	$1.91e-3$	$9.57e-4$	$4.60e-4$	$2.90e-4$
22373	$5.53e-3$	$3.48e-4$	$1.72e-4$	$8.60e-5$	$5.59e-5$
90158	$1.57e-3$	$6.27e-5$	$3.23e-5$	$1.81e-5$	$1.30e-5$
351649	$9.04e-4$	$2.07e-5$	$1.03e-5$	$5.06e-6$	$3.30e-6$
eco	**1.14**	**2.05**	**2.03**	**2.09**	**2.10**

Table 3.2: Local errors for graded meshes.

non	$R = 0$	$R = 0.05$	$R = 0.1$	$R = 0.2$	$R = 0.3$
102	$5.08e-2$	$4.07e-2$	$3.43e-2$	$3.07e-2$	$2.94e-2$
380	$1.23e-2$	$8.91e-3$	$8.09e-3$	$7.38e-3$	$6.92e-3$
1425	$3.53e-3$	$2.20e-3$	$1.97e-3$	$1.74e-3$	$1.62e-3$
5505	$1.09e-3$	$6.03e-4$	$5.39e-4$	$4.74e-4$	$4.41e-4$
22373	$2.84e-4$	$1.64e-4$	$1.31e-4$	$1.17e-4$	$1.08e-4$
90158	$6.14e-5$	$3.61e-5$	$3.27e-5$	$2.92e-5$	$2.71e-5$
351649	$1.92e-5$	$9.09e-6$	$8.22e-6$	$7.35e-6$	$6.83e-6$
eco	**1.90**	**2.02**	**2.00**	**2.01**	**2.01**

Motivated by these numerical results, we investigate in the following section standard Finite element techniques without a modification of the right hand side and without the usage of graded or adapted meshes. We show that no pollution effect for Delta point source terms occurs. For the lowest order case quasi-optimality and for higher order finite elements optimal order a priori estimates on a family of quasi-uniform meshes in a L^2-semi-norm can be recovered. The semi-norm is defined as a L^2-norm on a fixed sub domain which excludes the locations of the Delta source terms. In addition to that, we discuss alternative numerical solution techniques for **Model problem 1-3**, based on iterative approximation schemes. Contrary to the discretization technique discussed in [24][Chapter 5] this approach enables us to use meshes of different size for the 1D problem and the 3D problem.

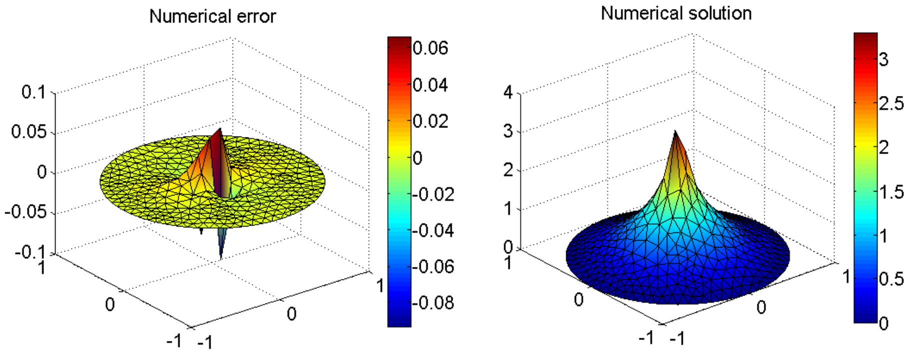

Figure 3.3: Point wise error of the finite element approximation for model problem 4 (left), numerical solution of model problem 4 (right)

Early work on the numerical solution of the Poisson equation with Delta terms on the right (**Model problem 4**) with Finite difference methods on uniformly structured meshes can be found in [95]. Here second order convergence can be recovered if a mesh-dependent smoothing kernel is applied to the source term. This results in a local modification of the right hand side and influences only a small and fixed number of entries. The analysis is then based on perturbation arguments and stability. Efficient multi-grid solvers for problems with singularities in the solution resulting from re-entrant corners, Delta source terms and heterogeneous coefficients are designed in [94]. The construction of suitable smoothing operators in terms of B-splines is investigated in [66] where also quite general distributions as right hand sides, such as, e.g., dipoles and quadrupoles, and alternative strategies, such as, e.g., boundary or domain modifications, are discussed. A combination of B-splines and numerical differentiation, τ-extrapolation and multi-grid strategies, see, e.g., [93], guarantees convergence up to order four and the efficiency of the numerical scheme.

3.2 Finite Element approximations for elliptic problems with Dirac source terms

3.2.1 Pollution effect

In order to prove that the singularities arising from Dirac point measures do not deteriorate the convergence behavior at a distance from the singularities, we consider an even more general Poisson problem than **Model problem 4** [64]:

$$\begin{aligned} -\Delta u &= f + 2\pi \sum_{i=0}^{N} q_i \delta_{x_i} \quad \text{in} \quad \Omega, \\ u &= 0 \quad \text{on} \quad \partial\Omega, \end{aligned} \tag{3.31}$$

where $\Omega \subset \mathbb{R}^d$, $d \in \{2,3\}$, is a bounded, open, convex and polyhedral domain, and δ_{x_i} denotes the Dirac measure concentrated at $x_i \in \Omega$, $i = 0, \ldots, N$. Moreover let $q_i \in \mathbb{R} \setminus \{0\}$, $i = 0, \ldots, N$, $x_i \neq x_j$, $0 \leq i < j \leq N$, and f be sufficiently smooth. Please note that the considerations presented in this subsection are taken from a former publication by the author [64]:

T. Köppl and B. Wohlmuth
Opt. a priori error estimates for an ell. problem with Dirac right-hand side
SINUM, 52(4), 1753-1769, 2014

Both (3.31) and **Model problem 4** form linear problems, such that the superposition principle for its solutions apply. Thus we focus on the discretization error resulting from the Dirac measure source terms. To do so, we study a simple model problem. We start by introducing Green's function $\hat{v}_0$ concentrated at x_0 [32]:

$$\hat{v}_0(x) = \begin{cases} -\ln(r(x)) & \text{for } d = 2, \\ \frac{1}{2 \cdot r(x)} & \text{for } d = 3. \end{cases} \tag{3.32}$$

The distance function r is given by: $r(x) = \|x - x_0\|$. Moreover we define a fixed cut-off function $\eta \in C^{\infty}(\Omega)$, having the properties:

$$\eta = 1 \text{ on } B,\ \eta = 0 \text{ on } \Omega \setminus \tilde{B} \text{ and } 0 \leq \eta \leq 1 \text{ on } \Omega.$$

The two subdomains B and $\tilde{B}$ are fixed open subdomains with $x_0 \in B \Subset \tilde{B} \Subset \Omega$. Defining $f_0 \in L^2(\Omega)$ by:

$$f_0 := -\left(2\nabla\eta \cdot \nabla\hat{v}_0 + \Delta\eta\hat{v}_0\right) \text{ in } \tilde{B} \setminus B,$$

the solution of the Dirac problem

$$-\Delta v = f_0 + 2\pi\eta\delta_{x_0} \quad \text{in } \Omega, \qquad v = 0 \quad \text{on } \partial\Omega, \tag{3.33}$$

is given by: $v = \eta \cdot \hat{v}_0$. A straightforward computation shows that $\hat{v}_0$ and v are no H^1-functions but that $\hat{v}_0, v \in W_0^{1,p}(\Omega)$, $p \in [1, 3 - d/2)$ holds. Therefore the term solution of (3.33) has to be defined in a careful way. Doing so, we follow an approach presented in [8, 96] and consider the solution v of (3.33) as an element of $W_0^{1,p}(\Omega)$, $p \in (1, 3 - \frac{d}{2})$. Defining our test space $W_0^{1,q}(\Omega)$ by:

$$W_0^{1,q}(\Omega) = \left\{ \varphi \in W^{1,q}(\Omega) \,|\, \varphi = 0 \text{ on } \partial\Omega \right\}, \ \frac{1}{p} + \frac{1}{q} = 1,$$

the weak formulation of (3.33) is given by: Find $v \in W_0^{1,p}(\Omega)$ such that

$$(\nabla v, \nabla \varphi) = (f_0, \varphi) + 2\pi \varphi(x_0) \quad \forall \varphi \in W_0^{1,q}(\Omega), \tag{3.34}$$

where $(\cdot, \cdot)$ stands for the duality pairing of $L^p(\Omega)$ and $L^q(\Omega)$. The right-hand side in (3.34) is well defined, because we have for $d \in \{2, 3\}$ and $p \in (1, 3 - \frac{d}{2})$ the continuous embedding: $W^{1,q}(\Omega) \hookrightarrow C(\Omega)$ [1, Chapter 4, Theorem 4.12]. Moreover the weak formulation (3.34) has a unique solution (see [10, Theorem 2.1]) for $p \in (1, 3 - d/2)$. Here we fix from now on $p = \frac{7}{5}$, the choice is somehow arbitrary, but guarantees that $H^2(\Omega) \subset W^{1,q}(\Omega)$, $q = \frac{7}{2}$. For the numerical solution, we introduce a family of quasi-uniform simplicial triangulations $\mathcal{T}_h$ of Ω, where h is the mesh size. The Finite element space is then defined by standard conforming elements:

$$V_h^k = \left\{ \varphi_h \in H_0^1(\Omega) \,|\, \varphi_h|_K \in \mathcal{P}_k(K), \ \forall K \in \mathcal{T}_h \right\}.$$

$\mathcal{P}_k(K)$ denotes the space of polynomials on K of degree at most k. The Finite element solution $v_h \in V_h^k$ of (3.33) satisfies:

$$(\nabla v_h, \nabla \varphi_h) = (f_0, \varphi_h) + 2\pi \varphi_h(x_0) \quad \forall \varphi_h \in V_h^k. \tag{3.35}$$

This Finite element formulation is well defined because $V_h^k \subset W_0^{1,q}(\Omega)$ holds. The rest of this section is mostly concerned with the proof of the following theorem.

Theorem 3.1. *Let $v \in W_0^{1,p}(\Omega)$ be the weak solution of (3.34) and let $v_h \in V_h^k$ be the finite element approximation given by (3.35). Then we have for the L^2-error $\|v - v_h\|_{L^2(\Omega \setminus B)}$ the following upper bound:*

$$\|v - v_h\|_{L^2(\Omega\setminus B)} \lesssim \begin{cases} h^2 \left|\ln h\right|, & \text{if } k = 1, \\ h^{k+1}, & \text{if } k > 1. \end{cases} \tag{3.36}$$

Here we use the inequality sign $\lesssim$, if we want to omit a generic constant on the right hand side independent of h, but possibly depending on $\operatorname{dist}(x_0, \partial B)$, $\operatorname{dist}(B, \partial\Omega)$, the solution and the order k of the finite element approximation. The relative position of x_0 with respect to the vertices of the mesh does not play a role, and Theorem 3.1 holds for any $x_0 \in B$, $\operatorname{dist}(x_0, \partial B) > 0$.

A similar result can be proved using the bounds presented in [96, Theorem 6.1]. Based on interior maximum norm estimates, point wise error estimates for the numerical approximation of Green's function are derived. As a consequence of these results, one can prove for the finite element error e_h of a Dirac problem with homogeneous Neumann boundary conditions the following estimates:

$$|e_h| \lesssim \begin{cases} h^2 \left|\ln h\right|, & \text{if } k = 1, \\ h^{k+1}, & \text{if } k > 1. \end{cases}$$

for all $x \in \Omega_1 \setminus \overline{B_R\left(x_0\right)}$, where Ω_1 is a open domain such that $B_R\left(x_0\right) \Subset \Omega_1 \Subset \Omega$. Since this estimate only holds in the interior, we cannot directly apply this result to obtain (3.36).

Corollary 3.1. *Let $u \in W_0^{1,p}(\Omega)$ be the weak solution of* (3.31) *and $u_h \in V_h^k$ its finite element approximation. Under the assumption, that $f \in H^{k-1}\left(\Omega\right)$ and $u \in H^{k+1}\left(\Omega \setminus \overline{B}\right)$, we have for $x_i \in B, i = 0, \ldots, N$:*

$$\|u - u_h\|_{L^2(\Omega\setminus B)} \lesssim \begin{cases} h^2 \left|\ln h\right|, & \textit{if } k = 1, \\ h^{k+1}, & \textit{if } k > 1. \end{cases}$$

The proof is a simple consequence of the superposition principle, interior regularity results [116] and the regularity assumption on u on $\Omega \setminus \overline{B}$. We note that our convexity assumption on Ω guarantees that $u \in H^2\left(\Omega \setminus \overline{B}\right)$ but higher regularity is not guaranteed from the smoothness of the right hand side f. In the case of a reduced regularity of u, it steems from the corners of the domain and can be compensated, e.g., by energy corrected finite element methods [30]. Higher order estimates on smooth domains require the use of non–affine element mappings and will be not considered here.

Outline of the proof

Now we present an outline of the proof for Theorem 3.1. The a priori result (3.36) is proved by induction with respect to the approximation order k. From now on B_s stands for a ball centered at x_0 having $s > 0$ as radius. We introduce a sequence of nested concentric balls B_{r_l}, $l = 0, \ldots, k$, with:

$$0 < r_{l-1} < r_l, \quad r_l - r_{l-1} = \mathcal{O}(1), \quad l = 1, \ldots, k$$

and $B_{r_k} \subset B$. Setting $r_l' = (r_l + r_{l-1})/2$, $l = 0, \ldots, k$, with $r_{-1} = 0$, we obtain the following sequence of non-empty properly nested sub domains

$$B_{r_0'} \subset B_{r_0} \subset B_{r_1'} \subset B_{r_1} \subset \ldots \subset B_{r_k'} \subset B_{r_k} \subset B.$$

On each ball B_{r_l} suitable bounds for the L^2-errors: $\|v - v_h\|_{L^2\left(\Omega\setminus B_{r_l}\right)}$ are derived. To do so, we define for $l = 0, \ldots, k$ a dual problem for the Poisson equation (3.33) and its Finite element approximation $v_h \in V_h^k$ as follows:

$$\begin{aligned} -\Delta w_l &= e\mathcal{X}_{\Omega\setminus B_{r_l}} && \text{in} \quad \Omega, \\ w_l &= 0 && \text{on} \quad \partial\Omega, \end{aligned} \tag{3.37}$$

where $\mathcal{X}_{\Omega\setminus B_{r_l}}$ is the characteristic function of $\Omega \setminus B_{r_l}$ and $e = v - v_h$. It is obvious that $e\mathcal{X}_{\Omega\setminus B_{r_l}} \in L^{\frac{7}{2}}(\Omega) \subset L^2(\Omega)$ holds. Then the assumed convexity of Ω yields $w_l \in H^2(\Omega) \cap H_0^1(\Omega)$ see, e.g., [43, Chapter 8]. By a Sobolev embedding [1, Theorem 4.12] it follows that $w_l \in W^{1,\frac{7}{2}}(\Omega)$. The weak formulation of (3.37) now reads as: Find $w_l \in W_0^{1,\frac{7}{2}}(\Omega)$

$$(\nabla\phi, \nabla w_l) = \left(\phi, e\mathcal{X}_{\Omega\setminus B_{r_l}}\right) \quad \forall\phi \in W_0^{1,\frac{7}{5}}(\Omega) \tag{3.38}$$

and is well defined. Due to an interior regularity result [32, Chapter 2.2, Theorem 7], we have $w_l \in W^{1,\infty}\left(B_{r_l'}\right)$. For $\phi = e$ in (3.38), we can write the square of the L^2-error as follows:

$$\begin{aligned}\|v - v_h\|^2_{L^2\left(\Omega\setminus B_{r_l}\right)} &= \left(\nabla(v - v_h), \nabla w_l\right) = \left(\nabla(v - v_h), \nabla(w_l - S_h w_l)\right)\\ &= \left(\nabla(v - v_h), \nabla(w_l - S_h w_l)\right)_{\Omega\setminus B_{r_l'}} + \left(\nabla(v - v_h), \nabla(w_l - S_h w_l)\right)_{B_{r_l'}},\end{aligned} \tag{3.39}$$

where S_h is a suitable interpolation operator onto V_h^k which will be specified later. We apply to both terms on the right the Hölder inequality yielding the following bounds:

$$\begin{aligned}&\left(\nabla(v - v_h), \nabla(w_l - S_h w_l)\right)_{\Omega\setminus B_{r_l'}}\\ &\qquad\qquad \le \|\nabla(v - v_h)\|_{L^2\left(\Omega\setminus B_{r_l'}\right)} \|\nabla(w_l - S_h w_l)\|_{L^2\left(\Omega\setminus B_{r_l'}\right)},\end{aligned} \tag{3.40}$$

$$\left(\nabla(v - v_h), \nabla(w_l - S_h w_l)\right)_{B_{r_l'}} \le \|\nabla(v - v_h)\|_{L^1\left(B_{r_l'}\right)} \|\nabla(w_l - S_h w_l)\|_{L^\infty\left(B_{r_l'}\right)}. \tag{3.41}$$

From (3.40) and (3.41) it follows that we have to derive suitable upper bounds of the four error terms occurring on the right. The upper bounds for the four terms will be provided in Lemmas 3.3, 3.5, 3.6 and 3.10, respectively.

Auxiliary results

Next several technical results are provided which are important ingredients for the proof of Theorem 3.1.

Properties of the fundamental solution

The upper bounds for the four terms on the right of (3.40) and (3.41) depend crucially on the properties of the weighted fundamental solution $v = \eta\hat{v}_0$, solving (3.34). These properties play also an important role in the L^∞-analysis of finite elements, see, e.g., [96]. We recall that $v \in C^\infty(\Omega \setminus B_{ch})$ for all $c \in \mathbb{N}$ and that $\nabla v \in L^1(\Omega)$ but not in $L^2(\Omega)$.

Lemma 3.1. *Let v be the solution of* (3.34)*, then we have for $c \in \mathbb{N}$ and $0 < \epsilon < 1$ fixed, the following L^1 and L^2-estimates. β denotes an index vector.*

Upper bounds for the gradient restricted to B_{ch}:

$$\begin{aligned} \|\nabla v\|_{L^1(B_{ch})} &\lesssim h, && (3.42a)\\ \left\|r^{1-\epsilon}\nabla v\right\|_{L^2(B_{ch})} &\lesssim h^{1-\epsilon},\ d=2, && (3.42b)\\ \|r\nabla v\|_{L^2(B_{ch})} &\lesssim \sqrt{h},\ d=3. && (3.42c) \end{aligned}$$

Upper bounds for second derivatives restricted to $\Omega \setminus B_{ch}$:

$$\begin{aligned} \|v\|_{W^{2,1}(\Omega\setminus B_{ch})} &\lesssim |\ln h|, && (3.43a)\\ \left\|r^{\frac{d-1}{2}}D^\beta v\right\|_{L^2(\Omega\setminus B_{ch})} &\lesssim \frac{1}{\sqrt{h}},\ |\beta|=2 && (3.43b)\\ \left\|r^{\frac{d}{2}}D^\beta v\right\|_{L^2(\Omega\setminus B_{ch})} &\lesssim \sqrt{|\ln h|},\ |\beta|=2. && (3.43c) \end{aligned}$$

Upper bounds for third derivatives restricted to $\Omega \setminus B_{ch}$:

$$\begin{aligned} \|v\|_{W^{3,1}(\Omega\setminus B_{ch})} &\lesssim \frac{1}{h}, && (3.44a)\\ \left\|r^{\frac{d}{2}+\epsilon}D^\beta v\right\|_{L^2(\Omega\setminus B_{ch})} &\lesssim h^{\epsilon-1},\ |\beta|=3. && (3.44b) \end{aligned}$$

Proof. We consider only (3.42a), the remaining estimates are left to the reader. Without loss of generality, we assume that ch is sufficiently small such that $\eta = 1$ holds on B_{ch} which yields together with (3.32):

$$\|\nabla v\|_{L^1(B_{ch})} \lesssim \int_0^{ch} \frac{1}{r^{d-1}} r^{d-1}\, dr \lesssim h.$$

The estimates involving derivates can be easily verified, by taking the following upper bound into account:

$$\left|D^\beta v\right| \lesssim r^{2-d-|\beta|}, \quad \text{for} \quad |\beta| \geq 1.$$

□

Lemma 3.1 shows that the space dimension d does not enter into the L^1-bounds whereas the L^2-bounds do depend on d. In addition to the bounds on v, we need an upper bound for the discretization error in the L^2-norm. We refer to [98, Theorem 1] for a proof of the following result.

Lemma 3.2. *Let $v \in W_0^{1,p}(\Omega)$ be the solution of* (3.34) *and $v_h \in V_h^k$ its finite element approximation given by* (3.35)*, then we have for the global L^2-discretization error:*

$$\|v - v_h\|_{L^2(\Omega)} \lesssim h^{2-\frac{d}{2}}.$$

Lemma 3.2 shows that globally, we can only expect an error decay of $\mathcal{O}(\sqrt{h})$ for $d = 3$ and of $\mathcal{O}(h)$ for $d = 2$ independently of t the used polynomial order k. The proof given in [98] relies on suitably weighted Sobolov spaces, see also, e.g., [59, 74].

Interpolation errors

Considering the outline of the proof, we have to specify the interpolation operator:

$$S_h : W^{n,p}(\Omega) \to V_h^k.$$

Due to its local stability and approximation properties, we choose an operator of Scott–Zhang type [99, Theorem 4.1, Corollary 4.1]. In the following, we recall some of its properties. Note that this operator is well defined, if the parameters n and p satisfy the following conditions:

$$n \geq 1 \text{ and } p \in [1, \infty].$$

Lemma 3.3. *For $z \in W^{n,p}(\Omega)$ and $\rho > 0$ fixed, we have the following local upper bound for the approximation error:*

$$\|z - S_h z\|_{W^{m,p}(B_\rho)} \lesssim h^{n-m} |z|_{W^{n,p}(B_{\rho+2h})}, \; 0 \leq m \leq n, \; 1 \leq n \leq k+1, \tag{3.45a}$$

and the stability estimate:

$$\|S_h z\|_{W^{n,p}(B_\rho)} \lesssim \|z\|_{W^{n,p}(B_{\rho+2h})}, \; 0 \leq n \leq k+1. \tag{3.45b}$$

If $z \in W^{n,p}(\Omega \setminus B_{\rho-2h})$, we have the approximation bound:

$$\|z - S_h z\|_{W^{m,p}(\Omega\setminus B_\rho)} \lesssim h^{n-m} |z|_{W^{n,p}\left(\Omega\setminus B_{\rho-2h}\right)}, \; 0 \leq m \leq n, \; 1 \leq n \leq k+1. \tag{3.45c}$$

Lemma 3.3 provides interpolation results for S_h in $W^{m,p}$-norms. In addition to that, we need interpolation bounds for weighted L^2-norms.

Lemma 3.4. *Let $c, c^* \in \mathbb{N}$ and $c - c^* \geq 2$. Then we have for $z \in W^{k+1,2}(\Omega \setminus B_{c^*h})$, the following estimate for $\alpha \in [0.5, 2.0]$ fixed:*

$$\|r^\alpha \nabla (z - S_h z)\|_{L^2(\Omega\setminus B_{ch})} \lesssim h^l \sum_{|\beta|=l+1} \left\| r^\alpha D^\beta z \right\|_{L^2(\Omega\setminus B_{c^*h})}, \quad l \in \{1, \ldots, k\}.$$

Proof. Replacing S_h by the nodal Lagrange interpolation operator, the proof of the approximation error in the weighted L^2-norm can be found in [24, Theorem 3.2]. It also applies to locally defined operators, such as S_h, having local stability and approximation properties in standard norms. Of crucial importance is the observation that for each $K \in \mathcal{T}_h$ with $K \cap (\Omega \setminus B_{ch}) \neq \emptyset$ and $c \geq 3$ the ratio $\sup_{x\in\omega_K} r(x) / \inf_{x\in\omega_K} r(x)$ is uniformly bounded. Here ω_K is the smallest union of elements in $\mathcal{T}_h$ such that $S_h z|_K$ depends only on $z|_{\omega_K}$. □

In (3.40), it is sufficient that the interpolation error $\|\nabla(w_l - S_h w_l)\|_{L^2(\Omega\setminus B_{r_l'})}$ yields an order h bound. This follows directly from Lemma 3.3. In (3.41), the interpolation error $\|\nabla(w_l - S_h w_l)\|_{L^\infty(B_{r_l'})}$ has to bring in an order h^k. This can be achieved in terms of interior regularity arguments.

Lemma 3.5. *Let w_l be the solution of (3.38) for B_{r_l} and assume that $4h < r_l - r_l'$. Then we have the following estimate:*

$$\|\nabla (w_l - S_h w_l)\|_{L^\infty\left(B_{r_l'}\right)} \lesssim h^k \|v - v_h\|_{L^2\left(\Omega\setminus B_{r_l}\right)}.$$

Proof. Using the approximation property of S_h and the Sobolev embedding $W^{k+3,2}\left(B_{r_l'+2h}\right) \hookrightarrow W^{k+1,\infty}\left(B_{r_l'+2h}\right)$ [1, Theorem 4.12], we have:

$$\|\nabla (w_l - S_h w_l)\|_{L^\infty\left(B_{r_l'}\right)} \lesssim h^k |w_l|_{W^{k+1,\infty}\left(B_{r_l'+2h}\right)} \lesssim h^k \|w_l\|_{W^{k+3,2}\left(B_{r_l'+2h}\right)}.$$

An interior regularity result [43, Theorem 8.10], the H^2-regularity of w_l and the fact that w_l is harmonic within the ball B_{r_l} yields:

$$\|w_l\|_{W^{k+3,2}\left(B_{r_l'+2h}\right)} \lesssim \|w_l\|_{W^{1,2}\left(B_{r_l}\right)} \lesssim \|v - v_h\|_{L^2\left(\Omega\setminus B_{r_l}\right)}$$

which completes the proof. □

Upper bounds for the Finite element solution

In the previous section, we provided estimates for the interpolation errors in (3.40) and (3.41). It still remains to estimate the terms in $\nabla(v - v_h)$. The L^2-norm on $\Omega \setminus B_{r_l'}$ can be easily bounded by Wahlbin type arguments, see, e.g., [87, 116, 117].

Lemma 3.6. *Let $v \in W^{k+1,2}\left(\Omega\setminus B_{r_0'}\right)$ be defined by (3.34) and let $v_h \in V_h^k$ defined by (3.35), then it holds for $l = 1, \dots, k$:*

$$\|\nabla (v - v_h)\|_{L^2\left(\Omega\setminus B_{r_l'}\right)} \lesssim h^k + \|v - v_h\|_{L^2\left(\Omega\setminus B_{r_{l-1}}\right)}, \tag{3.46}$$

where k denotes the polynomial order of the Finite element approximation v_h.

Proof. The proof is based on a local a priori estimate of Wahlbin type [116, Chapter III, Theorem 9.1]:

$$\|\nabla (v - v_h)\|_{L^2\left(\Omega\setminus B_{r_l'}\right)} \lesssim \|v - S_h v\|_{H^1\left(\Omega\setminus B_{r_{l-1}}\right)} + \frac{1}{r_l' - r_{l-1}} \|v - v_h\|_{L^2\left(\Omega\setminus B_{r_{l-1}}\right)}.$$

Originally it is stated for solutions in $H^1(\Omega)$ and its Galerkin approximations. However, it can be easily extended to our settings, i.e., $H^1\left(\Omega\setminus B_{r_0'}\right)$. The approximation result (3.45c) and $r_l' - r_{l-1} = \mathcal{O}(1)$ yield (3.46). □

We note that the regularity requirement $v \in H^{k+1}\left(\Omega \setminus B_{r_{l-1}}\right)$ in the proof of Lemma 3.6 is fulfilled by the solution v of the auxiliary problem (3.33).

In the rest of this section, we focus on the L^1-error term. The main result will be provided in Lemma 3.10. We start with a global bound. The triangle inequality trivially yields:

$$\left\|\nabla\left(v-v_h\right)\right\|_{L^1(\Omega)} \lesssim \left\|\nabla\left(v-S_h v\right)\right\|_{L^1(\Omega)} + \left\|\nabla\left(S_h v-v_h\right)\right\|_{L^1(\Omega)}. \tag{3.47}$$

The first summand can be directly bounded by the approximation properties of S_h which is done in the next lemma.

Lemma 3.7. *Let $v \in W_0^{1,p}(\Omega)$ be defined by (3.34), then we have the following estimate:*

$$\left\|\nabla\left(v-S_h v\right)\right\|_{L^1(\Omega)} \lesssim \begin{cases} h\left|\ln h\right|, & \text{if } k=1, \\ h, & \text{if } k>1, \end{cases}$$

where k denotes the polynomial order of the finite element approximation.

Proof. We decompose Ω into B_{ch} and $\Omega \setminus B_{ch}$, $c \geq 3$, and have:

$$\left\|\nabla\left(v-S_h v\right)\right\|_{L^1(\Omega)} = \left\|\nabla\left(v-S_h v\right)\right\|_{L^1(B_{ch})} + \left\|\nabla\left(v-S_h v\right)\right\|_{L^1(\Omega\setminus B_{ch})}.$$

The local stability (3.45b) of S_h in combination with the local bound (3.42a) yields that the first summand is bounded by $\mathcal{O}(h)$ independently of k. The bound for the second term on the right depends on k. Setting in (3.45a) $p=1$, $m=1$ and $n=2$ and $n=3$ for $k=1$ and $k>1$, respectively, we find the required bound by using (3.43a) and (3.44a), respectively. $\square$

Before we can bound the second term on the right of (3.47), we have to provide two technical results on weighted L^2-norms. Firstly, we consider a negative exponent in the weighting factor and restrict ourselves to $d=2$.

Lemma 3.8. *Let $v \in W_0^{1,p}(\Omega)$ be defined by (3.34) and let $v_h \in V_h^k$ defined by (3.35). Then we have for $d=2$ and for $0<\epsilon<1$ fixed:*

$$\left\|r^{-\epsilon}\left(v-v_h\right)\right\|_{L^2(\Omega)} \lesssim h^{1-\epsilon}.$$

Proof. The main ingredient for the proof is the local bound

$$\left\|r^{-\epsilon} w\right\|_{L^2(B_{ch})} \lesssim \left\|r^{1-\epsilon}\nabla w\right\|_{L^2(B_{ch})} + h^{-\epsilon}\left\|w\right\|_{L^2(B_{ch})}, \quad r^{-\epsilon} w, r^{1-\epsilon}\nabla w \in L^2(\Omega), \tag{3.48}$$

which follows from [79, Lemma A.1.7] and a scaling argument. We decompose Ω in $\Omega \setminus B_{ch}$ and B_{ch}, where c is sufficiently large, and note that $r^{-\epsilon}$ restricted to $\Omega \setminus B_{ch}$ is bounded by $h^{-\epsilon}$. Applying (3.48) to $w = v - v_h$, we get

$$\left\|r^{-\epsilon}\left(v-v_h\right)\right\|_{L^2(\Omega)} \lesssim \left\|r^{1-\epsilon}\nabla\left(v-v_h\right)\right\|_{L^2(B_{ch})} + h^{-\epsilon}\left\|v-v_h\right\|_{L^2(\Omega)}.$$

For the first term, we apply the triangle inequality twice and use the local stability of S_h with respect to different norms. We recall that we have local L^1-stability of $\nabla S_h v$, then (3.42a) guarantees for $d = 2$

$$\left\|r^{1-\epsilon}\nabla S_h v\right\|_{L^2(B_{ch})} \lesssim h^{1-\epsilon}h^{-1}\left\|\nabla S_h v\right\|_{L^1(B_{ch})} \lesssim h^{-\epsilon}\left\|\nabla v\right\|_{L^1\left(B_{(c+2)h}\right)} \lesssim h^{1-\epsilon}.$$

Using this observation in combination with (3.42b) and the local L^2-stability of S_h, we find in terms of Lemma 3.2

$$\begin{aligned}\left\|r^{-\epsilon}\left(v-v_h\right)\right\|_{L^2(\Omega)} &\lesssim h^{1-\epsilon}+h^{1-\epsilon}h^{-1}\|S_h(v-v_h)\|_{L^2(B_{ch})}+h^{-\epsilon}\left\|v-v_h\right\|_{L^2(\Omega)}\\ &\lesssim h^{1-\epsilon}+h^{-\epsilon}\left\|v-v_h\right\|_{L^2(\Omega)} \lesssim h^{1-\epsilon}.\end{aligned}$$

□

Secondly we consider a positive exponent in the weighting factor depending on the space dimension. A crucial role for the proof of the next two lemmas play weighted Wahlbin type estimates. We refer to [116, Chapter III, Theorem 9.1] for more details and point out that although $v \notin H^1(\Omega)$, we can conclude that for suitable $c_2 < c_1$ large enough and $\alpha \in [(d-1)/2, (d+1)/2)$ fixed:

$$\left\|r^{\alpha}\nabla\left(v-v_h\right)\right\|_{L^2\left(\Omega\setminus B_{c_1 h}\right)} \lesssim \left\|r^{\alpha}\nabla\left(v-S_h v\right)\right\|_{L^2\left(\Omega\setminus B_{c_2 h}\right)}+\left\|r^{\alpha-1}\left(v-v_h\right)\right\|_{L^2(\Omega)}. \tag{3.49}$$

This estimate can be established from standard Wahlbin estimates by using a sequence of dyadic balls. Each ring between two dyadic balls is again covered by some suitable chosen balls. The weighted error estimate on each of this second type of balls can be carried out like the estimate in Lemma 3.4, making use of the standard estimate in [116, Chapter III, Theorem 9.1]. Due to the dyadic scaling of the balls, the sum of all weighted errors is bounded by the right hand side of (3.49). Weighted Wahlbin estimates like (3.49) can also be found in [80].

Lemma 3.9. *Let $v \in W_0^{1,p}(\Omega)$ be defined by (3.34) and let $v_h \in V_h^k$ its finite element approximation. Then we have for $0 \le \epsilon < \frac{1}{2}$ fixed:*

$$\left\|r^{\frac{d}{2}+\epsilon-1}\left(v-v_h\right)\right\|_{L^2(\Omega)} \lesssim h^{1+\epsilon}.$$

Proof. We define a sequence of dyadic concentric balls B_{ρ_l}, $\rho_l = 2^l(ch)$, $l \in \mathbb{N}_0$, covering the domain Ω and fix $c \in \mathbb{N}$ sufficiently large. Then we have:

$$\begin{aligned}\left\|r^{\frac{d}{2}+\epsilon-1}\left(v-v_h\right)\right\|^2_{L^2(\Omega)} &= \sum_{l\geq 1}\left\|r^{\frac{d}{2}+\epsilon-1}\left(v-v_h\right)\right\|^2_{L^2(\Omega\cap S_l)}\\ &\quad+\left\|r^{\frac{d}{2}+\epsilon-1}\left(v-v_h\right)\right\|^2_{L^2\left(B_{\rho_0}\right)},\end{aligned} \tag{3.50}$$

where $S_l = B_{\rho_l} \setminus B_{\rho_{l-1}}$. In terms of $\rho_0 \in \mathcal{O}(h)$ and Lemma 3.2, we have:

$$\left\|r^{\frac{d}{2}+\epsilon-1}\left(v-v_h\right)\right\|^2_{L^2\left(B_{\rho_0}\right)} \lesssim h^{2(1+\epsilon)}. \tag{3.51}$$

Associated with each l, we define a dual problem:

$$-\Delta z_l = \mathcal{X}_l\left(v - v_h\right), \text{ where } \mathcal{X}_l = \begin{cases} 1 \text{ on } S_l, \\ 0 \text{ otherwise.} \end{cases}$$

By the Hölder inequality, we have:

$$\begin{aligned} \left\|\mathcal{X}_l\left(v-v_h\right)\right\|_{L^2(\Omega)}^2 &\leq \left(\mathcal{X}_l\left(v-v_h\right), v-v_h\right) \lesssim \left(-\Delta z_l, v-v_h\right) \\ &\lesssim \left\|r^{-\frac{d-1}{2}} \nabla\left(z_l - S_h z_l\right)\right\|_{L^2(\Omega)} \left\|r^{\frac{d-1}{2}} \nabla\left(v-v_h\right)\right\|_{L^2(\Omega)}. \end{aligned} \tag{3.52}$$

As we will see the second factor on the right can be bounded by $\mathcal{O}(\sqrt{h})$. We use the weighted Wahlbin estimate (3.49) for $\alpha = (d-1)/2$. Applying Lemma 3.4 and (3.43b) for the first term on the right in (3.49), Lemma 3.3 if $d = 3$ and Lemma 3.8 if $d = 2$ for the second term, we get

$$\begin{aligned} \left\|r^{\frac{d-1}{2}} \nabla\left(v-v_h\right)\right\|_{L^2(\Omega)} &\lesssim \sqrt{h} + \left\|r^{\frac{d-1}{2}} \nabla v\right\|_{L^2\left(B_{c_1 h}\right)} \\ &+ \left\|r^{\frac{d-1}{2}} \nabla S_h v\right\|_{L^2\left(B_{c_1 h}\right)} + \left\|r^{\frac{d-1}{2}} \nabla\left(S_h v - v_h\right)\right\|_{L^2\left(B_{c_1 h}\right)}. \end{aligned}$$

Using (3.42c), the same arguments as in the proof of Lemma 3.8 for the term in $\nabla S_h v$ and an inverse estimate in combination with Lemma 3.2, we get that all terms on the right are bounded by $\mathcal{O}(\sqrt{h})$, and thus (3.52) simplifies to:

$$\left\|\mathcal{X}_l\left(v-v_h\right)\right\|_{L^2(\Omega)}^2 \lesssim \sqrt{h} \left\|r^{-\frac{d-1}{2}} \nabla\left(z_l - S_h z_l\right)\right\|_{L^2(\Omega)}. \tag{3.53}$$

The $L^2(\Omega)$-norm of $r^{-\frac{d-1}{2}} \nabla\left(z_l - S_h z_l\right)$ will be decomposed into two terms. The first one is associated with $B_{\rho_{l-2}}$, $\rho_{-1} = \rho_0/2$, and we exploit that z_l is harmonic on $B_{\rho_{l-1}}$. Using the Hölder inequality and the approximation property (3.45a) we have:

$$\begin{aligned} \left\|r^{-\frac{d-1}{2}} \nabla\left(z_l - S_h z_l\right)\right\|_{L^2\left(B_{\rho_{l-2}}\right)} &\lesssim \left\|r^{-d+1}\right\|_{L^1\left(B_{\rho_{l-2}}\right)}^{\frac{1}{2}} \left\|\nabla\left(z_l - S_h z_l\right)\right\|_{L^\infty\left(B_{\rho_{l-2}}\right)} \\ &\lesssim h\sqrt{\rho_{l-2}} \left\|z_l\right\|_{W^{2,\infty}\left(B_{\rho_{l-1}}\right)}. \end{aligned}$$

An interior regularity result for harmonic functions (see, e.g., [32, Chapter 2.2, Theorem 7]) in combination with a scaling argument and the H^2-regularity of z_l, we get:

$$\left\|r^{-\frac{d-1}{2}} \nabla\left(z_l - S_h z_l\right)\right\|_{L^2\left(B_{\rho_{l-2}}\right)} \lesssim h\rho_{l-2}^{\frac{1-d}{2}} \left\|\mathcal{X}_l(v-v_h)\right\|_{L^2(\Omega)}.$$

The bound for the second term relies on the H^2-regularity and a trivial bound for $r^{\frac{1-d}{2}}$ on $\Omega \setminus B_{\rho_{l-2}}$

$$\left\|r^{-\frac{d-1}{2}} \nabla\left(z_l - S_h z_l\right)\right\|_{L^2\left(\Omega\setminus B_{\rho_{l-2}}\right)} \lesssim h\rho_{l-2}^{\frac{1-d}{2}} \left\|\mathcal{X}_l(v-v_h)\right\|_{L^2(\Omega)}.$$

Now (3.53) results in the upper estimate

$$\left\|\mathcal{X}_l \left(v - v_h\right)\right\|_{L^2(\Omega)} \lesssim h^{\frac{3}{2}} \rho_{l-2}^{\frac{1-d}{2}}.$$

Observing $\sum_{l \geq 0} \frac{1}{\left(2^{1-2\epsilon}\right)^l} \lesssim 1$, we have using (3.50) and (3.51):

$$\left\| r^{\frac{d}{2}+\epsilon-1} \left(v - v_h\right)\right\|^2_{L^2(\Omega)} \lesssim \sum_{l \geq 1} \frac{h^3}{\rho_{l-2}^{1-2\epsilon}} + h^{2(1+\epsilon)} \lesssim h^{2(1+\epsilon)} \sum_{l \geq 0} \frac{1}{\left(2^{1-2\epsilon}\right)^l} \lesssim h^{2(1+\epsilon)}.$$

□

By means of Lemma 3.9, we are now able to prove an upper bound of the gradient error $\left\|\nabla \left(v - v_h\right)\right\|_{L^1(\Omega)}$.

Lemma 3.10. *Let $v \in W_0^{1,p}(\Omega)$ be the solution of (3.34) and let $v_h \in V_h^k$ be its finite element approximation. Then we have the following estimate:*

$$\left\|\nabla \left(v - v_h\right)\right\|_{L^1(\Omega)} \lesssim \begin{cases} h\left|\ln h\right|, & \text{if } k = 1, \\ h, & \text{if } k > 1. \end{cases}$$

Proof. Lemma 3.7 and the triangle inequality (3.47) show that it is sufficient to study the term $\left\|\nabla \left(S_h v - v_h\right)\right\|_{L^1(\Omega)}$. As before we decompose Ω. Applying the Cauchy–Schwarz inequality, an inverse estimate and the local L^2-stability of S_h, Lemma 3.2 guarantees that the local $L^1\left(B_{ch}\right)$ norm is bounded by h. Thus it remains to consider the term restricted to $\Omega \setminus B_{ch}$. The Hölder inequality and the stability of S_h give for $0 \leq \epsilon < \frac{1}{2}$:

$$\begin{aligned} \left\|\nabla \left(S_h v - v_h\right)\right\|_{L^1(\Omega\setminus B_{ch})} &\lesssim \left\| r^{-\frac{d}{2}-\epsilon} r^{\frac{d}{2}+\epsilon} \nabla \left(v - v_h\right)\right\|_{L^1(\Omega\setminus B_{ch})} \\ &\lesssim \xi_\epsilon(h) \left\| r^{\frac{d}{2}+\epsilon} \nabla \left(v - v_h\right)\right\|_{L^2(\Omega\setminus B_{ch})}, \end{aligned}$$

where:

$$\xi_\epsilon(h) \lesssim \begin{cases} \sqrt{\left|\ln h\right|}, & \text{if } \epsilon = 0, \\ h^{-\epsilon}, & \text{if } 0 < \epsilon < \frac{1}{2}. \end{cases}$$

In order to derive an upper bound for the weighted error $\left\| r^{\frac{d}{2}+\epsilon} \nabla \left(v - v_h\right)\right\|_{L^2(\Omega\setminus B_{ch})}$, we recall the weighted bound (3.49) and set $\alpha = d/2 + \epsilon < (d+1)/2$. For $k = 1$, we set $\epsilon = 0$ and apply Lemma 3.4 for $l = 1$ in combination with (3.43c) and Lemma 3.9. For $k > 1$ we fix $0 < \epsilon < \frac{1}{2}$ and use Lemma 3.4 for $l = 2$ in combination with (3.44b) and Lemma 3.9. □

Proof of the main result

Considering the outline of the proof, we are now able to prove our main result formulated in Theorem 3.1 by the help of the auxiliary results which are given in the previous subsection.

The idea of the proof is to show Theorem 3.1 by induction. Due to (3.39), it remains to estimate the four terms on the right of (3.40) and (3.41). By Lemmas 3.5, 3.6, 3.10 and (3.45c) for $m = 1, n = 2, p = 2$, we find for the L^2-error restricted to $\Omega \setminus B_{r_l}$ a recursive structure:

$$\|v - v_h\|_{L^2(\Omega\setminus B_{r_l})} \lesssim h\, \|v - v_h\|_{L^2(\Omega\setminus B_{r_{l-1}})} + \begin{cases} h^2\,|\ln h|\,, & \text{if } k = 1, \\ h^{k+1}, & \text{if } k > 1. \end{cases} \tag{3.54}$$

By Lemma 3.2 we have for $l = 0$:

$$\|v - v_h\|_{L^2(\Omega\setminus B_{r_0})} \lesssim h^{\frac{3}{2}} + \begin{cases} h^2\,|\ln h|\,, & \text{if } k = 1, \\ h^{k+1}, & \text{if } k > 1. \end{cases}$$

If $k = 1$, we get $\|v - v_h\|_{L^2(\Omega\setminus B_{r_1})} \lesssim h^2\,|\ln h|$. If $k > 1$, we have $\|v - v_h\|_{L^2(\Omega\setminus B_{r_1})} \lesssim h^2$, and thus by induction it follows for $2 \leq l \leq k$:

$$\|v - v_h\|_{L^2(\Omega\setminus B_{r_l})} \lesssim h^{l+1}.$$

Numerical results

Finally, we illustrate our theoretical results by numerical examples and consider the boundary value problem (3.31) with:

$$\Omega = (0,1)^d\,, \quad d \in \{2,3\}\,.$$

For the computation of the finite element approximation, we use the PDE-framework DUNE [12]. The expression eco in the tables abbreviates the numerical convergence order.

Single Dirac distribution ($d = 2$)

We choose $f = 0$ and $q_0 = 0.5$ and set the Dirichlet boundary values such that the exact solution is given by:

$$u(x) = -0.5 \cdot \ln \sqrt{(x_1 - x_{01})^2 + (x_2 - x_{02})^2},$$

where $x = (x_1, x_2)^T \in \Omega$ and $x_0 = (x_{01}, x_{02})^T = (0.5, 0.5)^T$. In the following, we consider the L^2-error $e_R = \|u - u_h\|_{L^2(\Omega\setminus B_R(x_0))}$ for different radii $R \in \{0, 0.05, 0.1, 0.2\}$ and different approximation orders $k \in \{1, 2\}$. In order to compute this error norm, we use an adaptive quadrature formula, defined on a finer sub mesh to guarantee an accurate error evaluation. Note that in the case $R = 0$ no second order convergence can be expected.

Tables 3.3 and 3.4 show the numerical results for $k = 1$ and $k = 2$, respectively. In both cases, the theoretically obtained upper bounds hold for our numerical results. The theoretically predicted log-factor in the case $k = 1$ is difficult to identify in numerics. We point out that in the pre-asymptotic range, i.e., $R \lesssim h$, a reduced convergence rate is obtained. The smaller R, the later the asymptotic starts, see the bold marked rates in Tables 3.3 and 3.4. For a mesh size h that is smaller than R the computed convergence rates are optimal. As expected from the well-known L^2-analysis, the global error is qualitatively independent of k and only of order h.

Table 3.3: L^2-error e_R on $\Omega \setminus B_R(x_0)$ for $x_0 = (0.5, 0.5)^T$, $k = 1$.

l	$R = 0.0$	eco	$R = 0.05$	eco	$R = 0.1$	eco	$R = 0.2$	eco
1	3.21e-1		2.11e-1		1.60e-1		1.37e-1	
2	1.61e-1	**1.00**	5.68e-2	1.89	4.24e-2	1.92	3.61e-2	1.92
3	8.03e-2	**1.00**	1.77e-2	1.68	1.27e-2	1.73	9.03e-3	**2.00**
4	4.15e-2	**1.00**	3.21e-3	**2.46**	2.66e-3	**2.26**	2.11e-3	**2.10**
5	2.08e-2	**1.00**	8.51e-4	**1.92**	6.86e-4	**1.96**	5.31e-4	**1.99**
6	1.04e-2	**1.00**	2.12e-4	**2.00**	1.75e-4	**1.97**	1.35e-4	**1.98**

Table 3.4: L^2-error e_R on $\Omega \setminus B_R(x_0)$ for $x_0 = (0.5, 0.5)^T$, $k = 2$.

l	$R = 0.0$	eco	$R = 0.05$	eco	$R = 0.1$	eco	$R = 0.2$	eco
1	5.05e-2		3.52e-2		2.84e-2		2.55e-2	
2	2.53e-2	**1.00**	1.20e-2	1.55	8.62e-3	1.72	3.04e-3	**3.07**
3	1.26e-2	**1.01**	1.95e-3	2.62	9.38e-4	**3.20**	3.11e-4	**3.29**
4	6.32e-3	**1.00**	6.34e-4	1.62	1.21e-4	**2.95**	3.78e-5	**3.04**
5	3.16e-3	**1.00**	4.82e-5	**3.72**	1.51e-5	**3.00**	4.75e-6	**3.00**
6	1.58e-3	**1.00**	6.32e-6	**2.94**	2.00e-6	**2.92**	5.94e-7	**3.00**

Single Dirac distribution ($d = 3$)

We choose again $f = 0$ and $q_0 = 1$ and set the Dirichlet boundary values such that the exact solution is given by:

$$u(x) = \frac{1}{2 \cdot r(x)}, \text{ where } r(x) = \sqrt{(x_1 - x_{01})^2 + (x_2 - x_{02})^2 + (x_3 - x_{03})^2},$$

$x = (x_1, x_2, x_3)^T \in \Omega$ and $x_0 = (x_{01}, x_{02}, x_{03})^T = (0.5, 0.5, 0.5)^T$. In three dimensions the expected global L^2-error decay is even of lower order compared to the two dimensional case, see, e.g., [98, Theorem 1]. However, our theoretical results for the error e_R are independent of the space dimension. Table 3.5 shows the case $k = 1$ whereas Table 3.6 gives the results for $k = 2$. For $R > 0$, we observe the predicted quasi-optimal and optimal convergence order.

Multiple Dirac distributions

Now, we consider more than one Dirac measure, and choose:

$$f(x, y) = 2\pi^2 \sin(\pi x) \sin(\pi y).$$

Three Dirac measures are placed at $x_0 \approx (0.55, 0.55)$, $x_1 \approx (0.6, 0.4)$, $x_2 \approx (0.47, 0.52)$ weighted with $q_0 = 0.25$, $q_1 = 0.1$, $q_2 = -0.2$, and a uniform mesh is used. None of these

Table 3.5: L^2-error e_R on $\Omega \setminus B_R(x_0)$ for $x_0 = (0.5, 0.5, 0.5)^T$, $k = 1$.

l	$R = 0.0$	eco	$R = 0.05$	eco	$R = 0.1$	eco	$R = 0.2$	eco
1	7.48e-2		5.81e-2		4.55e-2		3.34e-2	
2	4.92e-2	**0.60**	3.12e-2	0.90	2.42e-2	0.87	1.82e-2	0.88
3	3.46e-2	**0.51**	1.72e-2	0.86	1.31e-2	0.88	6.12e-3	1.57
4	2.45e-2	**0.50**	9.13e-3	0.81	4.46e-3	1.55	1.54e-3	**1.99**
5	1.73e-2	**0.50**	3.17e-3	1.53	1.10e-3	**2.01**	3.91e-4	**1.98**
6	1.22e-2	**0.50**	8.00e-4	**1.99**	2.84e-4	**1.97**	9.88e-5	**1.98**

Table 3.6: L^2-error e_R on $\Omega \setminus B_R(x_0)$ for $x_0 = (0.5, 0.5, 0.5)^T$, $k = 2$.

l	$R = 0.0$	eco	$R = 0.05$	eco	$R = 0.1$	eco	$R = 0.2$	eco
1	4.87e-2		3.62e-2		3.33e-2		2.84e-2	
2	3.09e-2	**0.66**	2.41e-2	0.59	2.01e-2	0.72	1.14e-2	1.32
3	2.18e-2	**0.50**	1.44e-2	0.74	7.94e-3	1.33	1.74e-3	2.71
4	1.54e-2	**0.50**	5.61e-3	1.36	1.23e-3	2.69	1.28e-4	**3.76**
5	1.09e-2	**0.50**	8.72e-4	2.67	9.53e-5	**3.69**	1.13e-5	**3.50**
6	7.73e-3	**0.50**	6.71e-4	**3.70**	1.06e-5	**3.17**	1.33e-6	**3.32**

Table 3.7: L^2-error on $\Omega \setminus B_{0.25}(0.5, 0.5)$, $k = 1$, $k = 2$ and $k = 3$.

l	$k = 1$	eco	$k = 2$	eco	$k = 3$	eco
1	1.21e-1		1.43e-2		5.48e-3	
2	2.79e-2	**2.11**	3.01e-3	2.25	8.73e-4	3.74
3	7.06e-3	**1.98**	2.67e-4	**3.49**	3.47e-5	**4.65**
4	1.74e-3	**2.02**	3.05e-5	**3.13**	1.44e-6	**4.59**
5	4.53e-4	**1.94**	3.63e-6	**3.07**	9.25e-8	**3.96**

points coincides with an edge or a node of an element. As before, the Dirichlet boundary values are chosen such that the exact solution can be computed by the superposition principle.

Considering the numerical results in Table 3.7 for linear, quadratic and cubic elements, we observe that the L^2-error $\|u - u_h\|_{L^2(\Omega \setminus B_{0.25}(0.5,0.5))}$ has approximately the same convergence behavior as in the previous subsections, dealing with only one Dirac measure. The computation of the convergence order reveals a good agreement with Corollary 3.1.

3.2.2 2D coupled problem

The numerical treatment of coupled problems like **Model problem 1-3** (3.24)-(3.28) is not straightforward, since their source terms involve average terms of the solution. The presence of averages within the source terms makes the assembly of the discretization matrices more complex than those which arise from standard differential operators. Incorporating the averages into the discretization matrices the structures of the standard matrices are destroyed, due to the fact that the elements containing the line Λ or the point x_0 are linked to elements intersected by the balls or cylinders around the measures. In order to circumvent the additional effort assembling the matrix and to be able to use optimal solvers for elliptic problems, we consider the average values $\bar{u}$ as an additional unknown and insert it into the solution vector.

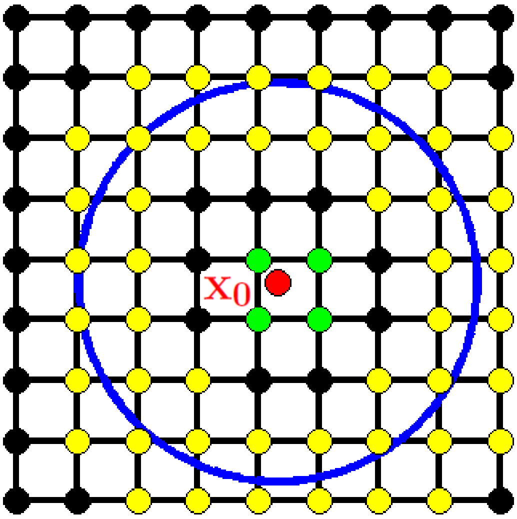

Figure 3.4: The picture shows a blue ball around x_0 in two space dimensions ($B_R(x_0)$). The green grid nodes are the nodes which are adjacent to the Dirac measure x_0 and define the index set I_D. The yellow marked grid nodes belong to elements which are intersected by the ball $B_R(x_0)$. The corresponding index set is denoted by I_B.

This approach is illustrated by the simplest of our coupled model problems, i.e., **Model problem 3** (3.28). For the sake of simplicity our considerations are outlined by means of linear Lagrange elements [15][Chapter 5]. Doing so, we define the index set I_D as the indices whose corresponding grid nodes p_i are adjacent to the location of the Dirac source term $\mathbf{x_0}$ (green nodes in Figure 3.4). The index set of grid nodes belonging to elements intersected by the ball $B_R(x_0)$ is denoted by I_B. Discretizing (3.28) by means of standard finite elements, we obtain for the corresponding solution vector $\mathbf{u} = (\mathbf{u_h}, \bar{u}_h)^T$ the following linear system of equations:

$$\underbrace{\left(\begin{array}{c|c} A_L & c_h \\ \hline I_h & -1 \end{array}\right)}_{=:A_h} \underbrace{\begin{pmatrix} \mathbf{u_h} \\ \bar{u}_h \end{pmatrix}}_{=:\mathbf{u}} = \underbrace{\begin{pmatrix} b_d \\ 0 \end{pmatrix}}_{=:b_h}. \tag{3.55}$$

It holds that $\mathbf{u_h} \in \mathbb{R}^N$ and $\mathbf{u} \in \mathbb{R}^{N+1}$, where N denotes the number of degrees of freedom associated to the chosen finite element space. $A_L \in \mathbb{R}^{N \times N}$ is the matrix discretizing the Laplacian operator. The sub matrix $I_h \in \mathbb{R}^{1 \times N}$ approximates the average value $\bar{u}$, it can be computed as follows: Let the finite element solution u_h be represented as follows:

$$u_h(x) = \sum_{i=1}^{N} \mathbf{u_h}(i) \cdot \varphi_i(x),$$

where $\{\varphi_i\}_{i=1}^N$ is the nodal finite element basis. By this we have for $\bar{u}$ the approximation:

$$\begin{aligned}\bar{u} &= \int_0^1 u\left(\mathbf{x_0}, 2\pi\theta, R\right) d\theta \approx \sum_{j=1}^{N_Q} \omega_j u_h\left(\mathbf{x_0}, 2\pi\theta_j, R\right) \\ &= \sum_{j=1}^{N_Q} \sum_{i=1}^{N} \omega_j \mathbf{u_h}(i) \cdot \varphi_i\left(\xi_j\right) = \sum_{i=1}^{N} \left(\sum_{j=1}^{N_Q} \omega_j \varphi_i\left(\xi_j\right) \right) \cdot \mathbf{u_h}(i) =: \bar{u}_h.\end{aligned}$$

ω_j and θ_j denote the weights and nodes of a suitable quadrature rule. The nodes ξ_j are given by:

$$\xi_j = \begin{pmatrix} x_{0,1} \\ x_{0,2} \end{pmatrix} + R \cdot \begin{pmatrix} \cos\left(2\pi\theta_j\right) \\ \sin\left(2\pi\theta_j\right) \end{pmatrix}.$$

Due to the fact that the basis functions have a compact support concentrated on the adjacent elements, only the grid nodes contained in the index set I_B have to be considered:

$$\overline{u_h} = \sum_{i \in I_B} \left(\sum_{j=1}^{N_Q} \omega_j \varphi_i\left(\xi_j\right) \right) \cdot \mathbf{u_h}(i).$$

All in all, it follows for the i-th entry of the sub matrix I_h:

$$I_h(i) = \begin{cases} \sum_{\xi_j \in \operatorname{supp}(\varphi_i)} \omega_j \varphi_i\left(\xi_j\right), & i \in I_B, \\ 0, & i \notin I_B. \end{cases}$$

The sub matrix $c_h \in \mathbb{R}^{N \times 1}$ is the discrete counterpart of the term $2\pi R D \delta_{x_0}$, its entries are given by:

$$c_h(i) = \begin{cases} 2\pi R D \varphi_i\left(\mathbf{x_0}\right), & i \in I_D, \\ 0, & i \notin I_D. \end{cases}$$

The right hand side b_d has a similar structure. It contains the boundary values u_e and discretizes the term $2\pi R D u_0 \delta_{\mathbf{x_0}}$. Defining by I_{Bo} the set of boundary indices, we have for the entries of b_d, provided that $I_D \cap I_{Bo} = \emptyset$:

$$b_d(i) = \begin{cases} 2\pi R D u_0 \varphi_i\left(\mathbf{x_0}\right), & i \in I_D, \\ u_e\left(p_i\right), & i \in I_{Bo}, \\ 0, & i \notin I_D \cup I_{Bo}. \end{cases} \tag{3.56}$$

To enforce the boundary conditions into the system of equations the discretization matrix A_h one has to modify the discretization matrix as follows:

$$A_h(i,j) = \delta_{ij}, \quad j \in \{1,\dots,N+1\}, \quad i \in I_{Bo},$$

where δ_{ij} denotes the Kronecker symbol and $A_h(i,j)$ the entry in the i-th line and j-th column. For the numerical solution of (3.55), we construct an iterative scheme. Each iteration step of this scheme consists of two sub steps. In the $(k+1)$-th iteration, we firstly solve the following system of equations:

$$A_L \mathbf{u_h}^{(k+1)} = b_d - c_h \overline{u_h^{(k)}}, \quad \mathbf{u_h}^{(0)} = \mathbf{0}, \quad \overline{u_h^{(0)}} = 0, \tag{3.57}$$

where $\mathbf{u_h^{(k)}}$ denotes the solution vector and $\overline{u_h^{(k)}}$ the average value from the k-th iteration. In the second step, a new value for the average $\overline{u_h}$ is computed as follows:

$$\overline{u_h^{(k+1)}} = I_h \mathbf{u_h^{(k)}}. \tag{3.58}$$

The iteration is stopped, if it holds:

$$\left| \overline{u_h^{(k+1)}} - \overline{u_h^{(k)}} \right| < TOL \quad \text{or} \quad k > ITmax.$$

TOL is a given tolerance and $ITmax$ defines the maximum of the permissible iteration steps (see Algorithm 6). We solve the system of equations (3.57) in the first substep by the help of a direct solver or a multi-grid method. A suitable quadrature rule combined with an efficient interpolation technique is used for the second sub step (3.58). Due to the fact that there is no pollution effect (see Subsection 3.2.1) the average value can be computed with a small numerical error, if the grid is sufficiently fine. Now the crucial issue is to examine under which conditions the iterative scheme is converging. A closer examination shows that the first substep in each iteration is the discrete version of the following Dirac problem:

Algorithm 6 Iterative solution scheme for the system of equations (3.55)

```
$\mathbf{u_h}^{(0)} = \mathbf{0}$, $\overline{u_h^{(0)}} = 0$
while $k \leq ITmax$ AND $\left| \overline{u_h^{(k+1)}} - \overline{u_h^{(k)}} \right| > TOL$ do
    Solve $A_L \mathbf{u_h^{(k+1)}} = b_d - c_h \overline{u_h^{(k)}}$
    Compute $\overline{u_h^{(k+1)}} = I_h \mathbf{u_h^{(k)}}$
end while
```

$$-\Delta u^{(k+1)} = 2\pi R D \left(u_0 - \overline{u^{(k)}} \right) \delta_{\mathbf{x_0}}. \tag{3.59}$$

From literature we know that the solution of (3.59) in the sense of distributions is given by [32]:

$$u^{(k+1)} = -RD \left(u_0 - \overline{u^{(k)}} \right) \ln r. \tag{3.60}$$

For the first three iterations, we obtain:

$$\begin{aligned} u^{(1)} &= -RD\left(u_0 - \overline{u^{(0)}}\right)\ln r \\ &= -RDu_0 \ln r \\ u^{(2)} &= -RD\left(u_0 - \overline{u^{(1)}}\right)\ln r \\ &= -RDu_0\left(1 + RD\ln R\right)\ln r \\ u^{(3)} &= -RD\left(u_0 - \overline{u^{(2)}}\right)\ln r \\ &= -RDu_0\left(1 + (RD\ln R) + (RD\ln R)^2\right)\ln r \end{aligned}$$

By induction with respect to k one can prove:

$$u^{(k+1)} = -RDu_0 \sum_{l=0}^{k} \left(RD\ln R\right)^l \, \ln r. \tag{3.61}$$

From this it follows, if $|RD\ln R| < 1$ holds:

$$\begin{aligned} \lim_{k\to\infty} u^{(k+1)} &= -RDu_0 \sum_{l=0}^{\infty} \left(RD\ln R\right)^l \ln r \\ &= -u_0 \frac{RD}{1 - RD\ln R} \ln r = u_e. \end{aligned}$$

Finally we observe that the iteration given by Algorithm 6 is convergent for **Model problem 3** if

$$|RD\ln R| < 1 \tag{3.62}$$

holds. Clearly, the system of equations (3.55) can be written in a more compact form:

$$\left(A_L + c_h I_h\right)\mathbf{u_h} = b_d$$

and solved directly. Considering the average value $\overline{u}$ as an additional unknown is a preparation for the numerical treatment of time dependent 3D-1D coupled problems. A separation of the average values from the standard coordinate vector $\mathbf{u_h}$ enables us to apply semi-implicit methods, where we treat the average values explicitly. Furthermore the submatrix I_h does not have to be assembled anymore.

Single Dirac measure

Next we want to test, if the observation (3.62) can be seen in numerical experiments. For these tests, we choose $D = u_0 = 1$, $\Omega = (0,1)^2$ and $\mathbf{x_0} = (0.5, 0.5)^T$. Concerning the iteration scheme, we choose: $ITmax = 20$ and $TOL = 1.0e-8$. At first we report the L^2-errors $e_R := L^2\left(\Omega \setminus B_R\left(\mathbf{x_0}\right)\right)$ for $R \in \{0.05, 0.1, 0.2, 0.3\}$ on a sequence of uniform grids having the mesh size $h = 2^{1-l} \cdot \frac{1}{16}$, $l \in \{1,2,3,4,5\}$. This is motivated by the fact that in applications one is interested in an optimal convergence behavior in $\Omega \setminus B_R\left(\mathbf{x_0}\right)$, because in $B_R\left(\mathbf{x_0}\right)$ the physics is governed by the fracture flow and not by the solution for the porous

Table 3.8: L^2-error e_R on $\Omega \setminus B_R(x_0)$ for $x_0 = (0.5, 0.5)^T$.

l	$R = 0.05$	nco	$R = 0.1$	nco	$R = 0.2$	nco	$R = 0.3$	nco
1	$4.14e-4$		$6.39e-4$		$4.55e-4$		$3.14e-4$	
2	$1.72e-4$	1.27	$1.32e-4$	**2.28**	$1.04e-4$	**2.13**	$8.68e-5$	1.85
3	$3.59e-5$	**2.26**	$3.06e-5$	**2.11**	$2.56e-5$	**2.02**	$2.15e-5$	**2.01**
4	$8.34e-6$	**2.11**	$7.54e-6$	**2.02**	$6.57e-6$	**1.97**	$5.26e-6$	**2.03**
5	$2.05e-6$	**2.02**	$1.90e-6$	**1.99**	$1.64e-6$	**2.00**	$1.31e-6$	**2.01**

matrix. Some simple calculations reveal that the stability condition (3.62) is fulfilled for all $R \in \{0.05, 0.1, 0.2, 0.3\}$. Thus we expect our iteration scheme to converge in all cases.

The results in Table 3.8 show that we have for every $R \in \{0.05, 0.1, 0.2, 0.3\}$ optimal convergence on $\Omega \setminus B_R(x_0)$.

Varying D

For a further numerical test, we vary the parameter D such that $D \in \{3, 4, 6, 7\}$. The other parameters are chosen as follows: $u_0 = 1$, $R = 0.1$ and $h \in \left\{\frac{1}{32}, \frac{1}{64}\right\}$. For our iteration scheme, we have: $ITmax = 40$ and $TOL = 1.0e-8$. Apparently the stability condition (3.62) is fulfilled for $D \in \{3, 4\}$ and not fulfilled for $D \in \{6, 7\}$. In the following figure we report for each iteration the logarithm of the local discretization error e_R.

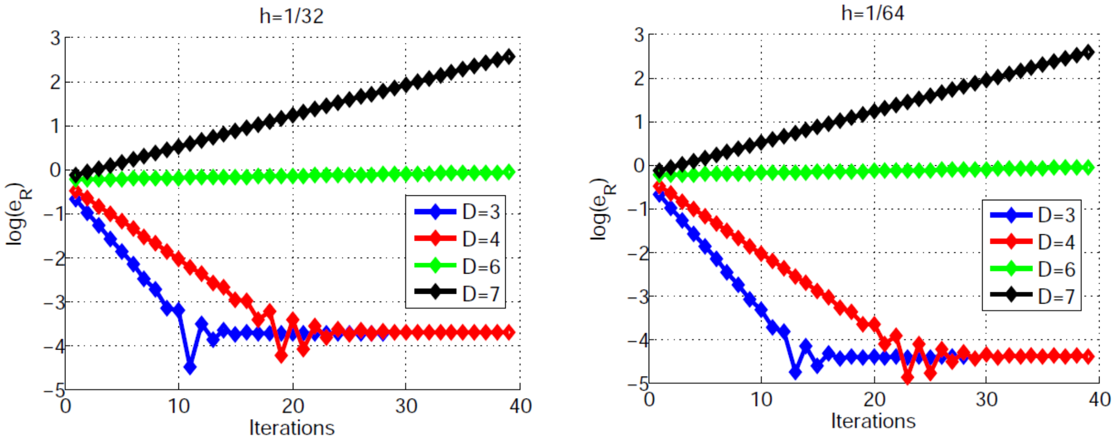

Figure 3.5: Convergence behavior of the iteration scheme for $h = 1/32$ (left), convergence behavior of the iteration scheme for $h = 1/64$ (right).

Obviously, the iteration scheme is not convergent for $D \in \{6, 7\}$, but for $D \in \{3, 4\}$. This is in agreement with 3.62 and shows the significance of the stability condition.

Two Dirac measures

For our last example, we consider a coupled Poisson equation having two Dirac measures at $\mathbf{x_0} = (0.25, 0.5)^T$ and $\mathbf{x_1} = (0.75, 0.5)^T$ at its right hand side:

$$\begin{aligned} -\Delta u = 2\pi R \left(u_0 - \bar{u}_0\right) \delta_{\mathbf{x_0}} + 2\pi R \left(u_0 - \bar{u}_1\right) \delta_{\mathbf{x_1}} \quad &\text{in} \quad \Omega = (0,1)^2, \\ u = u_{e,1} \quad &\text{on} \quad \partial\Omega, \end{aligned} \tag{3.63}$$

where

$$\overline{u_i} = \int_0^1 u\left(\mathbf{x_i}, R, 2\pi\theta\right) \, d\theta, \quad i \in \{0,1\}.$$

The exact solution $u_{e,1}$ is given by:

$$u_{e,1} = \frac{-Ru_0}{1 - R\ln R - R\ln r_{01}} \left(\ln r_0 + \ln r_1\right), \; r_i\left(\mathbf{x}\right) = \left\|\mathbf{x} - \mathbf{x_i}\right\|, \; i \in \{0,1\}, \; r_{01} = \left\|\mathbf{x_0} - \mathbf{x_1}\right\|.$$

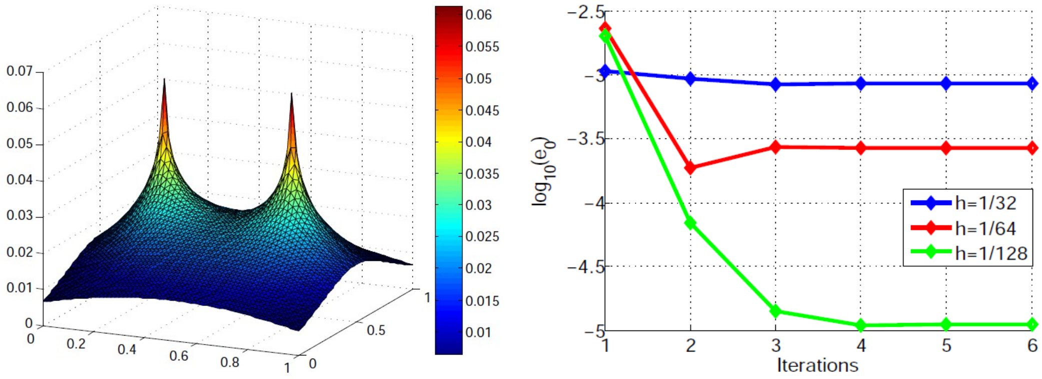

Figure 3.6: Solution plot of (3.63) (left), convergence behavior of the iteration scheme for $R = 0.1$ (right)

For our numerical test, we choose: $u_0 = 1$, $ITmax = 10$, $TOL = 1.0e-8$ and $R \in \{0.025, 0.05, 0.1, 0.2\}$ and report the L^2-errors $e_R := L^2\left(\Omega \setminus \left(B_R\left(\mathbf{x_0}\right) \cup B_R\left(\mathbf{x_1}\right)\right)\right)$ for $R \in \{0.025, 0.05, 0.1, 0.2\}$ on a sequence of uniform grids having the mesh size $h = 2^{1-l} \cdot \frac{1}{16}$, $l \in \{1,2,3,4,5\}$. The discretization yields a similar equation system like (3.55). Besides the standard matrix for the Laplacian there are two more rows and lines discretizing the coupling terms, if we consider the average values $\overline{u_0}$ and $\overline{u_1}$ as further unknowns. Furthermore the vector b_d contains the discretization of two Dirac source terms instead of only one Dirac source term. The results are reported in Table 3.9.

It can be observed that we have besides a few exceptions an optimal convergence rate of order 2 for linear elements. In Figure 3.6 one can see on the left hand side the numerical solution of (3.63). The other picture shows the logarithm of the approximation error e_0

Table 3.9: L^2-error e_R on $\Omega \setminus (B_R(\mathbf{x_0}) \cup B_R(\mathbf{x_1}))$ for $\mathbf{x_0} = (0.25, 0.5)^T$ and $\mathbf{x_1} = (0.75, 0.5)^T$.

l	$R = 0.025$	nco	$R = 0.05$	nco	$R = 0.1$	nco	$R = 0.2$	nco
1	$2.80e-3$		$2.40e-3$		$3.40e-3$		$1.40e-3$	
2	$6.91e-4$	**2.02**	$1.00e-3$	1.26	$7.03e-4$	**2.27**	$3.27e-4$	**2.10**
3	$2.86e-4$	1.27	$2.25e-4$	**2.15**	$1.62e-4$	**2.12**	$8.04e-5$	**2.02**
4	$6.23e-5$	**2.20**	$5.46e-5$	**2.15**	$4.01e-5$	**2.01**	$2.10e-5$	1.94
5	$1.52e-5$	**2.04**	$1.35e-5$	**2.02**	$1.02e-5$	**1.98**	$5.27e-6$	**1.99**

for $R = 0.1$ depending on the iteration number of our numerical scheme. The error e_0 is defined as follows:

$$e_0 = \left| \overline{u_0} - \int_0^1 u_h\left(\mathbf{x_0}, R, 2\pi\theta\right)\, d\theta \right| .$$

We note that the error becomes constant after 4 iterations.

3.2.3 3D-1D coupled problem

In the last subsection, we developed an iterative scheme for the numerical solution of a 2D coupled problem **(Model problem 3)**. This solution technique is now extended to treat a 3D-1D coupled problem **(Model problem 1)** (3.24)-(3.26). For convenience of the reader, we rewrite **Model problem 1**:

$$-\Delta u_{3d} + \beta\left(\overline{u_{3d}} - u_{1d}\right)\delta_\Lambda = 0 \quad \text{in} \quad \Omega = (0,1)^3 \subset \mathbb{R}^3, \tag{3.64a}$$

$$-\frac{d}{ds}\left(K_{1d}\frac{d}{ds}u_{1d}\right) + \beta\left(u_{1d} - \overline{u_{3d}}\right) = 0 \quad \text{in } \Lambda \subset \Omega, \tag{3.64b}$$

with $K_{1d}(z) = 1 + z + \frac{1}{2}z^2$, $\beta = \dfrac{2\pi}{2\pi + \ln R}$ and $\Lambda = \{(x,y,z)\,|x = y = 0.5,\ z \in (0,1)\}$. The set Λ defining the main axis of the fracture can be parameterized as follows:

$$\Lambda : [0,1] \to \Omega, \quad s \mapsto (0.5, 0.5, s)^T .$$

Comparing (3.64a) and (3.64b) with (3.24)-(3.26) one observes that $K_{3d} \equiv I$, $m_{3d} = 0$, $r_{3d} = 0$ and $\beta = 2\pi RD$ holds. For these parameters a solution of (3.64a) and (3.64b) is given by:

$$u_{3d}^{ex}(x,y,z) = -\frac{1+z}{2\pi}\ln r, \quad r = \sqrt{(x-0.5)^2 + (y-0.5)^2}, \quad u_{1d}^{ex}(s) = 1 + s.$$

Providing the boundary conditions:

$$\begin{cases} \frac{\partial u_{3d}}{\partial n} = -\frac{1}{2\pi}\ln r & \text{on } \partial\Omega \cap \{(x,y,z) \in \Omega\,|z = 1\}, \\ \frac{\partial u_{3d}}{\partial n} = \frac{1}{2\pi}\ln r & \text{on } \partial\Omega \cap \{(x,y,z) \in \Omega\,|z = 0\}, \\ u_{3d} = u_{3d}^{ex} & \text{on } \partial\Omega \setminus \{(x,y,z) \in \Omega\,|z = 0 \vee z = 1\}, \end{cases} \quad \text{and} \quad \begin{cases} u_{1d}(0) = 1, \\ u_{1d}(1) = 2, \end{cases}$$

u_{3d}^{ex} and u_{1d}^{ex} are the unique solutions of (3.64a) and (3.64b). To solve the above PDE system numerically, we decouple the PDEs (3.64a) and (3.64b) by establishing the following iterative scheme:

$$-\Delta u_{3d}^{(k+1)} = -\beta \left(\overline{u_{3d}^{(k+1)}} - u_{1d}^{(k)} \right) \delta_\Lambda, \tag{3.65a}$$

$$-\frac{d}{ds}\left(K_{1d} \frac{d}{ds} u_{1d}^{(k+1)} \right) + \beta u_{1d}^{(k+1)} = \beta \overline{u_{3d}^{(k+1)}}, \tag{3.65b}$$

where $u_{1d}^{(0)}(s) \equiv 0,\ s \in (0,1),\ u_{3d}^{(0)}(\mathbf{x}) \equiv 0,\ \mathbf{x} \in \Omega$. The boundary conditions are for each iteration the same as for problem (3.64a), (3.64b). One observes that for a fixed curve parameter $s \in (0,1)$ problem (3.65a) can be considered as a 2D coupled problem **ModelProblem 3**, if one restricts the PDE to a plain perpendicular to the tangent in s and containing the point $\Lambda(s) \in \Omega$. Based on this observation, we establish similar to the iteration scheme presented in the previous subsection a further iteration scheme for the solution of (3.65a):

$$\begin{aligned} u_{3d}^{(k+1,0)}(\mathbf{x}) &= u_{3d}^{(k)},\ \mathbf{x} \in \Omega, \\ -\Delta u_{3d}^{(k+1,l+1)} &= -\beta \left(\overline{u_{3d}^{(k+1,l)}} - u_{1d}^{(k)} \right) \delta_\Lambda. \end{aligned} \tag{3.66}$$

On the assumption that $\overline{u_{3d}^{(k+1,l)}}$ is known from the last iteration, the PDE (3.66) corresponds to a Poisson problem with line source term. As a first step towards a numerical solution of the 3D problem (3.66), we introduce a finite element space $V_{h_{3d}}$ based on an uniform grid $\mathcal{T}_{h_{3d}}$ of mesh size h_{3d} partitioning the domain Ω into disjoint cubes. A possible basis for $V_{h_{3d}}$ is given by a nodal Lagrange basis $\{\varphi_i\}_{i=1}^{N_{3d}}$, where N_{3d} denotes the dimension of $V_{h_{3d}}$. By means of this basis a function $u_{3d}^{(k+1,l+1)} \in V_{h_{3d}}$ can be represented as follows:

$$u_{3d}^{(k+1,l+1)}(\mathbf{x}) = \sum_{i=1}^{N_{3d}} \mathbf{u}_{3d}^{(k+1,l+1)}(i) \cdot \varphi_i(\mathbf{x}),\ \mathbf{x} \in \Omega,$$

where $\mathbf{u}_{3d}^{(k+1,l+1)}(i)$ denotes the i-th component of the coordinate vector $\mathbf{u}_{3d}^{(k+1,l+1)} \in \mathbb{R}^{N_{3d}}$. Applying a standard finite element approximation to (3.66), we obtain a linear system of equations to compute $\mathbf{u}_{3d}^{(k+1,l+1)}$:

$$A_{3d}\mathbf{u}_{3d}^{(k+1,l+1)} = \mathbf{b}_{3d}^{(k+1,l)}. \tag{3.67}$$

$A_{3d} \in \mathbb{R}^{N_{3d} \times N_{3d}}$ is the standard stiffness matrix related to the Laplacian operator [28]. Besides the incorporation of the boundary conditions, the assembly of the right hand side involves the discretization of a line integral, see, e.g., [24][Chapter 4,5] [44]. For every φ_i with $\operatorname{supp}(\varphi_i) \cap \Lambda \neq \emptyset$ and $\operatorname{supp}(\varphi_i) \cap \partial\Omega = \emptyset$, we have to compute the following integral for the i-th entry of the right hand side vector:

$$\begin{aligned} b_{3d}^{(k+1,l)}(i) &= -\beta \int_{\Lambda} \left(\overline{u_{3d}^{(k+1,l)}} - u_{1d}^{(k)} \right) \cdot \varphi_i \, d\Lambda \\ &= -\beta \int_{t_{1,i}}^{t_{2,i}} \left(\overline{u_{3d}^{(k+1,l)}} - u_{1d}^{(k)} \right)(s) \cdot \varphi_i\left(\Lambda(s)\right) \left\| \dot{\Lambda}(s) \right\|_2 \, ds. \end{aligned} \tag{3.68}$$

The curve parameters $t_{1,i}$ and $t_{2,i}$ corresponding to a basis function φ_i exhibit the following features:

(i) $t_{1,i} = \inf\left\{ s \in [0,1] \mid \Lambda(s) \in \operatorname{supp}\left(\varphi_i\right) \right\}$,

(ii) $t_{2,i} = \sup\left\{ s \in [0,1] \mid \Lambda(s) \in \operatorname{supp}\left(\varphi_i\right) \right\}$,

(iii) $\left\{ \Lambda(s) \mid s \in \left(t_{1,i}, t_{2,i}\right) \right\} \subset \operatorname{supp}\left(\varphi_i\right)$.

Approximating the integral in (3.68) by a Gauss quadrature, we have:

$$\begin{aligned} b_{3d}^{(k+1,l)}(i) &\approx -\beta \frac{t_{2,i} - t_{1,i}}{2} \int_{-1}^{1} \left(\overline{u_{3d}^{(k+1,l)}} - u_{1d}^{(k)} \right)\left(s_i\left(\xi\right)\right) \cdot \varphi_i\left(\Lambda\left(s_i\left(\xi\right)\right)\right) \, d\xi \\ &= -\beta \frac{t_{2,i} - t_{1,i}}{2} \sum_{j=1}^{nGP} \omega_j \cdot \left(\overline{u_{3d}^{(k+1,l)}} - u_{1d}^{(k)} \right)\left(s_i\left(\xi_j\right)\right) \cdot \varphi_i\left(\Lambda\left(s_i\left(\xi_j\right)\right)\right), \end{aligned} \tag{3.69}$$

where we assume that the curve is parameterized such that $\left\| \dot{\Lambda}(s) \right\|_2 \equiv 1$ holds. The variable transformation s_i is defined as follows:

$$s_i : [-1,1] \to \left[t_{1,i}, t_{2,i}\right], \quad \xi \mapsto \frac{t_{2,i}}{2}\left(1+\xi\right) + \frac{t_{1,i}}{2}\left(1-\xi\right).$$

By ξ_j and ω_j, $j = 1, \ldots, nGP$ we denote the weights and nodes of the quadrature rule.

The values for $u_{1d}^{(k)}$ at the quadrature nodes are determined by standard interpolation techniques (see Figure 3.7, left). For the approximation of the average values $\overline{u_{3d}^{(k+1,l)}}$ (see also (3.26)) we first construct a circle of radius R around $\Lambda\left(s_i\left(\xi_j\right)\right)$. The plane defining the location of the circle contains the curve point $\Lambda\left(s_i\left(\xi_j\right)\right)$ and is perpendicular to the tangent t_j on Λ at $s_i\left(\xi_j\right)$ (see Figure 3.7, right). As a next step we distribute nC nodes on this circle in an uniform or in an adaptive manner. The circle nodes are denoted by $c_{m,j} \in \Omega$. Finally the solution $u_{3d}^{(k+1,l)}$ is interpolated at the nodes $c_{m,j}$ and the average is computed by an arithmetic mean of these values:

$$\overline{u_{3d}^{(k+1,l)}} \approx \frac{1}{nC} \sum_{m=1}^{nC} u_{3d}^{(k+1,l)}\left(c_{m,j}\right). \tag{3.70}$$

For the numerical solution of (3.65b), we choose standard linear finite elements [15, 28]. The corresponding finite element space is denoted by $V_{h_{1d}}$ and is based on an uniform grid

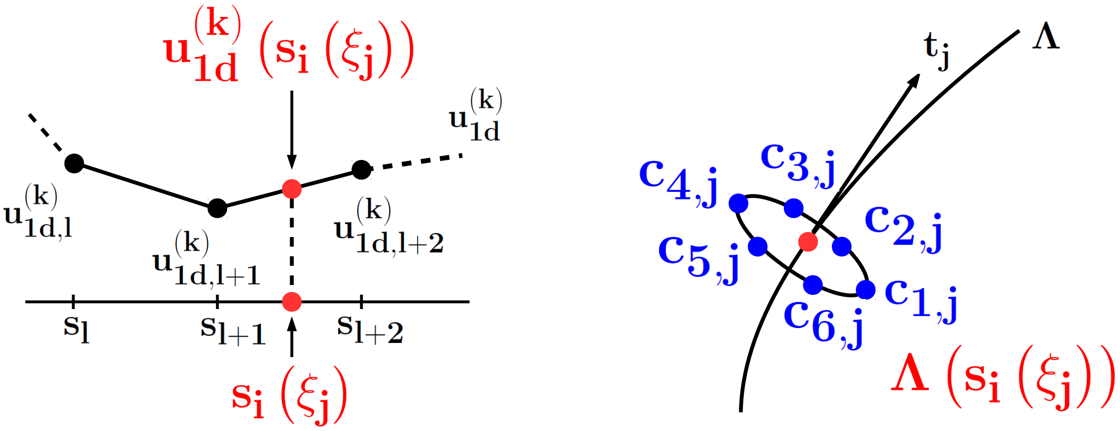

Figure 3.7: Left: Computation of $u_{1d}^{(k)}$ at $s_i\left(\xi_j\right)$ by linear interpolation. The values $u_{1d,l}^{(k)}$, $u_{1d,l+1}^{(k)}$, $u_{1d,l+2}^{(k)}$ indicate the values of $u_{1d}^{(k)}$ at the grid nodes s_l, s_{l+1} and s_{l+2}. Right: Circle nodes $c_{m,i}$, $m \in \{1,\ldots,nC\}$, $nC = 6$ around the midpoint $\Lambda\left(s_i\left(\xi_j\right)\right)$.

$\mathcal{T}_{h_{1d}}$ of mesh size h_{1d} partitioning the unit interval $[0,1]$. For $u_{1d}^{(k)} \in V_{h_{1d}}$, we have the following representation:

$$u_{1d}^{(k)}(s) = \sum_{i=1}^{N_{1d}} \mathbf{u}_{1d}^{(k)}(i) \cdot \hat{\varphi}_i(s),\ s \in [0,1]\,.$$

N_{1d} is the dimension of $V_{1d,h}$ and $\hat{\varphi}_i$ its Lagrange basis. By $\mathbf{u}_{1d,i}$, $i = 1,\ldots,N_{1d}$, we denote the coordinates related to $u_{1d,h}$. Following the standard finite element approach, one obtains for the computation of the coordinate vector

$$\mathbf{u}_{1d}^{(k)} = \left(\mathbf{u}_{1d}^{(k)}(1),\ldots,\mathbf{u}_{1d}^{(k)}\left(N_{1d}\right)\right)^T \in \mathbb{R}^{N_{1d}}$$

in the $(k+1)$-th iteration a linear system of equations:

$$A_{1d}\mathbf{u}_{1d}^{(k+1)} = \mathbf{b}_{1d}^{(k)}. \tag{3.71}$$

where $A_{1d} \in \mathbb{R}^{N_{1d}\times N_{1d}}$ arises from the discretization of the elliptic operator

$$-\frac{d}{ds}\left(K_{1d}\frac{d}{ds}\bullet\right) + \beta\,\bullet\,.$$

The right hand side vector has the following shape:

$$b_{1d}^{(k)}(i) = \begin{cases} 1 & \text{for } i = 1, \\ 2 & \text{for } i = N_{1d}, \\ \beta\int_{\operatorname{supp}(\hat{\varphi}_i)} \overline{u_{3d}^{(k+1)}}(s)\cdot\hat{\varphi}_i(s)\,ds & \text{for } i \neq 1, N_{1d}. \end{cases} \tag{3.72}$$

Note that the entries of the first and last row of A_{1d} have to be zero except of the diagonal entries, if one wants to integrate the boundary conditions into the right hand side. Let us assume that $\operatorname{supp}(\hat{\varphi}_i) = (s_{1,i}, s_{2,i}) \subset [0,1]$, then we can write:

$$\int_{\operatorname{supp}(\hat{\varphi}_i)} \overline{u_{3d}^{(k+1)}}(s) \cdot \hat{\varphi}_i(s)\, ds = \int_{s_{1,i}}^{s_{2,i}} \overline{u_{3d}^{(k+1)}}(s) \cdot \hat{\varphi}_i(s)\, ds.$$

Algorithm 7 Iterative solution scheme for the PDE system (3.64a), (3.64b).

```
$k = 0$
$u_{1d}^{(0)}(s) \equiv 0,\ s \in (0,1)$
$u_{1d}^{(1)}(s) = u_{1d}^{(0)}(s) + 2 \cdot TOL_k,\ s \in (0,1)$
$u_{3d}^{(0,0)}(\mathbf{x}) \equiv 0,\ \mathbf{x} \in \Omega$
$u_{3d}^{(1,0)}(\mathbf{x}) \equiv 0,\ \mathbf{x} \in \Omega$
while $k \leq ITmax_k$ AND $\left\| \mathbf{u}_{1d}^{(k+1)} - \mathbf{u}_{1d}^{(k)} \right\|_2 > TOL_k$ do
  $l = 0$
  $\mathbf{u}_{3d}^{(k+1,1)} = \mathbf{u}_{3d}^{(k+1,0)} + 2 \cdot TOL_l$
  while $l \leq ITmax_l$ AND $\left\| \mathbf{u}_{3d}^{(k+1,l+1)} - \mathbf{u}_{3d}^{(k+1,l)} \right\|_2 > TOL_l$ do
    Assemble $b_{3d}^{(k+1,l)}$ using (3.69)
    Solve system (3.67)
    $l = l + 1$
  end while
  Assemble $b_{1d}^{(k)}$ using (3.72)
  Solve system (3.71)
  $\mathbf{u}_{3d}^{(k+1,0)} = \mathbf{u}_{3d}^{(k,l)}$
  $k = k + 1$
end while
```

Using a Gauss quadrature rule for the numerical approximation of the integral, we obtain:

$$\begin{aligned} \int_{s_{1,i}}^{s_{2,i}} \overline{u_{3d}^{(k+1)}}(s) \cdot \hat{\varphi}_i(s)\, ds &= \frac{s_{2,i} - s_{1,i}}{2} \cdot \int_{-1}^{1} \overline{u_{3d}^{(k+1)}}\left(\hat{s}_i(\xi)\right) \cdot \hat{\varphi}_i\left(\hat{s}_i(\xi)\right)\, d\xi \\ &\approx \frac{s_{2,i} - s_{1,i}}{2} \cdot \sum_{j=1}^{nGP} \overline{u_{3d}^{(k+1)}}\left(\hat{s}_i(\xi_j)\right) \cdot \hat{\varphi}_i\left(\hat{s}_i(\xi_j)\right)\, \omega_j. \end{aligned}$$

ξ_j and $\omega_j,\ j \in \{1, \ldots, nGP\}$ are as for the 3D problem the nodes and weights of the quadrature rule. The transformation $\hat{s}_i$ is given by:

$$\hat{s}_i : [-1,1] \to [s_{1,i}, s_{2,i}], \quad \xi \mapsto \frac{s_{2,i}}{2}(1+\xi) + \frac{s_{1,i}}{2}(1-\xi).$$

To compute the average values at $\hat{s}_i(\xi_j)$ one can use the same techniques which were applied to derive (3.70). Providing two tolerances TOL_k and TOL_l together with two upper bounds for the iteration numbers $ITmax_k$ and $ITmax_l$, we have the following algorithm for the numerical solution of the PDE system (3.64a), (3.64b). Comparing this solution algorithm to the discretization technique presented in [24][Chapter 5] this approach has two advantages:

1. **In every iteration standard elliptic PDEs have to be solved.**
2. **Different mesh sizes for the 1D problem and the 3D problem can be used.**

Numerical tests

The following figures show some numerical results for $R = 0.05$. In Figure 3.8 the numerical solutions $u_{1d}^{(k)}$, $k = 1, \ldots, 4$, of the 1D-problem for the first four iterations are depicted. It can be observed that the 1D-solution converges very fast towards the exact solution. After the forth iteration the numerical solution is very close to the exact solution $u_{1d}^{ex}(s) = 1 + s$ and can not be distinguished from it. Figure 3.9 shows a cross section of the 3D-solution and the 3D-solution in two slices at $z = 0.75$ and $z = 0.25$. u_{1d} is plotted on a straight tube of radius $R = 0.05$ around the middle axis Λ. As expected u_{3d} is rotationally symmetric around the curve Λ.

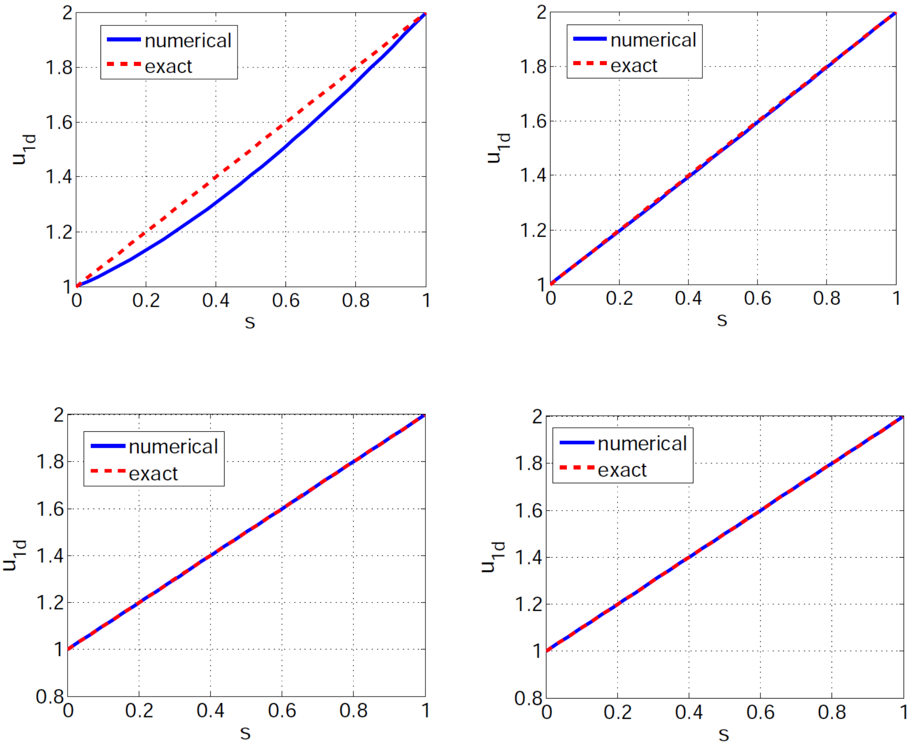

Figure 3.8: Convergence of the solution u_{1d}. After Iteration 1 (top left), Iteration 2 (top right), Iteration 3 (bottom left) and Iteration 4 (bottom right).

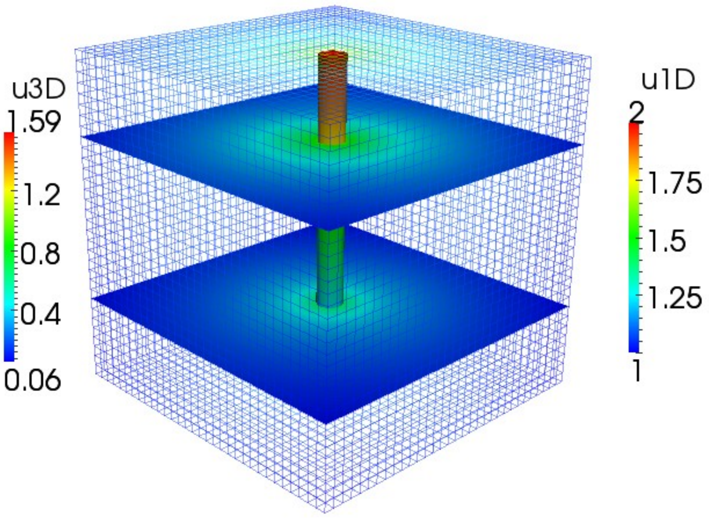

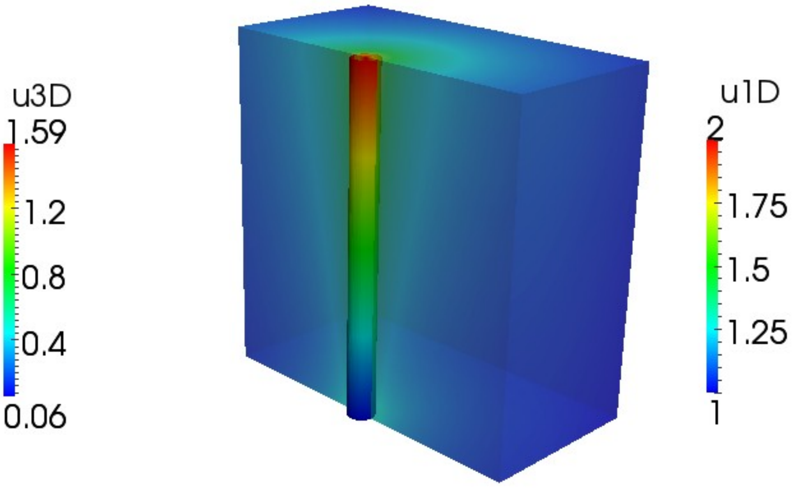

Figure 3.9: Numerical approximations for the 1D-3D problem. The picture at the bottom shows the surface plot of the 3D unit cube Ω, the solution u_{3d} at $y = 0$ and the solution u_{1d} on a tube of radius R around the axis Λ. At the top the solution u_{3D} can be seen in two slices at $z = 0.75$ and $z = 0.25$.

Table 3.10: Local L^2-error $L^2(\Omega \setminus Z_R)$ for $R = 0.05$

l	$c = 1$	nco	$c = 1/2$	nco	$c = 1/4$	nco
1	$3.50e-3$		$5.60e-3$		$6.00e-3$	
2	$5.48e-4$	**2.68**	$3.50e-3$	0.68	$5.60e-3$	0.10
3	$1.03e-4$	**2.41**	$5.48e-4$	**2.68**	$3.50e-3$	0.68
4	$2.72e-5$	**1.92**	$1.03e-4$	**2.41**	$5.48e-4$	**2.68**

Table 3.11: L^2-error $L^2(0,1)$ for $R = 0.05$

l	$c = 1$	nco	$c = 1/2$	nco	$c = 1/4$	nco
1	$1.70e-3$		$3.10e-3$		$1.60e-3$	
2	$4.49e-5$	**5.24**	$1.70e-3$	0.87	$3.20e-3$	-1.00
3	$2.38e-6$	**4.23**	$4.53e-5$	**5.23**	$1.70e-3$	0.87
4	$5.80e-7$	**2.04**	$2.46e-6$	**4.20**	$4.55e-5$	**5.22**

Table 3.12: Local L^2-error $L^2(\Omega \setminus Z_R)$ for $R = 0.1$

l	$c = 1$	nco	$c = 1/2$	nco	$c = 1/4$	nco
1	$1.00e-3$		$4.00e-3$		$5.20e-3$	
2	$1.99e-4$	**2.33**	$1.00e-3$	**2.00**	$4.00e-3$	0.38
3	$5.32e-5$	**1.90**	$1.99e-4$	**2.33**	$1.00e-3$	**2.00**
4	$1.31e-5$	**2.02**	$5.10e-5$	**1.96**	$1.99e-4$	**2.33**

Table 3.13: L^2-error $L^2(0,1)$ for $R = 0.1$

l	$c = 1$	nco	$c = 1/2$	nco	$c = 1/4$	nco
1	$4.77e-5$		$1.60e-3$		$2.80e-3$	
2	$3.22e-6$	**3.89**	$4.84e-5$	**5.05**	$1.70e-3$	0.72
3	$8.11e-7$	**1.99**	$3.34e-6$	**3.86**	$4.87e-5$	**5.12**
4	$6.69e-8$	**3.60**	$8.35e-7$	**2.00**	$3.35e-6$	**3.86**

Finally we investigate at the end of this section, how a different meshing for the 1D-problem and the 3D-problem affects the convergence behavior of the numerical scheme. In order to reduce the computational effort, one is interested in keeping the mesh for the expensive 3D problem as coarse as possible while keeping the mesh for the cheap 1D problem sufficiently fine. Therefore the above PDE system is discretized by two different mesh sizes h_{1d} and h_{3d} with $h_{1d} = c \cdot h_{3d},\ c \in \left\{1, \frac{1}{2}, \frac{1}{4}\right\}$. For the numerical solution, we have chosen the following parameters:

$$h_{1d} = \frac{1}{16 \cdot 2^{(l-1)}},\ l \in \{1,2,3,4\}$$

and $R \in \{0.05, 0.1\}$. For the iteration scheme, we choose: $TOL_l = TOL_k = 1.0e-10$ and

$ITmax_k = ITmax_l = 7$. The following tables (Table 3.10-3.13) show the $L^2(0,1)$-error with respect to the 1D-solution u_{1d} and the local $L^2(\Omega \setminus Z_R)$-error with respect to the 3D-solution u_{3d}, where Z_R denotes a cylinder around Λ with radius R.

As the factor c decreases, the preasymptotic range for both the 3D-problem and the 1D-problem is enlarged by one level. As in the previous subsections, the full convergence can only be seen in numerics, if $h_{3D} \lesssim R$ holds. Furthermore it can be observed that for every c and the first refinement levels matching the condition $h_{3D} \lesssim R$, the 1D-solution converges faster than it can be expected, in general. This is due to the fact that the analytical solution u_{1d}^{ex} is linear and can thus be represented exactly by linear Finite elements.

4 Blood flow and oxygen transport in vascularized human tissue

Based on the numerical models for network flow and stationary diffusion-reaction problems, developed in the previous chapters of this thesis, we derive in this final chapter a multi-scale (3D-1D-0D coupled) model to simulate biological transfer mechanisms between blood vessels and tissue. In particular, the impact of an arterial stenosis on oxygen delivery to the tissue is investigated.

Arterial stenosis, a serious form of arterial disease is frequently found to reduce blood flow and transport of oxygen through large and middle sized arteries. Due to pressure drops and reduced oxygen supply, ischemia in the distal tissue results. In severe cases, this may lead to an amputation of legs or arms. To make such serious and painful procedures obsolete, a better understanding of the hemodynamic effects caused by a stenosis is essential [14, 73, 106, 120]. As a first step towards a better insight into this problem, we study in this thesis the influence of a stenosis located in a distal artery (artery 54, see Figure 4.5, left).

Artery 54 is part of an arterial tree consisting of the 55 main arteries like the aorta (artery 1), the carotids (artery 12,13,15 and 16) and the largest arteries in legs and arms, e.g. artery 10 and 25. Within this network, we compute pressure and velocity waves together with oxygen transport from the heart to the arterioles. In order to decrease the computational effort, we use as in Chapter 2 *reduced 1D transport equation systems* to determine pressure, velocity and concentration within the arteries. At the outlets of the terminal vessels, we couple the 1D models as in Subsection 2.3.2 with *lumped parameter models (0D)*, e.g., a R_1CR_2-model, to incorporate the resistance and compliance of the omitted arteries, arterioles and capillaries. The corresponding values for the total resistances $R = R_1 + R_2$ and compliances C are provided in Table 4.3. For R_1 we choose as in Subsection 2.4 the characteristic impedance (2.125).

Since we are only interested in the local impact of the stenosis on tissue perfusion not the entire network is embedded into tissue, but only artery 54, 55 and the lower third of artery 53 are coupled with surrounding tissue (red rectangle in Figure 4.1). The leg consists on a macroscale, besides the bones, of large arteries, small arteries branching out of them and tissue that is supplied by the small arteries and the capillaries connected to them. According to medical understanding [105], the velocity of the flow within the large arteries ranges from 10 cm/s to 20 cm/s, while in the smaller arteries the flow velocity is about 1 cm/s. Within the capillary bed and tissue, we have a slow and rather diffusion dominated flow.

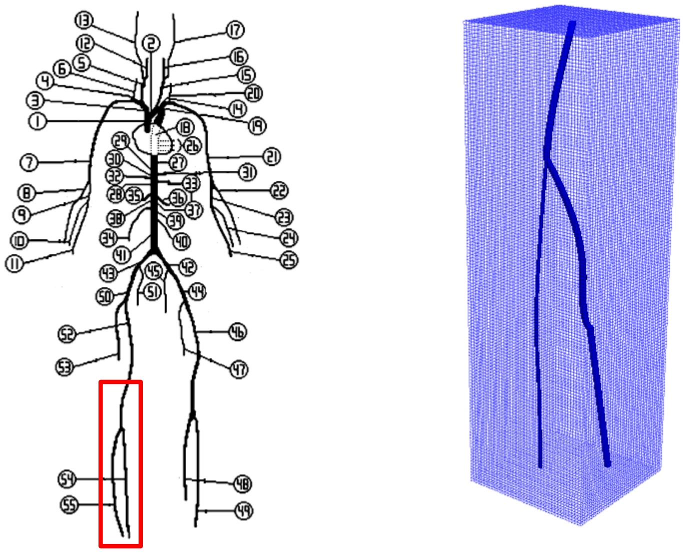

Figure 4.1: Simplified geometry of the right leg's lower part (red rectangle, left). The small arteries and the tissue are considered as a porous medium and summarized together with the larger arteries in a cuboid (right)

All in all there are different types of flow in the considered domain. To create a numerical model which accounts for this heterogeneous flow behavior, we apply a two domain approach, i.e., we treat the small arteries and the tissue as a 3D porous medium and put them together with the larger arteries in a cuboid (see Figure 4.1, right).

As a next step, the fast flow region consisting of the larger arteries is separated from the rest of the domain. Since fast blood flow and oxygen transport in these vessels are governed by 1D transport equations, other models are required for the slow 3D porous medium flow and transport processes. The challenges are now to assign an appropriate model to the 3D porous medium and to establish a coupling between the 3D and the 1D problems (see Figure 4.2). In the following subsections, we give a detailed description of a coupling strategy by line source terms. Furthermore we discuss the discretization of the resulting PDE systems and provide some simulation results.

4.1 Coupling of 0D, 1D and 3D problems

At first we discuss the coupling between the 1D problems for the network flow and the surrounding 3D tissue. The unknowns associated with the 3D problems are indicated by $k_{3d},\ k \in \{p, c\}$, whereas the unknowns for the i-th vessel of the network are denoted by $k_{1d,i},\ k \in \{p, q, c\}$. The unknowns related to the whole embedded network are denoted by $k_{1d},\ k \in \{p, q, c\}$. p stands for the pressure variable, q for the flow rate and c for

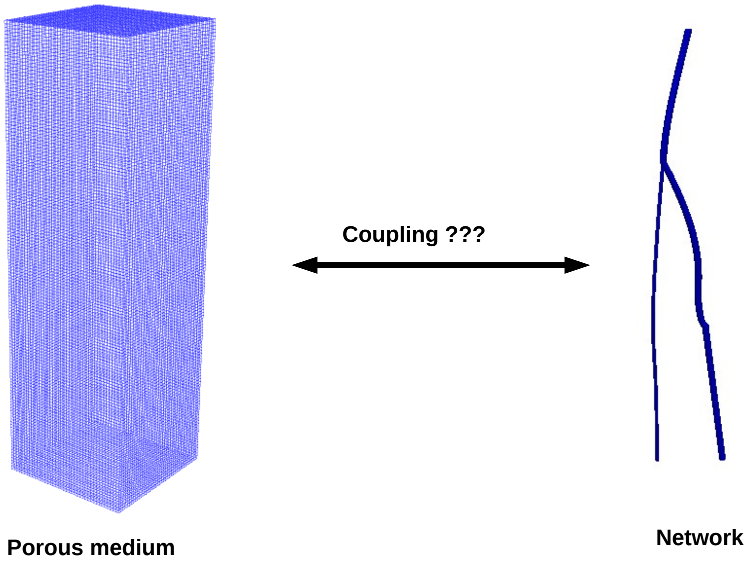

Figure 4.2: Separation of the larger arteries representing the fast flow region from the slow flow region modeled as a porous medium. The 3D porous medium consists of the arterioles and the tissue of the considered domain.

the volumetric concentration. Our model concerning the 3D-1D coupling is based on the following assumptions:

(A1) The pressure p_{3d} within the tissue is governed by the following parabolic PDE [24, Chapter 6.3]:

$$C_{3d}\frac{\partial}{\partial t}p_{3d} - \nabla \cdot K_{3d}\nabla p_{3d} + \alpha p_{3d} - \phi_{3d} = f_p. \tag{4.1}$$

The parameter C_{3d} $\left[kPa^{-1}\right]$ denotes the hydraulic compliance of the tissue. K_{3d} $\left[cm^2\ kPa^{-1}\ s^{-1}\right]$ is the tissue permeability for blood, α $\left[kPa^{-1}\ s^{-1}\right]$ is the hydraulic conductance and the source term f_p is given by:

$$f_p = \alpha p_{ven} + \frac{q_{out}\left(t\right)}{V},\ t \geq 0, \tag{4.2}$$

where p_{ven} is the average venous blood pressure, V denotes the volume of the tissue domain and $q_{out}(t)$ is the flow rate at the outlets of the embedded vessel system. The exchange term ϕ_{3d} will be specified in the remainder of this section. Note that this model does not account for different flow behavior within the tissue. Since a system of blood vessels in tissue exhibits a hierarchical structure, each vessel has a certain branching order, having its specific properties, which depend mainly on the radius. Consequently, one should not assign single values to the hydraulic tissue permeability and other averaged porous medium quantities. To incorporate the hierarchical structure into the model one can consider hierarchical flow models that have been investigated by Huyghe and Vancampen [54, 112].

(A2) The transport problem for the oxygen concentration in tissue c_{3d} $\left[\frac{mmol}{cm^3}\right]$ is given by [24, Chapter 6.3]:

$$\frac{\partial}{\partial t} c_{3d} + \nabla \cdot \left(-D_{3d} \nabla c_{3d} + \mathbf{v} c_{3d}\right) + \omega_{3d} c_{3d} - \theta_{3d} = f_c. \tag{4.3}$$

D_{3d} $\left[\frac{cm^2}{s}\right]$ denotes the diffusion coefficient for oxygen in tissue. The velocity field $\mathbf{v}$ is provided by Darcy's law:

$$\mathbf{v} = -\frac{K_{3d}}{n_{3d}} \nabla p_{3d}, \tag{4.4}$$

where n_{3d} denotes the porosity of the 3D tissue volume. The value ω_{3d} accounts for the tissue perfusion, i.e., it quantifies the blood flow rate from the tissue into the venous vessel system:

$$\omega_{3d} = \alpha p_{3d} - f_p = \alpha \left(p_{3d} - p_{ven}\right) - \frac{q_{out}\left(t\right)}{V}. \tag{4.5}$$

The source term f_c can be used to describe metabolic or biochemical processes. θ_{3d} is a coupling term which is again discussed in the remainder of this section.

(A3) For the vessels embedded into the tissue, we restrict ourselves to the linearized problem (2.24a),(2.24b). The exchange terms ϕ_M and ϕ_p are defined later. For the computation of flow and transport through the remaining network, one can use the non-linear models (2.14a),(2.14b).

(A4) The small vessels that are branching out of the arteries to supply the surrounding tissue are not resolved by the 1D models. This kind of flow can be accounted for by a proportionality coefficient L_p weighting the difference between blood pressure in the vessel and in the tissue. In literature this coefficient is often referred to as *effective hydraulic conductivity* [24, Chapter 6.5].

(A5) Due to the fact that blood flows from the vessels into the tissue matrix, the oxygen concentration on the vessel wall is equal to the oxygen concentration within the vessel, i.e., the interface between vessel and tissue is the inlet of the tissue domain [24, Chapter 6.5].

In Section 3.1 we have already shown, how a diffusion-reaction problem in a 3D domain containing a vessel V_R of radius R can be simplified in the limit $R \to 0$ to a 3D-1D coupled problem. Applying suitable boundary conditions on the surface of V_R, it turns out that the 1D problem and the 3D problem are coupled by their source terms, where the source term of the 3D problem is concentrated on a Dirac measure given by the main axis Λ of the vessel. Both source terms consist of the difference between the solution of the 1D problem u_{1d} and an averaged value $\overline{u_{3d}}$ for each curve parameter s of Λ (see Chapter 3, **Model problem 1**, (3.24)).

The subnetwork included in the considered tissue block $\Omega \subset \mathbb{R}^3$, is now decomposed into four single vessels, where we split the artery containing the stenosis into a proximal and a distal part. The vessels embedded into the porous medium are denoted by V_1, V_2, V_3 and

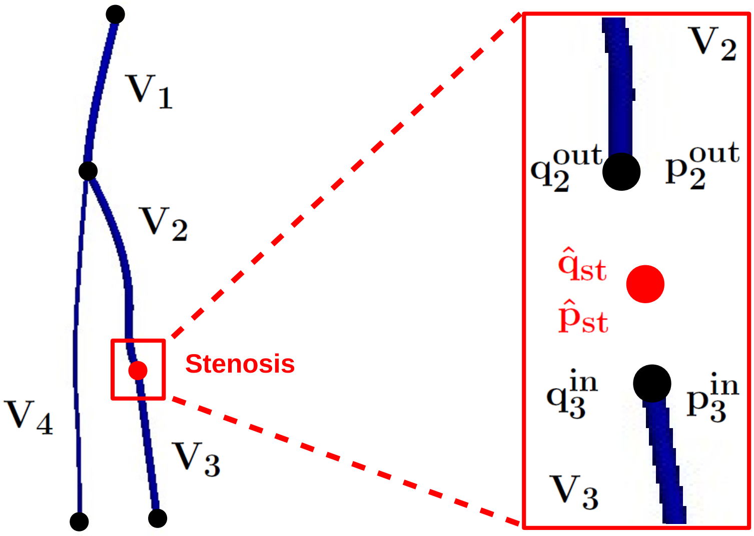

Figure 4.3: Decomposition of the subnetwork embedded in the tissue block. The vessel containing the stenosis is split into two parts. By $V_i,\ i \in \{1,2,3,4\}$, we denote the vessels of the subnetwork embedded in the porous matrix (left). In order to account for the impact of the stenosis, one has to solve the ODE system (4.6)-(4.7) for $\hat{p}_{st}$ and $\hat{q}_{st}$. By these values and p_2^{out}, p_3^{in}, q_2^{out}, q_3^{in}, the upwinded fluxes at the outlet of V_2 and the inlet of V_3 can be determined (right).

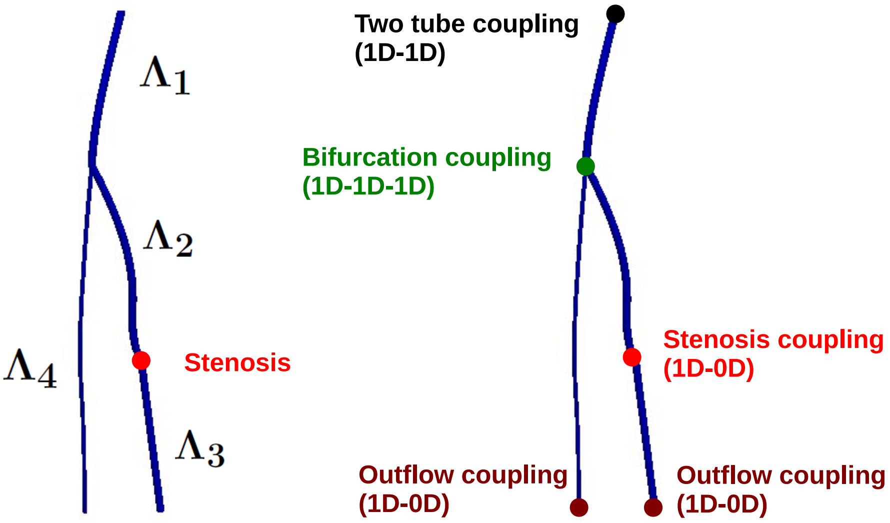

Figure 4.4: Decomposition of the subnetwork embedded in the tissue block. The vessel containing the stenosis is split into two parts. By $\Lambda_i,\ i \in \{1,2,3,4\}$, we denote the main axes of the corresponding vessels on which the 1D models are defined (left). The single vessels are interconnected by different coupling problems (right).

V_4 (see Figure 4.3). By $\Lambda_i,\ i \in \{1,2,3,4\}$, we denote the main axes of the corresponding vessels V_1-V_4 (see Figure 4.4), where the different lines Λ_i are parameterized as follows:

$$\Lambda_i : [0, l_i] \to \Omega,\ s \mapsto \mathbf{x}_{\mathbf{c}i}(s).$$

l_i is the length of vessel $\Lambda_i,\ i \in \{1,2,3,4\}$. Combining the lines Λ_i yields a 1D representation Λ of the embedded network:

$$\Lambda = \bigcup_{i=1}^{4} \Lambda_i.$$

The outlet of V_2 and the inlet of V_3 adjacent to the stenosis are coupled by a *0D model*, similar to the ODE-system (2.133)-(2.134) presented in Subsection 2.4. To adapt this model to the problem which is investigated in this chapter, one has to replace Q_6 and Q_{34} by q_2^{out} and q_3^{in}, denoting the flow rates at the outlet of V_2 and the inlet of V_3:

$$C_{st} \frac{\partial \hat{p}_{st}}{\partial t} = q_2^{out} - q_3^{in}, \tag{4.6}$$

$$-\frac{K_u \rho l_{st}}{A_0} \frac{\partial \hat{q}_{st}}{\partial t} = \Delta p_{st} + \frac{K_v \eta}{A_0 D_0} \hat{q}_{st} + \frac{K_t \rho}{2{A_0}^2} \left(\frac{A_0}{A_{st}} - 1 \right)^2 \hat{q}_{st} \left| \hat{q}_{st} \right|. \tag{4.7}$$

Pressure and flow rate within the stenosis ($\hat{p}_{st},\ \hat{q}_{st}$) are approximated analogous to (2.135):

$$\hat{p}_{st} \approx \frac{p_2^{up} + p_3^{up}}{2}, \qquad \hat{q}_{st} \approx \frac{q_2^{up} + q_3^{up}}{2}, \tag{4.8}$$

where p_2^{up}, p_3^{up},q_2^{up} and q_3^{up} are the upwinded values at the outlet of V_2 and the inlet of V_3. Δp_{st} is given by: $\Delta p_{st} = p_3^{in} - p_2^{out}$, the values p_3^{in} and p_2^{out} are interpolated at the inlet of V_3 and the outlet of V_2. A_0 in (4.7) is the section area at rest of vessel 54 (see Figure 4.5 and Table 4.3 for the radius of A_0). The remaining parameters can be adopted from Table 2.10 and 2.11. For the computation of the upwinded values adjacent to the stenosis one has to close the system by the outgoing characteristics of the linearized 1D system (Theorem 2.3). The upwinded concentration values are determined by standard upwinding.

The 3D-1D coupled problem for blood flow is obtained by similar techniques as in Subsection 3.1, [24, Chapter 6.5]. Using (4.1) and (2.24a) the coupled 3D-1D model for tissue perfusion is directly obtained by the coupling strategy discussed in Section 3.1 [24].

Tissue perfusion problem

$$C_{3d} \frac{\partial p_{3d}}{\partial t} - \nabla \cdot \left(K_{3d} \nabla p_{3d} \right) + \alpha p_{3d} - \phi \left(p_{3d}, p_{1d} \right) \delta_\Lambda \quad = f_p, \quad t > 0,\ \mathbf{x} \in \Omega, \tag{4.9a}$$

$$\frac{\partial}{\partial t} \begin{pmatrix} p_{1d,i} \\ q_{1d,i} \end{pmatrix} + \begin{pmatrix} 0 & \frac{1}{C_{1d,i}} \\ \frac{1}{L_{1d,i}} & 0 \end{pmatrix} \frac{\partial}{\partial s} \begin{pmatrix} p_{1d,i} \\ q_{1d,i} \end{pmatrix} + \begin{pmatrix} \frac{\phi(p_{3d}, p_{1d})}{C_{1d,i}} \\ R_{1d,i} q_{1d,i} \end{pmatrix} \quad = \mathbf{0}, \quad t > 0,\ s \in (0, l_i) \tag{4.9b}$$

$i \in \{1,2,3,4\}$. The term $\phi\delta_\Lambda$ has to be understood as a Dirac measure concentrated on Λ. The line density ϕ is defined as follows:

$$\phi\left(p_{3d}, p_{1d}\right)(s) = 2\pi R_i L_{p,i}\left(p_{1d,i}(s) - \overline{p_{3d,i}(s)}\right), \quad \overline{p_{3d,i}(s)} = \int_0^1 p_{3d}\left(s, R_i, 2\pi\theta\right)\, d\theta. \qquad \text{if } s \in [0, l_i]\,. \tag{4.10}$$

It can be interpreted as the blood flow leakage from the vessels to the tissue (per unit length). For the computation of $p_{3d,i}\left(s, R_i, 2\pi\theta\right)$ in (4.10) one has to integrate the pressure in 3D (p_{3d}) on a circle of radius R_i with center $\mathbf{x_c}_i(s)$ and perpendicular to the tangent in $\mathbf{x_c}_i(s)$. If it holds: $p_{1d,i} > \overline{p_{3d,i}}$, then blood is leaving vessel V_i into the porous medium. In the other case, blood is entering the vessel from the porous matrix, however this case is of no concern in the considered application. The leakage term is weighted by the proportionality factor $L_{p,i}$ modeling the effective hydraulic conductivity (see (A4)). Finally, the value q_{out} in f_p is the sum of the flow rates q_3^{out} and q_4^{out} at the outlets of vessel V_3 and V_4:

$$q_{out}(t) = q_3^{out}(t)\delta_{\Lambda_3(l_3)} + q_4^{out}(t)\delta_{\Lambda_4(l_4)}.$$

$\delta_{\Lambda_i(l_i)}$ is the Dirac measure concentrated on the point $\Lambda_i\left(l_i\right) \in \Omega$.

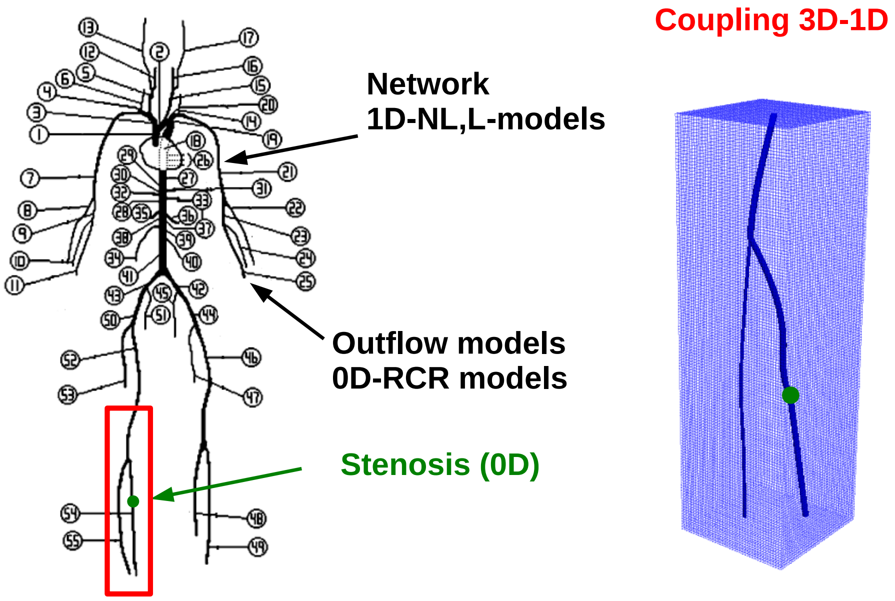

Figure 4.5: Multi-scale model for network flow in tissue. Flow and transport within the tissue are modeled by 3D models, while the network flow is governed by 1D models. The influence of the omitted vessels and the stenosis is simulated by the help of lumped or 0D models. This yields us a 3D-1D-0D coupled model.

Analogously to the tissue perfusion problem, we establish a coupled mass transfer problem which can be obtained by combining the 3D problem (4.3) and the 1D problem (2.24b).

Mass transport problem

$$\frac{\partial c_{3d}}{\partial t} + \nabla \cdot \left(-D_{3d} \nabla c_{3d} + \mathbf{v} c_{3d}\right) + \omega_{3d} c_{3d} - \theta\left(c_{3d}, c_{1d}\right) \delta_\Lambda = f_c, \; t > 0, \; \mathbf{x} \in \Omega, \tag{4.11a}$$

$$\frac{\partial c_{1d,i}}{\partial t} + \frac{\partial}{\partial s}\left(\frac{c_{1d,i} \cdot q_{1d,i}}{A_{0,i}}\right) + \frac{\phi\left(p_{3d}, p_{1d}\right)}{A_{0,i}} c_{1d,i} = 0, \; t > 0, \; s \in (0, l_i) \tag{4.11b}$$

where ω_{3d} and $\mathbf{v}$ are given by (4.5) and (4.4), $i \in \{1, 2, 3, 4\}$. The coupling term θ_{3d} is defined as follows:

$$\theta_{3d}\left(c_{3d}, c_{1d}\right)(s) = 2\pi R_i L_{c,i}\left(c_{1d,i} - \overline{c_{3d,i}}\right), \quad \overline{c_{3d,i}(s)} = \int_0^1 c_{3d}\left(s, R_i, 2\pi\theta\right)\, d\theta,$$
$$\text{if } s \in [0, l_i]\,. \tag{4.12}$$

The coupling term can be considered as a penalization term to weakly enforce the condition $c_{1d,i} = \overline{c_{3d,i}}$ obtained from assumption (A5). The equation $c_{1d,i} = \overline{c_{3d,i}}$ means that the cross-sectional concentration at the actual vessel surface equals the vessel concentration $c_{1d,i}$. $L_{c,i}$ accounts for the permeability of the vessel wall and $A_{0,i} = R_i^2 \pi$ denotes the section area of the vessel associated with Λ_i, where we neglect the variations in the cross-sectional area, i.e., we assume that the vessel walls are rigid walls. By conservation of the blood flow rate we have:

$$\frac{\partial q_{1d,i}}{\partial s} + \phi \approx 0,$$

so that in this case an alternative version of the 1D transport equation (4.11b) is given by:

$$\frac{\partial c_{1d,i}}{\partial t} + q_{1d,i} \frac{\partial c_{1d,i}}{\partial s} = 0, \quad t > 0, \; s \in (0, l_i)\,.$$

The source term f_c is given by the amount of oxygen leaving the network through the outlets of V_3 and V_4 and a Michaelis-Menten law for the metabolic rate:

$$f_c = f_c^{out} - C_{co} \cdot \frac{c_{3d}}{c_{3d,0} + c_{3d}}, \tag{4.13}$$

where C_{co} denotes the consumption rate of oxygen in tissue and $c_{3d,0}$ is the average oxygen concentration in tissue. Furthermore f_c^{out} is given by:

$$f_c^{out} = \frac{q_3^{out} \cdot c_3^{out}}{V} \delta_{\Lambda_3(l_3)} + \frac{q_4^{out} \cdot c_4^{out}}{V} \delta_{\Lambda_4(l_4)}.$$

V is the volume perfused by the outlets of vessel V_3 and V_4.

Initial and boundary conditions

The boundary and initial conditions for the **Tissue perfusion** and **Mass transport problem** are provided in (4.14a)-(4.14d).

$$K_{3d}\frac{\partial p_{3d}}{\partial \mathbf{n}} = 0, \quad t > 0,\ \mathbf{x} \in \partial\Omega, \tag{4.14a}$$

$$\frac{\partial c_{3d}}{\partial \mathbf{n}} = 0, \quad t > 0,\ \mathbf{x} \in \partial\Omega, \tag{4.14b}$$

$$p_{3d}\left(0,\mathbf{x}\right) \equiv 0,\ c_{3d}\left(0,\mathbf{x}\right) \equiv 0, \qquad \mathbf{x} \in \Omega, \tag{4.14c}$$

$$p_{1d}\left(0,s\right) \equiv 0,\ q_{1d}\left(0,s\right) \equiv 0,\ c_{1d}\left(0,s\right) \equiv 0, \qquad s \in \left(0,l_i\right), \tag{4.14d}$$

where $\mathbf{n}$ is the outer normal in $\mathbf{x} \in \partial\Omega$. The boundary values for the 1D problems associated to Λ_i are provided by coupling the 1D models with the reduced or lumped models adjacent to the corresponding inflow ($s = 0$) or outflow ($s = l_i$) boundaries. The different coupling problems are summarized in Table 4.1 and Figure 4.4.

Considering the PDE systems (4.9a),(4.9b); (4.11a),(4.11b) and Table 4.1, it becomes evident that we have a multi-scale (3D-1D-0D) coupled problem (see Figure 4.5).

Table 4.1: Coupling problems at the inflow and outflow boundaries of the different vessels. For each coupling problem, we indicate the corresponding formulas and subsections.

	Inflow boundaries ($s = 0$)	**Outflow boundaries** ($s = l_i$)
$i = 1$	1D-1D coupling between the proximal and the distal part of vessel 52 (see Subsection 2.3.3)	Coupling at a bifurcation (see Subsection 2.3.4)
$i = 2$	Coupling at a bifurcation (see Subsection 2.3.4)	1D-0D coupling at the stenosis (see (4.6)-(4.7))
$i = 3$	1D-0D coupling at the stenosis (see (4.6)-(4.7))	1D-0D coupling at an outflow boundary (see Subsection (2.3.2))
$i = 4$	Coupling at a bifurcation (see Subsection 2.3.4)	1D-0D coupling at an outflow boundary (see Subsection (2.3.2))

4.2 Algorithmic and numerical details

The numerical approximations of the 3D-1D problems (4.9a),(4.9b) and (4.11a),(4.11b) are achieved by applying *multiple time-stepping schemes* [5, 42]. Multi rate or multiple time-stepping methods have been introduced for time dependent systems in which a partitioning in *slow* and *fast* flow variables is meaningful. As we already pointed out at the beginning of this chapter, flow and transport within the blood vessels are fast compared to flow and transport within the porous matrix. To capture the fast wave propagation within the 1D network, small time steps are required to resolve it. On the other hand it is desirable to exert large time steps for the computational expensive 3D problems.

For our numerical simulations we consider a finite time interval $[0, t_{end}]$ which is discretized by a uniform time step size Δt_{3d} for the 3D problems and a uniform time step size Δt_{1d}

for the 1D problems. The number of time steps for the 3D problems is denoted by N_{3d}. Analogous to that we define the same quantity for the 1D problem by N_{1d}. It holds that

$$\Delta t_{1d} = \frac{t_{end}}{N_{1d}} \text{ and } \Delta t_{3d} = \frac{t_{end}}{N_{3d}},$$

where we postulate that $\Delta t_{3d} = m \cdot \Delta t_{1d},\ m \in \mathbb{N},\ m \geq 1$ holds, i.e., for each (slow) step of the 3D problems, m (fast) sub steps of the 1D problems are exerted. The discrete time steps for the 1D problems and the 3D problems are given by:

$$t_{1d}^{(i)} = i \cdot \Delta t_{1d}, \quad i \in \{0, \ldots, N_{1d}\} \text{ and } t_{3d}^{(j)} = j \cdot \Delta t_{3d}, \quad j \in \{0, \ldots, N_{3d}\}.$$

Since the backward Euler scheme is unconditionally stable concerning the choice of the time step size Δt_{3d}, we use this scheme for the time integration in 3D. For the time stepping of the 1D transport equation systems, the third order SSP-Runge Kutta scheme is used (see Subsection 2.2.5). This scheme is TVD and requires a time step restriction which is at least as strict as the one of the forward Euler scheme. However, this property is no drawback in this context, since we need small time steps for the fast flow and transport within the network. Moreover one time step for the 1D problem requires no great computational effort compared to the 3D problems.

For the spacial discretization, the cuboid $\Omega \subset \mathbb{R}^3$ is decomposed into uniform and disjoint cells ω_i. The number of cells is given by M_{3d}:

$$\Omega = \bigcup_{i=1}^{M_{3d}} \omega_i, \quad \omega_i \cap \omega_j = \emptyset \text{ for } i \neq j.$$

Each cell ω_i has an edge length h_{3d}. The nodes of the corresponding cartesian grid are denoted by $\mathbf{x}_i \in \overline{\Omega},\ i = 1, \ldots, M_{3d}'$ and the triangulation of Ω is denoted by $\mathcal{T}_{h_{3d}}$. As a discretization method in space standard Finite elements or Finite Volumes proved to be very effective for the parabolic problem (4.9a). For the convection-diffusion equation (4.11a) cell centered Finite Volumes are well suited, due to their robustness with respect to the convective term. In this thesis we use $\mathbb{Q}^1$-elements for the numerical treatment of the parabolic problem (4.9a) and cell centered Finite Volumes to solve (4.11a) numerically. The family $\{V_{h_{3d}}\}$ of $\mathbb{Q}^1$ finite element spaces is defined as follows:

$$V_{h_{3d}} = \left\{ f \in C(\Omega) \,\middle|\, f|_{\omega_i} \in \mathbb{Q}^1(\omega_i),\ \forall \omega_i \in \mathcal{T}_{h_{3d}} \right\}.$$

As a basis for this space, we choose the Lagrangian Finite element basis $\{\varphi_i\},\ i = 1, \ldots, M_{3d}'$, satisfying: $\varphi_i(\mathbf{x}_j) = \delta_{ij}$. A fully implicit discretization of (4.9a) is given by:

$$\begin{aligned} \frac{1}{\Delta t_{3d}}\left(C_{3d} \cdot p_{3d}^{(n+1)}, \varphi\right)_\Omega + \left(K_{3d} \cdot \nabla p_{3d}^{(n+1)}, \nabla \varphi\right)_\Omega + \left(\alpha p_{3d}^{(n+1)}, \varphi\right)_\Omega + \left(\beta_p \cdot \overline{p_{3d}^{(n+1)}}, \varphi\right)_\Lambda &= \\ \frac{1}{\Delta t_{3d}}\left(C_{3d} \cdot p_{3d}^{(n)}, \varphi\right)_\Omega + \left(\beta_p \cdot p_{1d}^{(m(n+1))}, \varphi\right)_\Lambda + \left(f_p^{(n+1)}, \varphi\right)_\Omega, \quad \forall \varphi \in V_{h_{3d}}, \end{aligned} \tag{4.15}$$

where

$$\beta_p(s) = 2\pi R_i L_{p,i}, \quad \text{if } s \in [0, l_i],\ i = 1, \ldots, 4.$$

The symbols $(\cdot,\cdot)_\Omega$ and $(\cdot,\cdot)_\Lambda$ abbreviate the L^2-scalar product on the 3D domain Ω and on the 1D network Λ, respectively. $p_{3d}^{(l)}$ and $p_{1d}^{(l)}$ denote the numerical approximations at the l-th time step:

$$t_{3d}^{(l)} = l \cdot \Delta t_{3d} = l \cdot m \cdot \Delta t_{1d} \text{ and } t_{1d}^{(l)} = l \cdot \Delta t_{1d}.$$

For the numerical discretization of the 1D transport equation system (4.9b), we a use higher order discontinuous Galerkin method in space and a SSP Runge Kutta method in time. Since these discretization methods have been discussed in Section 2.2, we abbreviate the resulting 1D discretization by an operator $\Phi_{h_{1d},\Delta t_{1d}}^{(p,q)}$ and skip a detailed discussion of the numerical methods for (4.9b) at this point. By h_{1d} and Δt_{1d} we indicate the spacial mesh size in 1D and the time step size, respectively. Considering a time interval:

$$\left(t_{1d}^{(n')}, t_{1d}^{(n'+1)}\right), \quad \Delta t_{1d} = t_{1d}^{(n'+1)} - t_{1d}^{(n')}$$

the discretization operator $\Phi_{h_{1d},\Delta t_{1d}}^{(p,q)}$ maps the numerical approximations $p_{1d}^{(n')}$, $q_{1d}^{(n')}$ and $p_{3d}^{(\lfloor n'/m \rfloor)}$ to the new approximations $p_{1d,i}^{(n'+1)}$, $q_{1d,i}^{(n'+1)}$:

$$\left(p_{1d,i}^{(n'+1)}, q_{1d,i}^{(n'+1)}\right) = \Phi_{h_{1d},\Delta t_{1d}}^{(p,q)} \left(p_{1d}^{(n')}, q_{1d}^{(n')}, p_{3d}^{(\lfloor n'/m \rfloor)}\right). \tag{4.16}$$

Finally, we have the following discretization scheme for the coupled **Tissue perfusion problem** (4.9a),(4.9b):

$$\begin{aligned} &\frac{1}{\Delta t_{3d}} \left(C_{3d} \cdot p_{3d}^{(n+1)}, \varphi\right)_\Omega + \left(K_{3d} \cdot \nabla p_{3d}^{(n+1)}, \nabla\varphi\right)_\Omega + \left(\alpha p_{3d}^{(n+1)}, \varphi\right)_\Omega + \left(\beta_p \cdot \overline{p_{3d}^{(n+1)}}, \varphi\right)_\Lambda = \\ &\qquad \frac{1}{\Delta t_{3d}} \left(C_{3d} \cdot p_{3d}^{(n)}, \varphi\right)_\Omega + \left(\beta_p \cdot p_{1d}^{(m(n+1))}, \varphi\right)_\Lambda + \left(f_p^{(n+1)}, \varphi\right)_\Omega, \quad \forall \varphi \in V_{h_{3d}}, \end{aligned} \tag{4.17}$$

$$\left(p_{1d,i}^{(n'+1)}, q_{1d,i}^{(n'+1)}\right) = \Phi_{h_{1d},\Delta t_{1d}}^{(p,q)} \left(p_{1d}^{(n')}, q_{1d}^{(n')}, p_{3d}^{(\lfloor n'/m \rfloor)}\right), \ i = 1, \dots, 4. \tag{4.18}$$

This numerical scheme is decoupled into two implicit phases (see Figure 4.6):

1. We exert m mirco-steps of step size Δt_{1d} of the 1D network problem, where we use for every sub step the last computed 3D solution: $p_{3d}^{(\lfloor n'/m \rfloor)}$.
2. We advance by one macro-step of the 3D problem (step size Δt_{3d}), using the last computed 1D solution: $p_{1d}^{(m(n+1))}$.

In every macro time step $\left(t_{3d}^{(n)}, t_{3d}^{(n+1)}\right)$ an elliptic problem has to be solved to determine the coordinate vector $\mathbf{p}_{3d}^{(n+1)}$ related to the Finite element solution $p_{3d}^{(n+1)} \in V_h$.

Phase 1

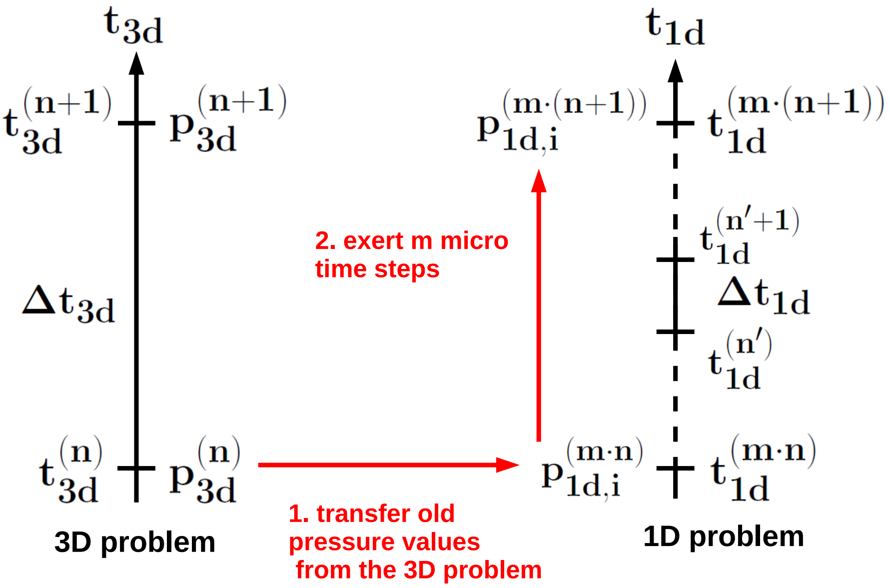

Phase 2

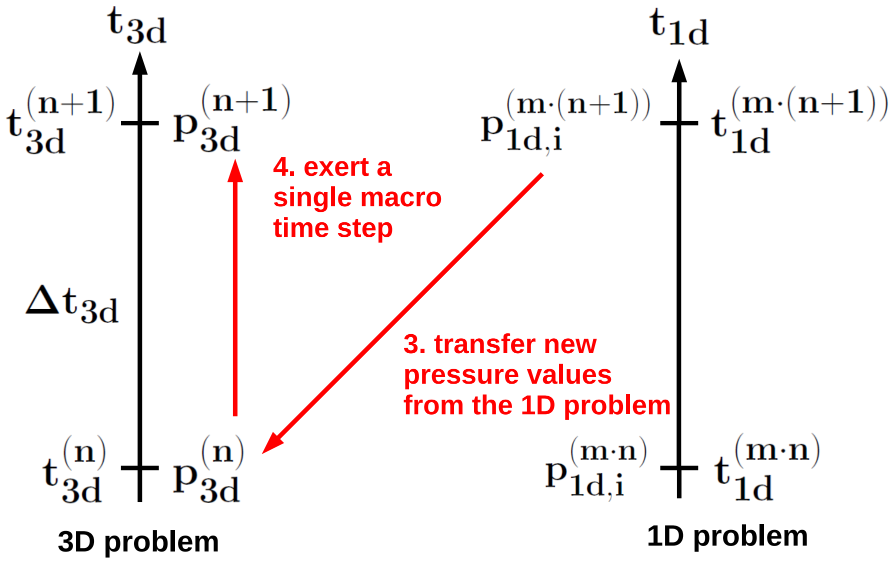

Figure 4.6: Multiple time stepping scheme for the Tissue perfusion problem (4.9a), (4.9b).

To discretize the convection-diffusion equation for mass transport by the cell centered Finite Volume scheme we integrate the PDE (4.11a) over a cell ω_j and a time interval $\left(t_{3d}^{(n)}, t_{3d}^{(n+1)}\right)$:

$$\begin{aligned}\int_{\omega_j} \int_{t_{3d}^{(n)}}^{t_{3d}^{(n+1)}} \frac{\partial c_{3d}}{\partial t} \, dtdx + \int_{\omega_j} \int_{t_{3d}^{(n)}}^{t_{3d}^{(n+1)}} \nabla \cdot \left(-D_{3d} \nabla c_{3d} + \mathbf{v} c_{3d}\right) \, dtdx + \\ \int_{\omega_j} \int_{t_{3d}^{(n)}}^{t_{3d}^{(n+1)}} \omega_{3d} c_{3d} \, dtdx - \int_{\omega_j \cap \Lambda} \int_{t_{3d}^{(n)}}^{t_{3d}^{(n+1)}} \beta_c \left(c_{1d} - \overline{c_{3d}}\right) \, dtd\Lambda = \\ \int_{\omega_j} \int_{t_{3d}^{(n)}}^{t_{3d}^{(n+1)}} f_c \, dtdx. \; \forall \; j = 1, \ldots, M_{3d}, \end{aligned} \tag{4.19}$$

where:

$$\beta_c(s) = 2\pi R_i L_{c,i}, \quad \text{if } s \in [0, l_i], \; i = 1, \ldots, 4.$$

Using integration by parts we arrive at:

$$\begin{aligned}\int_{\omega_j} c_{3d}\left(t_{3d}^{(n+1)}, x\right) \, dx - \int_{\omega_j} c_{3d}\left(t_{3d}^{(n)}, x\right) \, dx - \int_{t_{3d}^{(n)}}^{t_{3d}^{(n+1)}} \int_{\partial \omega_j} D_{3d} \nabla c_{3d} \cdot \mathbf{n} \, dsdt \\ + \int_{t_{3d}^{(n)}}^{t_{3d}^{(n+1)}} \int_{\partial \omega_j} c_{3d} \mathbf{v} \cdot \mathbf{n} \, dsdt - \int_{\omega_j \cap \Lambda} \int_{t_{3d}^{(n)}}^{t_{3d}^{(n+1)}} \beta_c \cdot c_{1d} \, dtd\Lambda + \int_{\omega_j \cap \Lambda} \int_{t_{3d}^{(n)}}^{t_{3d}^{(n+1)}} \beta_c \cdot \overline{c_{3d}} \, dtd\Lambda \\ + \int_{\omega_j} \int_{t_{3d}^{(n)}}^{t_{3d}^{(n+1)}} \omega_{3d} c_{3d} \, dtdx = \int_{\omega_j} \int_{t_{3d}^{(n)}}^{t_{3d}^{(n+1)}} f_c \, dtdx \; \forall \; j = 1, \ldots, M_{3d} \end{aligned} \tag{4.20}$$

Next we approximate c_{3d} by a cell-wise constant function C, where $C_{3d,j}^{(n)}$ denotes the value in cell ω_j at time $t_{3d}^{(n)}$. Moreover we subdivide the boundary $\partial \omega_j$ into facets γ_{jl} which are either intersections with other cells $\partial \omega_j \cap \partial \omega_l$ or intersections with the boundary $\partial \omega_j \cap \partial \Omega$. Based on this notation (see Figure 4.7) and the proposed approximation, we approximate the first two integrals occurring in (4.20) by:

$$\int_{\omega_j} c_{3d}\left(t_{3d}^{(n+1)}, x\right) \, dx \approx C_{3d,j}^{(n+1)} \left|\omega_j\right|, \quad \int_{\omega_j} c_{3d}\left(t_{3d}^{(n)}, x\right) \, dx \approx C_{3d,j}^{(n)} \left|\omega_j\right| \tag{4.21}$$

For the third integral, we have:

$$\begin{aligned}\int_{t_{3d}^{(n)}}^{t_{3d}^{(n+1)}} \int_{\partial \omega_j} D_{3d} \nabla c_{3d} \cdot \mathbf{n} \, dsdt &\approx \Delta t_{3d} D_{3d} \int_{\partial \omega_j} \nabla c_{3d}^{(n+1)} \cdot \mathbf{n} \, ds \\ &= \Delta t_{3d} D_{3d} \sum_{\gamma_{jl}} \int_{\gamma_{jl}} \nabla c_{3d}^{(n+1)} \cdot \mathbf{n} \, ds \\ &\approx \Delta t_{3d} D_{3d} \sum_{\gamma_{jl}} \left|\gamma_{jl}\right| \nabla c_{3d}^{(n+1)} \cdot \mathbf{n}|_{x_{M,jl}}, \end{aligned}$$

where $x_{M,jl}$ denotes the center of the face γ_{jl}. The term $\nabla c_{3d}^{(n+1)} \cdot \mathbf{n}|_{x_{M,jl}}$ is approximated by central differences:

$$\nabla c_{3d}^{(n+1)} \cdot \mathbf{n}|_{x_{M,jl}} \approx \begin{cases} 0 & \text{if } \gamma_{jl} \subset \partial\Omega \\ \frac{C_{3d,l}^{(n+1)} - C_{3d,j}^{(n+1)}}{h_{3d}} & \text{if } \gamma_{jl} \not\subset \partial\Omega. \end{cases}$$

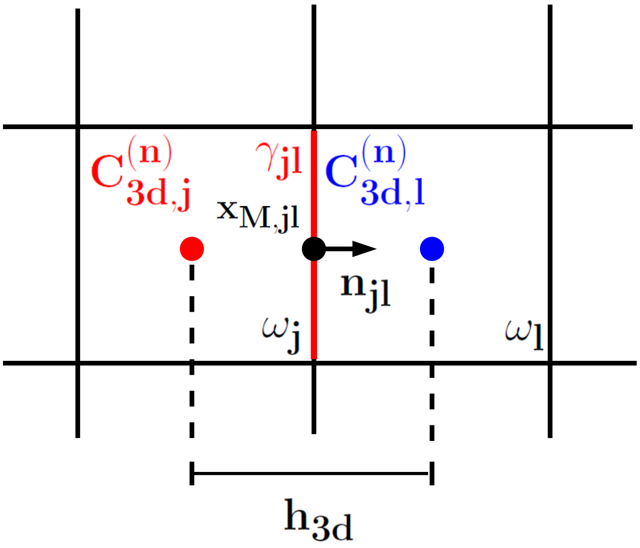

Figure 4.7: Notation used for the Finite Volume discretization.

The discretization of the diffusive part is abbreviated by the numerical flux ϕ_{diff}:

$$\phi_{diff}\left(c_{3d}^{(n+1)}\right) = D_{3d} \sum_{\gamma_{jl}} |\gamma_{jl}| \cdot \begin{cases} 0 & \text{if } \gamma_{jl} \subset \partial\Omega \\ \frac{C_{3d,l}^{(n+1)} - C_{3d,j}^{(n+1)}}{h_{3d}} & \text{if } \gamma_{jl} \not\subset \partial\Omega. \end{cases} \tag{4.22}$$

$$\int_{t_{3d}^{(n)}}^{t_{3d}^{(n+1)}} \int_{\partial\omega_j} D_{3d} \nabla c_{3d} \cdot \mathbf{n}\, dsdt \approx \Delta t_{3d} \cdot \phi_{diff}\left(c_{3d}^{(n+1)}\right)$$

The integral accounting for the convective part of the PDE is discretized by:

$$\begin{aligned} \int_{t_{3d}^{(n)}}^{t_{3d}^{(n+1)}} \int_{\partial\omega_j} c_{3d} \mathbf{v} \cdot \mathbf{n}\, dsdt &\approx \Delta t_{3d} \int_{\partial\omega_j} c_{3d}^{(n+1)} \mathbf{v}^{(n+1)} \cdot \mathbf{n}\, ds \\ &= \Delta t_{3d} \sum_{\gamma_{jl}} \int_{\gamma_{jl}} c_{3d}^{(n+1)} \mathbf{v}^{(n+1)} \cdot \mathbf{n}\, ds \\ &\approx \Delta t_{3d} \sum_{\gamma_{jl}} |\gamma_{jl}| \cdot \begin{cases} 0 & \text{if } \gamma_{jl} \subset \partial\Omega \\ C_{3d,j}^{(n+1)} \mathbf{v}_{jl}^{(n+1)} \cdot \mathbf{n_{jl}} & \text{if } \mathbf{v}_{jl}^{(n+1)} \cdot \mathbf{n_{jl}} \geq 0 \\ C_{3d,l}^{(n+1)} \mathbf{v}_{jl}^{(n+1)} \cdot \mathbf{n_{jl}} & \text{if } \mathbf{v}_{jl}^{(n+1)} \cdot \mathbf{n_{jl}} < 0, \end{cases} \end{aligned}$$

where $\mathbf{v}_{jl}^{(n+1)}$ is the vector field $\mathbf{v}$ at the time $t_{3d}^{(n+1)} = (n+1) \cdot \Delta t_{3d}$ and at $x_{M,jl}$. In this case the numerical flux ϕ_{conv} is given by:

$$\phi_{conv}\left(\mathbf{v}^{(n+1)}, c_{3d}^{(n+1)}\right) = \sum_{\gamma_{jl}} |\gamma_{jl}| \cdot \begin{cases} 0 & \text{if } \gamma_{jl} \subset \partial\Omega \\ C_{3d,j}^{(n+1)} \mathbf{v}_{jl}^{(n+1)} \cdot \mathbf{n_{jl}} & \text{if } \mathbf{v}_{jl}^{(n+1)} \cdot \mathbf{n_{jl}} \geq 0 \\ C_{3d,l}^{(n+1)} \mathbf{v}_{jl}^{(n+1)} \cdot \mathbf{n_{jl}} & \text{if } \mathbf{v}_{jl}^{(n+1)} \cdot \mathbf{n_{jl}} < 0, \end{cases} \tag{4.23}$$

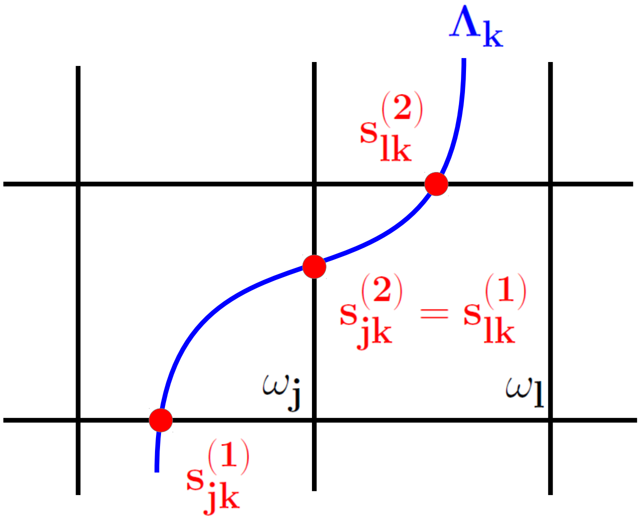

Figure 4.8: Notation used for the line integrals.

Now we have to discretize two terms involving line integrals:

$$\int_{\omega_j \cap \Lambda} \int_{t_{3d}^{(n)}}^{t_{3d}^{(n+1)}} \beta_c \cdot c_{1d} \, dt d\Lambda \approx \Delta t_{3d} \int_{\omega_j \cap \Lambda} \beta_c \cdot c_{1d}^{(n+1)} d\Lambda = \Delta t_{3d} \sum_{k=1}^{4} \int_{\omega_j \cap \Lambda_k} \beta_c \cdot c_{1d}^{(n+1)} d\Lambda_k$$

For every single line integral, we have:

$$\int_{\omega_j \cap \Lambda_k} \beta_c \cdot c_{1d}^{(n+1)} d\Lambda_k = \int_{s_{jk}^{(1)}}^{s_{jk}^{(2)}} \beta_c(s) \cdot c_{1d}^{(n+1)}(s) \left\| \dot{\Lambda}_k(s) \right\|_2 \, ds,$$

where it holds for the integral bounds $s_{jk}^{(1)}$ and $s_{jk}^{(2)}$:

(i) $s_{jk}^{(1)} = \inf \{ s \in [0,1] \mid \Lambda_k(s) \in \omega_j \}$,

(ii) $s_{jk}^{(2)} = \sup \{ s \in [0,1] \mid \Lambda_k(s) \in \omega_j \}$,

(iii) $\left\{ \Lambda_k(s) \middle| s \in \left(s_{jk}^{(1)}, s_{jk}^{(2)} \right) \right\} \subset \omega_j$.

Replacing c_{1d} by $\overline{c_{3d}}$ in the previous formulas, the numerical flux ϕ_{line} for both line integrals is given by:

$$\phi_{line}\left(\beta_c, c_{1d}^{(n+1)}, \overline{c_{3d}^{(n+1)}}\right) = \sum_{k=1}^{4} \int_{\omega_j \cap \Lambda_k} \beta_c \cdot c_{1d}^{(n+1)} d\Lambda_k - \int_{\omega_j \cap \Lambda_k} \beta_c \cdot \overline{c_{3d}^{(n+1)}} d\Lambda_k. \tag{4.24}$$

The remaining volume integrals are approximated as follows:

$$\int_{\omega_j} \int_{t_{3d}^{(n)}}^{t_{3d}^{(n+1)}} \omega_{3d} c_{3d}\, dtdx \approx \Delta t_{3d} \left|\omega_j\right| C_{3d,j}^{(n+1)}, \quad \int_{\omega_j} \int_{t_{3d}^{(n)}}^{t_{3d}^{(n+1)}} f_c\, dtdx \approx \Delta t_{3d} \left|\omega_j\right| f_{c,j}^{(n+1)}.$$

$f_{c,j}^{(n+1)}$ is the evaluation of the source term f_c at the center of cell ω_j and at the time of $t_{3d}^{(n+1)} = (n+1) \cdot \Delta t_{3d}$. As in the previous cases, we introduce also for these integrals a numerical flux ϕ_{vol}:

$$\phi_{vol}\left(c_{3d}^{(n+1)}, f_c\right) = \left|\omega_j\right| C_{3d,j}^{(n+1)} - \left|\omega_j\right| f_{c,j}^{(n+1)}. \tag{4.25}$$

Summarizing the fluxes defined by (4.2)-(4.25), we have:

$$\begin{aligned}\phi_{cd}\left(c_{3d}^{(n+1)}, \overline{c_{3d}^{(n+1)}}, c_{1d}^{(n+1)}, \mathbf{v}^{(n+1)}, \beta_c, f_c\right) &= -\phi_{diff}\left(c_{3d}^{(n+1)}\right) + \phi_{conv}\left(\mathbf{v}^{(n+1)}, c_{3d}^{(n+1)}\right) \\ &- \phi_{line}\left(\beta_c, c_{1d}^{(n+1)}, \overline{c_{3d}^{(n+1)}}\right) + \phi_{vol}\left(c_{3d}^{(n+1)}, f_c\right)\end{aligned} \tag{4.26}$$

From (4.20), (4.21) and (4.26) it follows for the Finite Volume discretization concerning the time interval $\left(t_{3d}^{(n)}, t_{3d}^{(n+1)}\right)$:

$$C_{3d,j}^{(n+1)} - C_{3d,j}^{(n)} + \frac{\Delta t_{3d}}{\left|\omega_j\right|} \phi_{cd}\left(c_{3d}^{(n+1)}, \overline{c_{3d}^{(n+1)}}, c_{1d}^{(n+1)}, \mathbf{v}^{(n+1)}, \beta_c, f_c\right) = 0, \forall j = 1, \ldots, M_{3d}. \tag{4.27}$$

For the numerical solution of the 1D problem (4.11b) governing the oxygen transport within the vessel system, we choose for the spacial discretization, as for (4.9b), a higher order DG method and a SSP Runge Kutta scheme for the time integration. In order to stabilize the solution in the vicinity of steep gradients or shocks, we apply a limiter technique described in Subsection 2.2. As for the **Tissue Perfusion Problem**, we summarize the resulting 1D discretization for a mesh size h_{1d} and a time step size Δt_{1d} by an operator $\Phi_{h_{1d},\Delta t_{1d}}^{(c)}$. It maps the old variable $c_{1d}^{(n')}$ of a micro time step $\left(t_{1d}^{n'}, t_{1d}^{n'+1}\right)$ to the new variables $c_{1d,i}^{(n'+1)}$, where we use for the source term ϕ the pressure values $p_{3d}^{(\lfloor n'/m \rfloor)}$ and $p_{1d,i}^{(\lfloor n'/m \rfloor)}$ from the last macro time step:

$$c_{1d,i}^{(n'+1)} = \Phi_{h_{1d},\Delta t_{1d}}^{(c)}\left(c_{1d}^{(n')}, p_{3d}^{(\lfloor n'/m \rfloor)}, p_{1d,i}^{(\lfloor n'/m \rfloor)}\right), \; i = 1, \ldots, 4. \tag{4.28}$$

Analogously to the multiple time stepping scheme (4.17),(4.18), we couple the discrete systems (4.27) and (4.30) as follows:

$$C_{3d,j}^{(n+1)} - C_{3d,j}^{(n)} + \frac{\Delta t_{3d}}{|\omega_j|}\phi_{cd}\left(c_{3d}^{(n+1)}, \overline{c_{3d}^{(n+1)}}, c_{1d}^{m(n+1)}, \mathbf{v}^{(n+1)}, \beta_c, f_c\right) = 0, \forall j = 1, \ldots, M_{3d}. \tag{4.29}$$

$$c_{1d,i}^{(n'+1)} = \Phi^{(c)}_{h_{1d},\Delta t_{1d}}\left(c_{1d}^{(n')}, p_{3d}^{(\lfloor n'/m \rfloor)}, p_{1d,i}^{(\lfloor n'/m \rfloor)}\right),\ i = 1, \ldots, 4. \tag{4.30}$$

Similarly to (4.17) and (4.18), the system is also decoupled into two phases:

1. We exert m mirco-steps of step size Δt_{1d} of the 1D network problem, where we use for every sub step the last computed 3D and 1D pressure: $p_{3d}^{(\lfloor n'/m \rfloor)}$ and $p_{1d}^{(\lfloor n'/m \rfloor)}$.
2. We advance by one macro-step of the 3D problem (step size Δt_{3d}), using the last computed 1D solution: $c_{1d}^{(m(n+1))}$.

4.3 Results and discussion

Having the model established in the previous sections at hand, we present in this final section some simulation results on the influence of an arterial stenosis in a leg artery (artery 54, **right posterior tibial artery**). The degree of the stenosis is varied between 0%, 90% and 100% and the results are compared with each other. Before we discuss the numerical results, the simulation parameters for the arterial network, the embedded subnetwork and the porous matrix are listed.

4.3.1 Simulation parameters

Parameters arterial network

The different lengths, radii and the remaining vessel parameters are provided in Table 4.3. An outline of the arterial tree is depicted, e.g., in Figure 4.1. For the simulation time we consider a period of twenty seconds: $[0s, 20s]$. The initial conditions for pressure, flow rate and oxygen concentration are set to be zero in every vessel. At the inlet of the aorta (Vessel 1), we prescribe just as in Section 2.4, the following flow rate profile:

$$Q(t) = \begin{cases} 485 \cdot \sin\left(\frac{\pi}{T}t\right)\ \frac{cm^3}{s} & \text{for } 0.0s \leq t \leq T, \\ 0\ \frac{cm^3}{s} & \text{for } T < t \leq 1.0s. \end{cases} \tag{4.31}$$

For $t > 1$ it holds: $Q(t) = Q(t+1)$. The parameter T is given by: $T = 0.3s$.

As a boundary value C_{in} for the oxygen concentration, we choose the mean value of the volumetric oxygen concentration in blood [24][Chapter 2]:

$$C_{in} = 8.75\ \frac{\mu mol}{cm^3}.$$

Table 4.2: List of the fluid parameters and Poisson ratio. Please note that the permeability parameters ϕ_M and ϕ_p are zero for the vessels which are not embedded in the porous medium, i.e., Vessel 1-51 and the proximal part of Vessel 52.

Physical Parameter	sign	value	unit
blood density	ρ	1.028	g/cm^3
blood viscosity	η	4.500	$mPa\ s$
Poisson ratio	ν	0.500	$---$
permeability (blood)	ϕ_M	0.0	$\frac{cm^2}{s}$
permeability (oxygen)	ϕ_p	0.0	$\frac{cm^2}{s}$

At the outflow boundaries, the 1D solutions are determined by 0D-R_1CR_2 models (see Subsection 2.3.2). The total resistances $R = R_1 + R_2$ and compliances C are listed in Table 4.3. An exception is Vessel 52. It is split into two parts. The lower third is embedded into the porous matrix, whereas the remaining part, i.e., the proximal part is not included in the 3D porous medium. To couple both parts of Vessel 52, we use the 1D-1D coupling strategy described in Subsection 2.3.3.

The remaining fluid parameters are summarized in Table 4.2. Please note that the permeability parameters ϕ_M and ϕ_p are zero for the vessels which are not embedded in the porous medium. For the other vessels the permeabilities are chosen according to (4.9a),(4.9b) and (4.11a),(4.11b).

Table 4.3: Physiological data used within the second scenario [108, 118]. The units of the elasticity parameters, peripheral resistances and the peripheral compliances are given by $\left[10^6\ Pa\right]$, $\left[10^2\ Pa\ s\ cm^{-3}\right]$ and $\left[10^{-4} cm^3 Pa^{-1}\right]$ respectively.

Arterial segment	Length $l\ [cm]$	Radius $r\ [cm]$	Thickness $h\ [cm]$	Elastic modulus E	Periph. res. R	Periph. comp. C
1. Ascending aorta	4.0	1.470	0.163	0.4	—	—
2. Aortic arch I	2.0	1.263	0.126	0.4	—	—
3. Brachiocephalic	3.4	0.699	0.080	0.4	—	—
4. R. subclavian I	3.4	0.541	0.067	0.4	—	—
5. R. carotid	17.7	0.473	0.063	0.4	—	—
6. R. vertebral	14.8	0.240	0.045	0.8	60.10	0.30955
7. R. subclavian II	42.2	0.515	0.067	0.4	—	—
8. R. radius	23.5	0.367	0.043	0.8	52.80	0.35235
9. R. ulnar I	6.70	0.454	0.046	0.8	—	—
10. R. interosseous	7.90	0.194	0.028	1.6	843.0	0.02207
11. R. ulnar II	17.1	0.433	0.046	0.8	52.80	0.35235
12. R. int. carotid	17.6	0.382	0.045	0.8	139.00	0.13384
13. R. ext. carotid	17.7	0.382	0.042	0.8	139.00	0.13384
14. Aortic arch II	3.9	1.195	0.115	0.4	—	—
15. L. carotid	20.8	0.413	0.063	0.4	—	—
16. L. int. carotid	17.6	0.334	0.045	0.8	139.00	0.13384
17. L. ext. carotid	17.7	0.334	0.042	0.8	139.00	0.13384

18. Thoracic aorta I	5.2	1.120	0.110	0.4	—	—
19. L. subclavian I	3.4	0.474	0.066	0.4	—	—
20. L. vertebral	14.8	0.203	0.045	0.8	60.10	0.30955
21. L. subclavian II	42.2	0.455	0.067	0.4	—	—
22. L. radius I	23.5	0.324	0.043	0.8	52.80	0.35235
23. L. ulnar I	6.7	0.401	0.046	0.8	—	—
24. L. interosseous	7.9	0.172	0.028	1.6	843.00	0.02207
25. L. ulnar II	17.1	0.383	0.046	0.8	52.80	0.35235
26. Intercoastals	8.0	0.317	0.049	0.4	13.90	1.33840
27. Thoracic aorta II	10.4	1.017	0.100	0.4	—	—
28. Abdominal aorta I	5.3	0.920	0.090	0.4	—	—
29. Celiac I	2.0	0.588	0.064	0.4	—	—
30. Celiac II	1.0	0.200	0.064	0.4	—	—
31. Hepatic	6.6	0.458	0.049	0.4	36.30	0.51251
32. Gastric	7.1	0.375	0.045	0.4	54.10	0.34389
33. Splenic	6.3	0.386	0.054	0.4	23.20	0.80191
34. Sup. mensenteric	5.9	0.499	0.069	0.4	9.30	2.00050
35. Abdominal aorta II	1.0	0.834	0.080	0.4	—	—
36. L. renal	3.2	0.350	0.053	0.4	11.30	1.64640
37. Abdominal aorta III	1.0	0.794	0.080	0.4	—	—
38. R. renal	3.2	0.350	0.053	0.4	—	—
39. Abdominal aorta IV	10.6	0.665	0.075	0.4	—	—
40. Inf. mesenteric	5.0	0.194	0.043	0.4	68.80	0.27041
41. Abdominal aorta V	1.0	0.631	0.065	0.4	—	—
42. R. com. iliac	5.9	0.470	0.060	0.4	—	—
43. L. com. iliac	5.8	0.470	0.060	0.4	—	—
44. L. ext. iliac	14.4	0.482	0.053	0.8	—	—
45. L. int. iliac	5.0	0.301	0.040	1.6	79.36	0.23443
46. L. femoral	44.3	0.361	0.050	0.8	—	—
47. L. deep femoral	12.6	0.356	0.047	0.8	47.70	0.39003
48. L. post. tibial	32.1	0.376	0.045	1.6	47.70	0.39003
49. L. ant. tibial	34.3	0.198	0.039	1.6	55.90	0.33281
50. R. ext. iliac	14.5	0.482	0.053	0.8	—	—
51. R. int. iliac	5.0	0.301	0.040	1.6	79.36	0.23443
52. R. femoral	44.4	0.361	0.050	0.8	—	—
53. R. deep femoral	12.7	0.356	0.047	0.8	47.70	0.39003
54. R. post. tibial	32.2	0.375	0.045	1.6	47.70	0.39003
55. R. ant. tibial	34.4	0.197	0.039	1.6	55.90	0.33281

Parameters subnetwork

The following table contains some additional information concerning the vessels V_1-V_4, which are embedded into the porous matrix (see Section 4.1 for the definition of V_1-V_4).

Table 4.4: Parameters for the subnetwork in the porous medium. The values for $L_{p,i}$ are adapted from [24, Subsection 6.6.4].

Vessel	V_1	V_2	V_3	V_4
Length l_i $[cm]$	14.4	14.6	14.6	34.4
Radius R_i $[cm]$	0.361	0.375	0.375	0.197
Permeability $L_{c,i}$ $\left[cm\ s^{-1}\right]$	10.0	10.0	10.0	10.0
Permeability $L_{p,i}$ $\left[cm\ kPa^{-1}\ s^{-1}\right]$	0.114	0.114	0.114	0.114

Table 4.5: Coordinates and tangents for the lines/mid axes Λ_i.

Λ_1	Coordinates: $(7.5, 7.5, 50.0)^T$; $(4.5, 7.5, 42.0)^T$; $(3.5, 7.5, 36.8)^T$ Tangents: $(0.0, 0.0, -1.0)^T$; $(0.0, 0.0, -1.0)^T$
Λ_2	Coordinates: $(3.5, 7.5, 36.8)^T$; $(5.5, 5.0, 29.0)^T$; $(6.0, 4.5, 21.0)^T$; $(6.5, 4.0, 19.0)^T$ Tangents: $(-1.0, 0.0, -3.0)^T$; $(0.0, 0.0, -1.0)^T$
Λ_3	Coordinates: $(6.5, 4.0, 19.0)^T$; $(7.0, 3.0, 11.0)^T$; $(7.5, 2.0, 3.0)^T$ Tangents: $(0.0, 0.0, -1.0)^T$; $(0.0, 0.0, -1.0)^T$
Λ_4	Coordinates: $(3.5, 7.5, 36.8)^T$; $(2.5, 7.5, 28.5)^T$; $(2.0, 7.5, 20.0)^T$; $(2.5, 7.5, 11.5)^T$; $(2.8, 7.5, 3.0)^T$ Tangents: $(1.0, 0.0, -2.0)^T$; $(0.0, 0.0, -1.0)^T$

The mid axes Λ_i are given by cubic splines through the coordinates, where the tangents of the splines at the beginning and the end of the spline are equal to the provided tangents. The coordinates and tangents are listed in Table 4.5.

The parameters for the stenosis model are provided in Table 2.10 and 2.11. For the length of the stenosis l_{st} we have chosen: $3.0\ cm$. The maximal section area A_0 at the inlet and outlet of the stenosis is equal to the section area of vessel 54 (see Table 4.3), the minimal section area A_{st} is given by: $A_{st} = \beta \cdot A_0$. To model a stenosis degree of 0%, 90%, the factor β is given by: $\beta \in \{1,\ 0.1\}$. A complete occlusion (stenosis degree of 100%) can be modeled by setting the in going characteristic at the outlet of V_2 to the negative value of the outgoing characteristic.

Parameters porous medium

The computational domain is given by:

$$\Omega = 15\ cm \times 15\ cm \times 50\ cm.$$

For the tissue volume perfused by the outlets of vessel V_3 and V_4 we assume the following value: $V = 1.10\ dm^3$. The parameters for the 3D problems (4.9a) and (4.11a) are chosen as follows [24, Subsection 6.6.4]:

$$C_{3d} = 0.01\ kPa^{-1},\ K_{3d} = 0.1\ cm^2\ kPa^{-1}\ s^{-1},\ \alpha = 9.4 \cdot 10^{-4}\ kPa^{-1}\ s^{-1},$$

$$D_{3d} = 1.7 \cdot 10^{-5}\ cm^2\ s^{-1},\ n_b = 0.02,\ p_{ven} = 0\ kPa,\ C_{co} = 0.08\ \mu mol\ cm^{-3}\ s^{-1},$$

$$c_{3d,0} = 0.72\ \mu mol\ cm^{-3},\ p_{3d}\left(0, \mathbf{x}\right) \equiv 0\ kPa,\ c_{3d}\left(0, \mathbf{x}\right) \equiv 0\ mmol\ cm^{-3},\ \forall \mathbf{x} \in \Omega.$$

Parameters discretization

For the spacial discretization of the 1D problems, we use a mesh size h_{1d} of 0.5 cm or 1.0 cm, depending on the length of the vessel. As a time step size Δt_{1d}, we choose: $\Delta t_{1d} = 2.5 \cdot 10^{-5}\ s$. The number of micro time steps m is given by: $m = 200$. Consequently the time step size Δt_{3d} for the 3D problem is equal to $5.0 \cdot 10^{-3}\ s$. Ω is discretized by $h_{3d} \approx 0.375\ cm$ in every space dimension.

4.3.2 Simulation results

The following pages contain some simulation results concerning the scenario described in the previous sections. The concentration values, flow rates and pressure values are reported in the middle of all vessels, for all the narrowing degrees: 0%, 95%, 100%. To illustrate the impact of the stenosis within the peripheral artery 54, we compute the ratio between the normal condition (0%) and the other narrowing degrees.

For an physiologist these values can be used to estimate the risk of an aneurysm caused by an increased pressure in a certain vessel. An aneurysm is a localized, blood filled balloon-like bulge in the wall of a blood vessel [13]. As an aneurysm grows, the risk of rupture becomes higher and higher. When it is torn apart, it can lead to bleeding and a subsequent hypovolemic shock leading to death.

The relative values of the quantities for the embedded subnetwork can be seen in Figure 4.9. Not surprisingly, the pressure and the flow rate break down in Vessel 3 beyond the stenosis. Considering the same physical values within the other embedded vessels, one can observe that the pressure is remarkably increased (up to 37.0% for an occlusion). If the walls of these vessels are weakened at a certain location, there is a high risk that an aneurysm is formed. The flow rates in the feeding vessels V_1 and V_2 are decreased. This blood flow reduction leads to an insufficient blood and oxygen supply of the tissue (see Figure 4.14 and 4.15). Apparently this reduction can not be compensated by the increased flow rate (up to 27.0% for an occlusion) within vessel V_4.

In Figure 4.10 and 4.11, we report the ratios of pressure and flow rate in some vessels which are not embedded in the tissue, to study the global effect of the stenosis on blood flow. It can be seen that there is not only a local impact on blood pressure and flow rate, but the whole vessel system is affected. If we have an narrowing factor of 95%, the pressure is increased about 5% to 6%. For an occlusion the pressure is rising about 9% to 11%. Comparing the flow rate ratios for Vessel 52, 41 and 27 in Figure 4.11 it appears that the flow rate is reduced up to 12% for a narrowing factor of 95% and 15% for a narrowing factor of 100%.

Figures 4.12 and 4.13 show the pressure and the concentration values within the cross section at $y = 7.0\ cm$ at certain time points. Due to the stabilization techniques for the 1D discretization and the robust Finite Volume discretization for the 3D problem there are neither for the 3D problem nor for the 1D problem unphysical oscillations around the concentration fronts. Behind the concentration front in 3D, the concentration values range from 0.0070 $mmol/cm^3$ to 0.0074 $mmol/cm^3$. This is in agreement with other literature [24, Section 6.6], in which the value 0.0072 $mmol/cm^3$ was taken as a reference value for blood oxygen concentration in tissue.

However the propagation speed of the concentration front is too slow, and the pressure values within the porous matrix are too low compared to other literature [24, Section 6.6]. To compute a more realistic propagation of the oxygen concentration, a better estimation of the involved parameters combined with a hierarchical model for flow and transport within the porous medium is required.

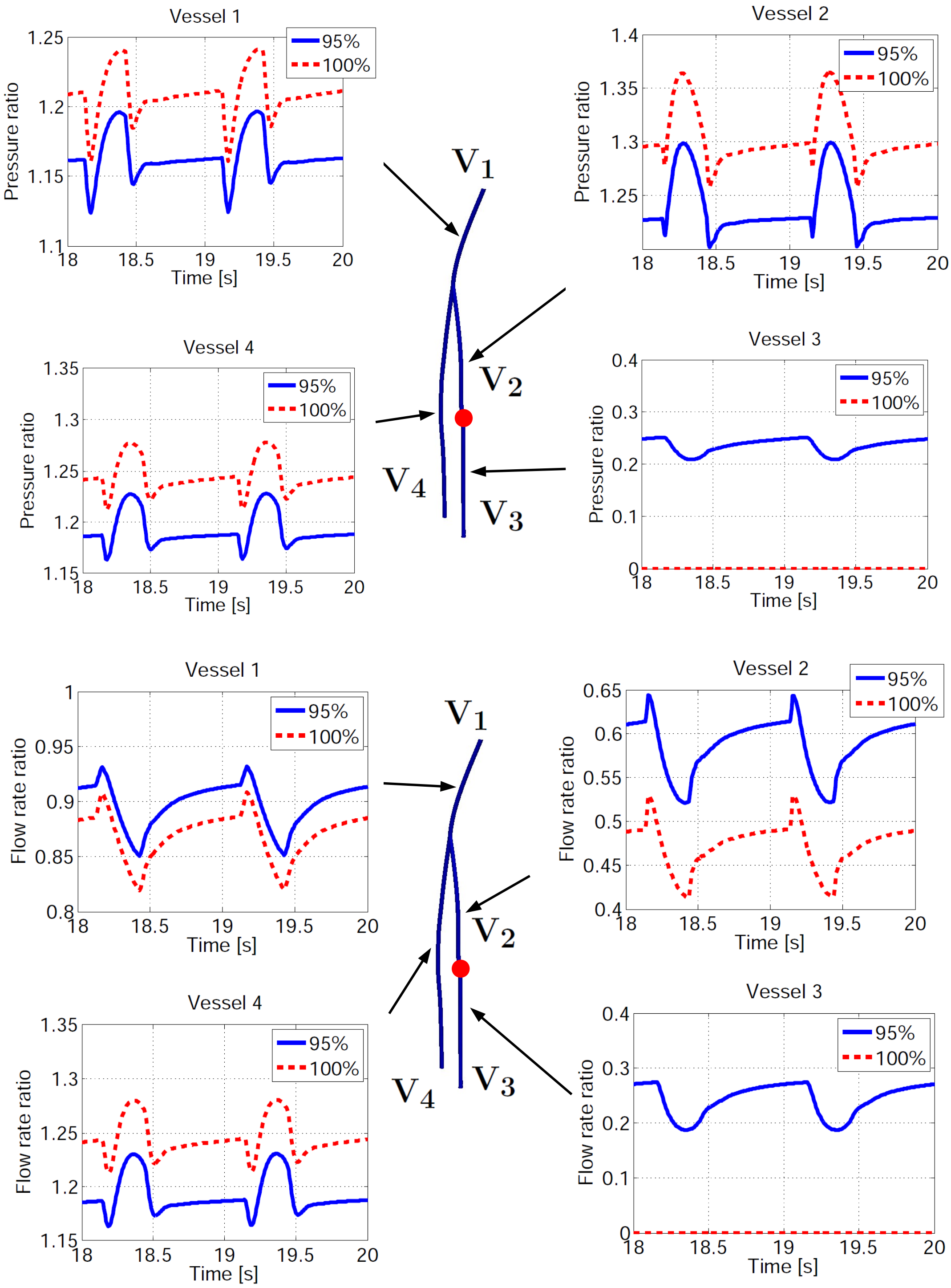

Figure 4.9: Pressure and flow rate ratios within the embedded vessels. The ratios are computed by comparing the abnormal states (95%, 100% narrowing) to the healthy state (0% narrowing).

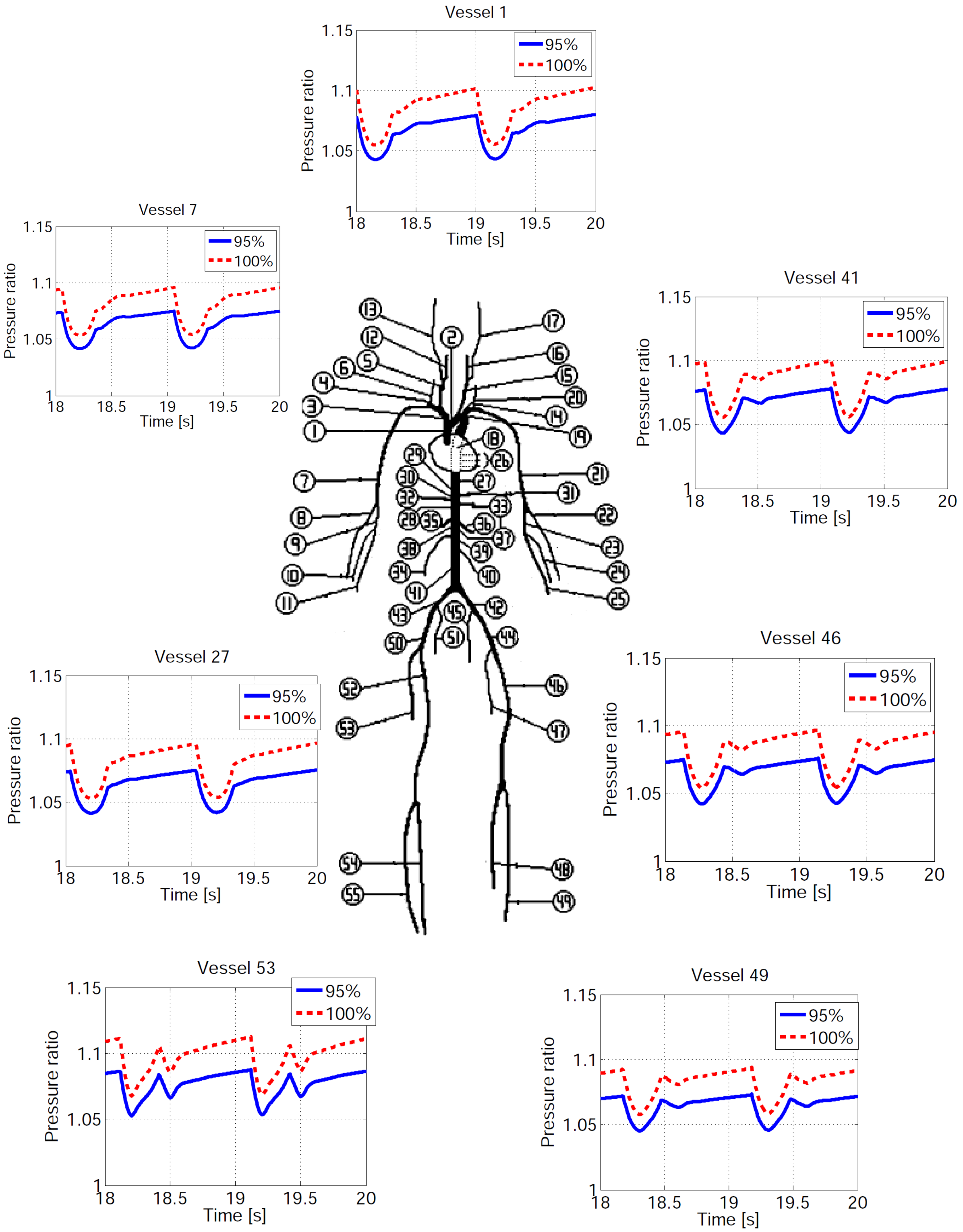

Figure 4.10: Pressure ratios within some arterial vessels which are not included in the porous medium. The ratios are in relation to the healthy state (0% narrowing).

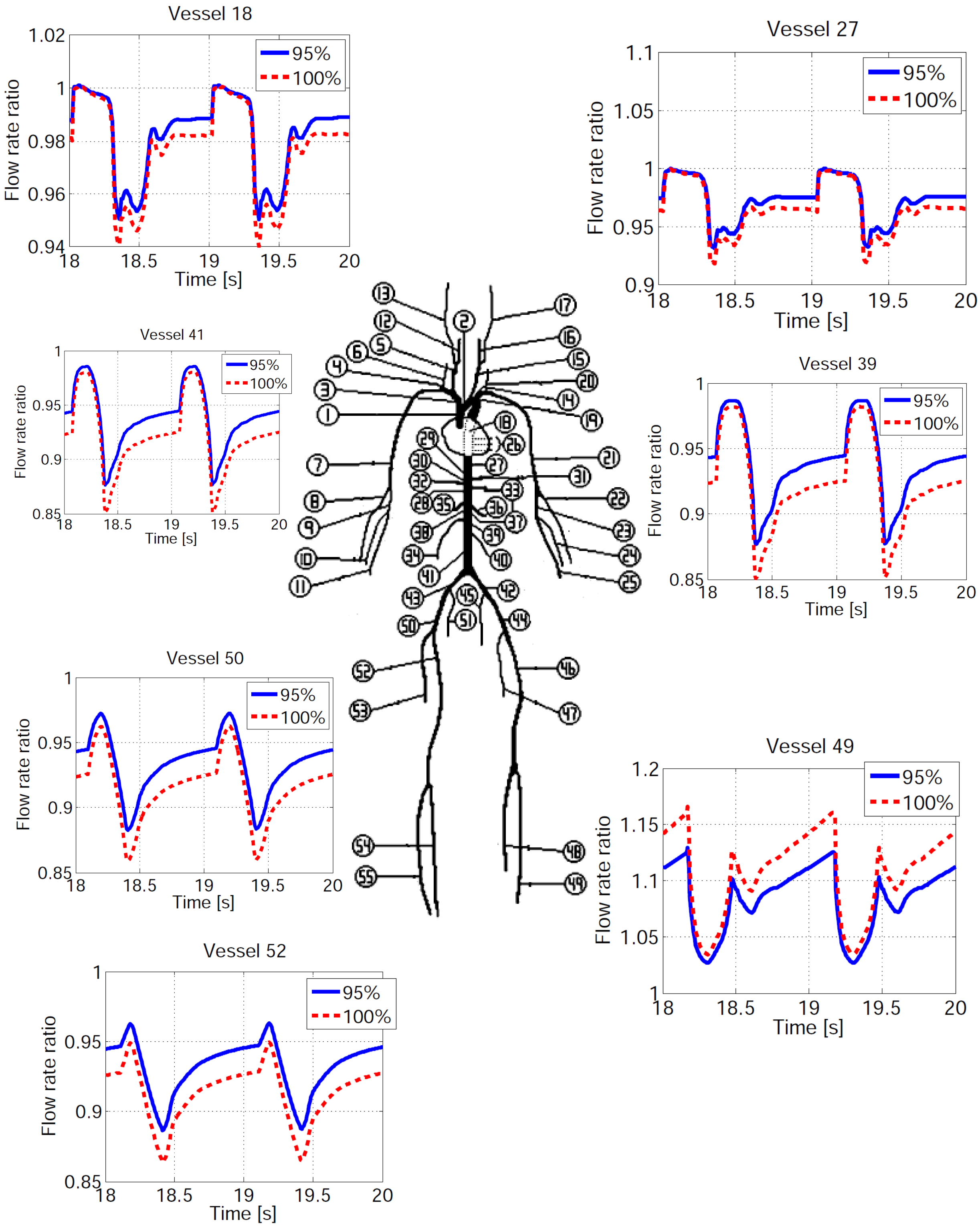

Figure 4.11: Flow rate ratios within some arterial vessels which are not included in the porous medium. The ratios are in relation to the healthy state (0% narrowing).

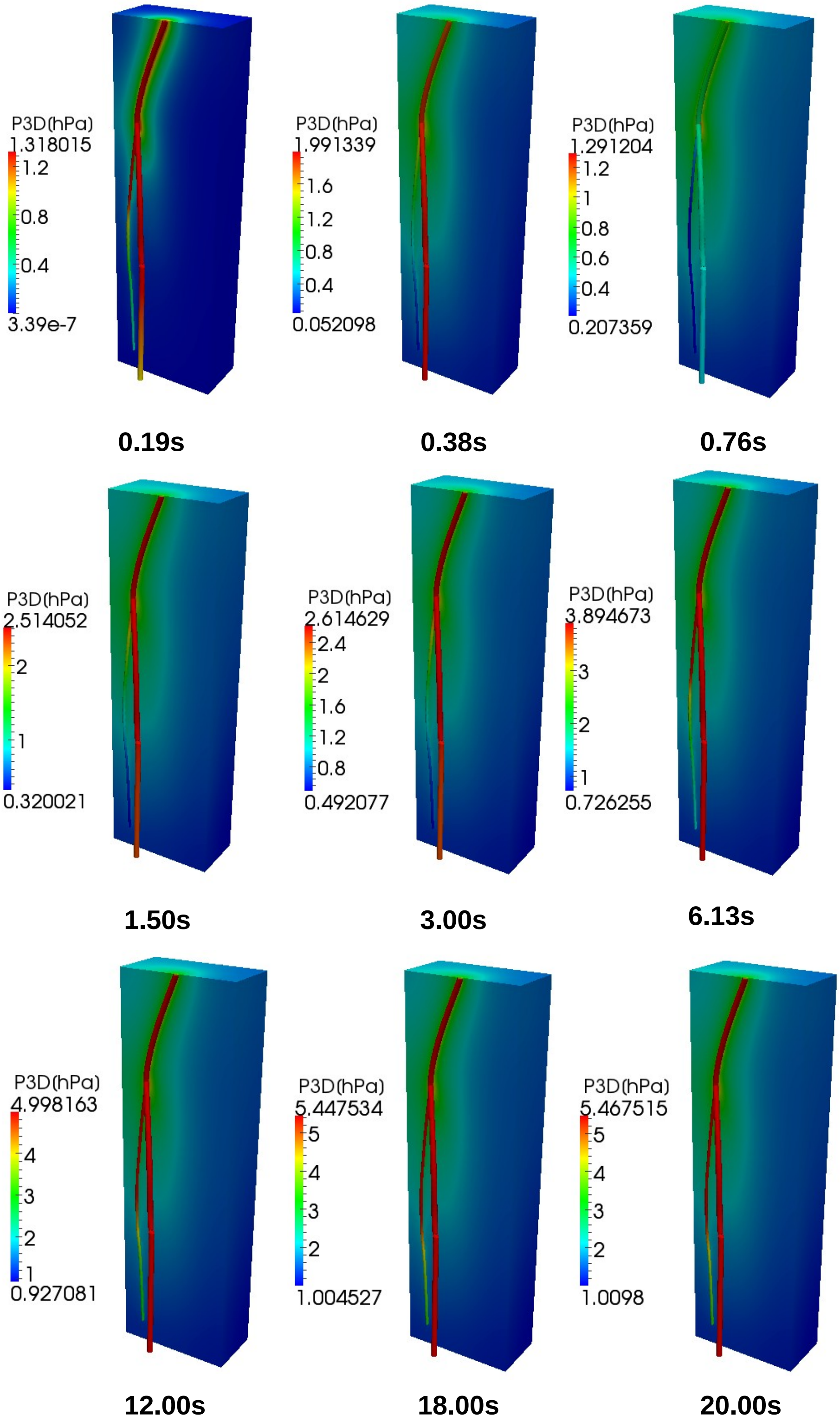

Figure 4.12: Snapshots of the pressure distribution p_{3d}. The cross section is placed at $y = 7.5\ cm$.

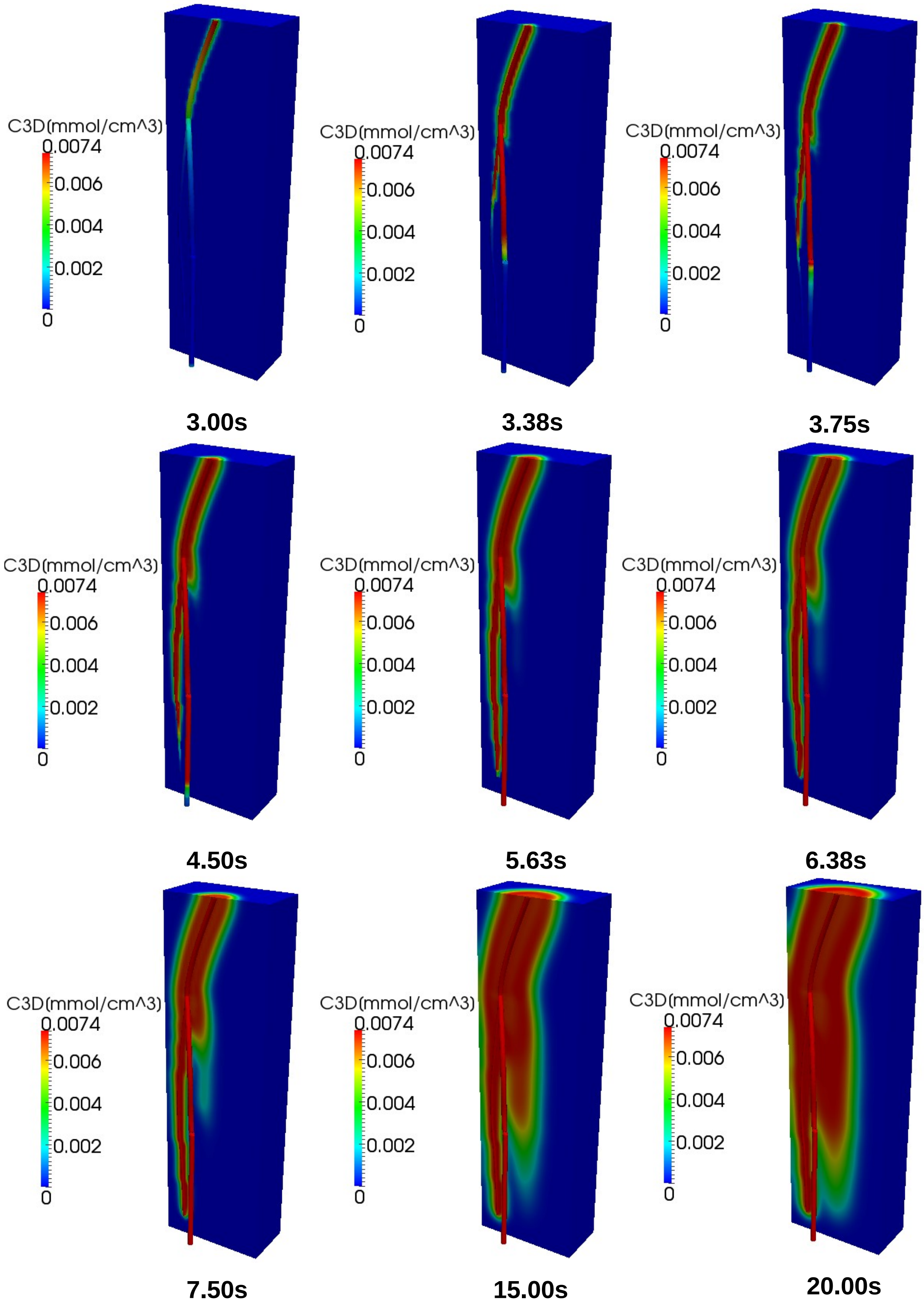

Figure 4.13: Snapshots of the oxygen concentration distribution c_{3d}. The cross section is placed at $y = 7.5\ cm$.

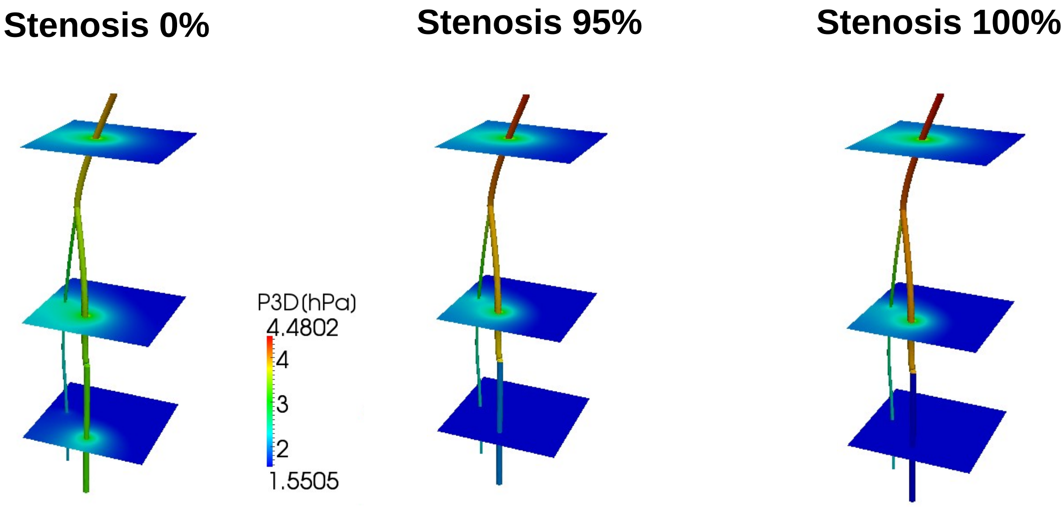

Figure 4.14: Pressure distribution p_{3d} (at $t = 20\ s$) within three different slices at $z = 45$, $z = 25$ and $z = 10$ and for different narrowing factors: 0%, 95% and 100%.

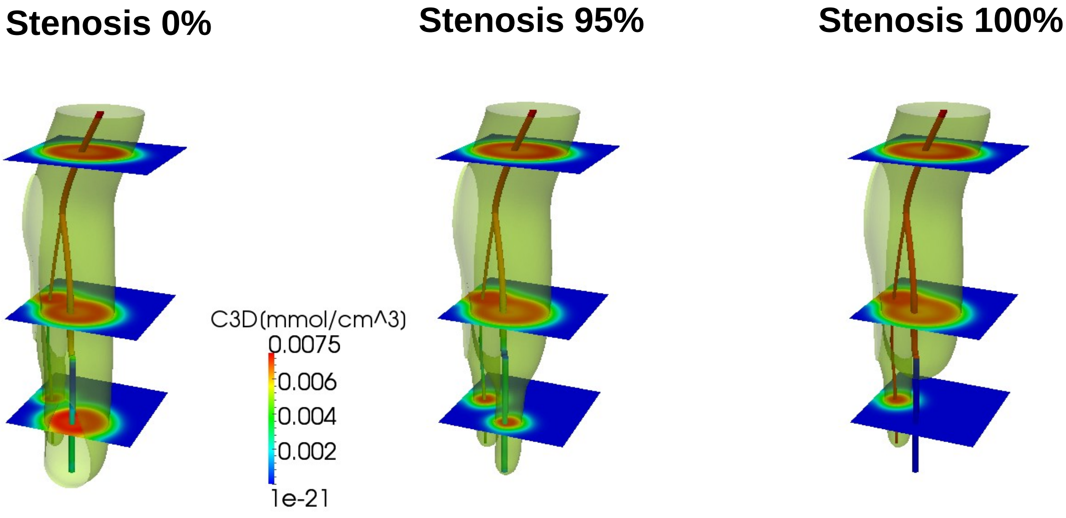

Figure 4.15: Oxygen concentration distribution c_{3d} (at $t = 20\ s$) within three different slices at $z = 45$, $z = 25$ and $z = 10$ and for different narrowing factors: 0%, 95% and 100%. The concentration front corresponds to the value 0.005 $mmol/cm^3$.

5 Summary and outlook

In this thesis, we have presented a mathematical model for blood flow and mass transport in vascularized human tissue. The basis of this model is formed by a domain decomposition approach [24, 35, 38] separating the fast flow region (main arteries) from the slow flow region (tissue, capillary bed) and assigning different models to them. By this mean the heterogeneous flow behavior can be better accounted for.

Since the human blood vessel system is composed of a huge number of blood vessels, the corresponding flow and mass transport processes are governed by reduced 1D and 0D models to decrease the computational cost. Thereby, the 1D models having the shape of non-linear or linear transport equation systems have been used to model the large and middle sized arteries branching out of the heart. For arteries of small length 0D lumped parameter models have been used (see Section 2.1). In order to reduce numerical diffusion, dispersion and oscillations higher order DG-methods in combination with hierarchical limiter developed in [58, 61, 62] have been generalized to the considered transport equation systems (see Section 2.2). The reduced models have been applied to single vessels of a given network. A global solution is obtained by coupling the single PDE or ODE systems at the bifurcations by an algebraic system of equations. Up to now only a single type of model (e.g. non-linear 1D model) was assigned to each vessel. Here, we have shown how different types of models (non-linear, linear 1D models and 0D models) can be connected at a bifurcation. Furthermore the existing models [3, 40] have been extended to enable the simulation of mass transport through a bifurcation [65].

By this mathematical model, we resolve only a small part of the circulatory system. The influence of the omitted vessels is incorporated by coupling the models in the terminal vessels with homogenized 0D models. These models have a similar structure as the 0D lumped parameter models which are used for the small vessels within the network [4]. As in the case of the bifurcations these models had to be extended by an equation governing the mass transport (see Section 2.3).

In the final section of the Chapter 2 (Section 2.4), we have investigated an issue from medical engineering, i.e., the influence of a unilateral carotid stenosis on brain oxygenation. The stenosis was modeled by a 0D lumped parameter model [100, 108, 120]. To model mass transport through a stenosis the existing model has been extended by an additional coupling equation. According to medical knowledge there are essentially two ways to balance the reduced blood flow and oxygen transport due to a carotid stenosis. The brain tissue is supplied by a ring like vessel system (Circle of Willis) containing collateral backup vessels which are not required in the healthy case. If the blood flow through a carotid is reduced, the missing blood flow can be compensated by the other carotid and the backup vessels within the Circle of Willis (see Figure 2.30). The other way is the reduction of cerebral resistances at the outlets of the cerebral arteries. In our model this compensation mechanism is based on the metabolic demand of the brain tissue [2, 63]. For a medical scientist it is of great interest to judge the significance of these auxiliary mechanisms. By the help of our model, it has been revealed that a unilateral stenosis becomes critical starting from a narrowing degree of 85%. In the case of a severe stenosis (narrowing degree of 95%) the oxygen supply can only be balanced, if *both* compensation mechanisms work.

The simulation of blood flow and transport from the blood vessels into the surrounding 3D tissue requires the derivation of coupling conditions. Due to the fact that flow and transport are governed by 1D and 0D models it is necessary to derive 3D-1D or 3D-0D coupled problems. Doing so, we adapted an approach presented in [24, 26]. In these publications the pressure within the tissue has been computed by a parabolic or elliptic equation and the velocity field by Darcy's law. A convection diffusion equation has been used to determine the transport of a substance like oxygen within the tissue. Since the coupling of dimensionally reduced models with 3D models is not standard, the basic principles of this coupling strategy were introduced and analyzed by elliptic 3D-1D diffusion reaction equations. The 3D and 1D equations are linked by their source terms, where the source term of the 3D equation contains Dirac point or line source terms concentrated on the outlets and the main axes of the vessels. The associated reduction of regularity deteriorates the convergence of Finite element methods and makes the numerical analysis more difficult. In order to overcome these difficulties weighted Sobolev spaces and graded meshes were used to prove optimal convergence results [25]. Our approach concerning the numerical analysis is not based on graded or adapted meshes but on uniform meshes. Furthermore the approximation errors are not measured by weighted norms, but by a L^2-seminorm excluding the locations of the Delta source terms. It has been shown that standard Finite element methods converge optimal with respect to this seminorm. This means that Finite elements cause no pollution effect in the computational domain. Numerical investigations in 2D and 3D confirm this theoretical result. By the help of this insight, iterative solution schemes for coupled problems have been designed and a convergence criterium has been derived. Numerical results show that the convergence criterium is sharp and that the method converges optimal at a fixed distance to the singularities.

After studying the coupling strategy for stationary 3D-1D coupled problems, time dependent models for blood flow and transport from the blood vessels into the tissue have been established. Flow and transport within the blood vessels are governed by the PDE or ODE systems considered in Chapter 2. The dynamics in the 3D tissue matrix is governed by a parabolic equation for the pressure field, by Darcy's law for the velocity field and a convection diffusion equation for the transport. To couple the 3D and 1D models, we use the strategy discussed in Chapter 3. The numerical approximations of the coupled problems are achieved by applying multiple time-stepping schemes [5, 42].

This mathematical model has been used to determine the impact of a peripheral stenosis on tissue perfusion and the local impact on blood flow within the vessels. The blood vessel network consists of the 55 main arteries of the human body. A stenosis is placed in an artery of the lower right foot. For convenience not the whole arterial vessel system is embedded into the tissue, but only the arteries adjacent to the stenosis are surrounded by tissue. We varied the degree of the stenosis and reported the pressure drops together with the reduced oxygen transport in the tissue. In addition to that it has been shown how the pressures and flow rates are changed within the arteries due to the stenosis. For an occlusion we have seen that the pressures in the proximal arteries near the stenosis are remarkably increased compared to the healthy state. This insight is very important for physiologists to identify high risk areas for aneurysms.

The achieved results raise new interesting issues concerning the modeling of blood flow and transport, numerical analysis and discretization methods. In this thesis, we have assumed that the initial section areas and elasticity parameters are constant for each vessel. If one is interested to examine the effect of a tapered vessel, the models considered in Chapter 2 have to be enhanced. In particular, a different area-pressure relation has to be used (see Remark 2.1) [37].

The numerical analysis which has been done for elliptic problems with Dirac point source terms can be extended to elliptic and parabolic problems with line source terms [44]. Furthermore 3D-1D coupled problems can be analyzed.

The last chapter of this thesis provides some possiblities for future work. Concerning the time dependent coupled PDE systems presented in Chapter 4, it would be interesting to test the performance of space time methods. Contrary to the standard discretization approaches, these methods consider the time variable as an additional space variable and treat both space and time simultaneously. Thus it is possible to use within a computational domain different time step sizes [111]. Obviously in the vicinity of the blood vessels smaller time step sizes are required than in other parts of the tissue domain, since there the flow velocities are much higher.

The numerical results presented in Section 4.3 show no oscillations and a qualitatively meaningful behavior. However, the pressure values in the porous tissue are too small and the resulting speed of the concentration front is too low. This should be improved by introducing a hierarchical flow model for the tissue [54, 112] and a better estimation of the involved simulation parameters. Moreover it would be interesting from a modeling point of view to examine compensation mechanisms for peripheral stenoses, as we have done it in the context of carotid stenoses.

Publications by the author

- T.Weinzierl and T. Köppl:
  A Geometric Space-time Multigrid Algorithm for the Heat Equation
  Numerical Mathematics: Theory, Methods and Applications, 5(1), 110-130, 2012
- T. Köppl, B. Wohlmuth and R. Helmig:
  Reduced one-dimensional modelling and numerical simulation for mass transport in fluids
  Int. J. Numer. Meth. Fluids, 72(2), 135-156, 2013
- T. Köppl and B. Wohlmuth:
  Optimal a priori error estimates for an elliptic problem with Dirac right-hand side
  SIAM J. Numer. Anal., 52(4), 1753-1769, 2014
- T. Köppl, M. Schneider, U. Pohl and B. Wohlmuth:
  The influence of an unilateral carotid artery stenosis on brain oxygenation
  Medical Engineering and Physics, 36(7), 905-914, 2014

Notations and abbreviations

- **Mathematical symbols:**

  $\mathbb{R}$: field of real numbers

  $\mathbf{v}(i)$: i-th component of a vector $\mathbf{v} \in \mathbb{R}^n,\ 1 \leq i \leq n$

  $A(i,j)$: entry of a matrix $A \in \mathbb{R}^{m \times n},\ 1 \leq i \leq m,\ 1 \leq j \leq n$ in the i-th row and the j-th column

  δ_{ij} : Kronecker symbol: $\delta_{ij} = \begin{cases} 1 \text{ if } i = j \\ 0 \text{ if } i \neq j \end{cases}$

  $\mathcal{O}$: Landau symbol

  $C_c^\infty(\Omega)$: space of test functions with compact support in Ω

  3D: abbreviation for three dimensional

  1D: abbreviation for one dimensional

  0D: abbreviation for zero dimensional

- **Medical terms:**

  systole: Period of time during the heart cycle in which blood is pushed out of the heart

  diastole: Period of time during the heart cycle in which no blood is pushed out of the heart

  proximal and distal: Terms from anatomy that are used to describe parts of a feature that are respectively close (proximal) to or distant (distal) from the heart

List of Figures

List of Tables

Bibliography

[1] R. Adams and J. Fournier. *Sobolev Spaces.* Elsevier Ltd. Amsterdam, 2003.

[2] J. Alastruey, S.M. Moore, K.H. Parker, T. David, J. Peiró, and S.J. Sherwin. Reduced modelling of blood flow in the cerebral circulation: Coupling 1-d, 0-d and cerebral autoregulation models. *International journal for numerical methods in fluids*, 56(8):1061–1067, 2008.

[3] J. Alastruey, K.H. Parker, J. Peiro, S.M. Byrdc, and S.J. Sherwin. Modelling the circle of Willis to assess the effects of anatomical variations and occlusions on cerebral flows. *Journal of Biomechanics*, 40:1794–1805, 2007.

[4] J. Alastruey, K.H. Parker, J. Peiro, and S.J. Sherwin. Lumped parameter outflow models for 1-D blood flow simulations: effect on pulse waves and parameter estimation. *Communications in Computational Physics*, 4:317–336, 2008.

[5] J. F. Andrus. Numerical solution of systems of ordinary differential equations separated into subsystems. *SIAM Journal on Numerical Analysis*, 16(4):605–611.

[6] T. Apel, O. Benedix, D. Sirch, and B. Vexler. A priori mesh grading for an elliptic problem with Dirac right-hand side. *SIAM J. Numer. Anal.*, 49:992–1005, 2011.

[7] T. Apel, A.-M. Sändig, and J. R. Whiteman. Graded mesh refinement and error estimates for finite element solutions of elliptic boundary value problems in non-smooth domains. *Math. Methods Appl. Sci.*, 19:63–85, 1996.

[8] R. Araya, E. Behrens, and R. Rodriguez. A posteriori error estimates for elliptic problems with Dirac delta source terms. *Numer. Math.*, 105:193–216, 2006.

[9] K. Baber. *Coupling Fuelcells and Bloodflow, PhD Thesis.* University of Stuttgart, 2014.

[10] I. Babuška. Error bounds for finite element method. *Numer. Math.*, 16:322–333, 1971.

[11] T. Barth and D. Jepersen. The design and application of upwind schemes on unstructured meshes . *AIAA, Aerospace Sciences Meeting*, 27th Reno:3.5.2, 1999.

[12] P. Bastian, M. Blatt, A. Dedner, C. Engwer, R. Klöfkorn, R. Kornhuber, M. Ohlberger, and O. Sander. A Generic Grid Interface for Parallel and Adaptive Scientific Computing. Part II: Implementation and Tests in DUNE. *Computing*, 82(2-3):121–138, 2008.

[13] J. Behrends, J. Bischofberger, and R. Deutzmann et. al. *Duale Reihe Physiologie, 2. Auflage.* Thieme Verlag Stuttgart, 2012.

[14] C. Bertolotti, Z. Qin, and B. Lamontagne et al. Influence of multiple stenosis on Echo-Doppler functional diagnosis of peripheral arterial disease: a numerical and experimental study. *Ann. Biomed. Eng.*, 34:564–574.

[15] D. Braess. *Finite Elemente.* 4. Auflage, Springer-Verlag Berlin Heidelberg, 2007.

[16] S. Canic and E.H. Kim. Mathematical analysis of quasilinear effects in a hyperbolic model blood flow through compliant axi-symmetric vessels. *Math. Meth. Appl. Sci.*, 26:1161–1186, 2003.

[17] E. Casas. L^2 estimates for the finite element method for the Dirichlet problem with singular data. *Numer. Math.*, 47:627–632, 1985.

[18] E. Casas. Control of an elliptic problem with pointwise state constraints. *SIAM J. Control Optim.*, 24:1309–1318, 1986.

[19] E. Casas, C. Clason, and K. Kunisch. Parabolic control problems in measure spaces with sparse solutions. *SIAM J. Control Optim.*, 51(1):28–63, 2013.

[20] E. Casas and E. Zuazua. Spike controls for elliptic and parabolic PDEs. *Syst. Control Lett.*, 62(4):311–318, 2013.

[21] L. Cattaneo and P. Zunino. Computational models for fluid exchange between microcirculation and tissue interstitium. *Networks and Heterogeneous Media*, 9:135–159.

[22] B. Cockburn, S.Y. Lin, and C.-W. Shu. TVB Runge–Kutta local projection discontinuous Galerkin methods for scalar conservation laws III: one dimensional systems. *Journal of Computational Physics*, 84:90–113, 1989.

[23] A. Cristiano, I. Malossi, P. J. Blanco, P. Crosetto, S. Deparis, and A. Quarteroni. Implicit coupling of one-dimensional and three-dimensional blood flow models with compliant vessels. *Multiscale Model. Simul.*, 11(2):474–506, 2013.

[24] C. D'Angelo. *Multi scale modelling of metabolism and transport phenomena in living tissues, PhD Thesis.* EPFL, Lausanne, 2007.

[25] C. D'Angelo. Finite element approximation of elliptic problems with Dirac measure terms in weighted spaces. Applications to 1D-3D coupled problems. *SIAM J. Numer. Anal.*, 50:194–215, 2012.

[26] C. D'Angelo and A. Quarteroni. On the coupling of 1D and 3D diffusion-reaction equations. Applications to tissue perfusion problems. *Mathematical Models and Methods in Applied Sciences*, 18(8):1481–1504, 2008.

[27] P. Deuflhard and A. Hohmann. *Numerische Mathematik I.* de Gruyter Verlag Berlin, 2002.

[28] P. Deuflhard and M. Weiser. *Adaptive Lösung partieller Differentialgleichungen.* De Gruyter Verlag, 2011.

[29] K. Devault, P. A. Gremaud, V. Novak, M. S. Olufsen, G. V.Eresek, and P. Zhao. Blood flow in the Circle of Willis: Modeling and calibration. *SIAM Journal on Multiscale Modeling and Simulation*, 7(2):888–909, 2008.

[30] H. Egger, U. Rüde, and B. Wohlmuth. Energy-corrected finite element methods with optimal convergence for corner singularities. *SIAM J. Numer Anal.*, 52(1):171–193, 2014.

[31] K. Erbertseder. *A multi-scale model for describing cancer-therapeutic transport in the human lung, PhD Thesis.* University of Stuttgart, 2012.

[32] L. Evans. *Partial Differential Equations.* American Mathematical Society Providence, Rhode Island, 1998.

[33] R. Fahrig, H. Nikolov, A.J. Fox, and D.W. Holdsworth. A threedimensional cerebrovascular flow phantom. *Medical Physics*, 26:1589–1599, 1999.

[34] M. Fernandez, V. Milisic, and A. Quarteroni. Analysis of a geometrical multiscale blood flow model based on the coupling of ODE's and hyperbolic PDE's. *SIAM Multiscale Model. Simul.*, 4(1):215–236, 2005.

[35] L. Formaggia, D. Lamponi, and A. Quarteroni. One-dimensional models for blood flow in arteries. *Journal of Engineering Mathematics*, 47:251–276, 2003.

[36] L. Formaggia, F. Nobile, and A. Quarteroni. *A one-dimensional model for blood flow: application to vascular prosthesis.* I. Babuška, T. Miyoshi and P.G. Ciarlet (eds), Mathematical Modeling and Numerical Simulation in Continuum Mechanics. Volume 19 of Lecture Notes in Computational Science and Engineering. Springer-Verlag, Berlin pp. 137–153., 2002.

[37] L. Formaggia, F. Nobile, A. Veneziani, and A. Quarteroni. Multiscale modelling of the circulatory system: a preliminary analysis. *Vis. Sci.*, 2:75–83, 1999.

[38] L. Formaggia, A. Quarteroni, and A. Veneziani. *Cardiovascluar Mathematics-Modelling and simulation of the circulatory system.* Springer-Verlag, Italia, Milano, 2009.

[39] O. Forster. *Analysis 1.* Vieweg Verlag Wiesbaden, 2004.

[40] V.E. Franke, K.H. Parker, L.Y.Wee, N.M. Fisk, and S.J. Sherwin. Time domain computational modelling of 1D arterial networks in monochorionic placentas. *Mathem. Mod. and Num. Analysis*, 37:557–580, 2003.

[41] R. Fritzsch. *Optimale Finite-Elemente-Approximationen für Funktionen mit Singularitäten, PhD Thesis.* TU Dresden, 1990.

[42] C.W. Gear and D.R. Wells. Multirate linear multistep methods. *BIT*, 24(4):484–502.

[43] D. Gilbarg and N. Trudinger. *Elliptic Partial Differential Equations of Second Order.* Springer-Verlag Berlin Heidelberg New York, 1998.

[44] W. Gong, G. Wang, and N. Yan. Approximations of elliptic optimal control problems with controls acting on a lower dimensional manifold. *SIAM J. Control Optim.*, 52(3):2008–2035, 2014.

[45] S. Gottlieb and C.-W. Shu. Total Variation Diminishing Runge-Kutta schemes. *Math. Comp.*, 67:73–85, 1998.

[46] S. Gottlieb, C.-W. Shu, and E. Tadmor. Strong stability-preserving high-order time discretization methods. *SIAM Review*, 43:89–112, 2001.

[47] J. Grote, O. Laue, P. Eiring, and M. Wehler. Evaluation of brain tissue O_2 supply based on results of PO_2 measurements with needle and surface microelectrodes. *J. Auton. Nerv. Syst.*, 57:68–72, 1996.

[48] M. Gurris. *Implicit Finite Element Schemes for Compressible Gas and Particle-Laden Gas Flows.* TU Dortmund, 2009.

[49] M. Hacker, I.I. Messer, S. William S, and K. Bachmann. *Pharmacology: principles and practice.* Academic Press, 2009.

[50] E. Hairer and G. Wanner. *Solving Ordinary Differential Equations, Nonstiff Problems.* Springer Verlag, Berlin, 1993.

[51] A. Han, D.Y. Yoon, S.K. Chang, K.J. Lim, B.M. Cho, Y.C. Shin, S.S. Kim, and K.H. Kim. Accuracy of CT angiography in the assessment of the circle of Willis: comparison of volume-rendered images and digital subtraction angiography. *Acta Radiol.*, 52:889–893, 2011.

[52] A. Harten. High resolution schemes for hyperbolic conservation laws. *J. Comp. Phys.*, 49:357–393, 1983.

[53] R. Helmig. *Multiphase Flow and Transport Processes in the Subsurface.* Springer, Berlin, Heidelberg, 1997.

[54] J.M. Huyghe and D.H. Van Campen. Finite deformation theory of hierarchically arranged porous solids. 2. Constitutive behavior. *Int. J. Eng. Sci.*, 33:1873–1886.

[55] J.D Jackson. *Classical Electrodynamics.* Wiley, New York, 1999.

[56] K. Koenigsberger. *Analysis 1.* Springer-Verlag Berlin Heidelberg New York, 2004.

[57] L. Krivodonova, J. Xinb, J.-F. Remacle, N. Chevaugeon, and J.E. Flaherty. Shock detection and limiting with discontinuous Galerkin methods for hyperbolic conservation laws. *Applied Numerical Mathematics*, 48:323–338, 2004.

[58] L. Krivodovona. Limiters for high-order discontinuous Galerkin methods. *Journal of Computational Physics*, 226:879–896, 2007.

[59] A. Kufner. *Weighted Sobolev spaces.* Teubner Verlagsgesellschaft, 1980.

[60] D. Kuzmin. A vertex-based hierarchical slope limiter for p-adaptive discontinuous Galerkin methods. *J. Comput. Appl. Math.*, 233:3077–3085, 2010.

[61] D. Kuzmin. Slope limiting for discontinuous Galerkin approximations with possibly non-orthogonal Taylor basis. *Int. J. Numer. Meth. Fluids*, 1:1–12, 2011.

[62] D. Kuzmin, R. Löhner, and S. Turek. *Flux-Corrected Transport - Principles, Algorithms and Applications.* Springer-Verlag, Berlin, 2004.

[63] T. Köppl, M. Schneider, U. Pohl, and B. Wohlmuth. The influence of an unilateral carotid artery stenosis on brain oxygenation. *Medical Engineering and Physics*, 36(7):905–914.

[64] T. Köppl and B. Wohlmuth. Optimal a priori error estimates for an elliptic problem with Dirac right-hand side. *SINUM*, 52(4):1753–1769, 2014.

[65] T. Köppl, B. Wohlmuth, and R. Helmig. Reduced one-dimensional modelling and numerical simulation for mass transport in fluids. *Int. J. Numer. Meth. Fluids.*, 72(2):135–156, 2013.

[66] H. Köstler. *Akkurate Behandlung von Singularitäten bei partiellen Differentialgleichungen, Diploma Thesis.* Friedrich–Alexander–Universität Erlangen Nürnberg, 2003.

[67] E.G. Lakatta. Age-associated cardiovascular changes in health: impact on cardiovascular disease in older persons. *Heart Fail Rev.*, 7:29–49, 2002.

[68] P. D. Lax. *Hyperbolic Systems of Conservation Laws and the Mathematical Theory of Shock Waves.* SIAM Publications, Philadelphia, 1973.

[69] D. Leaykekhman, D. Meidner, and B. Vexler. Optimal error estimates for finite element discretization of elliptic optimal control problems with finitely many pointwise state constraints. *COAP*, 55(3):769–802, 2013.

[70] R. J. LeVeque. *Numerical Methods for Conservation Laws.* Birkhäuser Verlag, Basel, Boston, Berlin, 1992.

[71] R. J. LeVeque. *Finite Volume Methods for Hyperbolic Problems.* Cambridge Texts in Applied Mathematics, Cambridge University Press, 2002.

[72] H. Li, A. Mazzucato, and V. Nistor. Analysis of the finite element method for transmission/ mixed boundary value problems on general polygonal domains. *Electron. Trans. Numer. Anal.*, 37:41–69, 2010.

[73] F. Liang, S. Takagi, R. Himeno, and H. Liu. Multi-scale modeling of the human cardiovascular system with applications to aortic valvular and arterial stenoses. *Med. Biol. Eng. Comput.*, 47:743–755, 2009.

[74] J.L. Lions and E. Magenes. *Non-homogeneous boundary value problems and applications. Vol. III. Translated from the French by P. Kenneth.* Springer Verlag, 1973.

[75] M. St. Louis, B.D. Park, M. Dahn, and P. Bozeman. Cerebral intolerance during flow arrested carotid angioplasty. *Vasc. Endovascular Surg.*, 26:85–88, 2012.

[76] H. Luo, J.D. Baum, and R. Löhner. A discontinuous Galerkin method based on a Taylor basis for the compressible flows on arbitrary grids. *J. Comput. Phys.*, 227:8875–8893, 2008.

[77] H. Manninen, K. Mäkinen, R. Vanninen, A. Ronkainen, and H. Tulla. How often does an incomplete circle of Willis predispose to cerebral ischemia during closure of carotid artery? Postmortem and clinical imaging studies. *Acta Neurochir (Wien)*, 151:1099–1105, 2009.

[78] Emilie Marchandise, Marie Willemet, and Valérie Lacroix. A numerical hemodynamic tool for predictive vascular surgery. *Medical Engineering and Physics*, 31(1):131–144, 2009.

[79] J. Melenk. *hp-Finite Element Methods for Singular Perturbations.* volume 1796 of Lecture Notes in Mathematics, Springer-Verlag Berlin Heidelberg, 2002.

[80] J. Melenk and B. Wohlmuth. Quasi-optimal approximation of surface based Lagrange multipliers in finite element methods. *SIAM Journal on Numerical Analysis*, 50:2064–2087, 2012.

[81] K. Michalak and C. Ollivier-Gooch. Limiters for unstructured higher-order accurate solutions of the Euler equations. *In: Proceedings of the AIAA Forty-Sixth Aerospace Meeting*, 2008.

[82] C. Michoski, C. Mirabito, C. Dawson, E.J Kubatko, D. Wirasaet, and J.J. Westerink. Adaptive hierarchic transformations for dynamically p-enriched slope-limiting over discontinuous Galerkin systems of generalized equations. *J. Comput. Phys.*, 27th Reno, 2010.

[83] V. Milisic and A. Quarteroni. Analysis of lumped parameter models for blood flow simulations and their relation with 1D models. *Math. Modelling and Num. Analysis*, 38(4):613–632, 2004.

[84] S.M. Moore, T. David, J. Chase, J. Arnold, and J. Fink. 3D models of blood flow in the cerebral vasculature. *Journal of Biomechanics*, 39:1454–1463, 2006.

[85] S.M. Moore, K.T. Moorhead, J.G. Chase, T. David, and J. Fink. One-dimensional and three-dimensional models of cerebrovascular flow. *Journal of Biomechanical Engineering*, 127:440–449, 2005.

[86] G. Ning, Y. Gong, S. Gong, Q. Pan, J. Yan, and A.R. Pries. Simulation of blood pressure wave pPropagation in a vessel by one-dimensional model. *WCB 2010, IFMBE Proceedings*, 31:1366–1369, 2010.

[87] J. Nitsche and A. Schatz. Interior estimates for Ritz-Galerkin methods. *Math. Comp.*, 28:937–958, 1974.

[88] V. Papantchev, V.Stoinova, A.Aleksandrov, D. Todorova-Papantcheva, S. Hristov, D. Petkov, G.Nachev, and W. Ovtscharoff. The role of Willis circle variations during unilateral selective cerebral perfusion: a study of 500 circles. *Eur. J. Cardiothorac Surg.*, 44:743–753, 2013.

[89] A. Quarteroni, R. Sacco, and F. Saleri. *Numerical mathematics.* Springer Verlag Berlin Heidelberg New York, 2002.

[90] A. Quarteroni and A. Valli. *Numerical approximation of partial differential equations.* Springer-Verlag Berlin Heidelberg, 2008.

[91] G. Raman, D. Moorthy, N. Hadar, I.J. Dahabreh, T.F. O'Donnell, D.E. Thaler, E. Feldmann, Lau J, and G.D. Kitsios. Management strategies for asymptomatic carotid stenosis: a systematic review and meta-analysis. *Ann Intern Med.*, 158:676–685, 2013.

[92] P.L Roe. Approximate Riemann solvers, parameter vectors and difference schemes. *Journal of Computational Physics*, 43(2):357–372, 1981.

[93] U. Rüde. Multiple τ-extrapolation for multigrid methods. Technical Report Bericht I-8701, Institut für Informatik, TU München, 1987.

[94] U. Rüde and C. Zenger. On the treatment of singularities in the multigrid method. Technical Report Bericht I-8526, Institut für Informatik, TU München, 1985.

[95] U. Rüde. On the accurate computation of singular solutions of Laplace's and Poisson's equation. *Proceedings of the Third Copper Mountain Conference, April 5-10*, 1987.

[96] A.H. Schatz and L.B. Wahlbin. Interior maximum norm estimates for finite element methods. *Math. of Comp.*, 31:414–442, 1977.

[97] R.F. Schmidt, F. Lang, and M. Heckmann. *Human Physiology, Second completely Revised Edition.* Springer–Verlag Berlin Heidelberg New York, 1989.

[98] R. Scott. Finite element convergence for singular data. *Numer. Math.*, 21:317–327, 1973.

[99] R. Scott and S. Zhang. Finite element interpolation of nonsmooth functions satisfying boundary conditions. *Math. of Comp.*, 54:483–493, 1990.

[100] B.D. Seeley and D.F. Young. Effect of geometry on pressure losses across models of arterial stenoses. *J. of Biomech.*, 9:439–448, 1976.

[101] T. Seidman, M. Gobbert, D. Trott, and M. Kružik. Finite element approximation for time-dependent diffusion with measure-valued source. *Numer. Math.*, 122:709–723, 2012.

[102] S. J. Sherwin, L. Formaggia, J. Piero, and V. Franke. Computational modelling of 1D blood flow with variable mechanical properties and its application to the simulation of wave propagation in the human arterial system. *Int. J. for Numerical Methods in Fluids*, 43:673–700, 2003.

[103] S.J. Sherwin, V.E. Franke, J. Peiro, and K.H. Parker. One-dimensional modelling of a vascular network in space-time variables. *J. Engng. Maths.*, 47:217–250, 2003.

[104] C.-W. Shu and S. Osher. Efficient implementation of essentially non-oscillatory shock-capturing schemes. *J. Comput. Phys.*, 77:439–471, 1988.

[105] S. Silbernagel and A. Despopoulos. *Taschenatlas der Physiologie.* Thieme-Verlag, 8. Auflage, 2012.

[106] M. Siouffi, V. Deplano, and R. Pelissier. Experimental analysis of unsteady flows through a stenosis. *Journal of Biomechanics*, 31:11–19.

[107] N.P. Smith, A.J. Pullan, and P.J. Hunter. An anatomically based model of transient coronary blood flow in the heart. *SIAM J. Appl. Math.*, 62:990–1018, 2001.

[108] N. Stergiopulos, D.F. Young, and T.R. Rogge. Computer simulation of arterial flow with applications to arterial and aortic stenoses. *J. of Biomech.*, 25:1477–1488, 1992.

[109] Q. Sun and G.X. Wu. Coupled finite difference and boundary element methods for fluid flow through a vessel with multibranches in tumours. *International journal for numerical methods in biomedical engineering*, 29(3):309–331.

[110] E.F. Toro. *Riemann Solvers and Numerical Methods for Fluid Dynamics, A Practical Introduction.* Springer Verlag Berlin Heidelberg New York, 1999.

[111] T.Weinzierl and T. Köppl. A geometric space-time multigrid algorithm for the heat equation. *Numerical Mathematics: Theory, Methods and Applications*, 5(1):110–130.

[112] W.J. Vankan, J.D. Janssen J.M.R.J. Huyghe and, A. Huson, W. Hacking, and W. Schreiner. Finite element analysis of blood perfusion through biological tissue. *Int. J. Eng. Sci.*, 35:375–385.

[113] A. Veneziani and C. Vergara. Flow rate defective boundary conditions in haemodynamics simulations. *International Journal for Numerical Methods in Fluids*, 47:803–816, 2005.

[114] M. Vinokur and J.L. Montagne. Generalized flux-vector splitting and roe average for an equilibrium real gas. *Journal of Computational Physics*, 89(2):276–300, 1990.

[115] A. Waaijer, M.S. van Leeuwen, H.B. van der Worp, H.J. Verhagen, W.P. Mali, and B.K. Velthuis. Anatomic variations in the circle of Willis in patients with symptomatic carotid artery stenosis assessed with multidetector row CT angiography. *Cerebrovasc. Dis.*, 23:267–274, 2007.

[116] L. Wahlbin. Local behavior in finite element methods. In P.G Ciarlet and J.L Lions, editors, *Handbook of numerical Analysis*, volume II: Finite element methods (Part 1), pages 353–522. North-Holland, 1991.

[117] L. Wahlbin. *Superconvergence in Galerkin Finite Element Methods*, volume 1605 of *LNM.* Springer, Berlin, 1995.

[118] J.J. Wang and K.H. Parker. Wave propagation in a model of the arterial circulation. *Journal of Biomechanics*, 37:457–470.

[119] M. Yang and Z. J. Wang. A parameter-free generalized moment limiter for high-order methods on unstructured grids. *Adv. in Appl. Math. Mech.*, 1:451–480, 2009.

[120] D.F. Young and F. Tsai. Flow characteristics in models of arterial stenoses II. *J. of Biomech.*, 6:547–559, 1973.

[121] C. Zhang, L. Wang, X. Li, S. Li, F. Pu, Y. Fan, and D. Li. Modeling the circle of Willis to assess the effect of anatomical variations on the development of unilateral internal carotid artery stenosis. *Bio-Medical Materials and Engineering.*, 23:511–519, 2013.